Electrochemical Studies of the Applications of Novel Carbon-Based Materials

A thesis submitted for the degree of

Doctor of Philosophy

in Physical and Theoretical Chemistry

Yifan Wang

Linacre College, University of Oxford

Trinity Term, 2022

Abstract

In this thesis, the electrochemical behaviour of novel carbon-based materials is investigated in respect of supercapacitor applications. The first chapter explains the concern over climate change, potential for renewable energy, and significance of energy storage. Much emphasis is placed on the mechanism (e.g., electric double-layer capacitance and pseudocapacitance) and electrode materials (e.g., carbon and metal oxides) for supercapacitors. The second chapter introduces the basic principles of electrochemistry as well as electrochemical methods and characterisation techniques used in this work.

In the first project, the electrochemical oxidation of Mn^{2+} ions to manganese dioxides is carried out on boron-doped diamond electrodes via cyclic voltammetry. A composite electrode is fabricated by potentiostatic deposition of MnO_2 on boron doped diamond, and its electrochemical performance is then measured. The motivation of this work is to illustrate that MnO_2, a cheap material with pseudocapacitance, can improve the overall performance of carbon-based composite electrodes for supercapacitor applications.

The second work exploits carbonised seaweed paper, which is a biomass-derived carbon material. MnO_2 is deposited on seaweed paper-derived carbon potentiostatically to form a composite for electrochemical measurements and characterisation. Seaweed paper after carbonisation benefits from electric double-layer capacitance, whilst incorporation of the pseudocapacitive MnO_2 further extends the potential window and specific capacitance of the hybrid electrode materials as supercapacitors.

The third study investigates nickel treated filter paper for supercapacitor applications. Carbon derived from filter paper is produced at low carbonisation temperature with *in situ* nickel treatment. Its electrochemical behaviour is researched by removing or keeping the nickel

particles. Particularly, faradaic battery-type characteristics is observed electrochemically on account of conversion of nickel into electroactive nickel hydroxide in aqueous alkaline media. Nickel treated filter paper acts as a promising supercapacitor material which is economical and environmentally friendly.

The fourth research involves a number of carbon materials derived from biomass and biowaste with bimetallic cobalt/manganese metal-organic frameworks (MOFs) modification. The composite materials take advantage of the electric double-layer capacitance from the biomass-derived carbon and faradaic battery-type contributions from the pyrolysed MOFs in alkaline electrolytes. In particular, the bulk carbon-based electrode material bears favourable comparison with its powdery counterpart in supercapacitor applications.

Overall, this thesis reports the electrochemical studies of novel carbon-based materials for supercapacitor applications in regard to renewable energy and energy storage.

Acknowledgements

First and foremost, I would express my sincerest and deepest gratitude to my supervisor, Professor John S. Foord, for accepting me as a DPhil student in his group. His support and guidance throughout these years have been most precious and memorable. Especially, many thanks for his patience and understanding during the pandemic in 2020 and 2021. This thesis would not have been accomplished without his help and kindness.

I would like to thank the postdoctoral group members, Dr. Luyun Jiang, Dr. Martin Rosillo-Lopez, and Dr. Emina Hadzifejzovic for their academic help and advice in the lab and in the office. I am also grateful to the other group members who are all doctorate degree holders now, Cai Xiaosheng, Thomas Hiu-Ming Lau, Ella Bentin, Wang Chenbo, and Scarlett Ma Yue for their support in daily life and help with my studies.

I would like to individually thank Yutang. I am especially grateful for his company in Oxford.

I would like to thank my classmates and friends in Fudan University Shanghai and Imperial College London, Chen Chen, Guo Yang, Fan Tao, Zhang Bingjie, and Li Yuxin for their friendship that lasts for ten years or more. I would also like to thank my friends and colleagues in PwC Shenzhen, Darren, Faye, Rebecca, Chris, Iris, and Kate for their support especially when I decided to resign and start my DPhil.

I would like to thank some friends whom I met in past years, Shen Shaojie, Su Guanglong, Deng Jialin, Guo Rujing, Ju Liyun, and Ma Xiaoshan. I would like to separately thank Xu Zheng for his friendship and our fun discussions.

Last but not least, my boundless gratitude must go to my beloved parents, Wang Lianfu and Chen Aili, and family members. They have given me everything and words just fail me. All the best to my cousin, Chen Bozhang.

May Shanghai have good fortune.

Contents

Glossary

Roman symbols

Symbol	Meaning	Usual Units
a	activity	none
A	area	cm^2
c, $[c]$	concentration of species c	mol cm^{-3}
C	capacitance	F
C_s	specific capacitance	F g^{-1} or F cm^{-2}
d	charge separation distance	m
D	diffusion coefficient	cm^2 s^{-1}
E	electrode potential	V
E^0	standard electrode potential	V
E_f^0	formal electrode potential	V
E_{eq}	equilibrium potential	V
f	F/RT	V^{-1}
F	the Faraday constant (≈ 96485)	C mol^{-1}
i	current	A
i_0	standard exchange current	A

$i_{a/c}$	anodic/cathodic current	A
i_p	peak current	A
i_f	faradaic current	A
i_c	charging current	A
j	flux	mol cm^{-2} s^{-1}
k^0	standard heterogenous rate constant	cm s^{-1}
$k_{c/a}$	rate constants for the cathodic/anodic reactions	c
m	mass	g
M	molar mass	g mol^{-1}
n	number of electrons transferred	none
q (Q)	charge	C
R	universal gas constant (≈ 8.314)	J mol^{-1} K^{-1}
R_{ct}	charge-transfer resistance	Ω
R_Ω	solution resistance	Ω
t	time	s
T	temperature	K
u	mobility of ion	cm^2 V^{-1} s^{-1}
v	linear potential scan rate	V s^{-1}
z	charge of the ion	none

Z_f	faradaic impedance	Ω
Z_{Im}	imaginary part of impedance	Ω
Z_{Re}	real part of impedance	Ω
Z_w	Warburg impedance	Ω

Greek symbols

Symbol	Meaning	Units
α	transfer coefficient	none
γ	activity coefficient	none
ε_r	dielectric constant	none
ε_0	permittivity of free space	$C^2\ N^{-1}\ m^{-1}$
η	overpotential	V
λ	wavelength of light	nm
φ	electrical potential	V
Φ	work function of a phase	eV
ν	frequency of light	s^{-1}
σ	charge density	$C\ cm^{-2}$
ω	angular frequency, $2\pi f$	s^{-1}

Abbreviations

Abbreviation	Meaning
AFC	alkaline fuel cells
BET	Brunauer-Emmett-Teller surface area
BDD	boron-doped diamond
CA	chronoamperometry
CE	counter electrode
CNT	carbon nanotube
CP	chronopotentiometry
CV	cyclic voltammetry
CVD	chemical vapour deposition
EDLC	electric double-layer capacitor
EDS/EDX	energy-dispersive X-ray spectroscopy
EIS	electrochemical impedance spectroscopy
ESR	equivalent series resistance
FESEM	field emission scanning electron microscopy
GCD	galvanostatic charge-discharge
H_4DOBDC	2,5-Dihydroxyterephthalic acid

HER	hydrogen evolution reaction
HTC	hydrothermal carbonisation
IHP	inner Helmholtz plane
IMFP	inelastic mean free path
LSV	linear sweep voltammetry
NHE	normal hydrogen electrode
OHP	outer Helmholtz plane
ORR	oxygen reduction reaction
PBS	Phosphate buffer solution
PEMFC	polymer electrolyte membrane fuel cell
RDS	rate determining step
RE	reference electrode
rGO	reduced graphene oxide
SHE	standard hydrogen electrode
SEM	scanning electron microscopy
SOFC	solid oxide fuel cell
WE	working electrode
XPS	X-ray photoelectron spectroscopy
XRD	X-ray diffraction

List of Figures

List of Tables

Chapter 1 Introduction

This introductory chapter presents a brief background of climate change, renewable energy and electrochemical energy storage devices including fuel cells, batteries and supercapacitors among which supercapacitors are specifically focused on. The electrode materials for supercapacitors are reviewed such as carbon materials and transition metal oxides/hydroxides. The discussion covers the production, properties, modifications and applications of these materials. The chapter ends with the aims and objectives of the subsequent chapters.

1.1 Energy storage devices – overview

1.1.1 Climate change

Adopted in December 2015, the Paris Agreement aims to tackle climate change and its negative impacts by limiting global warming and reaching global peaking of greenhouse gas emissions as soon as possible.[1] Although some development strategies are not mandatory, most countries have been carrying out ambitious action under this legally binding international treaty on climate change since it entered into force in November 2016.[2] To achieve the goals of the agreement, the competitive zero-carbon solutions are established by more and more countries.[3] In addition to financial assistance, climate-related capacity building support for developing countries as well as technology development and transfer are guaranteed under the framework.[4] Particularly, the power and transport sectors benefit from this trend where many opportunities have been sparked, encouraging countries to work out more ambitious and positive plans in the future.[5] For instance, advances in electric vehicles and hybrid electric vehicles do well in reducing greenhouse gas emissions.[6]

1.1.2 Renewable energy and energy storage

Apart from the global climate crisis, a swift transition to renewable and sustainable energy technologies is formidable but essential on account of fast depletion of conventional and non-renewable energy sources such as coal, natural gas and petroleum, also known as fossil fuels and increasing amount of energy consumption.[7] Therefore, clean and renewable energy resources are substituted for fossil fuels to help people to meet the goals of cutting down greenhouse gas emissions and maintaining considerably high energy demand.[8]

Nowadays, people have made great progress in utilising renewable energy sources including solar energy, wind energy, biomass, geothermal energy, hydropower from waves and tides.[9] However, power generation from some renewable sources is not always constant as wind power is uncontrolled and solar power is only available during daylight hours. On the other hand, energy consumption is not constant either due to the on-peak and off-peak characteristics of human activity and industrial production.[10, 11] Hence, development of energy storage devices where energy is stored after generation when unneeded, and converted for use on demand has become a prevalent strategy to utilise these new energy sources more efficiently, stably and reliably.[12, 13]

1.1.3 Electrochemical energy storage

Currently, four types of large-scale energy storage systems are available after power generation including mechanical, thermal, chemical and electrochemical storage.[14] Amid the mentioned technologies, storing energy in electrochemical methods is designed for use in industry and commerce where it has demonstrated high efficiency, flexibility, and versatility.[10] Batteries, supercapacitors and fuel cells are three representative energy storage devices which store and release energy in electrochemical processes and are studied on the frontiers of science.[14, 15]

In an electrochemical energy storage system, the fundamental principle is usually the same. In other word, the systems share common features to some extent. Normally, the device is composed of two electrodes separated by an electrolyte and a separator. The electrode where the oxidation reaction occurs is named the anode, while the other electrode where the reduction reaction occurs is called the cathode. The conducting electrolyte allows ionic flow, whereas the separator is electronically insulating which prevents electric contact of the electrodes. Thus, redox reactions take place at the electrodes, and electrons generated move through an external circuit when the device is discharged, and energy is released. On the opposite side, an external voltage is applied across the electrodes that drives the flow of electrons and redox reactions at the electrodes during device charge and energy storage.[10, 11, 14, 16]

However, the operating mechanisms are always different for the three systems. For example, the active materials for energy storage and conversion stay in the same compartment in a battery as a closed system. Contrast that with a fuel cell, an open system, whose active materials such as oxygen and hydrogen are delivered from the outside. On the other hand, the mechanisms of one system can be different as well. In a supercapacitor, energy storage may not involve redox reactions, instead, it is achieved via charge separation at the electrode/electrolyte interface (so-called electrical double layer by Helmholtz), and therefore this type of supercapacitor is named electric double-layer capacitors (EDLCs).[17]

Such difference in device mechanisms, materials and chemistry leads to distinguishable power-energy characteristics of energy storage devices, as depicted in a simplified Ragone plot in Figure 1.1. Batteries are considered as intermediate energy and power systems that own an established position in application markets. In comparison, fuel cells have high specific energy, whereas supercapacitors have prominent specific power characteristics. Up to now, no single electrochemical energy storage system can power the transport sector as competitively as internal combustion engines. However, high-performance electrochemical energy storage

devices have been progressing at full speed with the development of fabrication of hybrid structures, design strategies, novel materials and synthesis technologies.[10-16]

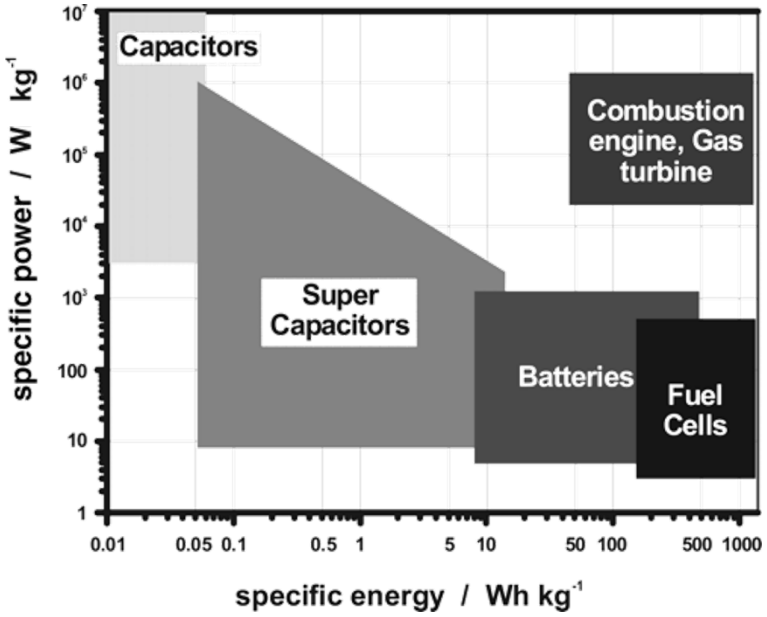

Figure 1.1 A simplified Ragone plot of various energy storage and conversion devices.[16]

1.1.3.1 Fuel cells

In fuel cells, chemical energy is stored in fuels such as hydrogen, methane and methanol, and then directly converted into electrical energy. Various types of fuel cells have been operating with different temperatures, net electrode reactions, and solid or liquid electrolytes, as depicted in Figure 1.2.[18] Alkaline fuel cells (AFC) and polymer electrolyte membrane fuel cells (PEMFC) work at low temperature where hydrogen is employed as fuel with high energy densities and less greenhouse emissions.[19] Unfortunately, small amounts of the undesirable CO in H_2 stream leads to poisoning of the Pt catalyst at the anode.[20] Furthermore, the precious metal catalyst Pt is costly in PEMFC.[21] On the contrary, solid oxide fuel cells (SOFC) require low-cost catalysts but higher operating temperature.[22] Fuels employed in SOFC are extremely flexible including gaseous, liquid and solid fuels such as dimethyl ether[23], n-butane[24], octane[25], biomass[26] and coal[27]. So far, utilisation of fuel cells as a stationary energy source is the most

promising commercial application. Meanwhile, they can be built in a hybrid configuration with batteries or supercapacitors for portable electronic automobiles.[28] The ability to reduce the material cost (e.g., catalysts and electrolytes) and the fabrication cost is the key to a large-scale fuel cell market.[29]

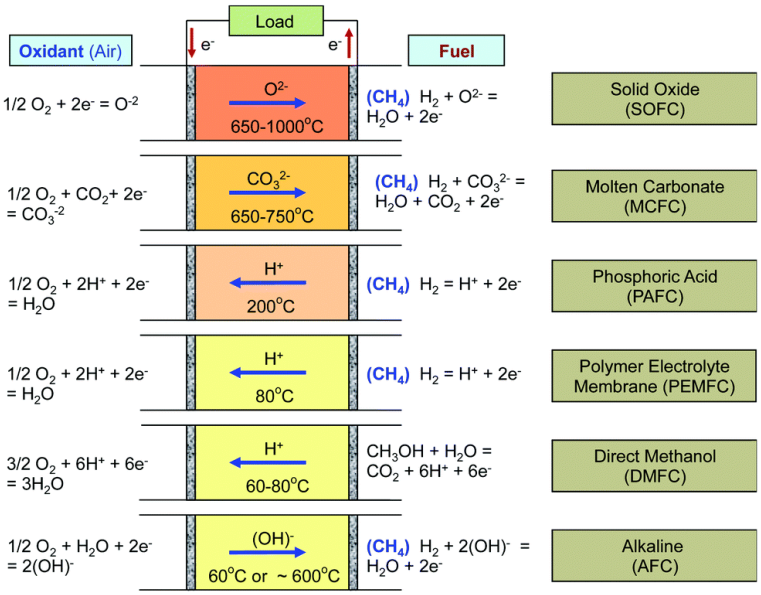

Figure 1.2 Summary of operating details of different types of fuel cells.[18]

1.1.3.2 Batteries

As the most commercially successful electrochemical devices, batteries are extensively used in portable electronic devices such as transport, mobiles, computers as well as stationary power storage. Although a variety of materials are available in commercial batteries, they can be divided into two categories: primary batteries (e.g., carbon-zinc, alkaline and lithium) that are non-rechargeable and secondary batteries (e.g., lead acid, lithium ion, NiMH and Ni-Cd) that are rechargeable.[14]

Li-ion batteries offer high specific energy and specific power compared to other batteries.[12] The operating mechanism involving lithiation (i.e. intercalation/insertion) and de-lithiation (i.e.

deintercalation/extraction) between the electrodes in a Li-ion battery is illustrated in Figure 1.3.[30] Currently, they have drawn most of the attention and are dominant in the global battery market owing to their excellent energy and power densities, cycle life, compact size and portability. A number of studies on negative electrode materials (anode), positive electrode materials (cathode), solid electrolyte interface and electrolytes for Li-ion batteries have been carried out to achieve significant improvement.[31] Alternatively, researchers are searching for novel battery systems with high performance so as to surpass the theoretical specific energy value of Li-ion batteries such as $LiCoO_2$/graphite and $LiFePO_4$/graphite systems (around 400 Wh kg^{-1}).[32] Among these new systems, Li-S, Na-ion, Na-S, Li-air, Zn-air and flow batteries (e.g., Zn-Br_2 and vanadium redox) are attempting to compete with or to replace the market position of Li-ion batteries.[33]

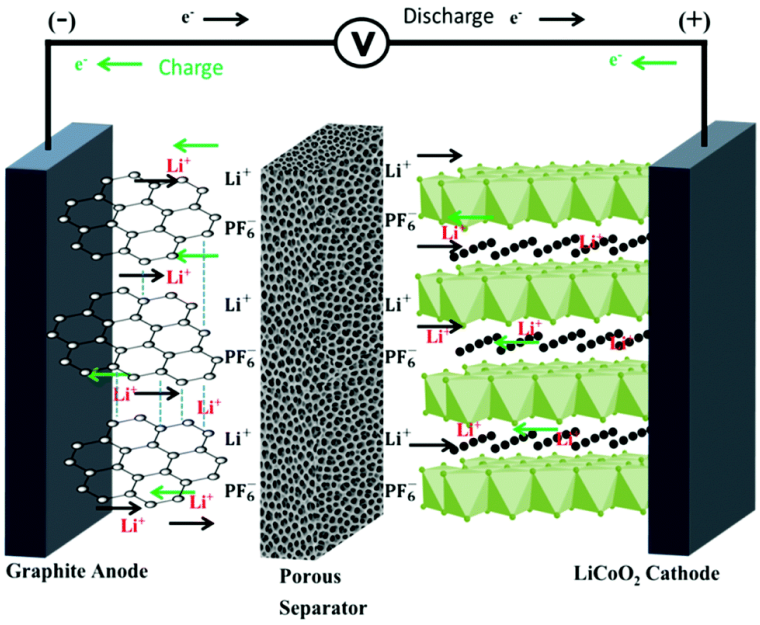

Figure 1.3 Schematic representation of operating mechanism of Li-ion battery with graphite anode and $LiCoO_2$ cathode.[30]

1.1.3.3 Supercapacitors

Supercapacitors, sometimes named electrochemical capacitors, ultracapacitors or hybrid capacitors, are energy storage devices lying between batteries and conventional dielectric capacitors. Supercapacitors are classified into two categories relying on their charge storage mechanisms: electric double layer capacitors (EDLCs) and pseudocapacitors.

In EDLCs, charge is stored at the electrode-electrolyte interface electrostatically. The mechanism is analogous to a conventional physical capacitor where no faradaic reactions take place, although conducting electrolytes in EDLCs are substituted for insulating barriers in dielectric capacitors between two electrodes. Upon polarisation, positive ions and negative ions in the electrolytes accumulate at the surfaces of two electrodes that are negatively and positively charged, respectively, forming two electrical double layers and accomplishing charge separation, as depicted in Figure 1.4 (a).[34] The electrical double layer refers to the charged electrode surface and the opposite charge layer formed by the ions in the electrolytes. During the discharge process in Figure 1.4 (b), charge rearrangement in the double layer gives rise to a displacement current. A more complicated model to describe the charge layer in the electrolytes involves a compact layer and a diffusive layer. In fact, details of the electrical double layer are complex and will be further discussed in Chapter 2.

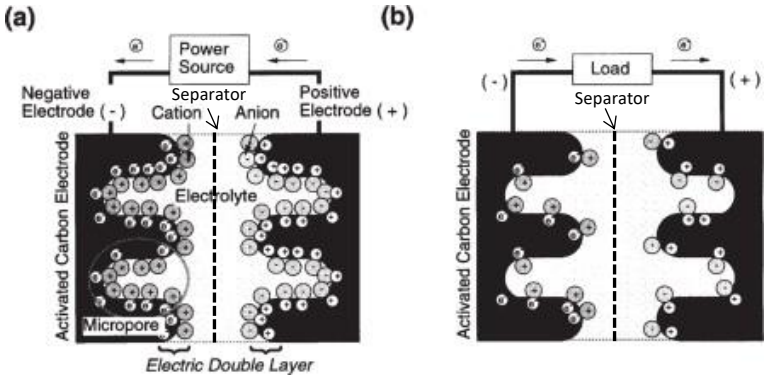

Figure 1.4 Schematic diagrams of (a) charge and (b) discharge mechanisms in electric double layer capacitors.[34]

Similar to a battery, the two electrodes in an EDLC are separated physically by an ion-permeable membrane (i.e., separator) to prevent short circuit. In addition, binder materials are always employed to provide adhesion among electrode active materials, current collectors and other additives to ensure the performance and flexibility of a supercapacitor. Polymers such as Nafion, polyvinylidene fluoride (PVDF) and polytetrafluoroethylene (PTFE) are conventional and widely-used binder materials in supercapacitors.[35] More recently, eco-friendly cellulose, lignin, and chitosan derived binders as well as conducting polymers such as polyaniline are produced with low cost.[36] Although binder materials are not as important as electrode active materials in affecting the performance of supercapacitors, they still play a role in electrode preparation.

As the energy is stored in charges at the electrode surface in an EDLC, it should have a rapid response to potential change and delivers energy quickly.[37] The non-faradaic process also contributes to long cycle lives and little capacity loss.[38] The capacitance of the double layer is defined as $C = \varepsilon_r \varepsilon_0 A/d$, where ε_r is the dielectric constant of the electrolyte, ε_0 is the vacuum dielectric constant, A is surface area of the electrode and d is the charge separation distance (or thickness of the double layer).[17, 34, 39] Since the d value is in angstrom range (2 to 10 Å) and the capacitance is proportional to A, high capacitance is anticipated for materials with high electrode surface area. However, the limited surface area of current electrode materials is responsible for inferior amounts of energy stored compared to batteries and pseudocapacitors, the other type of supercapacitors.[11, 15]

In Conway's definition, three faradaic processes can result in pseudocapacitance: (a) underpotential deposition, (b) surface redox reactions of electrode materials including RuO_2 and MnO_2, and (c) intercalation of ions into host compounds such as MoS_2 and TiS_2, as shown in Figure 1.5.[17, 40-43] In the field of pseudocapacitors, energy is mainly stored and released by fast and reversible redox reactions at the electrode surface, originating from the second charge

storage mechanism of supercapacitors mentioned above. The faradaic redox reactions that generate pseudocapacitance are always located on the surface or near-surface of the electrodes. The electrochemical behaviour of pseudocapacitors is similar to that of EDLCs where the electrode potential is a linear function of the charge stored, but the mechanism is faradaic in origin and this is why the prefix 'pseudo' is used here.[17, 42, 43]

A noble metal oxide, RuO_2, is a typical transition metal oxide material exhibiting pseudocapacitance through redox reactions. High specific capacitance up to 1300 F g^{-1} and good cycling stability are obtained for RuO_2.[44] However, further studies are hindered due to its disagreeable high cost and scarcity.[40] Instead, cheaper pseudocapacitive materials such as MnO_2 and conducting polymers (e.g., polyaniline and polypyrrole) are focused on in spite of their poor electrical conductivity and short cycling life. The approach to overcoming these problems will be explained later in this chapter.

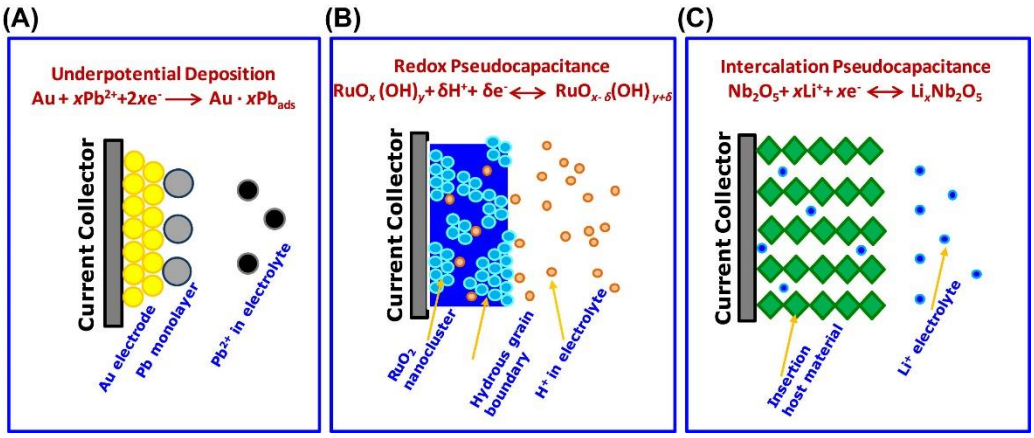

Figure 1.5 Schematic diagrams of faradaic mechanisms generating pseudocapacitance: (a) underpotential deposition, (b) surface redox system, and (c) intercalation system.[40]

At early stages of supercapacitor studies, a number of electroactive materials undergoing faradaic redox reactions are also described as pseudocapacitive by some researchers in supercapacitor applications such as NiO, $Ni(OH)_2$, CoO and Co_3O_4. However, they are classified into battery-type electrode materials by others because their electrochemical

behaviour is related to a battery (i.e., a flat discharge plateau under constant current, and well-defined redox peaks in CV) rather than a pseudocapacitor (i.e., a triangular charge/discharge curve under constant current, and a quasi-rectangular CV shape). In fact, most of these materials have been employed as active materials in primary or secondary batteries for a long history. To avoid confusion, only those materials (e.g., RuO_2 and MnO_2) that are faradaic in nature but share similar electrochemical signature of EDLCs are presented as pseudocapacitive electrodes, whereas the other electroactive materials (e.g., $Ni(OH)_2$ and CoO) are called faradaic battery-type electrodes in this work.

To construct a supercapacitor, it is uncommon and impractical to use only one material based on a single mechanism. For example, symmetrical EDLCs based on carbon black have a limited working window in aqueous solutions, leading to smaller energy density.[45] Inspired by battery design, asymmetric devices combining a EDLC negative electrode (e.g., activated carbon) with a faradaic positive electrode (e.g., pseudocapacitive MnO_2, battery-type PbO_2 and $Ni(OH)_2$) have been reported. These devices are labelled as graphene-MnO_2, carbon nanotubes-NiO, activated carbon-$Ni(OH)_2$ asymmetric supercapacitors, etc.[46] The electrochemical window and the energy density of such asymmetric devices are much higher than those of carbon-based symmetrical EDLCs.[41]

Furthermore, fabrication of hybrid materials has been proposed in single electrode design as well. In this case, composite electrodes are produced where carbon materials with high surface area serve as a support for other electroactive materials.[39] For instance, a carbon/metal oxide composite electrode was prepared by precipitating RuO_2 nanoparticles on reduced graphene oxides surface.[47] Such strategies not only enhance the electrical conductivity of metal oxides but also lead to improved electrochemical properties of the materials.[46] Various materials have been combined to develop composite electrodes for improved device performance including specific capacitance, energy density, power density, rate capability and cycling stability.[48]

Commercially, supercapacitors were first marketed in 1978 by NEC Corporation for computer memory back-up.[49] However, the market progressed slowly until Conway did much work on RuO_x based supercapacitors from 1980 to 1990s, who not only distinguished supercapacitor behaviour from battery, but also expanded the knowledge of EDLCs and pseudocapacitors in electrochemical energy storage.[43] In 1980s, the development of electrode materials enhanced capacitance values, while the improvement of electrolytes lowered internal resistance of the devices, leading to the use of supercapacitors in military applications.[50] In most commercial supercapacitors, their specific energy is typically 1 – 10 Wh kg^{-1}, equivalent to a specific capacitance value between 5 – 50 F g^{-1}.[51] Although the specific energy for a supercapacitor is lower than most batteries (10 – 250 Wh kg^{-1}), its charge/discharge rate (seconds to minutes) is much quicker than batteries (hours). Additionally, the cycle life of a supercapacitor (10^3 – 10^6 times) is greater than a battery (1000 – 1500 times).[52] Such properties enable supercapacitors to serve in industrial and commercial sectors where fast power delivery with long cycle life is demanded with some compromises to the energy density. Thus, a configuration of supercapacitors in conjunction with batteries or fuel cells as a hybrid energy storage system has become advantageous. Remarkably, one of the recent leading developments in supercapacitors is the regenerative braking systems of electric vehicles and hybrid electric vehicles (e.g., Toyota Yaris, Peugeot Citroën, Mazda 6).[53] Upon deceleration in a car, supercapacitors are able to recover almost 80% of the braking energy in a short time as they can store energy rapidly, whereas batteries can only reach 30% recovery within the same time.[54]

1.2 Electrode materials – carbon

1.2.1 Allotropes of carbon

Carbon, an essential element for living systems, also plays a significant role in energy storage devices.[55] For example, as an allotrope of carbon, graphite is the most popular negative electrode material in commercial Li-ion batteries.[10] At present, carbon-based materials have been widely investigated in supercapacitor applications due to their unique physical and chemical properties.[56] These carbonaceous materials range from conventional diamond, graphite and activated carbon to novel fullerene, carbon nanotubes (CNTs) and graphene.[57] Activated carbon is one of the most commonly used EDLC electrode materials with high surface area, moderate electrical conductivity and low cost.[58] Although activated carbon with a specific surface area as high as 3000 m^2 g^{-1} was obtained, its specific capacitance is limited by other parameters such as pore size distribution and pore structure.[39]

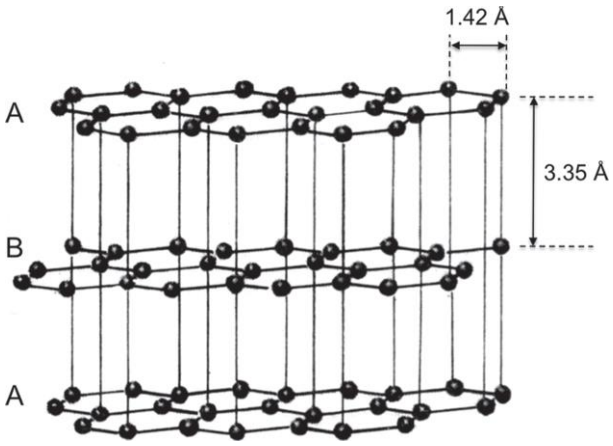

Figure 1.6 The graphite structure.[59]

Graphite has a hybridisation type of sp^2 where 2s orbital and two 2p orbitals in a carbon atom hybridise. Within the graphite plane, each carbon atom is covalently bonded with three carbon atoms in a hexagonal arrangement with a bond length of 0.142 nm and a bond angle of 120°. The interplanar distance of graphite is 0.335 nm with weak van der Waals force between layers,

as shown in Figure 1.6. The non-bonded valence electrons in carbon atoms become delocalised, enabling graphite to conduct electricity.[60]

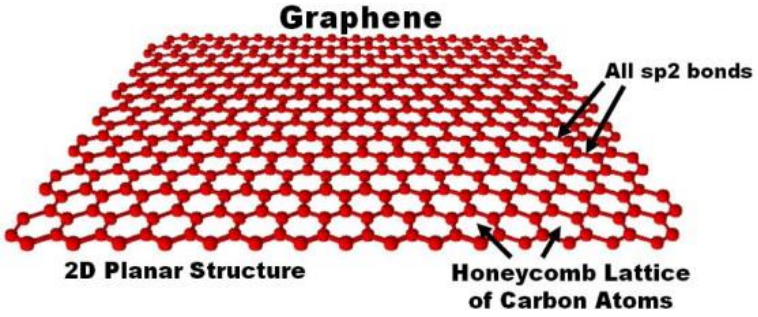

Figure 1.7 The graphene structure.[61]

In addition to conventional carbon for EDLC applications, novel allotropes of carbon have been discovered more recently such as C_{60}, graphene and CNTs.[62] Among all forms of carbon, graphene and CNTs have been broadly explored as potential electrode materials in energy storage because of their unique electrical conductivity, mechanical resilience, chemical and thermal stability.[63] Graphene consists of a two-dimensional layer of carbon atoms (sp^2 hybridised) in a hexagonal honeycomb lattice nanostructure (Figure 1.7). It is considered as a structural block to build other sp^2 carbon allotropes in different dimensionalities. For example, graphite is composed of stacked layers of graphene while one-dimensional CNT is formed by rolling graphene sheets. Geim and Novoselov were awarded the Nobel Prize in Physics in 2010 for they investigated and isolated graphene with groundbreaking experiments.[64] However, these artificial materials suffer from agglomeration, complex synthesis and fabrication processes, and high cost of large-scale production, limiting their scalability and commercial applications in supercapacitors.[65] An alternative is to obtain carbon from conventional and natural resources with modifications, such as heteroatom-doped carbons (e.g., boron doped diamond) and biomass-derived carbons (e.g., cellulose, lignin and starch derived carbon), which are abundant, eco-friendly and low-cost.[66]

1.2.2 Conductive diamond - boron-doped diamond

Diamond is a crystalline allotropic form of carbon with sp^3 hybridisation, where 2s orbital and three 2p orbitals in carbon hybridise to form four hybrid orbitals with similar characteristics. Each carbon atom in diamond is tetrahedrally bonded with four carbon atoms with same bond lengths (0.154 nm) and bond angles (109.47°), as shown in Figure 1.8.[67] It shows unique properties such as high mechanical hardness (1×10^4 kg mm^{-2}) and thermal conductivity (> 2200 W m^{-1} K^{-1}).[68] With a wide bandgap of 5.45 eV, diamond is insulating before doping with heteroatoms (e.g., boron, nitrogen, phosphorus and sulphur) to improve its electrical conductivity (~ 10^{-16} S cm^{-1}).[69] Boron is the most common dopant due to a low charge carrier activation energy (0.37 eV above the valence band), and boron-doped diamond (BDD) has been studied as a promising material in various fields.[70]

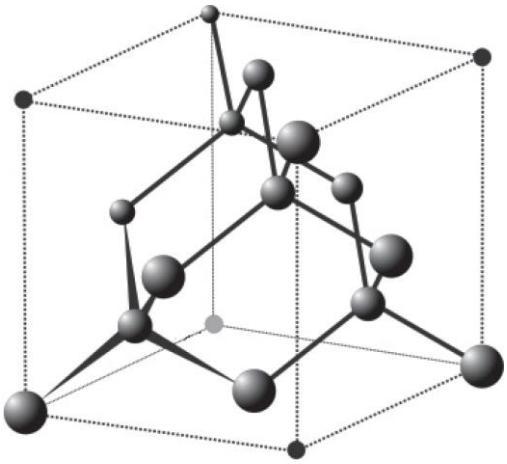

Figure 1.8 Structure of diamond.[67]

The boron doping level leads to different behaviour of BDD. A p-type semiconducting boron-doped diamond is obtained at a lower doping level (~ 10^{17} - 10^{18} B atoms cm^{-3}). Semi-metallic behaviour of BDD (electrical conductivity up to 10^3 S cm^{-1}) is achieved with a higher boron doping level (~ 10^{20} - 10^{21} B atoms cm^{-3}) as p-type holes in diamond overlap with boron acceptor state, allowing current to flow without thermal activation. Other dopants such as

nitrogen and phosphorus can provide diamond with n-type semiconducting property with charge carrier activation energy (i.e., 0.6 eV for phosphorus doping and 1.6 eV for nitrogen doping) below the conduction band, as shown in Figure 1.9.[68]

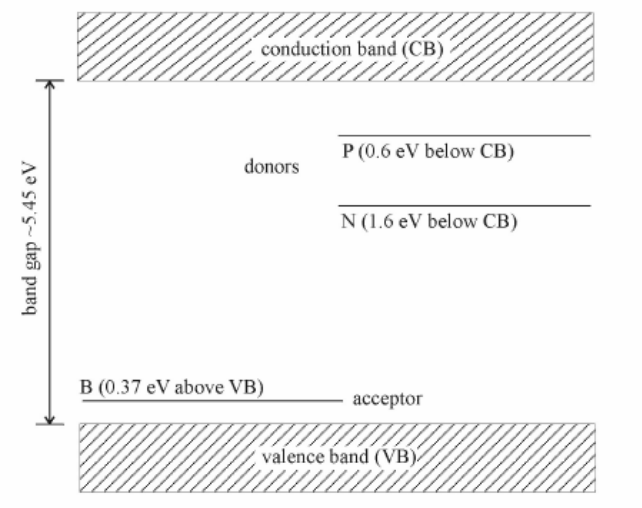

Figure 1.9 Representation of the energy diagram of selected states in the band gap of diamond.[68]

1.2.2.1 Synthesis

Chemical vapour deposition (CVD) is a major approach to growing thin-film diamond on a substrate. In a typical CVD process, a gas mixture of hydrocarbon and hydrogen (e.g., CH_4 and H_2) with or without a dopant (e.g., boron) is first activated via a hot filament or microwave plasma at a low pressure (~ 10 - 50 mbar) and a high temperature (~ 2200 - 2800 °C).[71] The mixture then undergoes reactions to produce radical precursors for sp^3 carbon deposition onto substrates such as silicon.[72] Meanwhile, formation of sp^2 bonds is inhibited due to hydrogen terminated surface sites.[73] Controlled electrical conductivity is achieved by adjusting the dopant source (e.g., B_2H_6, $B(CH_3)_3$ and $B(OCH_3)_3$) and doping amount (10^{18} - 10^{21} boron atoms cm^{-3}) during CVD growth.[74] In general, BDD exhibits the behaviour of a semiconductor with a low doping level (< 10^{19} atoms cm^{-3}), while it acts as a semi-metal with a high doping level over 10^{20} atoms cm^{-3}.[75]

1.2.2.2 Properties

In various electrochemical applications, BDD presents unique advantages over conventional metal-based and sp^2 carbon electrodes including:

- A wider electrochemical potential window. The potential window of BDD surpasses 3.0 V in aqueous solutions, which is much larger than that of other commonly used electrodes such as Au, Pt and glassy carbon resulting from high overpotentials for oxygen and hydrogen evolution reactions.[76] In non-aqueous media, the value is even higher (> 4.0 V) as the sp^3 carbon is too inert to catalyse the decomposition of organic solvents.[77]
- Lower background signals. The capacitive current and double layer capacitance of BDD is up to an order of magnitude lower than that of a glassy carbon electrode.[78] Furthermore, the faradaic contribution is negligible due to moderate numbers of electroactive oxygen functionalities on the BDD surface (non-diamond surface impurities). Therefore, the signal-to-background ratios of BDD are enhanced for sensing purpose as compared to other electrodes.[79]
- Resistance to fouling. BDD has a weak adsorption of contaminants, helping to maintain its clear electrochemical signals for sensing.[80]
- Physical and chemical stability. BDD remains stable and functional in sonoelectrochemical analysis owing to its mechanical robustness.[81] Its high tolerance to chemicals under extreme conditions is also favourable such as strong acid.[82]
- Biocompatibility. BDD is available for *in vivo* analysis of drugs and neuronal neurotransmitters.[83]

1.2.2.3 Surface modification

Although BDD possesses excellent physical and chemical properties, surface modification is necessary to enhance its catalytic activity and electrochemical responses for electrocatalysis and electrochemical energy storage applications.[84, 85] In addition to surface grafting by chemical reactions and metal ion implantation, electrodeposition of nanoparticles is another convenient way to modify BDD for improved performance.[73]

A number of species can be deposited onto BDD to form composite electrodes such as metals, alloys and metal oxides.[85] The metal elements used for modification include titanium (Ti), palladium (Pd), platinum (Pt), silver (Ag), copper (Cu), gold (Au), etc.[86] Deposition of metal alloys (e.g., Pt-Ni, Pt-Cu, Pt-Ru, Pd-Ni, etc.) always show better electrocatalytic activity compared to single metal decoration.[87] Metal oxides such as RuO_2, MnO_2, TiO_2 have also been widely employed, and sometimes metal-metal oxides/BDD composites are produced for different applications (e.g., Ta-TiO_2/BDD for supercapacitors and Pt-RuO_2/BDD for fuel cells).[88]

1.2.2.4 Applications

The excellent properties and easy modifications of BDD enable itself in various electrochemical applications such as electro-analysis, electrocatalysis, electrochemical energy storage and conversion, etc. BDD first found its extensive application in electrochemical sensors with high sensitivity and good reproducibility.[89] Inorganic pollutants (e.g., heavy metal ions and nitrite, etc.)[90], organic molecules (e.g., hydroquinone, ascorbic acid, phenol and dopamine, etc.)[91] and biomolecules (e.g., protein, RNA and DNA, etc.)[92] have been detected and analysed by BDD-based electrodes. Electrocatalysis of BDD includes synthesis of organics, degradation/oxidation of organic pollutants, and fuel cell related applications (e.g., CO_2 reduction, O_2 reduction, methanol and ethanol oxidation).[93] In particular, electrochemical and

photoelectrochemical reduction of CO_2 comes under the spotlight in recent years. Not only does it dispose of a greenhouse gas, but also useful compounds are formed as fuels. To achieve higher efficiency in CO_2 reduction, BDD electrodes are decorated with Ag and Cu nanoparticles.[94] BDD electrodes have also been reported to construct supercapacitors, Li-ion batteries and solar cells. In supercapacitor fabrication, BDD with porous structures was produced to improve the performance of EDLCs. For example, honeycomb nano-porous structured BDD exhibited a 200 times larger specific capacitance in comparison with as-deposited BDD films.[95] On the other hand, electroactive pseudocapacitive materials such as RuO_2, MnO_2 and conducting polymers are combined with BDD electrodes for higher capacitance.[96]

1.2.3 Biomass-derived carbon

Biomass materials are abundant renewable resources derived from plants, animal and marine organisms. Due to their sustainability and low cost, biomass-derived materials have been studied for different applications including hydrogen storage, energy storage, water treatment, carbon dioxide capture and catalysis.[97] Plant-based biomass is eco-friendlier compared to others, and can be used as energy sources directly.[98] It is often referred to as lignocellulose, which is composed of varying proportions of cellulose, hemicellulose and lignin.[99] The sources of biomass include forest crops (e.g., bamboo and wood), agricultural residues (e.g., rice husks, coffee shells, and wheat straw), industrial, domestic and marine wastes (e.g., waste paper, sugarcane bagasse, cassava peel, and seaweed biopolymer).[100]

1.2.3.1 Preparation

Biomass can be converted into carbon via carbonisation (i.e., pyrolysis and hydrothermal carbonisation), activation (e.g., physical activation, chemical activation, and microwave-induced activation), or a combination of both. In this way, materials with tuneable properties

such as specific surface area, pore size distribution, electrical and thermal conductivity, and mechanical strength are produced by controlling experimental parameters (e.g., gas atmosphere, chemical agents, temperature, ramping rate, and time).[97]

Pyrolysis is a carbonisation process carried out in a limited oxygen or inert gas atmosphere at high temperatures (500 - 1200 ℃).[101] Although biomass-derived carbon with high specific surface areas has been prepared by a direct pyrolysis step, it is always followed by an activation process to increase the specific surface area and porosity.[102] Furthermore, most biomass precursors contain considerable impurities, which could act as porogens and chemical agents for activation during the pyrolysis process.[103]

Compared to pyrolysis, hydrothermal carbonisation (HTC) is a thermo-chemical process where a lower temperature (120 - 250 ℃) and a pressurised aqueous atmosphere are selected. A product named hydrochar with a high content of oxygen-containing functional groups and a low specific surface area is prepared after the HTC process.[104] Although hydrochars can be employed as electrodes for energy storage directly, subsequent pyrolysis or activation is usually required to improve the properties of the materials (e.g., electrical conductivity, porosity, surface area, etc.).[105]

Physical activation is performed in an environment of air, steam or CO_2, commonly after the pyrolysis process. The temperature for air activation (< 500 ℃) is lower than that for steam (800 - 1200 ℃) and CO_2 (800 - 1000 ℃) activation. On the other hand, the latter two are more commonly used to tune pore size distribution by controlling the activation time. In general, the porous and electrochemical properties are improved after the physical activation process.[106]

Chemical activation is conducted at a lower temperature (450 - 900 ℃) compared to physical activation. Common agents include KOH, $ZnCl_2$, $FeCl_3$, H_3PO_4, and $KHCO_3$, among which KOH is mostly used to activate biomass precursors.[107] Materials induced by KOH activation

have large surface areas and porous structures, which not only benefit from chemical activation but also carbon lattice expansion by metallic K intercalation.[108] $ZnCl_2$ acts as a deoxygenating and dehydrating agent by reduction and removing water in a simple one-step activation process.[109] Other chemical agents as well as activation methods (e.g., microwave-induced and physicochemical activation) are also employed to enhance the properties and performance of biomass-derived carbon.[110]

1.2.3.2 Properties

Pore structure is important for the performance of carbon. According to IUPAC nomenclature, pores with different diameters are classified into micropores (< 2 nm), mesopores (2 – 50 nm) and macropores (> 50 nm).[111] Carbon materials with well-distributed pores enable ions to move with low resistance in the pores and pathways, which is achieved through changing the conditions of carbonisation/activation.[97]

As the materials are not fully graphitised during carbonisation and activation processes, some oxygen-containing groups still exist on the carbon surface, which contribute to pseudocapacitance.[98] Such contributions are derived from redox reactions of different functional groups including hydroxyl groups, carbonyl groups and carboxylic groups:[112]

$$C{-}OH \rightleftharpoons >C{=}O + H^+ + e^- \quad (1\text{-}1)$$

$$>C{=}O + e^- \rightleftharpoons >C{-}O^- \quad (1\text{-}2)$$

$$-COOH \rightleftharpoons -COO- + H^+ + e^- \quad (1\text{-}3)$$

However, excessive oxygen-containing groups lead to a low electrical conductivity.[113] The electrical conductivity of carbon is another parameter that affects its electrochemical performance. This can be improved by increasing the graphitisation degree during high-temperature preparation, facilitating ion diffusion and electron transfer in electrochemical

measurements.[114] When the temperature of treatment is increased, the surface wettability of carbon materials towards aqueous solutions is enhanced simultaneously.[115] On the other hand, higher temperature is not only energy consuming, but also harmful to the surface area and porosity of the materials.[116] Therefore, a certain balance between porosity, numbers of functional groups and graphitisation degree should be obtained for excellent electrochemical performance.

1.2.3.3 Modification

In order to produce carbon with higher specific capacitance, one strategy is to dope carbon with heteroatoms (e.g., sulphur, boron, oxygen, nitrogen, and phosphorus), accomplished by mixing biomass with heteroatom precursors or by post-treatment. For example, nitrogen doped carbon materials exhibited better wettability and electrical conductivity. Additionally, carbon with nitrogen and sulphur-containing functional groups shows larger capacitance through pseudocapacitive contributions.[117]

In addition to physical/chemical activation and heteroatom doping, other methods of modification such as compositing electrochemically active materials with biomass-derived carbon are conducted by researchers. Hybrid carbon-based hydrogels and aerogels are produced by incorporating other functional materials (e.g., CNTs and rGO) into biomass-derived carbon, showing good capacitance and stability in bent state.[118] Combination of faradaic active materials such as transition metal oxides and conducting polymers with biomass-derived carbon also provides improved performance of the hybrids because they have higher specific capacitance compared to carbon despite poorer electrical conductivity and cycling stability.[119]

1.2.3.4 Applications

Biomass-derived carbon has first been developed as adsorbents for environmental contaminants such as metallic (e.g., chromium, copper, lead, mercury, cadmium, etc.), non-metallic (e.g., phosphate, sulphur, fluoride, molybdate, thiocyanate, etc.) and organic (e.g., dyes, pesticides, phenolic compounds and pharmaceutical compounds) pollutants due to its excellent adsorption capacity.[120] In addition to pollutants from aqueous solutions, it acts as a promising material in gas adsorption (e.g., CO_2, H_2, NO_2 and H_2S). It is not only effective in capture of greenhouse gases and pollutant gases, but also in hydrogen storage with low cost, stability and regeneration.[120] Recently, biomass-derived carbon has been used in energy applications. Due to its unique 3D hierarchical porous structure, biomass-derived carbon serves as promising materials in fuel cells, supercapacitors and batteries. It is also fabricated into electrocatalysts for hydrogen evolution, oxygen evolution and oxygen reduction reactions to replace traditional noble metal catalysts.[121]

1.3 Electrode materials – carbon-based composites

Materials with pseudocapacitive or faradaic battery-type properties possess significantly higher theoretical specific capacitances and energy densities than carbon-based EDLCs. Therefore, composite electrodes combining faradaic active materials such as transition metal oxides or conducting polymers with conductive carbon materials have been widely investigated.[46] Hydrous ruthenium oxide ($RuO_2 \cdot xH_2O$) is one of the most studied intrinsic pseudocapacitive materials in supercapacitor applications as it undergoes a multi-electron transfer mechanism during fast faradaic redox reactions. The charge storage reaction for RuO_2 involves proton insertion/extraction in acidic solutions, expressed by the following reaction:

$$RuO_2 + xH^+ + xe^- = RuO_{2-x}(OH)_x \quad (0 < x < 2) \qquad (1\text{-}4)$$

RuO_2 has been coated on porous carbon structures such as activated carbon, CNTs, graphene, carbon black and carbon aerogels, resulting in improved specific capacitance without sacrificing the stability and power density of the composites.[14]

Unfortunately, the commercial application of RuO_2 is limited by its high cost, so another pseudocapacitive material, MnO_2, is substituted for RuO_2 and incorporated into carbon-based composite electrodes due to its cheapness and low toxicity.[10] Although MnO_2 suffers from poor electrical conductivity, dispersing MnO_2 particles onto conductive carbon networks can enhance the overall electrochemical performance as well as the mechanical strength and the effective utilisation of the composite materials.[122] A number of carbon backbones (e.g., graphene, carbon nanofibers, carbon paper, CNTs, etc.) are studied for MnO_2-based composites, exhibiting better stability and capacitance compared to a single component, either carbon or MnO_2. The charge storage reactions involve surface absorption/desorption and intercalation/deintercalation of protons or alkali metal cations,[123] as shown in Reaction 1-5:

$$MnO_2 + C^+ + e^- \rightleftharpoons MnOOC \quad (C^+ = H^+, Li^+, K^+, Na^+, \text{etc.}) \tag{1-5}$$

Some other compounds (e.g., Co_3O_4, MnO, $Ni(OH)_2$, NiO, etc.) that are redox active but not pseudocapacitive can be implemented in carbon-based composite electrodes as well.[40, 46] Most of these faradaic battery-type materials interact with hydroxide anions on changing the oxidation states, occurring not only at the surface but also in the bulk of the materials.[124] For example, some of the corresponding redox reactions proceed as:

$$CoO + OH^- \rightleftharpoons CoOOH + e^- \tag{1-6}$$

$$Co_3O_4 + OH^- + H_2O \rightleftharpoons 3CoOOH + e^- \tag{1-7}$$

$$CoOOH + OH^- \rightleftharpoons CoO_2 + H_2O + e^- \tag{1-8}$$

$$NiO + OH^- \rightleftharpoons NiOOH + e^- \tag{1-9}$$

$$Ni(OH)_2 + OH^- \rightleftharpoons NiOOH + H_2O + e^- \quad (1\text{-}10)$$

$$MnO + OH^- \rightleftharpoons MnOOH + e^- \quad (1\text{-}11)$$

More recently, transition metal complexes such as metal-organic-frameworks (MOFs) are introduced by researchers. MOFs are assembled from metal ions and organic ligands, and the metal ions can show redox properties for energy storage. However, the electrical conductivity of MOFs is even worse than most metal oxides, limiting their use in supercapacitors. To overcome their non-conducting nature, MOFs or precursors of MOFs can be dispersed within the carbon framework first. Afterwards, the mixture undergoes pyrolysis to obtain metal oxides/carbon composites. A variety of metal ions (e.g., Fe^{2+}, Co^{2+}, Mn^{2+}, Ni^{2+}, Cu^{2+}, and bimetallic/trimetallic ions) have been studied as well as organic functionalities and carbon substrates.[125]

In summary, fabrication of composite electrode materials based on carbon backbones and faradaic active species is a main approach to producing high-performance candidates for supercapacitor applications.

1.4 Aims

This thesis is composed of seven chapters, aiming to investigate the electrochemical behaviour of novel carbon materials (i.e., boron-doped diamond and biomass-derived carbon) and their composites for supercapacitor applications. The aims and objectives of the following chapters are:

Chapter 2 introduces the electrochemical theories and methods for the experiments. It covers the basic principles of electrochemistry and emphasises the application of electrochemical measurements to study real chemical systems. In addition, fundamental principles of characterisation techniques used in the projects are also explained.

Chapter 3 focuses on the electrochemical behaviour of Mn^{2+} on boron doped diamond electrodes first. The electrochemical performance of BDD/MnO_2 composite electrodes are then measured to increase the specific capacitance for supercapacitor applications.

Chapter 4 exploits the electrochemical properties of biomass-derived carbon using seaweed paper as the precursor. The carbonised seaweed paper then serves as a carbon substrate (EDLC source) for potentiostatic deposition of manganese dioxide (pseudocapacitive source) to obtain composite electrodes for further electrochemical measurements as supercapacitors.

Chapter 5 develops nickel treated biomass-derived carbon from filter paper. By removing or maintaining the nickel particles, its electrochemical behaviour is studied. The composite electrodes are then measured in alkaline electrolytes with nickel converted into faradaic active nickel hydroxide for supercapacitor applications.

Chapter 6 prepares a number of biomass-derived carbon materials from seaweed paper, rice husk, cypress wood and floorboard waste with bimetallic cobalt/manganese MOFs modification. After pyrolysis, the carbon/bimetallic metal oxides composites are studied for supercapacitor applications.

Chapter 7 concludes the thesis by summarising the key results.

References

(1) https://unfccc.int/process-and-meetings/the-paris-agreement/the-paris-agreement (accessed. Huang, M.-T.; Zhai, P.-M. Achieving Paris Agreement temperature goals requires carbon neutrality by middle century with far-reaching transitions in the whole society. *Advances in Climate Change Research* **2021**, *12* (2), 281-286. DOI: https://doi.org/10.1016/j.accre.2021.03.004. FALKNER, R. The Paris Agreement and the new logic of international climate politics. *International Affairs* **2016**, *92* (5), 1107-1125. DOI: 10.1111/1468-2346.12708 (acccessed 3/15/2022). Rogelj, J.; den Elzen, M.; Höhne, N.; Fransen, T.; Fekete, H.; Winkler, H.; Schaeffer, R.; Sha, F.; Riahi, K.; Meinshausen, M. Paris Agreement climate proposals need a boost to keep warming well below 2 °C. *Nature* **2016**, *534* (7609), 631-639. DOI: 10.1038/nature18307.

(2) Rajamani, L. AMBITION AND DIFFERENTIATION IN THE 2015 PARIS AGREEMENT: INTERPRETATIVE POSSIBILITIES AND UNDERLYING POLITICS. *International and Comparative Law Quarterly* **2016**, *65* (2), 493-514. DOI: 10.1017/S0020589316000130 From Cambridge University Press Cambridge Core.

(3) Bataille, C. G. F. Physical and policy pathways to net-zero emissions industry. *WIREs Climate Change* **2020**, *11* (2), e633. DOI: https://doi.org/10.1002/wcc.633.

(4) Rissman, J.; Bataille, C.; Masanet, E.; Aden, N.; Morrow, W. R.; Zhou, N.; Elliott, N.; Dell, R.; Heeren, N.; Huckestein, B.; et al. Technologies and policies to decarbonize global industry: Review and assessment of mitigation drivers through 2070. *Applied Energy* **2020**, *266*, 114848. DOI: https://doi.org/10.1016/j.apenergy.2020.114848.

(5) Robinius, M.; Otto, A.; Heuser, P.; Welder, L.; Syranidis, K.; Ryberg, D. S.; Grube, T.; Markewitz, P.; Peters, R.; Stolten, D. Linking the Power and Transport Sectors—Part 1: The Principle of Sector Coupling. *Energies* **2017**, *10* (7), 956. Han, S.; Zhang, B.; Sun, X.; Han,

S.; Höök, M. China's Energy Transition in the Power and Transport Sectors from a Substitution Perspective. *Energies* **2017**, *10* (5), 600.

(6) Khaligh, A.; Li, Z. Battery, Ultracapacitor, Fuel Cell, and Hybrid Energy Storage Systems for Electric, Hybrid Electric, Fuel Cell, and Plug-In Hybrid Electric Vehicles: State of the Art. *IEEE Transactions on Vehicular Technology* **2010**, *59* (6), 2806-2814. DOI: 10.1109/TVT.2010.2047877. Delucchi, M. A.; Yang, C.; Burke, A. F.; Ogden, J. M.; Kurani, K.; Kessler, J.; Sperling, D. An assessment of electric vehicles: technology, infrastructure requirements, greenhouse-gas emissions, petroleum use, material use, lifetime cost, consumer acceptance and policy initiatives. *Philosophical Transactions of the Royal Society A: Mathematical, Physical and Engineering Sciences* **2014**, *372* (2006), 20120325. DOI: doi:10.1098/rsta.2012.0325.

(7) Omer, A. M. Energy, environment and sustainable development. *Renewable and Sustainable Energy Reviews* **2008**, *12* (9), 2265-2300. DOI: https://doi.org/10.1016/j.rser.2007.05.001.

(8) Shahsavari, A.; Akbari, M. Potential of solar energy in developing countries for reducing energy-related emissions. *Renewable and Sustainable Energy Reviews* **2018**, *90*, 275-291. DOI: https://doi.org/10.1016/j.rser.2018.03.065.

(9) Ellabban, O.; Abu-Rub, H.; Blaabjerg, F. Renewable energy resources: Current status, future prospects and their enabling technology. *Renewable and Sustainable Energy Reviews* **2014**, *39*, 748-764. DOI: https://doi.org/10.1016/j.rser.2014.07.113.

(10) Liu, C.; Li, F.; Ma, L.-P.; Cheng, H.-M. Advanced Materials for Energy Storage. *Advanced Materials* **2010**, *22* (8), E28-E62. DOI: https://doi.org/10.1002/adma.200903328.

(11) Liu, J.; Wang, J.; Xu, C.; Jiang, H.; Li, C.; Zhang, L.; Lin, J.; Shen, Z. X. Advanced Energy Storage Devices: Basic Principles, Analytical Methods, and Rational Materials

Design. *Advanced Science* **2018**, *5* (1), 1700322. DOI: https://doi.org/10.1002/advs.201700322.

(12) Dunn, B.; Kamath, H.; Tarascon, J.-M. Electrical Energy Storage for the Grid: A Battery of Choices. *Science* **2011**, *334* (6058), 928-935. DOI: doi:10.1126/science.1212741.

(13) Yang, Z.; Zhang, J.; Kintner-Meyer, M. C. W.; Lu, X.; Choi, D.; Lemmon, J. P.; Liu, J. Electrochemical Energy Storage for Green Grid. *Chemical Reviews* **2011**, *111* (5), 3577-3613. DOI: 10.1021/cr100290v.

(14) Gür, T. M. Review of electrical energy storage technologies, materials and systems: challenges and prospects for large-scale grid storage. *Energy & Environmental Science* **2018**, *11* (10), 2696-2767, 10.1039/C8EE01419A. DOI: 10.1039/C8EE01419A.

(15) Simon, P.; Gogotsi, Y. Materials for electrochemical capacitors. *Nature Materials* **2008**, *7* (11), 845-854. DOI: 10.1038/nmat2297.

(16) Winter, M.; Brodd, R. J. What Are Batteries, Fuel Cells, and Supercapacitors? *Chemical Reviews* **2004**, *104* (10), 4245-4270. DOI: 10.1021/cr020730k.

(17) Conway, B. E. *Electrochemical supercapacitors: scientific fundamentals and technological applications*; Springer Science & Business Media, **2013**.

(18) Gür, T. M. Comprehensive review of methane conversion in solid oxide fuel cells: Prospects for efficient electricity generation from natural gas. *Progress in Energy and Combustion Science* **2016**, *54*, 1-64. DOI: https://doi.org/10.1016/j.pecs.2015.10.004.

(19) Sopian, K.; Wan Daud, W. R. Challenges and future developments in proton exchange membrane fuel cells. *Renewable Energy* **2006**, *31* (5), 719-727. DOI: https://doi.org/10.1016/j.renene.2005.09.003. Tang, D.; Pan, J.; Lu, S.; Zhuang, L.; Lu, J. Alkaline polymer electrolyte fuel cells: Principle, challenges, and recent progress. *Science China Chemistry* **2010**, *53* (2), 357-364. DOI: 10.1007/s11426-010-0080-5.

(20) Cheng, X.; Shi, Z.; Glass, N.; Zhang, L.; Zhang, J.; Song, D.; Liu, Z.-S.; Wang, H.; Shen, J. A review of PEM hydrogen fuel cell contamination: Impacts, mechanisms, and mitigation. *Journal of Power Sources* **2007**, *165* (2), 739-756. DOI: https://doi.org/10.1016/j.jpowsour.2006.12.012.

(21) Chen, Z.; Higgins, D.; Yu, A.; Zhang, L.; Zhang, J. A review on non-precious metal electrocatalysts for PEM fuel cells. *Energy & Environmental Science* **2011**, *4* (9), 3167-3192, 10.1039/C0EE00558D. DOI: 10.1039/C0EE00558D.

(22) Brett, D. J. L.; Atkinson, A.; Brandon, N. P.; Skinner, S. J. Intermediate temperature solid oxide fuel cells. *Chemical Society Reviews* **2008**, *37* (8), 1568-1578, 10.1039/B612060C. DOI: 10.1039/B612060C.

(23) Murray, E. P.; Harris, S. J.; Jen, H. Solid Oxide Fuel Cells Utilizing Dimethyl Ether Fuel. *Journal of The Electrochemical Society* **2002**, *149* (9), A1127. DOI: 10.1149/1.1496484.

(24) Costa-Nunes, O.; Vohs, J. M.; Gorte, R. J. A Study of Direct-Conversion SOFC with n-Butane at Higher Fuel Utilization. *Journal of The Electrochemical Society* **2003**, *150* (7), A858. DOI: 10.1149/1.1574807.

(25) Zhan, Z.; Barnett, S. A. An Octane-Fueled Solid Oxide Fuel Cell. *Science* **2005**, *308* (5723), 844-847. DOI: doi:10.1126/science.1109213.

(26) Alexander, B. R.; Mitchell, R. E.; Gür, T. M. Experimental and Modeling Study of Biomass Conversion in a Solid Carbon Fuel Cell. *Journal of The Electrochemical Society* **2012**, *159* (3), B347-B354. DOI: 10.1149/2.096203jes.

(27) Gür, T. M.; Homel, M.; Virkar, A. V. High performance solid oxide fuel cell operating on dry gasified coal. *Journal of Power Sources* **2010**, *195* (4), 1085-1090. DOI: https://doi.org/10.1016/j.jpowsour.2009.08.098.

(28) Wilberforce, T.; Alaswad, A.; Palumbo, A.; Dassisti, M.; Olabi, A. G. Advances in stationary and portable fuel cell applications. *International Journal of Hydrogen Energy* **2016**, *41* (37), 16509-16522. DOI: https://doi.org/10.1016/j.ijhydene.2016.02.057.

(29) Wang, J.; Wang, H.; Fan, Y. Techno-Economic Challenges of Fuel Cell Commercialization. *Engineering* **2018**, *4* (3), 352-360. DOI: https://doi.org/10.1016/j.eng.2018.05.007.

(30) Abraham, K. M. Prospects and Limits of Energy Storage in Batteries. *The Journal of Physical Chemistry Letters* **2015**, *6* (5), 830-844. DOI: 10.1021/jz5026273.

(31) Markevich, E.; Salitra, G.; Aurbach, D. Fluoroethylene Carbonate as an Important Component for the Formation of an Effective Solid Electrolyte Interphase on Anodes and Cathodes for Advanced Li-Ion Batteries. *ACS Energy Letters* **2017**, *2* (6), 1337-1345. DOI: 10.1021/acsenergylett.7b00163. Besenhard, J. O.; Winter, M. Advances in Battery Technology: Rechargeable Magnesium Batteries and Novel Negative-Electrode Materials for Lithium Ion Batteries. *ChemPhysChem* **2002**, *3* (2), 155-159. DOI: https://doi.org/10.1002/1439-7641(20020215)3:2<155::AID-CPHC155>3.0.CO;2-S. Ellis, B. L.; Lee, K. T.; Nazar, L. F. Positive Electrode Materials for Li-Ion and Li-Batteries. *Chemistry of Materials* **2010**, *22* (3), 691-714. DOI: 10.1021/cm902696j. Verma, P.; Maire, P.; Novák, P. A review of the features and analyses of the solid electrolyte interphase in Li-ion batteries. *Electrochimica Acta* **2010**, *55* (22), 6332-6341. DOI: https://doi.org/10.1016/j.electacta.2010.05.072. Xu, K. Electrolytes and Interphases in Li-Ion Batteries and Beyond. *Chemical Reviews* **2014**, *114* (23), 11503-11618. DOI: 10.1021/cr500003w.

(32) Kang, B.; Ceder, G. Battery materials for ultrafast charging and discharging. *Nature* **2009**, *458* (7235), 190-193. DOI: 10.1038/nature07853. Gao, X.-P.; Yang, H.-X. Multi-

electron reaction materials for high energy density batteries. *Energy & Environmental Science* **2010**, *3* (2), 174-189, 10.1039/B916098A. DOI: 10.1039/B916098A.

(33) Ji, X.; Nazar, L. F. Advances in Li–S batteries. *Journal of Materials Chemistry* **2010**, *20* (44), 9821-9826, 10.1039/B925751A. DOI: 10.1039/B925751A. Kubota, K.; Komaba, S. Review—Practical Issues and Future Perspective for Na-Ion Batteries. *Journal of The Electrochemical Society* **2015**, *162* (14), A2538-A2550. DOI: 10.1149/2.0151514jes. Xin, S.; Yin, Y.-X.; Guo, Y.-G.; Wan, L.-J. A High-Energy Room-Temperature Sodium-Sulfur Battery. *Advanced Materials* **2014**, *26* (8), 1261-1265. DOI: https://doi.org/10.1002/adma.201304126. Christensen, J.; Albertus, P.; Sanchez-Carrera, R. S.; Lohmann, T.; Kozinsky, B.; Liedtke, R.; Ahmed, J.; Kojic, A. A Critical Review of Li/Air Batteries. *Journal of The Electrochemical Society* **2011**, *159* (2), R1-R30. DOI: 10.1149/2.086202jes. Lee, J.-S.; Tai Kim, S.; Cao, R.; Choi, N.-S.; Liu, M.; Lee, K. T.; Cho, J. Metal–Air Batteries with High Energy Density: Li–Air versus Zn–Air. *Advanced Energy Materials* **2011**, *1* (1), 34-50. DOI: https://doi.org/10.1002/aenm.201000010. Weber, A. Z.; Mench, M. M.; Meyers, J. P.; Ross, P. N.; Gostick, J. T.; Liu, Q. Redox flow batteries: a review. *Journal of Applied Electrochemistry* **2011**, *41* (10), 1137. DOI: 10.1007/s10800-011-0348-2.

(34) Shiraishi, S. Chapter 27 - Electric Double Layer Capacitors. In *Carbon Alloys*, Yasuda, E.-i., Inagaki, M., Kaneko, K., Endo, M., Oya, A., Tanabe, Y. Eds.; Elsevier Science, 2003; pp 447-457.

(35) Poonam; Sharma, K.; Arora, A.; Tripathi, S. K. Review of supercapacitors: Materials and devices. *Journal of Energy Storage* **2019**, *21*, 801-825. DOI: https://doi.org/10.1016/j.est.2019.01.010.

(36) Salleh, N. A.; Kheawhom, S.; Ashrina A Hamid, N.; Rahiman, W.; Mohamad, A. A. Electrode polymer binders for supercapacitor applications: A review. *Journal of Materials*

Research and Technology **2023**, *23*, 3470-3491. DOI: https://doi.org/10.1016/j.jmrt.2023.02.013.

(37) Simon, P.; Gogotsi, Y.; Dunn, B. Where Do Batteries End and Supercapacitors Begin? *Science* **2014**, *343* (6176), 1210-1211. DOI: doi:10.1126/science.1249625.

(38) Hadjipaschalis, I.; Poullikkas, A.; Efthimiou, V. Overview of current and future energy storage technologies for electric power applications. *Renewable and Sustainable Energy Reviews* **2009**, *13* (6), 1513-1522. DOI: https://doi.org/10.1016/j.rser.2008.09.028.

(39) Zhang, L. L.; Zhao, X. S. Carbon-based materials as supercapacitor electrodes. *Chemical Society Reviews* **2009**, *38* (9), 2520-2531, 10.1039/B813846J. DOI: 10.1039/B813846J.

(40) Sarno, M. Chapter 22 - Nanotechnology in energy storage: the supercapacitors. In *Studies in Surface Science and Catalysis*, Basile, A., Centi, G., Falco, M. D., Iaquaniello, G. Eds.; Vol. 179; Elsevier, 2020; pp 431-458.

(41) Brousse, T.; Bélanger, D.; Long, J. W. To Be or Not To Be Pseudocapacitive? *Journal of The Electrochemical Society* **2015**, *162* (5), A5185-A5189. DOI: 10.1149/2.0201505jes.

(42) Conway, B. E.; Pell, W. G. Double-layer and pseudocapacitance types of electrochemical capacitors and their applications to the development of hybrid devices. *Journal of Solid State Electrochemistry* **2003**, *7* (9), 637-644. DOI: 10.1007/s10008-003-0395-7.

(43) Conway, B. E.; Birss, V.; Wojtowicz, J. The role and utilization of pseudocapacitance for energy storage by supercapacitors. *Journal of Power Sources* **1997**, *66* (1), 1-14. DOI: https://doi.org/10.1016/S0378-7753(96)02474-3. Conway, B. E. Transition from "Supercapacitor" to "Battery" Behavior in Electrochemical Energy Storage. *Journal of The Electrochemical Society* **1991**, *138* (6), 1539-1548. DOI: 10.1149/1.2085829.

(44) Wang, G.; Zhang, L.; Zhang, J. A review of electrode materials for electrochemical supercapacitors. *Chemical Society Reviews* **2012**, *41* (2), 797-828, 10.1039/C1CS15060J. DOI: 10.1039/C1CS15060J.

(45) Pell, W. G.; Conway, B. E. Peculiarities and requirements of asymmetric capacitor devices based on combination of capacitor and battery-type electrodes. *Journal of Power Sources* **2004**, *136* (2), 334-345. DOI: https://doi.org/10.1016/j.jpowsour.2004.03.021.

(46) Zhi, M.; Xiang, C.; Li, J.; Li, M.; Wu, N. Nanostructured carbon–metal oxide composite electrodes for supercapacitors: a review. *Nanoscale* **2013**, *5* (1), 72-88, 10.1039/C2NR32040A. DOI: 10.1039/C2NR32040A.

(47) Wu, Z.-S.; Wang, D.-W.; Ren, W.; Zhao, J.; Zhou, G.; Li, F.; Cheng, H.-M. Anchoring Hydrous RuO2 on Graphene Sheets for High-Performance Electrochemical Capacitors. *Advanced Functional Materials* **2010**, *20* (20), 3595-3602. DOI: https://doi.org/10.1002/adfm.201001054.

(48) Stoller, M. D.; Ruoff, R. S. Best practice methods for determining an electrode material's performance for ultracapacitors. *Energy & Environmental Science* **2010**, *3* (9), 1294-1301, 10.1039/C0EE00074D. DOI: 10.1039/C0EE00074D.

(49) Brodd, R. J.; Bullock, K. R.; Leising, R. A.; Middaugh, R. L.; Miller, J. R.; Takeuchi, E. Batteries, 1977 to 2002. *Journal of The Electrochemical Society* **2004**, *151* (3), K1. DOI: 10.1149/1.1641042.

(50) Jayalakshmi, M.; Balasubramanian, K. Simple Capacitors to Supercapacitors - An Overview. *International Journal of Electrochemical Science* **2008**, *3* (11), 1196-1217.

(51) Choi, J.-H.; Lee, C.; Cho, S.; Moon, G. D.; kim, B.-s.; Chang, H.; Jang, H. D. High capacitance and energy density supercapacitor based on biomass-derived activated carbons with reduced graphene oxide binder. *Carbon* **2018**, *132*, 16-24. DOI: https://doi.org/10.1016/j.carbon.2018.01.105. Burke, A. Ultracapacitors: why, how, and

where is the technology. *Journal of Power Sources* **2000**, *91* (1), 37-50. DOI: https://doi.org/10.1016/S0378-7753(00)00485-7.

(52) Kim, T.; Jung, G.; Yoo, S.; Suh, K. S.; Ruoff, R. S. Activated Graphene-Based Carbons as Supercapacitor Electrodes with Macro- and Mesopores. *ACS Nano* **2013**, *7* (8), 6899-6905. DOI: 10.1021/nn402077v.

(53) Hutchinson, T.; Burgess, S.; Herrmann, G. Current hybrid-electric powertrain architectures: Applying empirical design data to life cycle assessment and whole-life cost analysis. *Applied Energy* **2014**, *119*, 314-329. DOI: https://doi.org/10.1016/j.apenergy.2014.01.009.

(54) Dixon, J.; Nakashima, I.; Arcos, E. F.; Ortuzar, M. Electric Vehicle Using a Combination of Ultracapacitors and ZEBRA Battery. *IEEE Transactions on Industrial Electronics* **2010**, *57* (3), 943-949. DOI: 10.1109/TIE.2009.2027920.

(55) Hall, P. J.; Mirzaeian, M.; Fletcher, S. I.; Sillars, F. B.; Rennie, A. J. R.; Shitta-Bey, G. O.; Wilson, G.; Cruden, A.; Carter, R. Energy storage in electrochemical capacitors: designing functional materials to improve performance. *Energy & Environmental Science* **2010**, *3* (9), 1238-1251, 10.1039/C0EE00004C. DOI: 10.1039/C0EE00004C.

(56) Kumar, S.; Saeed, G.; Zhu, L.; Hui, K. N.; Kim, N. H.; Lee, J. H. 0D to 3D carbon-based networks combined with pseudocapacitive electrode material for high energy density supercapacitor: A review. *Chemical Engineering Journal* **2021**, *403*, 126352. DOI: https://doi.org/10.1016/j.cej.2020.126352.

(57) Hillier, N.; Yong, S.; Beeby, S. The good, the bad and the porous: A review of carbonaceous materials for flexible supercapacitor applications. *Energy Reports* **2020**, *6*, 148-156. DOI: https://doi.org/10.1016/j.egyr.2020.03.019.

(58) Gu, W.; Yushin, G. Review of nanostructured carbon materials for electrochemical capacitor applications: advantages and limitations of activated carbon, carbide-derived

carbon, zeolite-templated carbon, carbon aerogels, carbon nanotubes, onion-like carbon, and graphene. *WIREs Energy and Environment* **2014**, *3* (5), 424-473. DOI: https://doi.org/10.1002/wene.102.

(59) Quiroz, M. A.; Bandala, E. R. Types of Conducting Diamond Materials and their Properties. In *Synthetic Diamond Films*, 2011; pp 57-75.

(60) Poole, C. P.; Owens, F. J. Introduction to nanotechnology. **2003**.

(61) Berry, V. Impermeability of graphene and its applications. *Carbon* **2013**, *62*, 1-10. DOI: https://doi.org/10.1016/j.carbon.2013.05.052.

(62) Tiwari, S. K.; Kumar, V.; Huczko, A.; Oraon, R.; Adhikari, A. D.; Nayak, G. C. Magical Allotropes of Carbon: Prospects and Applications. *Critical Reviews in Solid State and Materials Sciences* **2016**, *41* (4), 257-317. DOI: 10.1080/10408436.2015.1127206.

(63) Jiang, H.; Lee, P. S.; Li, C. 3D carbon based nanostructures for advanced supercapacitors. *Energy & Environmental Science* **2013**, *6* (1), 41-53, 10.1039/C2EE23284G. DOI: 10.1039/C2EE23284G.

(64) Castro Neto, A. H.; Guinea, F.; Peres, N. M. R.; Novoselov, K. S.; Geim, A. K. The electronic properties of graphene. *Reviews of Modern Physics* **2009**, *81* (1), 109-162. DOI: 10.1103/RevModPhys.81.109. Novoselov, K. S.; Geim, A. K.; Morozov, S. V.; Jiang, D.; Zhang, Y.; Dubonos, S. V.; Grigorieva, I. V.; Firsov, A. A. Electric Field Effect in Atomically Thin Carbon Films. *Science* **2004**, *306* (5696), 666-669. DOI: doi:10.1126/science.1102896. Geim, A. K.; Novoselov, K. S. The rise of graphene. *Nature Materials* **2007**, *6* (3), 183-191. DOI: 10.1038/nmat1849.

(65) Yan, J.; Wang, Q.; Wei, T.; Fan, Z. Recent Advances in Design and Fabrication of Electrochemical Supercapacitors with High Energy Densities. *Advanced Energy Materials* **2014**, *4* (4), 1300816. DOI: https://doi.org/10.1002/aenm.201300816.

(66) Gao, F.; Wolfer, M. T.; Nebel, C. E. Highly porous diamond foam as a thin-film micro-supercapacitor material. *Carbon* **2014**, *80*, 833-840. DOI: https://doi.org/10.1016/j.carbon.2014.09.007. Gao, F.; Nebel, C. E. Diamond-Based Supercapacitors: Realization and Properties. *ACS Applied Materials & Interfaces* **2016**, *8* (42), 28244-28254. DOI: 10.1021/acsami.5b07027. Feng, X.; Bai, Y.; Liu, M.; Li, Y.; Yang, H.; Wang, X.; Wu, C. Untangling the respective effects of heteroatom-doped carbon materials in batteries, supercapacitors and the ORR to design high performance materials. *Energy & Environmental Science* **2021**, *14* (4), 2036-2089, 10.1039/D1EE00166C. DOI: 10.1039/D1EE00166C. Chen, L.-F.; Huang, Z.-H.; Liang, H.-W.; Gao, H.-L.; Yu, S.-H. Three-Dimensional Heteroatom-Doped Carbon Nanofiber Networks Derived from Bacterial Cellulose for Supercapacitors. *Advanced Functional Materials* **2014**, *24* (32), 5104-5111. DOI: https://doi.org/10.1002/adfm.201400590. Jiang, L.; Nelson, G. W.; Kim, H.; Sim, I. N.; Han, S. O.; Foord, J. S. Cellulose-Derived Supercapacitors from the Carbonisation of Filter Paper. *ChemistryOpen* **2015**, *4* (5), 586-589. DOI: https://doi.org/10.1002/open.201500150. Jiang, L.; Nelson, G. W.; Han, S. O.; Kim, H.; Sim, I. N.; Foord, J. S. Natural Cellulose Materials for Supercapacitors. *Electrochimica Acta* **2016**, *192*, 251-258. DOI: https://doi.org/10.1016/j.electacta.2015.12.138. Jiang, L.; Seong, Y.-H.; Han, S. O.; Kim, H.; Kim, H. H.; Foord, J. S. Nickel treatment of biomass-derived nanocarbon for energy devices. *Carbon* **2018**, *130*, 724-729. DOI: https://doi.org/10.1016/j.carbon.2018.01.063. Jiang, L.; Shanmuganathan, S.; Nelson, G.; Han, S.; Sim, I. N.; Foord, J. Hybrid system of nickel–cobalt hydroxide on carbonised natural cellulose materials for supercapacitors. *Journal of Solid State Electrochemistry* **2018**, *22*. DOI: 10.1007/s10008-017-3723-z. Jiang, L.; Han, S. O.; Pirie, M.; Kim, H. H.; Seong, Y.-H.; Kim, H.; Foord, J. S. Seaweed biomass waste-derived carbon as an electrode material for supercapacitor. *Energy & Environment* **2021**, *32* (6), 1117-1129. DOI: 10.1177/0958305x19882398.

(67) Brillas, E.; Mart, C. A. *Synthetic diamond films: preparation, electrochemistry, characterization, and applications*; John Wiley & Sons, 2011.

(68) Kraft, A. Doped Diamond: A Compact Review on a New, Versatile Electrode Material. *International Journal of Electrochemical Science* **2007**, *2*.

(69) Wort, C. J. H.; Balmer, R. S. Diamond as an electronic material. *Materials Today* **2008**, *11* (1), 22-28. DOI: https://doi.org/10.1016/S1369-7021(07)70349-8.

(70) Lee, K. W.; Pickett, W. E. Superconductivity in Boron-Doped Diamond. *Physical Review Letters* **2004**, *93* (23), 237003. DOI: 10.1103/PhysRevLett.93.237003.

(71) Schwander, M.; Partes, K. A review of diamond synthesis by CVD processes. *Diamond and Related Materials* **2011**, *20* (9), 1287-1301. DOI: https://doi.org/10.1016/j.diamond.2011.08.005.

(72) Butler, J. E.; Woodin, R. L.; Brown, L. M.; Fallon, P.; Lettington, A. H.; Steeds, J. W. Thin film diamond growth mechanisms. *Philosophical Transactions of the Royal Society of London. Series A: Physical and Engineering Sciences* **1993**, *342* (1664), 209-224. DOI: doi:10.1098/rsta.1993.0015. Watanabe, T.; Yoshioka, S.; Yamamoto, T.; Sepehri-Amin, H.; Ohkubo, T.; Matsumura, S.; Einaga, Y. The local structure in heavily boron-doped diamond and the effect this has on its electrochemical properties. *Carbon* **2018**, *137*, 333-342. DOI: https://doi.org/10.1016/j.carbon.2018.05.026.

(73) Luong, J. H. T.; Male, K. B.; Glennon, J. D. Boron-doped diamond electrode: synthesis, characterization, functionalization and analytical applications. *Analyst* **2009**, *134* (10), 1965-1979, 10.1039/B910206J. DOI: 10.1039/B910206J.

(74) Maeda, H.; Ohtsubo, K.; Kameta, M.; Saito, T.; Kusakabe, K.; Morooka, S.; Asano, T. Growth behavior of boron-doped diamond in microwave plasma-assisted chemical vapor deposition using trimethylboron as the dopant source. *Diamond and Related Materials* **1998**, *7* (1), 88-95. DOI: https://doi.org/10.1016/S0925-9635(98)80001-0. Morooka, S.; Fukui, T.;

Semoto, K.; Tsubota, T.; Saito, T.; Kusakabe, K.; Maeda, H.; Hayashi, Y.; Asano, T. Electrical properties of homoepitaxial boron-doped diamond thin films grown by chemical vapor deposition using trimethylboron as dopant. *Diamond and Related Materials* **1999**, *8* (1), 42-47. DOI: https://doi.org/10.1016/S0925-9635(98)00323-9.

(75) Yang, N.; Yu, S.; Macpherson, J. V.; Einaga, Y.; Zhao, H.; Zhao, G.; Swain, G. M.; Jiang, X. Conductive diamond: synthesis, properties, and electrochemical applications. *Chemical Society Reviews* **2019**, *48* (1), 157-204, 10.1039/C7CS00757D. DOI: 10.1039/C7CS00757D.

(76) Einaga, Y. Development of Electrochemical Applications of Boron-Doped Diamond Electrodes. *Bulletin of the Chemical Society of Japan* **2018**, *91* (12), 1752-1762. DOI: 10.1246/bcsj.20180268.

(77) Sun, J.; Lu, H.; Lin, H.; Du, L.; Huang, W.; Li, H.; Cui, T. Electrochemical oxidation of aqueous phenol at low concentration using Ti/BDD electrode. *Separation and Purification Technology* **2012**, *88*, 116-120. DOI: https://doi.org/10.1016/j.seppur.2011.12.022.

(78) Trouillon, R.; O'Hare, D. Comparison of glassy carbon and boron doped diamond electrodes: Resistance to biofouling. *Electrochimica Acta* **2010**, *55* (22), 6586-6595. DOI: https://doi.org/10.1016/j.electacta.2010.06.016.

(79) Granger, M. C.; Witek, M.; Xu, J.; Wang, J.; Hupert, M.; Hanks, A.; Koppang, M. D.; Butler, J. E.; Lucazeau, G.; Mermoux, M.; et al. Standard electrochemical behavior of high-quality, boron-doped polycrystalline diamond thin-film electrodes. *Anal Chem* **2000**, *72* (16), 3793-3804. DOI: 10.1021/ac0000675 From NLM.

(80) Tan, S. M.; Poh, H. L.; Sofer, Z.; Pumera, M. Boron-doped graphene and boron-doped diamond electrodes: detection of biomarkers and resistance to fouling. *Analyst* **2013**, *138* (17), 4885-4891, 10.1039/C3AN00535F. DOI: 10.1039/C3AN00535F.

(81) Saterlay, A. J.; Marken, F.; Foord, J. S.; Compton, R. G. Sonoelectrochemical investigation of silver analysis at a highly boron-doped diamond electrode. *Talanta* **2000**, *53* (2), 403-415. DOI: https://doi.org/10.1016/S0039-9140(00)00505-1. Compton, R. G.; Foord, J. S.; Marken, F. Electroanalysis at Diamond-Like and Doped-Diamond Electrodes. *Electroanalysis* **2003**, *15* (17), 1349-1363. DOI: https://doi.org/10.1002/elan.200302830.

(82) Zhu, C.; Jiang, C.; Chen, S.; Mei, R.; Wang, X.; Cao, J.; Ma, L.; Zhou, B.; Wei, Q.; Ouyang, G.; et al. Ultrasound enhanced electrochemical oxidation of Alizarin Red S on boron doped diamond(BDD) anode:Effect of degradation process parameters. *Chemosphere* **2018**, *209*, 685-695. DOI: https://doi.org/10.1016/j.chemosphere.2018.06.137.

(83) Sanghavi, B. J.; Wolfbeis, O. S.; Hirsch, T.; Swami, N. S. Nanomaterial-based electrochemical sensing of neurological drugs and neurotransmitters. *Microchimica Acta* **2015**, *182* (1), 1-41. DOI: 10.1007/s00604-014-1308-4.

(84) Svítková, J.; Ignat, T.; Švorc, Ľ.; Labuda, J.; Barek, J. Chemical Modification of Boron-Doped Diamond Electrodes for Applications to Biosensors and Biosensing. *Critical Reviews in Analytical Chemistry* **2016**, *46* (3), 248-256. DOI: 10.1080/10408347.2015.1082125. Sharma, S.; Singh, N.; Tomar, V.; Chandra, R. A review on electrochemical detection of serotonin based on surface modified electrodes. *Biosensors and Bioelectronics* **2018**, *107*, 76-93. DOI: https://doi.org/10.1016/j.bios.2018.02.013.

(85) Yang, N.; Zhao, G.; Foord, J. S. *Nanocarbon Electrochemistry*; Wiley, 2020.

(86) Toghill, K. E.; Compton, R. G. Metal Nanoparticle Modified Boron Doped Diamond Electrodes for Use in Electroanalysis. *Electroanalysis* **2010**, *22* (17-18), 1947-1956. DOI: https://doi.org/10.1002/elan.201000072.

(87) Nelson, G. W.; Foord, J. S. Nanoparticle-Based Diamond Electrodes. *Novel Aspects of Diamond* **2015**, 165-204. Mavrokefalos, C. K.; Hasan, M.; Rohan, J. F.; Foord, J. S. Enhanced Mass Activity and Stability of Bimetallic Pd-Ni Nanoparticles on Boron-Doped

Diamond for Direct Ethanol Fuel Cell Applications. *ChemElectroChem* **2018**, *5* (3), 455-463. DOI: https://doi.org/10.1002/celc.201701105.

(88) Shi, C.; Li, H.; Li, C.; Li, M.; Qu, C.; Yang, B. Preparation of TiO2/boron-doped diamond/Ta multilayer films and use as electrode materials for supercapacitors. *Applied Surface Science* **2015**, *357*, 1380-1387. DOI: https://doi.org/10.1016/j.apsusc.2015.10.006. Suffredini, H. B.; Tricoli, V.; Vatistas, N.; Avaca, L. A. Electro-oxidation of methanol and ethanol using a Pt–RuO2/C composite prepared by the sol–gel technique and supported on boron-doped diamond. *Journal of Power Sources* **2006**, *158* (1), 124-128. DOI: https://doi.org/10.1016/j.jpowsour.2005.09.040.

(89) Muzyka, K.; Sun, J.; Fereja, T. H.; Lan, Y.; Zhang, W.; Xu, G. Boron-doped diamond: current progress and challenges in view of electroanalytical applications. *Analytical Methods* **2019**, *11* (4), 397-414, 10.1039/C8AY02197J. DOI: 10.1039/C8AY02197J. Zhu, C.; Yang, G.; Li, H.; Du, D.; Lin, Y. Electrochemical Sensors and Biosensors Based on Nanomaterials and Nanostructures. *Analytical Chemistry* **2015**, *87* (1), 230-249. DOI: 10.1021/ac5039863.

(90) Radjenovic, J.; Sedlak, D. L. Challenges and Opportunities for Electrochemical Processes as Next-Generation Technologies for the Treatment of Contaminated Water. *Environmental Science & Technology* **2015**, *49* (19), 11292-11302. DOI: 10.1021/acs.est.5b02414. Zhu, X.; Ni, J.; Lai, P. Advanced treatment of biologically pretreated coking wastewater by electrochemical oxidation using boron-doped diamond electrodes. *Water Research* **2009**, *43* (17), 4347-4355. DOI: https://doi.org/10.1016/j.watres.2009.06.030.

(91) Bensalah; Gadri; Cañizares, P.; Sáez, C.; Lobato, J.; Rodrigo, M. A. Electrochemical Oxidation of Hydroquinone, Resorcinol, and Catechol on Boron-Doped Diamond Anodes. *Environmental Science & Technology* **2005**, *39* (18), 7234-7239. DOI: 10.1021/es0500660. Weng, J.; Xue, J.; Wang, J.; Ye, J.; Cui, H.; Sheu, F.; Zhang, Q. Gold-Cluster Sensors

Formed Electrochemically at Boron-Doped-Diamond Electrodes: Detection of Dopamine in the Presence of Ascorbic Acid and Thiols. *Advanced Functional Materials* **2005**, *15* (4), 639-647, https://doi.org/10.1002/adfm.200400049. DOI: https://doi.org/10.1002/adfm.200400049 (acccessed 2022/04/11).

(92) Baluchová, S.; Daňhel, A.; Dejmková, H.; Ostatná, V.; Fojta, M.; Schwarzová-Pecková, K. Recent progress in the applications of boron doped diamond electrodes in electroanalysis of organic compounds and biomolecules – A review. *Analytica Chimica Acta* **2019**, *1077*, 30-66. DOI: https://doi.org/10.1016/j.aca.2019.05.041.

(93) Lips, S.; Waldvogel, S. R. Use of Boron-Doped Diamond Electrodes in Electro-Organic Synthesis. *ChemElectroChem* **2019**, *6* (6), 1649-1660. DOI: https://doi.org/10.1002/celc.201801620. Klavarioti, M.; Mantzavinos, D.; Kassinos, D. Removal of residual pharmaceuticals from aqueous systems by advanced oxidation processes. *Environment International* **2009**, *35* (2), 402-417. DOI: https://doi.org/10.1016/j.envint.2008.07.009. Nakata, K.; Ozaki, T.; Terashima, C.; Fujishima, A.; Einaga, Y. High-Yield Electrochemical Production of Formaldehyde from CO2 and Seawater. *Angewandte Chemie International Edition* **2014**, *53* (3), 871-874, https://doi.org/10.1002/anie.201308657. DOI: https://doi.org/10.1002/anie.201308657 (acccessed 2022/04/11). Salazar-Banda, G. R.; Suffredini, H. B.; Calegaro, M. L.; Tanimoto, S. T.; Avaca, L. A. Sol–gel-modified boron-doped diamond surfaces for methanol and ethanol electro-oxidation in acid medium. *Journal of Power Sources* **2006**, *162* (1), 9-20. DOI: https://doi.org/10.1016/j.jpowsour.2006.06.045.

(94) Roy, N.; Shibano, Y.; Terashima, C.; Katsumata, K.-i.; Nakata, K.; Kondo, T.; Yuasa, M.; Fujishima, A. Ionic-Liquid-Assisted Selective and Controlled Electrochemical CO2 Reduction at Cu-Modified Boron-Doped Diamond Electrode. *ChemElectroChem* **2016**, *3* (7), 1044-1047. DOI: https://doi.org/10.1002/celc.201600105. Zhu, D. D.; Liu, J. L.; Qiao, S. Z.

Recent Advances in Inorganic Heterogeneous Electrocatalysts for Reduction of Carbon Dioxide. *Advanced Materials* **2016**, *28* (18), 3423-3452. DOI: https://doi.org/10.1002/adma.201504766. Roy, N.; Hirano, Y.; Kuriyama, H.; Sudhagar, P.; Suzuki, N.; Katsumata, K.-i.; Nakata, K.; Kondo, T.; Yuasa, M.; Serizawa, I.; et al. Boron-doped diamond semiconductor electrodes: Efficient photoelectrochemical CO2 reduction through surface modification. *Scientific Reports* **2016**, *6* (1), 38010. DOI: 10.1038/srep38010.

(95) Honda, K.; Yoshimura, M.; Uchikado, R.; Kondo, T.; Rao, T. N.; Tryk, D. A.; Fujishima, A.; Watanabe, M.; Yasui, K.; Masuda, H. Electrochemical characteristics for redox systems at nano-honeycomb diamond. *Electrochimica Acta* **2002**, *47* (27), 4373-4385. DOI: https://doi.org/10.1016/S0013-4686(02)00511-X.

(96) Raza, W.; Ali, F.; Raza, N.; Luo, Y.; Kim, K.-H.; Yang, J.; Kumar, S.; Mehmood, A.; Kwon, E. E. Recent advancements in supercapacitor technology. *Nano Energy* **2018**, *52*, 441-473. DOI: https://doi.org/10.1016/j.nanoen.2018.08.013. Yu, S.; Yang, N.; Jiang, X.; Zhang, W.; Liu, S. Conductive Diamond for Electrochemical Energy Applications. In *Nanocarbon Electrochemistry*, 2020; pp 171-199.

(97) Lu, H.; Zhao, X. S. Biomass-derived carbon electrode materials for supercapacitors. *Sustainable Energy & Fuels* **2017**, *1* (6), 1265-1281, 10.1039/C7SE00099E. DOI: 10.1039/C7SE00099E.

(98) Wang, Y.; Qu, Q.; Gao, S.; Tang, G.; Liu, K.; He, S.; Huang, C. Biomass derived carbon as binder-free electrode materials for supercapacitors. *Carbon* **2019**, *155*, 706-726. DOI: https://doi.org/10.1016/j.carbon.2019.09.018.

(99) Laurichesse, S.; Avérous, L. Chemical modification of lignins: Towards biobased polymers. *Progress in Polymer Science* **2014**, *39* (7), 1266-1290. DOI: https://doi.org/10.1016/j.progpolymsci.2013.11.004. Yang, H.; Ye, S.; Zhou, J.; Liang, T.

Biomass-Derived Porous Carbon Materials for Supercapacitor. *Frontiers in Chemistry* **2019**, *7*, Review. DOI: 10.3389/fchem.2019.00274.

(100) Abioye, A. M.; Ani, F. N. Recent development in the production of activated carbon electrodes from agricultural waste biomass for supercapacitors: A review. *Renewable and Sustainable Energy Reviews* **2015**, *52*, 1282-1293. DOI: https://doi.org/10.1016/j.rser.2015.07.129.

(101) Raveendran, K.; Ganesh, A.; Khilar, K. C. Pyrolysis characteristics of biomass and biomass components. *Fuel* **1996**, *75* (8), 987-998. DOI: https://doi.org/10.1016/0016-2361(96)00030-0.

(102) Luo, X.; Chen, S.; Hu, T.; Chen, Y.; Li, F. Renewable biomass-derived carbons for electrochemical capacitor applications. *SusMat* **2021**, *1* (2), 211-240. DOI: https://doi.org/10.1002/sus2.8.

(103) Wang, H.; Li, Z.; Mitlin, D. Tailoring Biomass-Derived Carbon Nanoarchitectures for High-Performance Supercapacitors. *ChemElectroChem* **2014**, *1* (2), 332-337. DOI: https://doi.org/10.1002/celc.201300127.

(104) Cheng, B.-H.; Zeng, R. J.; Jiang, H. Recent developments of post-modification of biochar for electrochemical energy storage. *Bioresource Technology* **2017**, *246*, 224-233. DOI: https://doi.org/10.1016/j.biortech.2017.07.060.

(105) Zhang, X.; Zhang, L.; Li, A. Hydrothermal co-carbonization of sewage sludge and pinewood sawdust for nutrient-rich hydrochar production: Synergistic effects and products characterization. *Journal of Environmental Management* **2017**, *201*, 52-62. DOI: https://doi.org/10.1016/j.jenvman.2017.06.018.

(106) Williams, P. T.; Reed, A. R. Development of activated carbon pore structure via physical and chemical activation of biomass fibre waste. *Biomass and Bioenergy* **2006**, *30* (2), 144-152. DOI: https://doi.org/10.1016/j.biombioe.2005.11.006.

(107) Wang, Y.; Zhang, M.; Shen, X.; Wang, H.; Wang, H.; Xia, K.; Yin, Z.; Zhang, Y. Biomass-Derived Carbon Materials: Controllable Preparation and Versatile Applications. *Small* **2021**, *17* (40), 2008079. DOI: https://doi.org/10.1002/smll.202008079.

(108) Wang, J.; Kaskel, S. KOH activation of carbon-based materials for energy storage. *Journal of Materials Chemistry* **2012**, *22* (45), 23710-23725, 10.1039/C2JM34066F. DOI: 10.1039/C2JM34066F.

(109) Thomas, P.; Lai, C. W.; Bin Johan, M. R. Recent developments in biomass-derived carbon as a potential sustainable material for super-capacitor-based energy storage and environmental applications. *Journal of Analytical and Applied Pyrolysis* **2019**, *140*, 54-85. DOI: https://doi.org/10.1016/j.jaap.2019.03.021.

(110) Gao, Z.; Zhang, Y.; Song, N.; Li, X. Biomass-derived renewable carbon materials for electrochemical energy storage. *Materials Research Letters* **2017**, *5* (2), 69-88. DOI: 10.1080/21663831.2016.1250834.

(111) Hu, Z.; Srinivasan, M. P.; Ni, Y. Novel activation process for preparing highly microporous and mesoporous activated carbons. *Carbon* **2001**, *39* (6), 877-886. DOI: https://doi.org/10.1016/S0008-6223(00)00198-6.

(112) Fang, Y.; Luo, B.; Jia, Y.; Li, X.; Wang, B.; Song, Q.; Kang, F.; Zhi, L. Renewing Functionalized Graphene as Electrodes for High-Performance Supercapacitors. *Advanced Materials* **2012**, *24* (47), 6348-6355. DOI: https://doi.org/10.1002/adma.201202774.

(113) Lv, Y.; Li, Y.; Han, C.; Chen, J.; He, Z.; Zhu, J.; Dai, L.; Meng, W.; Wang, L. Application of porous biomass carbon materials in vanadium redox flow battery. *Journal of Colloid and Interface Science* **2020**, *566*, 434-443. DOI: https://doi.org/10.1016/j.jcis.2020.01.118.

(114) He, J.; Zhang, D.; Wang, Y.; Zhang, J.; Yang, B.; Shi, H.; Wang, K.; Wang, Y. Biomass-derived porous carbons with tailored graphitization degree and pore size distribution

for supercapacitors with ultra-high rate capability. *Applied Surface Science* **2020**, *515*, 146020. DOI: https://doi.org/10.1016/j.apsusc.2020.146020.

(115) Usevičiūtė, L.; Baltrėnaitė-Gedienė, E. Dependence of pyrolysis temperature and lignocellulosic physical-chemical properties of biochar on its wettability. *Biomass Conversion and Biorefinery* **2021**, *11* (6), 2775-2793. DOI: 10.1007/s13399-020-00711-3.

(116) Gong, Y.; Li, D.; Luo, C.; Fu, Q.; Pan, C. Highly porous graphitic biomass carbon as advanced electrode materials for supercapacitors. *Green Chemistry* **2017**, *19* (17), 4132-4140, 10.1039/C7GC01681F. DOI: 10.1039/C7GC01681F.

(117) Gopalakrishnan, A.; Badhulika, S. Effect of self-doped heteroatoms on the performance of biomass-derived carbon for supercapacitor applications. *Journal of Power Sources* **2020**, *480*, 228830. DOI: https://doi.org/10.1016/j.jpowsour.2020.228830. Paraknowitsch, J. P.; Thomas, A. Doping carbons beyond nitrogen: an overview of advanced heteroatom doped carbons with boron, sulphur and phosphorus for energy applications. *Energy & Environmental Science* **2013**, *6* (10), 2839-2855, 10.1039/C3EE41444B. DOI: 10.1039/C3EE41444B.

(118) Gu, P.; Liu, W.; Hou, Q.; Ni, Y. Lignocellulose-derived hydrogel/aerogel-based flexible quasi-solid-state supercapacitors with high-performance: a review. *Journal of Materials Chemistry A* **2021**, *9* (25), 14233-14264, 10.1039/D1TA02281D. DOI: 10.1039/D1TA02281D.

(119) Deng, J.; Li, M.; Wang, Y. Biomass-derived carbon: synthesis and applications in energy storage and conversion. *Green Chemistry* **2016**, *18* (18), 4824-4854, 10.1039/C6GC01172A. DOI: 10.1039/C6GC01172A. Wang, J.; Nie, P.; Ding, B.; Dong, S.; Hao, X.; Dou, H.; Zhang, X. Biomass derived carbon for energy storage devices. *Journal of Materials Chemistry A* **2017**, *5* (6), 2411-2428, 10.1039/C6TA08742F. DOI: 10.1039/C6TA08742F.

(120) Reza, M. S.; Yun, C. S.; Afroze, S.; Radenahmad, N.; Bakar, M. S. A.; Saidur, R.; Taweekun, J.; Azad, A. K. Preparation of activated carbon from biomass and its' applications in water and gas purification, a review. *Arab Journal of Basic and Applied Sciences* **2020**, *27* (1), 208-238. DOI: 10.1080/25765299.2020.1766799.

(121) Zhou, S.; Zhou, L.; Zhang, Y.; Sun, J.; Wen, J.; Yuan, Y. Upgrading earth-abundant biomass into three-dimensional carbon materials for energy and environmental applications. *Journal of Materials Chemistry A* **2019**, *7* (9), 4217-4229, 10.1039/C8TA12159A. DOI: 10.1039/C8TA12159A.

(122) Wang, J.-G.; Kang, F.; Wei, B. Engineering of MnO2-based nanocomposites for high-performance supercapacitors. *Progress in Materials Science* **2015**, *74*, 51-124. DOI: https://doi.org/10.1016/j.pmatsci.2015.04.003.

(123) Shao, Y.; El-Kady, M. F.; Sun, J.; Li, Y.; Zhang, Q.; Zhu, M.; Wang, H.; Dunn, B.; Kaner, R. B. Design and Mechanisms of Asymmetric Supercapacitors. *Chemical Reviews* **2018**, *118* (18), 9233-9280. DOI: 10.1021/acs.chemrev.8b00252.

(124) Lokhande, C. D.; Dubal, D. P.; Joo, O.-S. Metal oxide thin film based supercapacitors. *Current Applied Physics* **2011**, *11* (3), 255-270. DOI: https://doi.org/10.1016/j.cap.2010.12.001.

(125) Borenstein, A.; Hanna, O.; Attias, R.; Luski, S.; Brousse, T.; Aurbach, D. Carbon-based composite materials for supercapacitor electrodes: a review. *Journal of Materials Chemistry A* **2017**, *5* (25), 12653-12672, 10.1039/C7TA00863E. DOI: 10.1039/C7TA00863E.

Chapter 2 Experimental Theories and Techniques

In this chapter, electrochemical fundamentals and methods featured in the thesis are explained. The emphasis is placed on electrode process, equilibrium electrochemistry, electrode kinetics and mass transport. Afterwards, electrochemical methods such as chronoamperometry (CA), cyclic voltammetry (CV), galvanostatic charge-discharge (GCD) and electrochemical impedance spectroscopy (EIS) are introduced as well as instrumentation and experimental set-up. Additionally, the background of characterisation techniques employed is described, including scanning electron microscopy (SEM), energy-dispersive X-ray spectroscopy (EDS), X-ray diffraction (XRD), and X-ray photoelectron spectroscopy (XPS).

2.1 Electrochemical fundamentals

2.1.1 Electrode processes

In an electrochemical cell, two kinds of processes occur at an electrode. The first type is called non-faradaic processes which refers to processes where charges (i.e. electrons) do not cross the electrode/solution interface.[1] However, external currents will still flow in these processes such as adsorption/desorption due to changes of solution composition or potential applied. In an extreme case (e.g., ideal polarised electrode) where only non-faradaic processes are observed, the behaviour of the electrode/solution interface resembles that of a dielectric capacitor, given by the equation:

$$C = \frac{q}{E} \tag{2-1}$$

where C is the capacitance (Farads, F), q us the charge stored (Coulombs, C), and E is the potential across the capacitor (Volts, V). Charge will accumulate on the metal sheets and a charging (also called capacitive) current will flow when a potential is applied across the capacitor.

Analogous to a capacitor, a charge q^M on the electrode and a charge q^S in the solution exist at the electrode/solution interface with $q^M + q^S = 0$ at all times at a given potential. q^M is caused by an excess or deficiency of electrons, while q^S arises from an excess of electrolyte ions or oriented dipoles in solvent. The electrical double layer formed by the two charged layers (i.e. Helmholtz model) can be thus interpreted as a capacitor with two metal plates.[2] However, the double layer capacitance is often dependant of the potential applied, which is different from that of a real capacitor. In fact, the structure of the electrical double layer is more complicated than the simple model above. Therefore, the Helmholtz electrical double layer model was further developed by others.[3]

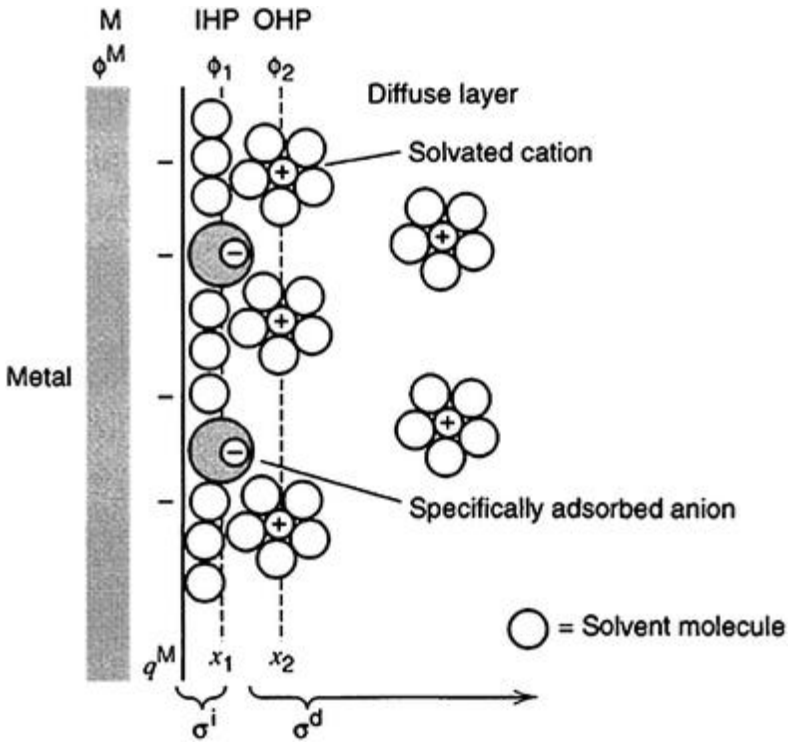

Figure 2.1 Schematic diagram of a proposed electrical double-layer model.[1]

Figure 2.1 shows an improved model of the double-layer region with multiple layers on the solution side. The closest layer to the electrode that contains specifically adsorbed species and solvent molecules is called the inner layer (also called the compact, Stern or Helmholtz layer). The inner Helmholtz plane (IHP) is defined by the centres of the specifically adsorbed ions in the inner layer with a potential ϕ_1 and a charge density of σ^i (μC cm^{-2}). Solvated ions that are non-specifically adsorbed can approach the electrode only to a longer distance via long-range electrostatic forces, and the locus of centres of these closest solvated species is called the outer Helmholtz plane (OHP) with a potential ϕ_2. Extending from the OHP to the bulk solution, the diffusion layer where solvated ions are distributed has an excess charge density of σ^d, and the total charge densities (where charges q are divided by the electrode area A) can be termed by:

$$\sigma^S = \sigma^i + \sigma^d = -\sigma^M \quad (2\text{-}2)$$

The overall double layer capacitance C_d is equal to the series capacitance of the OHP (C_H) and the diffuse region (C_D), depicted as[4]:

$$\frac{1}{C_d} = \frac{1}{C_H} + \frac{1}{C_D} \quad (2\text{-}3)$$

Notably, the energy storage mechanism of EDLCs is based on the presence of the non-faradaic processes and double layer capacitance.

The other type of processes where electrons are transferred across the electrode-electrolyte interface are called faradaic processes, resulting in oxidation and reduction reactions.[5] These processes are governed by Faraday's law as follows:

$$m = \frac{QM}{Fn} \quad (2\text{-}4)$$

where m is the mass of the reactant or product, Q is the charge passed, M is the molar mass of the reactant or product, F is Faraday constant (96485 C mol^{-1}), and n is the stoichiometric number of electrons transferred in the redox reaction.

The energy storage mechanism of pseudocapacitors and batteries is achieved via faradaic processes and redox reactions. In most electrochemical experiments, the faradaic currents for redox reactions are of key interest if the double layer capacitance is negligible. However, the non-faradaic current should also be considered when it has larger magnitudes.[6]

2.1.2 Equilibrium electrochemistry

In this part, electrochemical processes involving charge transfer across the electrode/solution interface (i.e., faradaic processes) will be presented through thermodynamics. Consider a faradaic electrode process:

$$O_{(aq)} + ne^-_{(m)} \rightleftharpoons R_{(aq)} \quad (2\text{-}5)$$

where the oxidised form *O* in the solution is reduced to species *R* in the solution phase by accepting *n* electrons which come from the electrode phase. A potential difference ($\phi_M - \phi_S$) is established at the electrode/solution interface when charge separation develops between the two phases, irrespective of the equilibrium.[5]

In order to measure the potential difference, a reference electrode chosen by convention and taken with zero potential (i.e., the standard hydrogen electrode) is introduced to complete the circuit. When a dynamic equilibrium is reached, the measured potential difference of the O/R electrode *E* is given by the Nernst equation:

$$E = E^0 + \frac{RT}{nF} \ln \frac{a_O}{a_R} \quad (2\text{-}6)$$

where E^0 is the standard electrode potential (V), *R* is the ideal gas constant (8.314 J K^{-1} mol^{-1}) *T* is the temperature (K), *n* is the number of electrons involved in Reaction 2-5, *F* is the Faraday constant (96485 C mol^{-1}), and a_O and a_R are the activities of *O* and *R*, respectively.

As the activities of the species are always unknown, the Nernst equation is rewritten as:

$$E = E^0 + \frac{RT}{nF}\ln\frac{a_O}{a_R} = E^0 + \frac{RT}{nF}\ln\frac{\gamma_O[O]}{\gamma_R[R]} \quad (2\text{-}7)$$

$$E = E^0 + \frac{RT}{nF}\ln\frac{\gamma_O}{\gamma_R} + \frac{RT}{nF}\ln\frac{[O]}{[R]} = E_f^0 + \frac{RT}{nF}\ln\frac{[O]}{[R]} \quad (2\text{-}8)$$

where $E_f^0 = E^0 + \frac{RT}{nF}\ln\frac{\gamma_O}{\gamma_R}$ is the formal potential (V), γ is the activity coefficient which is unitless, and *[O]* and *[R]* are the concentrations of species, respectively.

2.1.3 Electrode kinetics

For an electrode reaction, the electrode kinetics can be controlled by the rates of processes including mass transport, electron transfer, preceding or following chemical reactions (e.g., dimerization and protonation), and surface reactions (e.g., adsorption, desorption, and crystallisation), as shown in Figure 2.2. As some processes such as electron transfer depend on the electrode potential, a theory explaining the potential dependence of an electrode reaction is required quantitatively.

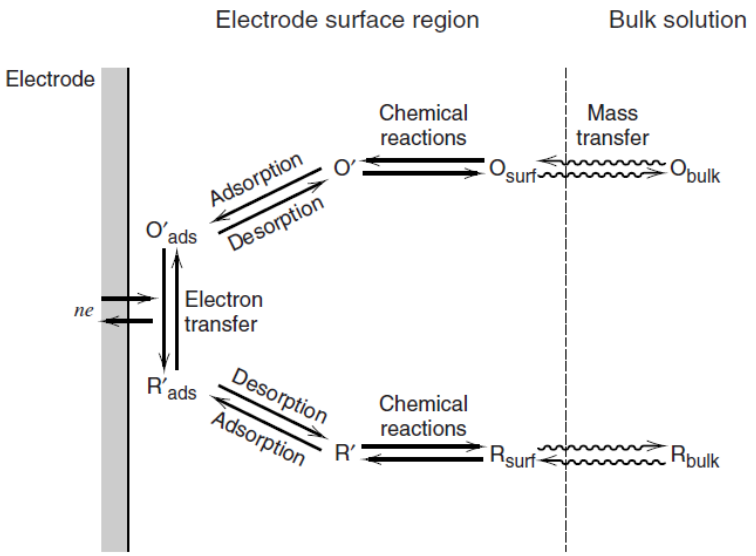

Figure 2.2 Schematic diagram of a general electrode reaction pathway.[1]

Considering a one-electron transfer process in Reaction 2-5, the net current *i* of the reaction is:

$$i = i_a + i_c = FA(k_a[R]_0 - k_c[O]_0) \quad (2\text{-}9)$$

$$i_a = FAk_a[R]_0 \tag{2-10}$$

$$i_c = -FAk_c[O]_0 \tag{2-11}$$

$$v_{net} = k_a[R]_0 - k_c[O]_0 \tag{2-12}$$

where i_a and i_c are the anodic and cathodic currents (A), respectively, A is the electrode area (cm^2), F is the Faraday constant, k_a and k_c are the respective heterogeneous rate constants for the oxidative (backward) and reductive (forward) reactions (cm s^{-1}), $[R]_0$ and $[O]_0$ are the surface concentrations of species A and B (mol cm^{-3}), respectively, and v_{net} is the net fluxes of material to the electrode surface (mol s^{-1} cm^{-2}). In particular, the anodic/oxidative current is taken as positive, different from conventional polarographic studies where i is positive for the cathodic/reductive current.

The heterogeneous rate constants are predicted using the transition state theory and are expressed in an Arrhenius form[7]:

$$k_a = k^0 \exp[(1-\alpha)f(E - E_f^0)] \tag{2-13}$$

$$k_c = k^0 \exp[-\alpha f(E - E_f^0)] \tag{2-14}$$

where k^0 is the standard rate constant, α is the transfer coefficient with a value between zero and unity, $f = F/RT$, E is the potential applied, and E_f^0 is the formal potential.

The current-potential relation then becomes:

$$i = FAk^0([R]_0 \exp\left[(1-\alpha)f\left(E - E_f^0\right)\right] - [O]_0 \exp\left[-\alpha f\left(E - E_f^0\right)\right]) \tag{2-15}$$

When equilibrium is reached where the net current i is zero and $E = E_{eq}$, Equation 2-15 becomes the exponential form of the Nernst equation 2-8: $e^{f\left(E_{eq} - E_f^0\right)} = [O]_*/[R]_*$.

At equilibrium, the cathodic or anodic current in Equation 2-15 can be expressed in i_0, the exchange current:

$$i_0 = FAk^0[O]_*^{1-\alpha}[R]_*^{\alpha} \quad (2\text{-}16)$$

where surface concentrations of the species $[]_0$ are the same as the bulk concentrations $[]_*$.

The variation of the current-potential characteristic, known widely as the Bulter-Volmer equation or the current-overpotential equation, is obtained[8]:

$$i = i_0[\frac{[R]_0}{[R]_*}e^{(1-\alpha)f\eta} - \frac{[O]_0}{[O]_*}e^{-\alpha f\eta}] \quad (2\text{-}17)$$

where the overpotential $\eta = E - E_{eq}$. The equation predicts how the current changes as a function of the overpotential and other parameters. When a large value of i_0 exists, a negligible activation overpotential is capable of driving the reaction. The electrode kinetics is so fast that the system is always at equilibrium, which is called a reversible or Nernstian system. In contrast, a large driving force (i.e., overpotential) is required to induce current flows if i_0 has a small value. The kinetics of the electrochemical system are so sluggish that it is regarded as an irreversible process. Particularly, the current is also limited by mass transport rather than the kinetics at extreme overpotential despite the exponential factors of η.

2.1.4 Mass transport

Mass transport, or mass transfer, may contribute to the overall reaction rate for particular reactions. Mass transport in solution takes place in three ways, which are diffusion, migration and convection.

Diffusion results from uneven concentration distributions and occurs down the concentration gradient. The diffusional flux j (mol s^{-1} cm^{-2}) for a species is quantified mathematically by Fick's 1st law of diffusion:

$$j = -D\frac{\partial c}{\partial x} \tag{2-18}$$

where D is the diffusion coefficient and is characteristic of the diffusing species, c is the concentration of that species, and $\frac{\partial c}{\partial x}$ is the concentration gradient at any point x.

Consider the change in concentration at point x as a function of time, and the relationship is expressed by Fick's 2nd law of diffusion:

$$\frac{\partial c}{\partial t} = D\frac{\partial^2 c}{\partial x^2} \tag{2-19}$$

In three dimensional Cartesian coordinates (x, y, z), the differential equation is extended as:

$$\frac{\partial c}{\partial t} = D\left(\frac{\partial^2 c}{\partial x^2} + \frac{\partial^2 c}{\partial y^2} + \frac{\partial^2 c}{\partial z^2}\right) \tag{2-20}$$

The concentration changes of reactants or products close to the electrode surface are predicted by this law.

Charged species can move to or from the electrode induced by the electrostatic force as a result of the potential gradient ($\phi_M - \phi_S$) between the electrode/solution interface and the external electric field ($d\phi/dx$) in bulk solutions. Such effects contributing to mass transport are called migration. The flux j_m caused by migration is given by:

$$j_m \propto -uc\frac{\partial \phi}{\partial x} = -\frac{|z|FD}{RT}c\frac{\partial \phi}{\partial x} \tag{2-21}$$

where u is the ionic mobility which is dependent on ionic charge and size, and solution viscosity, c is the concentration of the species, $\frac{\partial \phi}{\partial x}$ is the electric field or potential gradient, z is the charge of the ion, and other terms are defined above.

For many electrochemical reactions, interpretation of data is complex when rate of mass transport varies and migratory fluxes changes. To simplify the mathematical treatment of experiments, the migration effects of electroactive species are made negligible by adding an

excess of supporting/background electrolytes in high concentrations (≥ 0.1 M) compared to the analyte. The supporting electrolyte which does not participate in the electrochemical reaction carries most current in the bulk solution, and most electroactive species reach or leave the electrode by diffusion. The addition of supporting electrolyte also increases the solution conductivity and decreases the uncompensated resistance drop. Beyond the benefits above, the supporting electrolyte ensures a small thickness of the diffuse layer (10 - 20 Å), enabling electroactive species to experience almost full potential drop ($\phi_M - \phi_S$) with little ϕ_2 interference (i.e., $\phi_2 - \phi_S \approx 0$). In addition, a high concentration of supporting electrolyte helps to establish a constant ionic strength of the solution.[1, 2, 5]

Convection occurs when an imbalance of forces exists in the solution, including natural convection and forced ones. Natural convection which is always undesirable results from thermal gradients or density differences in the solution. Forced convection is carried out by external bubbling, pumping or stirring. Reproducible electrochemical results are obtained sometimes by deliberately introducing forced convection (e.g., a rotating disc electrode). The flux arises from concentration shifts due to movement of the solution with a velocity v_x is given by:

$$j = cv_x \tag{2-22}$$

In general, the Nernst-Planck equation to describe linear (one-dimensional) mass transport consisting of diffusion, migration and convection is written as:

$$J = -D\frac{\partial c}{\partial x} - \frac{zF}{RT}Dc\frac{\partial \phi}{\partial x} + cv_x \tag{2-23}$$

To avoid complex electrochemical systems, experiments conducted in this thesis are designed with elimination of migration and convection effects by adding supporting electrolyte and keeping still experimental conditions.[1, 2]

2.2 Electrochemical methods

2.2.1 Chronoamperometry

Chronoamperometry is a basic potential step where current is measured as a function of time. As shown in Figure 2.3 (a), the initial potential of the working electrode *E1* is in the region where no faradaic processes occur. The chronoamperometric experiment starts when the potential is stepped from *E1* to *E2*, and faradaic currents are yielded immediately. The current detected falls with time as the concentration gradient decreases, the diffusion layer thickens, and depletion of electroactive materials applies. The current-time response on a planar electrode in the diffusion-controlled region is described by the Cottrell equation:

$$i = \frac{nFAD^{1/2}C_*}{\pi^{1/2}t^{1/2}} \tag{2-24}$$

where the terms have been defined above.

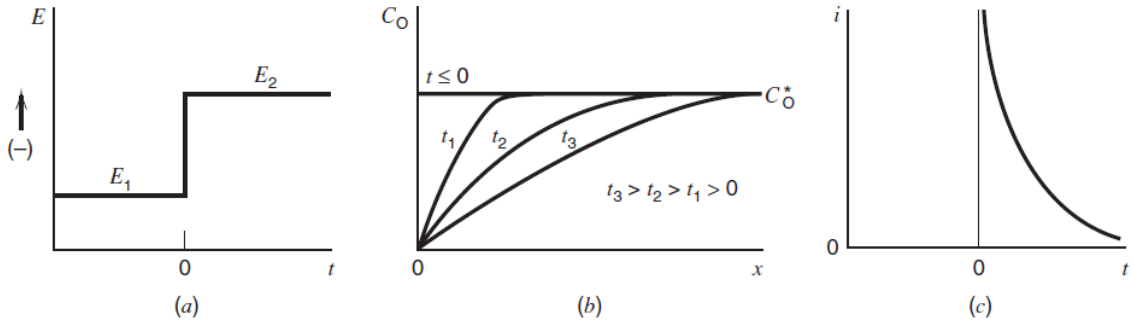

Figure 2.3 (a) A basic potential step experiment, (b) concentration profile of reactant for various experiment times, and (c) current recorded against time.[1]

2.2.2 Cyclic voltammetry

Cyclic voltammetry (CV) is an extremely powerful and widely practised potential sweep method for electrochemical studies. In a CV experiment shown in Figure 2.4, the potential is swept with a certain scan rate v (V s^{-1}) to a switching potential (E_λ) or time (t_λ). At the switching

point, the direction of the scan is reversed, and the potential is swept back to the initial value at the same scan rate. Meanwhile, the current is recorded as a function of potential, which are called the *i-E* curves (i.e., cyclic voltammograms). In particular, CV without a reversal scan is known as linear sweep voltammetry (LSV).[9]

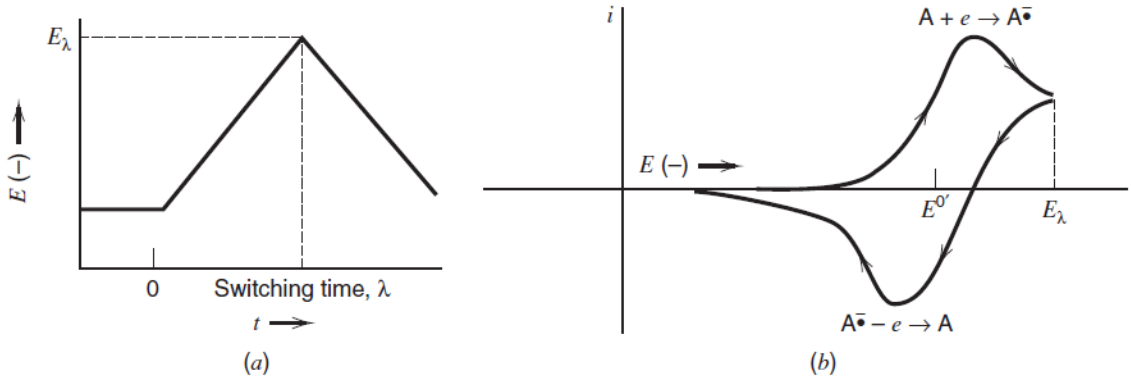

Figure 2.4 (a) A potential sweep experiment with reverse scan, and (b) the obtained cyclic voltammogram.[1]

The electrode behaviour is classified into three ranges: reversible (Nernstian), quasi-reversible and irreversible depending on the competition between the rate of electrode kinetics and mass transport.[5] In a reversible behaviour, the electrode kinetics are so rapid (large standard rate constant k_0 and exchange current i_0) compared to mass transport that Nernst equation is obeyed at the electrode surface. The peak current for a reversible system at 25 °C is given by Randles-Sevcik equation[10]:

$$i_p = (2.69 \times 10^5) n^{3/2} A D^{1/2} c v^{1/2} \quad (2\text{-}25)$$

For an irreversible process at 25 °C:[11]

$$i_p = (2.99 \times 10^5) n (n' + \alpha)^{1/2} A D^{1/2} c v^{1/2} \quad (2\text{-}26)$$

where *n'* is the number of electrons transferred before the rate determining step (RDS), and α is the transfer coefficient of the RDS.

2.2.3 Galvanostatic charge-discharge

Galvanostatic charge-discharge (GCD) is performed by applying a constant current step to a cell for characterisation. Normally, the potential is recorded as a function of the charge-discharge time in GCD, so this method is also called chronopotentiometry (CP). The electrochemical system (e.g., a battery or a supercapacitor) is charged to a cell potential at a constant current, after which the discharge process begins immediately at the same current. GCD is employed to measure the specific capacitance, energy and power densities of supercapacitors.[12, 13] Furthermore, the cycle life of a device can be investigated by simply prolonging charge-discharge cycles in GCD, as shown in Figure 2.5. Compared to CV, tests via GCD are closer to practical operating situations of an energy storage device.[12]

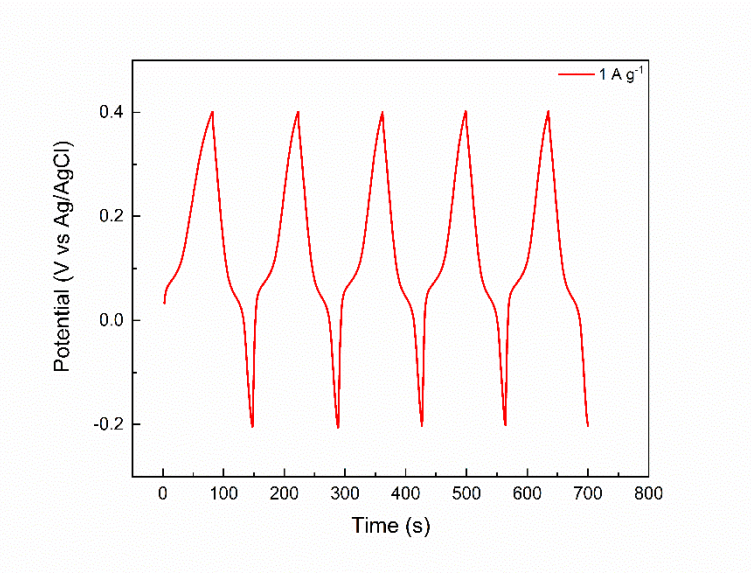

Figure 2.5 Schematic of GCD curves with several cycles.

2.2.4 Electrochemical impedance spectroscopy

In addition to potential steps/sweeps or current steps, the system can also be studied by imposing an alternating signal which is a small perturbation.[14] In electrochemical impedance

spectroscopy (EIS), the impedance (Z) is described as the response of the system to the frequency *(f)* of the a.c. voltages:

$$Z(f) = \frac{E(t)}{i(t)} \tag{2-27}$$

For a complex system with a phase angle difference between i and E, it is convenient to use the complex notation:

$$Z(\omega) = Z_{Re} - jZ_{Im} \tag{2-28}$$

where ω is the angular frequency $(\omega = 2\pi f)$, $j^2 = -1$, and Z_{re} and Z_{Im} are the real and imaginary parts of the impedance, respectively.

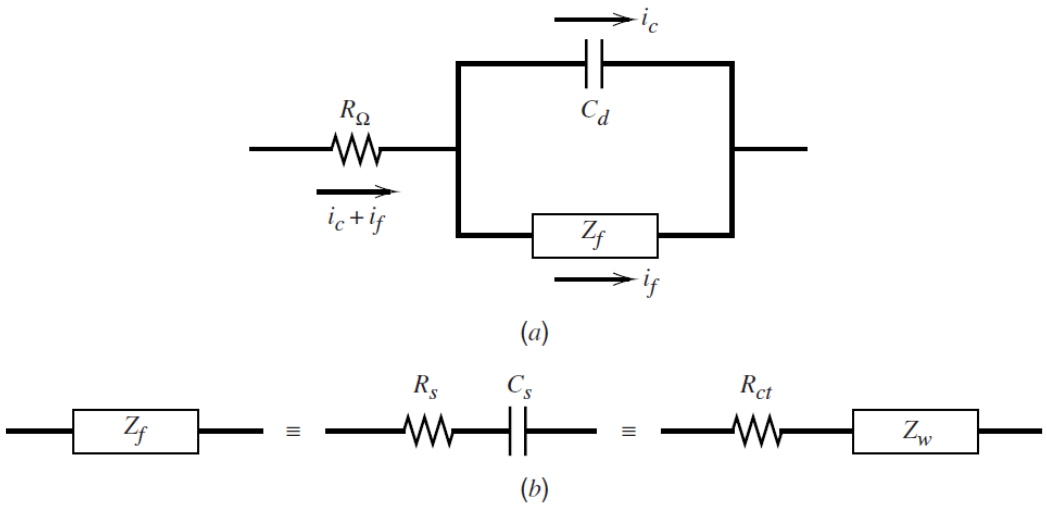

Figure 2.6 (a) Randles equivalent circuit. (b) Various equivalences of faradaic impedance.[1]

Z_{re} is plotted against Z_{Im} in a Nyquist plot for different frequency values. The Randles equivalent circuit is a frequently used model to represent the electrode processes, as shown in Figure 2.6.[15] In the equivalent circuit, the total current is composed of the faradaic current i_f and the non-faradaic current i_c. A series resistance R_Ω is present in the circuit which is related to the solution resistance. The double layer capacitance associated with the charging current i_c is represented by C_d, which is in parallel to the impedance of the faradaic process Z_f. The

faradaic impedance Z_f is considered as a combination of the charge transfer resistance R_{ct} which models the faradaic reaction and the Warburg impedance Z_w which depicts the resistance to mass transport. Other equivalences of the faradaic impedance have been proposed such as the subdivision of Z_f into the series resistance R_s and the pseudocapacity C_s. In the high frequency region of the Nyquist plot shown in Figure 2.7, the series resistance R_Ω is extracted from the real axis intercept, and the charge transfer resistance R_{ct} is given by the diameter of the circular plot. As the frequency falls, the Warburg impedance becomes a more important factor at low frequencies where mass transport plays a role.[1]

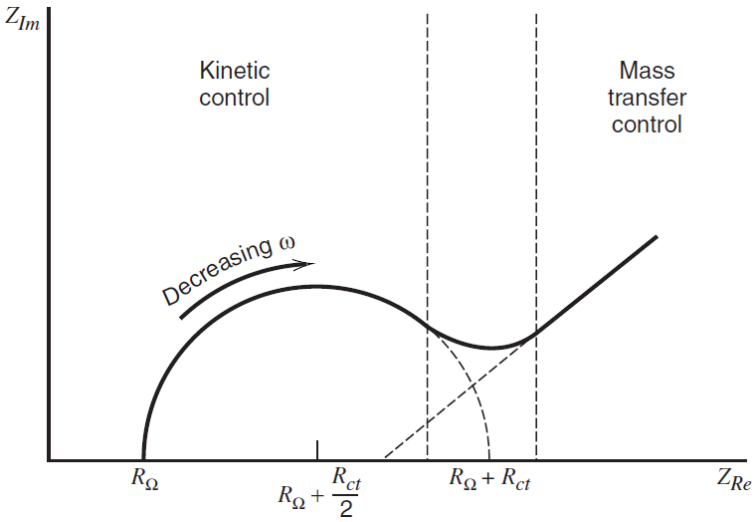

Figure 2.7 A Nyquist plot with kinetic control and mass transfer control regions at high and low frequencies, respectively.[1]

2.2.5 Electrochemical cells

In an electrochemical experiment, the experimental cell could comprise a working electrode (WE) where reactions of interest occur, and a reference electrode (RE) whose potential should be known and not affected by the passage of current. In this case, the potential of the working electrode is controlled or observed with respect to the reference electrode, and such arrangement is called a two-electrode cell, as depicted in Figure 2.8.[1]

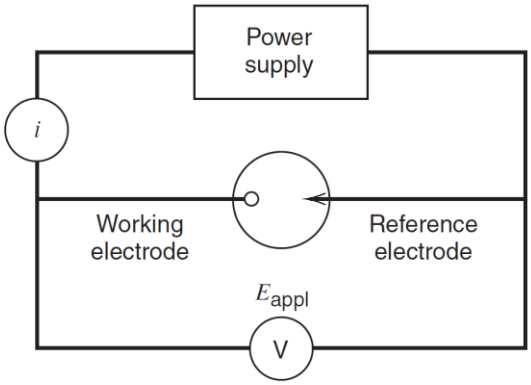

Figure 2.8 Schematic diagram of a two-electrode cell.[1]

Conventionally, the normal hydrogen electrode (NHE), or standard hydrogen electrode (SHE) is accepted as reference with a potential of zero and components at unit activity:

Pt|H_2 (1 atm) |H^+ (aqueous, a = 1)

For experimental convenience, potentials are measured with respect to some RE other than SHE. One common RE is the saturated calomel electrode (SCE):

Hg|Hg_2Cl_2|KCl (saturated in water), with a potential 0.242 V vs. SHE.

Another reference widely used is the silver-silver chloride electrode:

Ag|AgCl|KCl (saturated in water), the potential of which is 0.197 V vs. SHE.

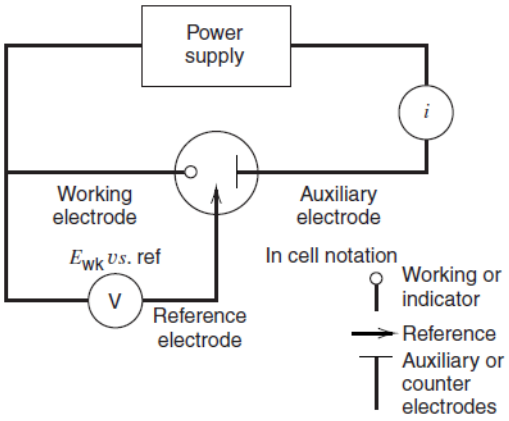

Figure 2.9 Schematic diagram of a three-electrode cell.[1]

When the passage of current i is appreciable, the potential of the RE may shift and it cannot serve as a constant reference. Furthermore, a voltage drop equal to iR_Ω in the measured potential is no longer negligible, which is caused by the solution resistance R_Ω. To eliminate these changes, a counter or auxiliary electrode (CE) is introduced in a three-electrode cell arrangement (Figure 2.9). In this design, the current is passed between the WE and the CE. Meanwhile, the potential difference is measured between the WE and the RE with tiny current passing through. As a result, the potential of the reference electrode is stable and the ohmic drop iR_Ω is insignificant.[1]

2.2.6 Instrumentation and experimental set-up

The electrochemical experiments were performed with an Autolab PGSTAT128N potentiostat/galvanostat (Metrohm Autolab, Utrecht, Netherlands) connected to a PC running NOVA software version 2.1.

The electrochemical cell is a typical three-electrode configuration which is composed of a working electrode, a reference electrode and a counter electrode. In Chapter 3, a boron-doped diamond electrode mounted in a PTFE holder serves as the working electrode. In Chapter 4, 5 and 6, bulk biomass materials are attached to a Pt current collector, which are used as the

working electrode. Powder biomass samples are drop coated on a glassy carbon electrode, assembled in a PTFE holder and employed as the working electrode. Chapter 4, 5 and 6 were accomplished in collaboration with the Korea Institute of Energy Research who have provided the biomass samples. Other experimental parameters are described in detail in the respective chapters.

2.3 Characterisation techniques

2.3.1 Scanning electron microscopy

In the scanning electron microscopy (SEM) technique, the surface of a sample is scanned with a focused electron beam, as shown in Figure 2.10. The electron beam irradiates the sample, creating useful images which contain information about the surface morphology of the sample. When incident electrons from an electron gun (e.g., tungsten filament, lanthanum hexaboride, and field emission) strike upon the sample surface, two types of electron scattering occur. Electrons that are deflected elastically are called backscattered electrons, which are scattered back to the detector without loss of kinetic energy. In contrast, secondary electrons with lower energy (< 50 eV) are outer shell electrons emitted from the sample due to inelastic scattering. As secondary electrons can only escape from 5 - 10 nm of the sample surface, more can reach the detector and the signal of topographic information is highly localised with better resolution. Backscattered electrons with less resolution from deeper locations within the sample can provide data for composition analysis especially for samples with larger atomic number.[16] In general, samples should be solid and stable in high vacuum as well as electrically conductive and completely dry for a conventional SEM test.

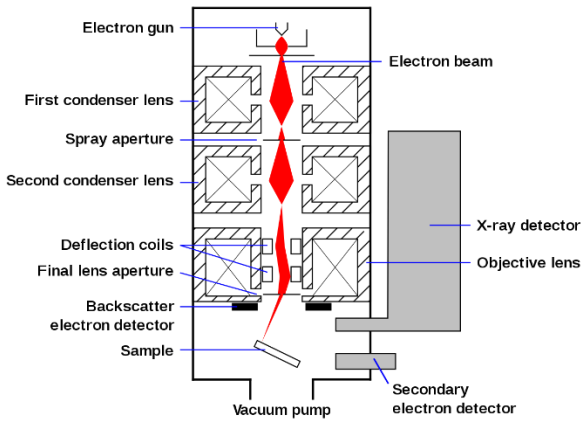

Figure 2.10 Simplified schematic of an SEM instrument.[17]

2.3.2 Energy-dispersive X-ray spectroscopy

Energy-dispersive X-ray spectroscopy (EDS or EDX) works as an addition to SEM. The excitation source of EDS is also an electron beam. However, an X-ray detector in EDS is substituted for the electron detector in SEM. In addition to signals from secondary electrons and backscattered electrons, characteristic X-rays are emitted when an electron beam interacts with a sample, which causes removal of an inner shell electron from the sample. The vacancy in that inner shell is then filled by an outer shell electron, and the energy difference is released as the characteristic X-rays.[18] The energy of the X-rays is characteristic of different atoms, and therefore is used to measure the abundance of elements and identify their distribution in the sample.

2.3.3 X-ray diffraction

X-ray diffraction (XRD) is widely used to characterise and identify unknown crystalline materials. An X-ray beam is generated by an X-ray arm and directed towards the sample, as shown in Figure 2.11. The diffracted rays are produced due to constructive interference of scattered rays when Bragg's law is satisfied:

$$n\lambda = 2dsin\theta \tag{2-29}$$

where *n* is the diffraction order, λ is the wavelength of radiation, *d* is the spacing between lattice planes, and θ is the incident angle.

The diffracted X-rays are collected, and their intensity is measured by a detector arm which rotates at different 2θ angles. The as obtained intensity, 2θ angles and peak widths of an XRD pattern are checked against a database to identify materials and determine their structures, orientations or spacings.[19] In this thesis, XRD analysis was conducted with a Philips X'Pert Pro diffractometer producing Cu-Kα (λ = 1.54 Å) radiation, operating at 30 mA and 40 kV.

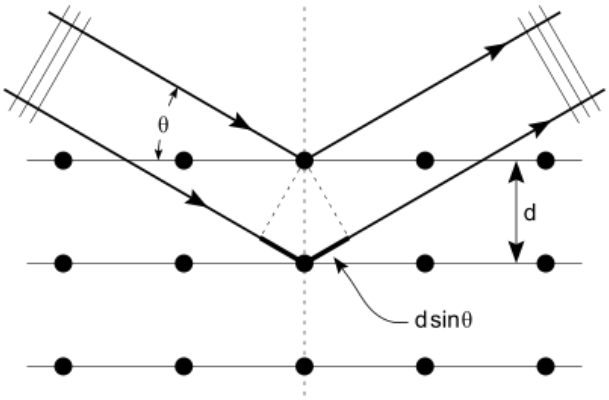

Figure 2.11 X-ray diffraction based on Bragg's law.[20]

2.3.4 X-ray photoelectron spectroscopy

2.3.4.1 XPS fundamentals

X-ray photoelectron spectroscopy (XPS), also known as electron spectroscopy for chemical analysis, is a powerful surface-sensitive quantitative technique based on the photoelectric effect to determine the surface elemental composition, chemical and electronic states, and electronic structure of a material.[21] The process of electron emission via electromagnetic radiation is called the photoelectric effect, and the electrons emitted in this way are named photoelectrons. In practice, a monochromatic X-ray beam (e.g., Mg K_α at 1253.6 eV or Al K_α at 1486.6 eV) bombards a sample, which causes ejection of core electrons from the material to the surrounding vacuum where they are detected, as shown in Figure 2.12. The X-rays are able to

penetrate up to 10 μm of the sample surface, but only electrons close enough to the top surface (< 10 nm) can escape without loss in kinetic energy. A photoelectron spectrum shows the distribution of photoelectrons and the kinetic energy measured *in vacuo*.[1] The kinetic energy of the photoelectron E_k detected has the following relationship:

$$E_K = hv - E_B - \phi \tag{2-30}$$

where hv is the energy of the photon, the binding energy E_B is the energy to remove the electron from the initial state, and ϕ (3 - 4 eV) is the work function of the spectrometer. Thus, it is common to display a plot of the electron intensity versus the binding energy E_B instead of E_k in a spectrum. As the binding energy of an electron for different elements and atomic levels is discrete, the elemental composition of the surface region can be determined except hydrogen and helium. The characteristic peak intensity (i.e., peak area) is proportional to the number of an atom in the sample surface:

$$n_i = I_i/S_i \tag{2-31}$$

$$n_i/n_j = \frac{I_i/S_i}{I_j/S_j} \tag{2-32}$$

$$C_i = \frac{n_i}{\sum_j n_j} = \frac{I_i/S_i}{\sum_j I_j/S_j} \tag{2-33}$$

where n is the number of the element i, I_i is the peak intensity, S_i is the sensitivity factor, C_i is the percentage atomic concentration, and j is another element in the sample.

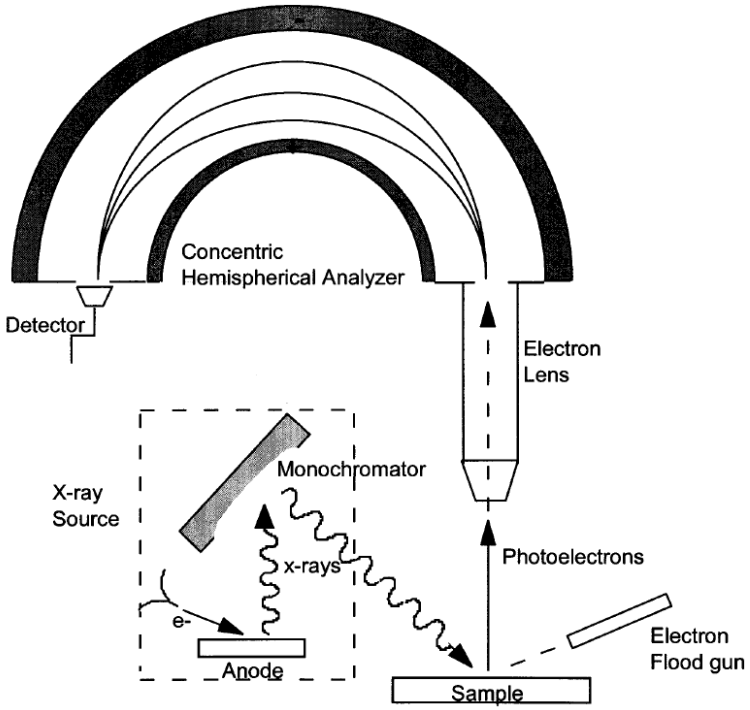

Figure 2.12 Schematic diagram of an XPS spectrometer.[22]

The intensity of an electron that reaches the surface is based on the Beer-Lambert law:

$$I_d = I_0 \times e^{-d/\lambda} \tag{2-34}$$

where I_d is the intensity of an electron after it has travelled from a depth of d in the solid to the surface, I_0 is the intensity of that electron when emitted at a depth of d, and λ is the inelastic mean free path (IMFP) of an electron in a solid, which is identical to the mean escape depth. The sampling depth is defined when the depth $d = 3\lambda$, where 95% of the detected electrons come from. For instance, λ is mostly in the range of 1 - 3.5 nm for Al K_α radiation, leading to an analysis depth of 3 - 10 nm for XPS under these conditions.[23]

The inelastic mean free path λ is dependent on the kinetic energy of the electron. As λ depends weakly on the material where the electron is travelling, it can be calculated or estimated from a 'universal curve' where λ is plotted as a function of the kinetic energy of the photoelectron (Figure 2.13). It can be seen from the curve that XPS is highly surface sensitive particularly in the kinetic energy range of 20 - 100 eV.

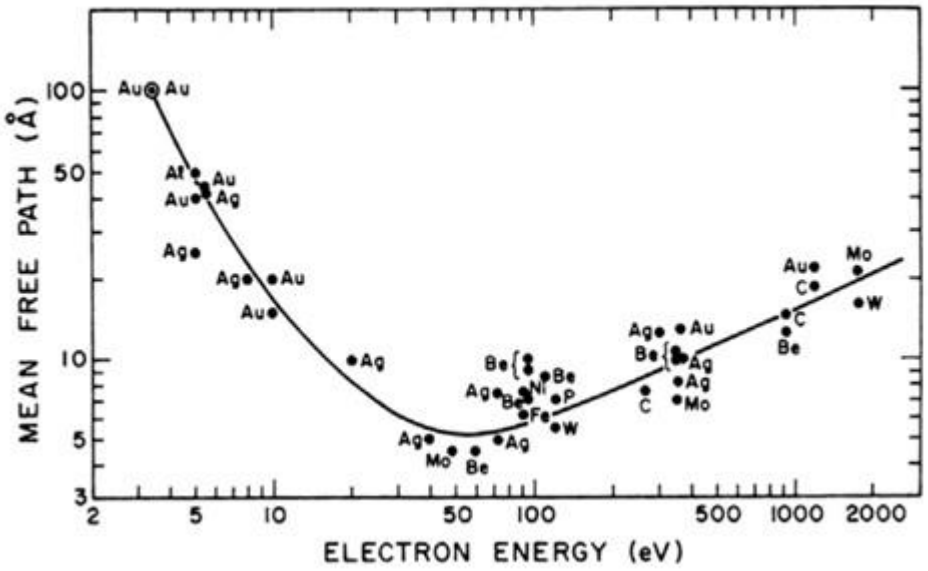

Figure 2.13 Inelastic mean free path of photoelectron as a function of kinetic energy with a fitted 'universal curve'.[23]

Furthermore, formation of a chemical bond can lead to a redistribution of charge of outer electrons, resulting in a slight change of the binding energy of a core electron. An increase in the binding energy is observed if valence electron charge is withdrawn from the atom (positive oxidation state), whereas a decrease in the binding energy results from addition of valence electron charge (negative oxidation state). Such subtle but reproducible change in the binding energy is called 'chemical shift', which can provide chemical bonding and oxidation state information of an element.[24] Apart from the photoemission process discussed above, other phenomena may be observed in XPS spectra.

2.3.4.2 Auger electron

A hole is available in the atomic core level after electron emission by irradiation with electrons (i.e. EDS) or X-rays (i.e. XPS) as above, after which an electron from an upper energy level can fill the vacancy and the excited state of the ionised atom will return to a lower energy state (i.e. relaxation).[25] Meanwhile, the energy difference resulted from this process can be released in the form of electron emission (Auger electron) or photon emission (X-ray fluorescence), as

shown in Figure 2.14. For example, a core vacancy in the K shell is filled by an electron from L_1 shell, and the energy liberated simultaneously ejects an Auger electron from the L_3 shell in Figure 2.11 (c).

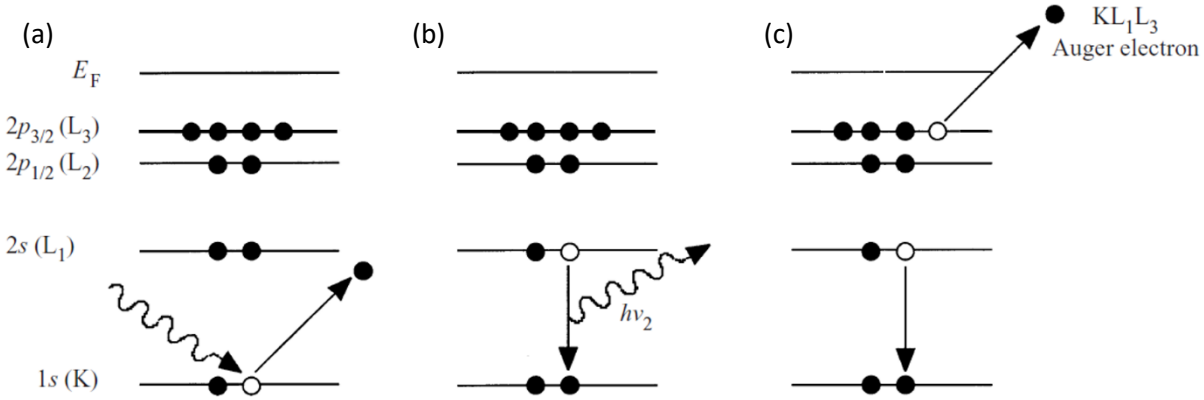

Figure 2.14 Schematic view of (a) photoelectron emission process, (b) X-ray fluorescence process, and (c) KL_1L_3 Auger emission process, adopted from[22].

2.3.4.3 Satellite peaks

Satellite structures may take place during the photoelectron emission process, leading to shake-up and shake-off peaks. In a shake-up transition shown in Figure 2.15 (a), a valence electron is excited to a bound state simultaneously when a photoelectron is emitted. Different from the shake-up effect, the excitation of a valence electron to a continuum state (ionised) occurs in the shake-off transition during the photoemission event. The kinetic energy of the photoelectrons involved in shake-up and shake-off transition is lower in this way, which is displayed as satellite peaks appearing at higher binding energy side of the main photoelectron peaks.[26]

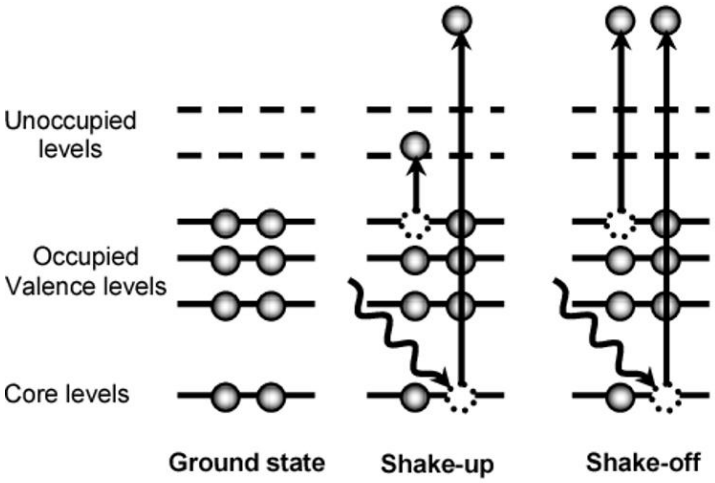

Figure 2.15 Schematic representation of shake-up and shake-off processes, adopted from[27].

2.3.4.4 Multiplet splitting

Multiplet splitting is an important phenomenon that occurs in atoms containing unpaired electrons in the ground state. When a vacancy in the core level (e.g., 2p, 3d, and 4f) is available due to photoelectron emission, spin-orbit interaction takes place and energy level splitting is produced. Therefore, a doublet of peak is observed for core levels with two final stated such as $2p_{1/2}$ and $2p_{3/2}$, $3d_{3/2}$ and $3d_{5/2}$, and $4f_{5/2}$ and $4f_{7/2}$.[28] For s orbit in most cases, no splitting is observed as the total angular momentum quantum number J can only be ½ (e.g., $1s_{1/2}$). However, the unpaired electron left in the s core level can couple with the unpaired electrons in the valence levels (e.g., coupling of Mn 3s electron with Mn 3d electrons). As a consequent, different final states are created and multiplet peaks are present in the spectrum.[29]

2.3.4.5 Plasmon loss peaks

Typically observed in metals or materials with free electrons, plasmon loss peaks occur in both XPS and Auger spectra. The photoelectrons emitted can excite collective oscillations of the conduction band electrons (i.e., plasmons), and thus discrete energy loss in integer multiples of the characteristic plasmon frequency (i.e., plasmon loss peaks) is seen in a spectrum. An example of these energy loss features of an aluminium metal (2s and 2p spectrum) is shown in

Figure 2.16 with several discrete plasmon loss structure of 15.3 eV.[30] In some cases, plasmon loss peaks can provide extra information, but some may only interfere with other characteristic peaks, complicating quantification of a spectrum.

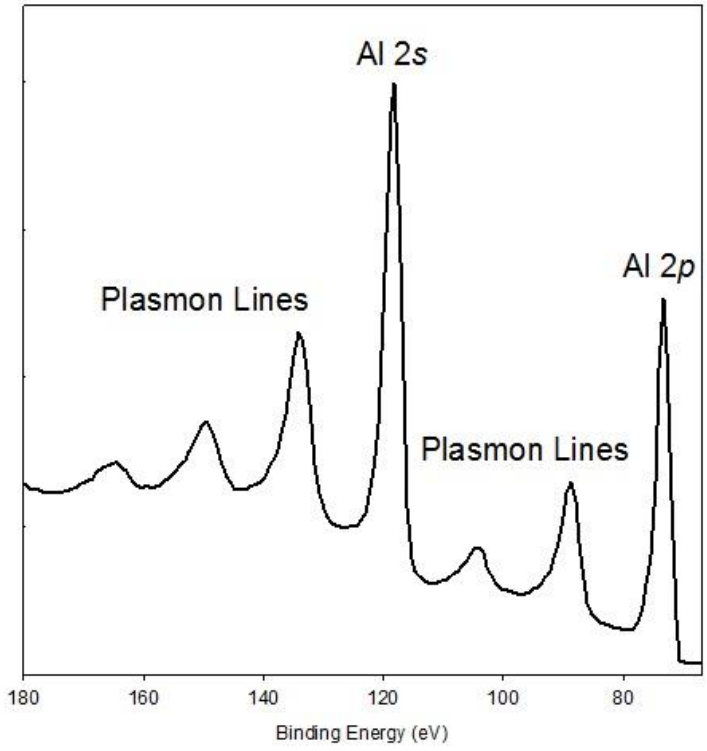

Figure 2.16 Aluminium 2s and 2p spectrum with plasmon loss peaks.[30]

References

(1) Bard, A. J.; Faulkner, L. R. *Electrochemical Methods: Fundamentals and Applications, 2nd Edition*; John Wiley & Sons, Incorporated, 2000.

(2) Fisher, A. C. *Electrode Dynamics*; Oxford University Press, 1996.

(3) Stern, O. ZUR THEORIE DER ELEKTROLYTISCHEN DOPPELSCHICHT. *Zeitschrift für Elektrochemie und angewandte physikalische Chemie* **1924**, *30* (21-22), 508-516. DOI: https://doi.org/10.1002/bbpc.192400182. Chapman, D. L. LI. A contribution to the theory of electrocapillarity. *The London, Edinburgh, and Dublin Philosophical Magazine and Journal of Science* **1913**, *25* (148), 475-481. DOI: 10.1080/14786440408634187. Gouy, M. Sur la constitution de la charge électrique à la surface d'un électrolyte. *J. Phys. Theor. Appl.* **1910**, *9* (1), 457-468.

(4) Levine, S.; Outhwaite, C. W. Comparison of theories of the aqueous electric double layer at a charged plane interface. *Journal of the Chemical Society, Faraday Transactions 2: Molecular and Chemical Physics* **1978**, *74* (0), 1670-1689, 10.1039/F29787401670. DOI: 10.1039/F29787401670.

(5) Compton, R. G.; Banks, C. E. *Understanding Voltammetry (Third Edition)*; World Scientific Publishing Company, 2018.

(6) Conway, B. E.; Birss, V.; Wojtowicz, J. The role and utilization of pseudocapacitance for energy storage by supercapacitors. *Journal of Power Sources* **1997**, *66* (1), 1-14. DOI: https://doi.org/10.1016/S0378-7753(96)02474-3.

(7) Cox, B. G. *Modern Liquid Phase Kinetics*; Oxford University Press, 1994.

(8) Butler, J. A. V. Studies in heterogeneous equilibria. Part III. A kinetic theory of reversible oxidation potentials at inert electrodes. *Transactions of the Faraday Society* **1924**, *19* (March), 734-739, 10.1039/TF9241900734. DOI: 10.1039/TF9241900734. Erdey-Grúz, T.;

Volmer, M. Zur Theorie der Wasserstoff Überspannung. *Zeitschrift für Physikalische Chemie* **1930**, *150A* (1), 203-213. DOI: doi:10.1515/zpch-1930-15020.

(9) Brett, C. M. A. B. A. M. O. *Electroanalysis*; Oxford University Press, 1998.

(10) Randles, J. E. B. A cathode ray polarograph. Part II.—The current-voltage curves. *Transactions of the Faraday Society* **1948**, *44* (0), 327-338, 10.1039/TF9484400327. DOI: 10.1039/TF9484400327. Ševčík, A. Oscillographic polarography with periodical triangular voltage. *Collection of Czechoslovak Chemical Communications* **1948**, *13*, 349-377.

(11) Batchelor-McAuley, C.; Compton, R. G. Voltammetry of multi-electron electrode processes of organic species. *Journal of Electroanalytical Chemistry* **2012**, *669*, 73-81. DOI: https://doi.org/10.1016/j.jelechem.2012.01.016.

(12) Yu, A.; Chabot, V.; Zhang, J. *Electrochemical Supercapacitors for Energy Storage and Delivery: Fundamentals and Applications*; Taylor & Francis, 2013.

(13) Kim, B. K.; Sy, S.; Yu, A.; Zhang, J. Electrochemical Supercapacitors for Energy Storage and Conversion. In *Handbook of Clean Energy Systems*, pp 1-25.

(14) Banica, F.-G. Chemical sensors and biosensors : fundamentals and applications. **2012**. From http://worldcat.org /z-wcorg/.

(15) Randles, J. E. B. Kinetics of rapid electrode reactions. *Discussions of the Faraday Society* **1947**, *1* (0), 11-19, 10.1039/DF9470100011. DOI: 10.1039/DF9470100011.

(16) Ul-Hamid, A. *A beginners' guide to scanning electron microscopy*; Springer.

(17) https://www.nanoscience.com/techniques/scanning-electron-microscopy/ (accessed.

(18) Bell, D.; Garratt-Reed, A. *Energy dispersive X-ray analysis in the electron microscope*; Garland Science, 2003.

(19) Leng, Y. *Materials characterization: introduction to microscopic and spectroscopic methods*; John Wiley & Sons, 2009.

(20) Parks, J. E.; Deserio, R. X-ray Diffraction and Absorption Rough Draft 04/15/2015. 2015.

(21) Siegbahn, K. Electron Spectroscopy for Chemical Analysis. In *Atomic Physics 3*, Boston, MA, 1973//, 1973; Smith, S. J., Walters, G. K., Eds.; Springer US: pp 493-522.

(22) Burrell, M. C. Chemical Analysis, Electron Spectroscopy. In *Encyclopedia of Materials: Science and Technology*, Buschow, K. H. J., Cahn, R. W., Flemings, M. C., Ilschner, B., Kramer, E. J., Mahajan, S., Veyssière, P. Eds.; Elsevier, 2001; pp 1142-1149.

(23) Seah, M. P.; Dench, W. A. Quantitative electron spectroscopy of surfaces: A standard data base for electron inelastic mean free paths in solids. *Surface and Interface Analysis* **1979**, *1* (1), 2-11. DOI: https://doi.org/10.1002/sia.740010103.

(24) McIntyre, N. S.; Sunder, S.; Shoesmith, D. W.; Stanchell, F. W. Chemical information from XPS—applications to the analysis of electrode surfaces. *Journal of Vacuum Science and Technology* **1981**, *18* (3), 714-721. DOI: 10.1116/1.570934 (acccessed 4/23/2023).

(25) Greczynski, G.; Hultman, L. X-ray photoelectron spectroscopy: Towards reliable binding energy referencing. *Progress in Materials Science* **2020**, *107*, 100591. DOI: https://doi.org/10.1016/j.pmatsci.2019.100591.

(26) do Rego, A. M. B.; Ferreira, L. F. V. Chapter 7 - PHOTONIC AND ELECTRONIC SPECTROSCOPIES FOR THE CHARACTERIZATION OF ORGANIC SURFACES AND ORGANIC MOLECULES ADSORBED ON SURFACES. In *Handbook of Surfaces and Interfaces of Materials*, Nalwa, H. S. Ed.; Academic Press, 2001; pp 275-313.

(27) Watcharinyanon, S. Structure of Self-Assembled Monolayers on Gold Studied by NEXAFS and Photoelectron Spectroscopy. Karlstads universitet, 2008.

(28) Fadley, C. S.; Shirley, D. A. Multiplet Splitting of Metal-Atom Electron Binding Energies. *Physical Review A* **1970**, *2* (4), 1109-1120. DOI: 10.1103/PhysRevA.2.1109.

(29) Fadley, C. S.; Shirley, D. A.; Freeman, A. J.; Bagus, P. S.; Mallow, J. V. Multiplet Splitting of Core-Electron Binding Energies in Transition-Metal Ions. *Physical Review Letters* **1969**, *23* (24), 1397-1401. DOI: 10.1103/PhysRevLett.23.1397.

(30) Moulder, J. F.; Stickle, W. F.; Sobol, P. E.; Bomben, K. D. Handbook of X-ray photoelectron spectroscopy; Chastain, J. *Perkin-Elmer Corp., Eden Prairie, MN* **1992**.

Chapter 3 Electrochemical Deposition of Manganese Oxides onto Boron-Doped Diamond Electrodes

In summary, Boron-doped diamond (BDD) is first characterised by cyclic voltammetry (CV) with three well-studied redox systems and several aqueous electrolytes. As a promising carbon material, the BDD electrode is then employed to study the electrochemical oxidation of Mn^{2+} ions to manganese oxides via CV. Afterwards, it serves as an electrode substrate to fabricate a pseudocapacitor, where the low cost and environmentally friendly MnO_2 is deposited potentiostatically. The as-prepared MnO_2/BDD composite electrode is characterised by SEM and XPS, followed with electrochemical characterisation using cyclic voltammetry. The CVs show that the capacitance rises with typical pseudocapacitive behaviour and excellent rate performance after the deposition of MnO_2. In the stability test, 84.5% of the capacitance is retained after 2000 cycles at a high scan rate of 100 mV s^{-1}. The results indicate when using diamond materials, the MnO_2 modified boron-doped diamond is a promising candidate for supercapacitor applications.

3.1 Introduction

Boron-doped diamond (BDD) electrodes have been studied in various electrochemical applications since the 1980s due to their excellent physical and electrochemical properties. These properties include low background current, wide potential windows, and high robustness both chemically and structurally, which allow their use in the field of electrochemical analysis, electrochemical and photoelectrochemical oxidation of environmental pollutants,

electrocatalysis and energy storage applications.[1] BDD electrodes have been considered as promising materials for electrochemical energy applications in past years. They are used for energy storage and conversion systems such as batteries, fuel cells, supercapacitors, solar cells and CO_2 conversion.[1]

BDD has been explored for the construction of lithium-ion batteries. With a boron doping level of 10^{21} B cm^{-3}, reversible specific capacity up to 370 mAh g^{-1} was found on BDD films grown on carbon felt substrates, indicating effective lithium intercalation into BDD electrodes.[2] Due to its stability and electrochemical properties, BDD acts as a substrate to support catalyst for fuel cell applications.[3] Catalysts including metals/alloys (e.g., Pt, Pt-Ru, Pd-Ni) and metal oxides (e.g., Pt-RuO_x, Pt-TiO_2, Pt-RuO_2-RhO_2) are decorated on BDDs via electroless or electrochemical deposition, thermal deposition and sol-gel process.[3, 4] For instance, Pt nanoparticles are coated on BDD electrodes for oxygen reduction and methanol oxidation reactions, showing excellent electrocatalytic activity and superior stability.[5] The photoelectrochemical and electrochemical reduction of CO_2 to CO on BDD electrodes has been explored widely.[6] BDD electrodes modified with silver nanoparticles show high selectivity of products (i.e., CO: H_2) under irradiation towards CO_2 reduction in neutral aqueous electrolytes on account of the synergetic effect of Ag particles and BDD substrates.[7] In addition to the formation of CO, organic compounds that serve as fuels are also produced via CO_2 reduction on BDD electrodes.[8] For example, copper nanoparticles are decorated on BDD electrodes via electrochemical deposition or simple wet chemistry process.[9] Species such as ethanol, formic acid, formaldehyde, acetic acid, acetaldehyde, and acetone can be formed through electroreduction of CO_2 on Cu modified BDD electrodes.[10]

As a conductive material with favourable properties, BDD has also been utilised as an electrode material as well as an electrode substrate to construct energy storage devices such as electrical double layer capacitors (EDLCs) and pseudocapacitors.[11, 12] However, the capacitance of a bare

BDD (i.e., 3 – 10 μF cm^{-2} or 10 – 20 F g^{-1}) in aqueous solutions is lower due to limited surface area compared to other nanocarbons such as graphene (i.e., theoretical value ~21 μF cm^{-2} or 550 F g^{-1}).[13] To improve the performance of BDD-based supercapacitors, two approaches have been proposed. The first one is to expand the surface area by creating diamond nanostructures. For instance, diamond foam (0.60 mF cm^{-2}), honeycomb structured diamond (0.67 mF cm^{-2}), porous diamond (0.14 mF cm^{-2}), steam activated BDD (0.84 mF cm^{-2}) and BDD coated silicon nanowires (0.10 mF cm^{-2}) with enlarged surface areas have been produced to achieve better performance.[14, 15] The alternative way is to modify BDD substrates with redox species (e.g., conducting polymers and transition metal oxides) to construct composite electrodes.[12] Pseudocapacitive metal oxides including RuO_x (132 F g^{-1}) and MnO_2 (326 F g^{-1}) are coated on BDD electrodes to produce supercapacitors with improved performance.[11, 16] Other composite electrodes such as BDD/$Ni(OH)_2$ (1601 F g^{-1}) and BDD/polyaniline (526 F g^{-1}) are also fabricated with enhanced capacitive behaviour.[17] However, it should be noted that the mass loading of these faradaic active species is low (~ μg cm^{-2}), which may lead to much worse capacitive value when scaled up. A higher specific capacitance value is easily obtained if the 'dead' weight of the BDD substrate is neglected by some researchers during the capacitance calculation. Furthermore, the capacitance retention for some of these electrodes are relatively poor (~70% after 1000 cycles), limiting their potential applications as practical supercapacitors.[12]

To summarise, both approaches mentioned could be combined to produce a BDD-based supercapacitor with larger surface area and redox species modification. Among these materials, researchers have drawn their attention to MnO_2 as it is low-cost, abundant and environmentally friendly. MnO_2 can be incorporated into BDD through various techniques such as cathodic/anodic electrodeposition, sol-gel coating, electrochemical oxidation of Mn and electrophoretic deposition.[18]

One aim of this chapter is to explore the electrochemical properties of BDD as electrodes for EDLCs. The second aim is to fabricate MnO_2/BDD composite electrodes via potentiostatic anodic electrodeposition for pseudocapacitor applications. The electrochemical oxidation of Mn^{2+} ions on BDD electrodes is studied using CV before the anodic electrodeposition of MnO_2 on BDD surface.

3.2 Experimental

3.2.1 Chemicals and materials

Hexaammineruthenium(III) chloride [$Ru(NH_3)_6Cl_3$, 98%], potassium hexacyanoferrate(III) [$K_3Fe(CN)_6$, ACS reagent, ⩾ 99.0%], ferrocenemethanol [$C_{11}H_{12}FeO$, 97%], potassium chloride [KCl, ACS reagent, 99.0-100.5%], manganese(II) chloride tetrahydrate [$MnCl_2 \cdot 4H_2O$, ACS reagent, ⩾ 98%], sodium chloride [NaCl, ACS reagent, ⩾ 99.0%], sodium sulphate [Na_2SO_4, ACS reagent, ⩾ 99.0%], potassium hydroxide [KOH, ACS reagent, ⩾ 85%], sulphuric acid (H_2SO_4, ACS reagent, 95.0-97.0%) were purchased from Sigma-Aldrich. Hydrochloric acid (HCl, 37%, Certified AR for Analysis) and nitric acid (HNO_3, 68-70%, Certified AR for Analysis) were purchased from Fisher Chemical. Chemical reagents were used as received without further purification. All aqueous solutions were prepared using ultra-pure water from Millipore (resistivity ~ 18.2 MΩ cm at 25°C).

3.2.2 Equipment and experimental set-up

All electrochemical experiments were performed with an Autolab PGSTAT128N potentiostat/galvanostat (Metrohm Autolab, Utrecht, Netherlands) equipped with Nova software. The measurements were conducted at room temperature using a standard three-electrode configuration, as described in Chapter 2. The set-up consists of a platinum coil counter electrode and a silver/silver chloride reference electrode (immersed in 3 M KCl), along

with a boron doped diamond wafer working electrode. BDD wafers ([B]>10^{20} atoms cm^{-3}) of 10 x 10 x 0.6 mm were purchased from Element Six Co (UK) and assembled in a home-built PTFE holder with a circular area of 0.38 cm^2 (a diameter of 0.70 cm) exposed to the solution.

3.2.3 Preparation and modification of BDD electrodes

Prior to use, BDD electrodes were soaked in aqua regia (1:3 HNO_3 and HCl) overnight to remove contaminants. The electrodes were then scanned in 0.1 M HNO_3 for 20 voltammetric cycles between -1.5 to +2.7 V at 100 mV s^{-1}. The electrochemical oxidation of Mn^{2+} was carried out by cyclic voltammetry in an aqueous solution of 0.1 M $MnCl_2$ and 0.1 M Na_2SO_4. The potentiostatic deposition of MnO_2 on BDD was conducted in the same solution at a constant potential. The electrochemical performance of the bare BDD and the MnO_2/BDD electrodes was examined in the selected aqueous solution. Other parameters including scan rate, potential window, deposition potential, deposition time, electrolyte type and cycle number are specifically mentioned in Chapter 3.3 below. All potentials mentioned in this chapter were measured against the Ag/AgCl electrode (3M KCl, +0.210 V vs NHE), unless specified.

3.3 Results and discussion

3.3.1 Electrochemical characterisation of BDD electrodes

3.3.1.1 Electrochemical characterisation: redox species

Prior to use, BDD electrodes were cleaned and scanned in 0.1 M nitric acid between -1.5 to +2.7 V at 100 mV s^{-1} for 20 cycles. This process aims to yield active surfaces with a high concentration of oxygen functional groups, and to remove contamination and deactivating layers.[19] Better electrochemical signals with less background contributions were produced after electrode scanning, as shown in Figure 3.1.

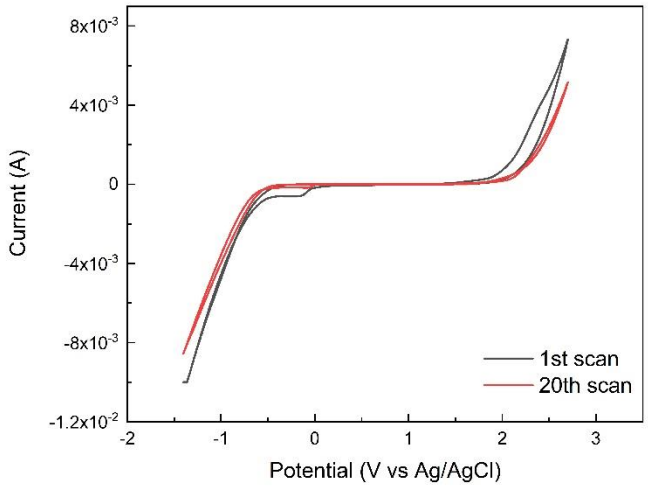

Figure 3.1 Cyclic voltammograms of BDD in 0.1 M nitric acid after electrode scanning. Scan rate: 100 mV s^{-1} for 20 cycles.

The electrochemical behaviour of BDD was first examined by cyclic voltammetry using ferrocenemethanol in 0.1 M KCl solution at a scan rate of 100 mV s^{-1}. The result is shown in Figure 3.2, and the reaction mechanism of the redox system is given in Reaction 3-1:

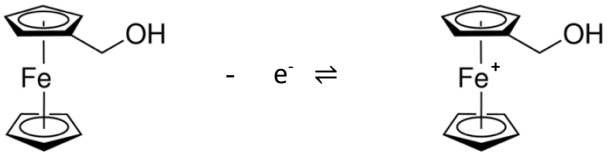

(3-1)

Peak separation, ΔE_p, was obtained as the potential difference between the anodic and the cathodic peak ($E_{p,a}$ and $E_{p,c}$). The ΔE_p values and the ratios of the anodic peak current to the cathodic peak current ($i_{p,a}/i_{p,c}$) of the redox couples are listed in Table 3.1.

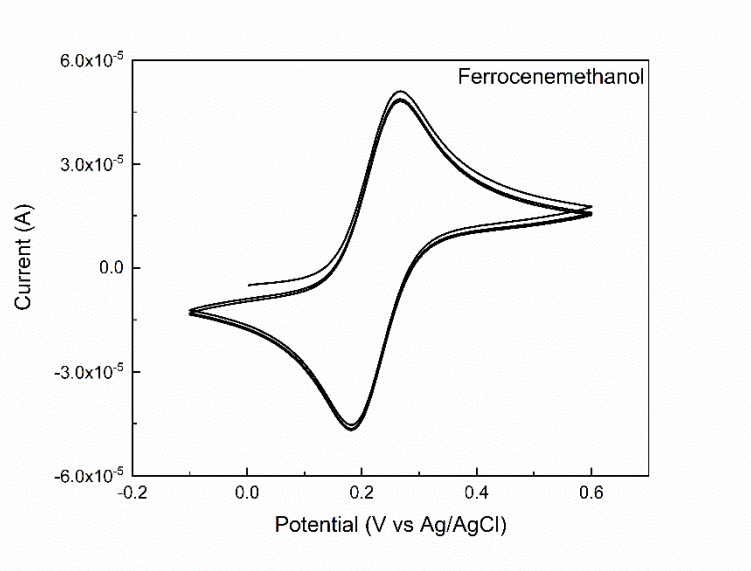

Figure 3.2 Cyclic voltammograms of 1.0 mM $FcCH_2OH$ in 0.1 M KCl at BDD electrodes. Scan rate: 100 mV s^{-1}. Potential range: -0.1 to +0.6 V vs Ag/AgCl.

Table 3.1 Cyclic voltammetric data for redox systems in KCl solution at BDD at 100 mV s^{-1}.

Redox Species	ΔE_p/mV	$i_{p,a}/i_{p,c}$
$FcCH_2OH$	85	1.05
$Ru(NH_3)_6^{3+}$	83	1.03
$[Fe(CN)_6]^{3-}$	236	0.95

A ΔE_p value of 85 mV is suggestive of rapid electron transfer for the $FcCH_2OH$ system, which is further confirmed by the $i_{p,a}/i_{p,c}$ value without deviation from unity.[20]

The voltammetry of another typical redox system, $Ru(NH_3)_6^{3+/2+}$, was then carried out at the electrodes, as shown in Figure 3.3 and Reaction 3-2:

$$Ru(NH_3)_6^{3+} + e^- \rightleftharpoons Ru(NH_3)_6^{2+} \quad (3\text{-}2)$$

This well-studied system has been reported to have outer-sphere electron transfer mechanism with rapid kinetics and is insensitive to electrode surface functionalities and impurities.[21, 22] The ΔE_p value is 83 mV, and the $i_{p,a}/i_{p,c}$ value is 1.03. Both values are similar to the ferrocenemethanol redox system, indicating nearly reversible electrode kinetics at the BDDs.

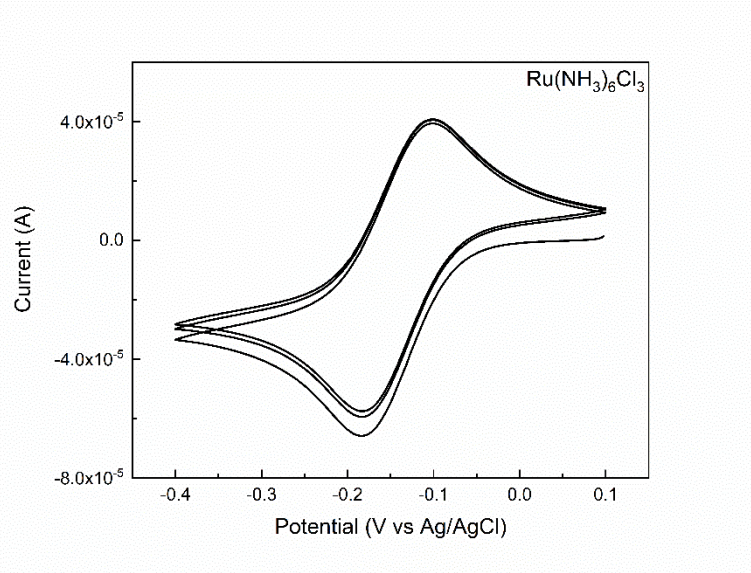

Figure 3.3 Cyclic voltammograms of 1.0 mM $Ru(NH_3)_6Cl_3$ in 0.1 M KCl at BDD electrodes. Scan rate: 100 mV s^{-1}. Potential range: -0.4 to +0.1 V vs Ag/AgCl.

Last, the ferrocyanide/ferricyanide redox couple was studied at BDD electrodes (Figure 3.4 and Reaction 3-3):

$$[Fe(CN)_6]^{4-} - e^- \rightleftharpoons [Fe(CN)_6]^{3-} \quad (3\text{-}3)$$

As an inner-sphere electron transfer reaction, this electron transfer process is more sensitive to electrode surfaces.[22] Different from the previous two redox systems, the ΔE_p value (236 mV) of the $[Fe(CN)_6]^{3-/4-}$ redox couple is in large excess of 57 mV, which is expected for slow electrode kinetics.

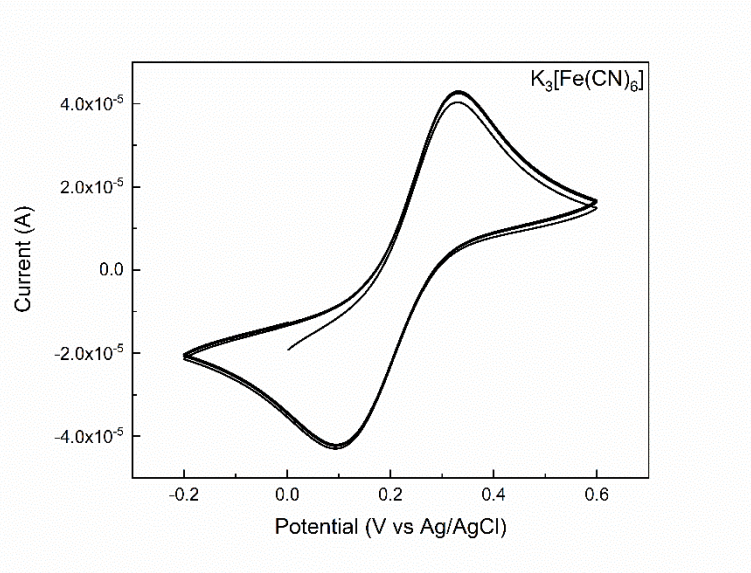

Figure 3.4 Cyclic voltammograms of 1.0 mM $K_3[Fe(CN)_6]$ in 0.1 M KCl at BDD electrodes. Scan rate: 100 mV s^{-1}. Potential range: -0.2 to +0.6 V vs Ag/AgCl.

In this session, three different electroactive species were investigated on the BDD electrodes. $FcCH_2OH/FcCH_2OH^+$ and $Ru(NH_3)_6^{3+/2+}$ exhibited fast electron transfer kinetics, whereas $[Fe(CN)_6]^{3-/4-}$ showed a quasi-reversible electrochemical response. Based on the characterisations above, the BDD electrode is a valid candidate for further electrochemical analysis.

3.3.1.2 Electrochemical characterisation: electrolyte

Four aqueous electrolytes were employed to investigate the operating potential window of BDD electrodes prior to MnO_2 deposition. The CVs of BDD electrodes in H_2SO_4, KOH, KCl and Na_2SO_4 are shown in Figure 3.5. It can be seen that in the acidic solution (H_2SO_4, etc.), the lower potential window is limited by hydrogen evolution reaction (HER). Furthermore, strong acidic electrolytes are less environmentally friendly, can cause corrosion of current collectors and impair device safety. By contrast, oxygen evolution reaction (OER) is related to the upper limit of its potential window in the alkaline solution (KOH, etc.). The oxygen produced may

cause loosening of active materials, which is detrimental to the long-term functionality of the electrode.[23]

Nearly only capacitive current (non-Faradaic process) was observed within a wide potential window of -1 to +1 V in the neutral aqueous electrolytes (KCl and Na_2SO_4, etc.). This range covers the normal potential window of a MnO_2 electrode (0 to +0.8 V vs Ag/AgCl), so neutral electrolytes would be used for subsequent experiments.[24]

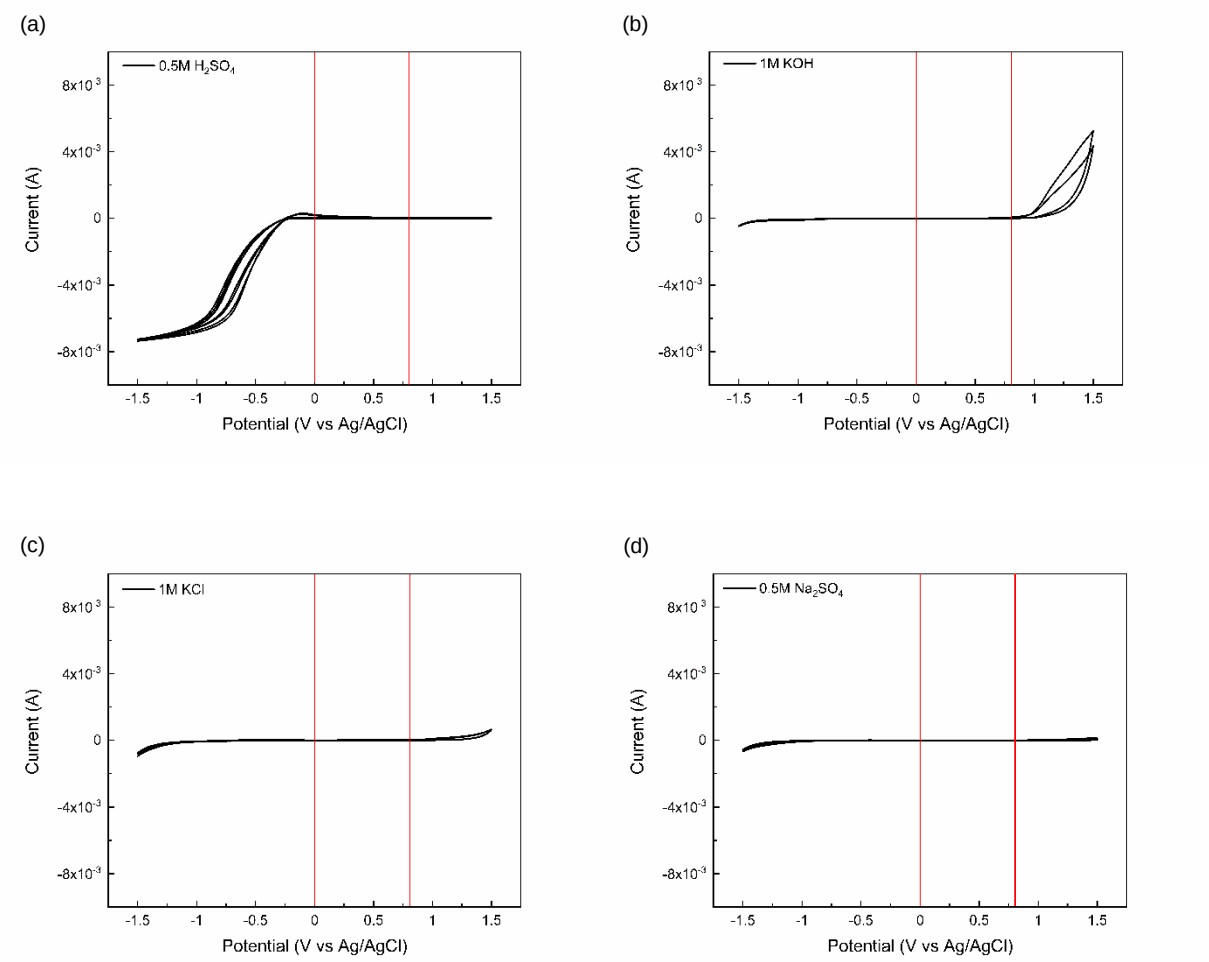

Figure 3.5 Cyclic voltammograms of bare BDD at 100 mV s^{-1} in (a) 0.5 M H_2SO_4, (b) 1 M KOH, (c) 1 M KCl and (d) 0.5 M Na_2SO_4, respectively. Potential range: -1.5 to +1.5 V. Red lines: operating window of MnO_2.

The comparison of CVs of a BDD and a glassy carbon (GC) electrode under the same condition is illustrated in Figure 3.6 (a). A GC electrode, which is produced by thermal degradation of polymer resins, is one of the most commonly used working electrodes in electrochemical experiments owing to its hardness, thermal stability, chemical and electrochemical inertness, wide potential window and high electrical conductivity.[25] The BDD electrode has lower background current response than the GC electrode, enabling itself to be a promising substrate material to investigate further electrodeposition of MnO_2. The influence of neutral electrolytes (e.g., type of cations and anions, and concentration) on the performance of BDD electrodes was also studied, as shown in Figure 3.6 (b). No correlation between type of the ions, concentration of the solutions and CV responses was found on BDD electrodes under the chosen potential window (0 to +0.8 V).

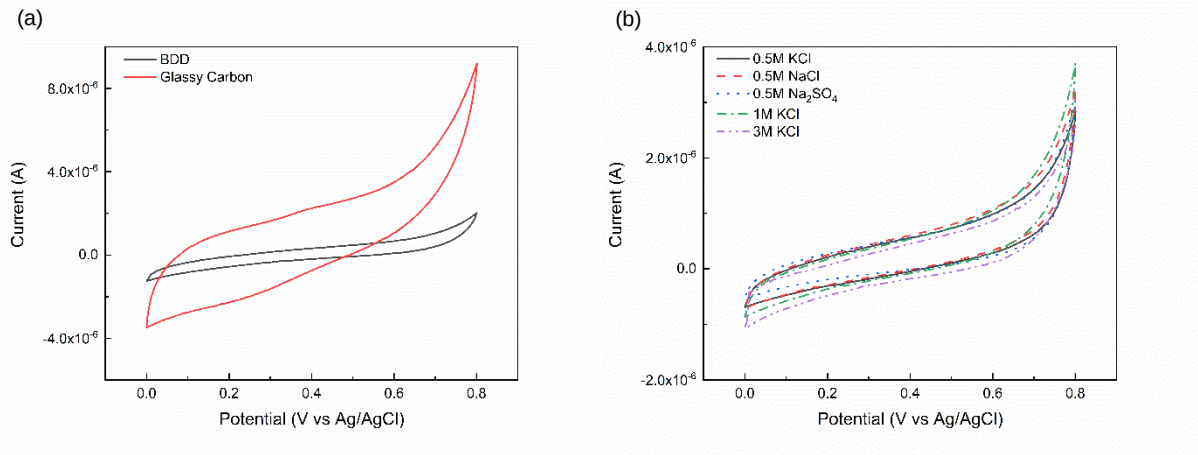

Figure 3.6 (a) Cyclic voltammograms of bare BDD and GC electrodes with the same geometric surface area exposed to solution, and (b) CVs of bare BDD in different neutral electrolytes. Scan rate: 100 mV s^{-1}.

3.3.2 Surface characterisation of BDD and MnO_2/BDD electrodes

3.3.2.1 Scanning electron microscopy

SEM images of a pure BDD electrode and MnO_2 modified BDD electrodes after different time of potentiostatic deposition are shown in Figure 3.7. No particles are observed on a bare BDD in Figure 3.7 (a). Afterwards, MnO_2 particles start growing from the edges of the BDD because of lateral electrical conductivity of BDD electrodes, as shown in Figure 3.7 (b). The areas that are not covered with MnO_2 particles at the beginning have less boron dopant concentrations, therefore are less conductive and consequently experiences inhibited MnO_2 deposition.[26] Visible agglomeration of particles is observed with longer deposition time in Figure 3.7 (c). Dense particles agglomerate together with cracks to cover the entire surface of the BDD with the undesirably long deposition time, as shown in Figure 3.7 (d).

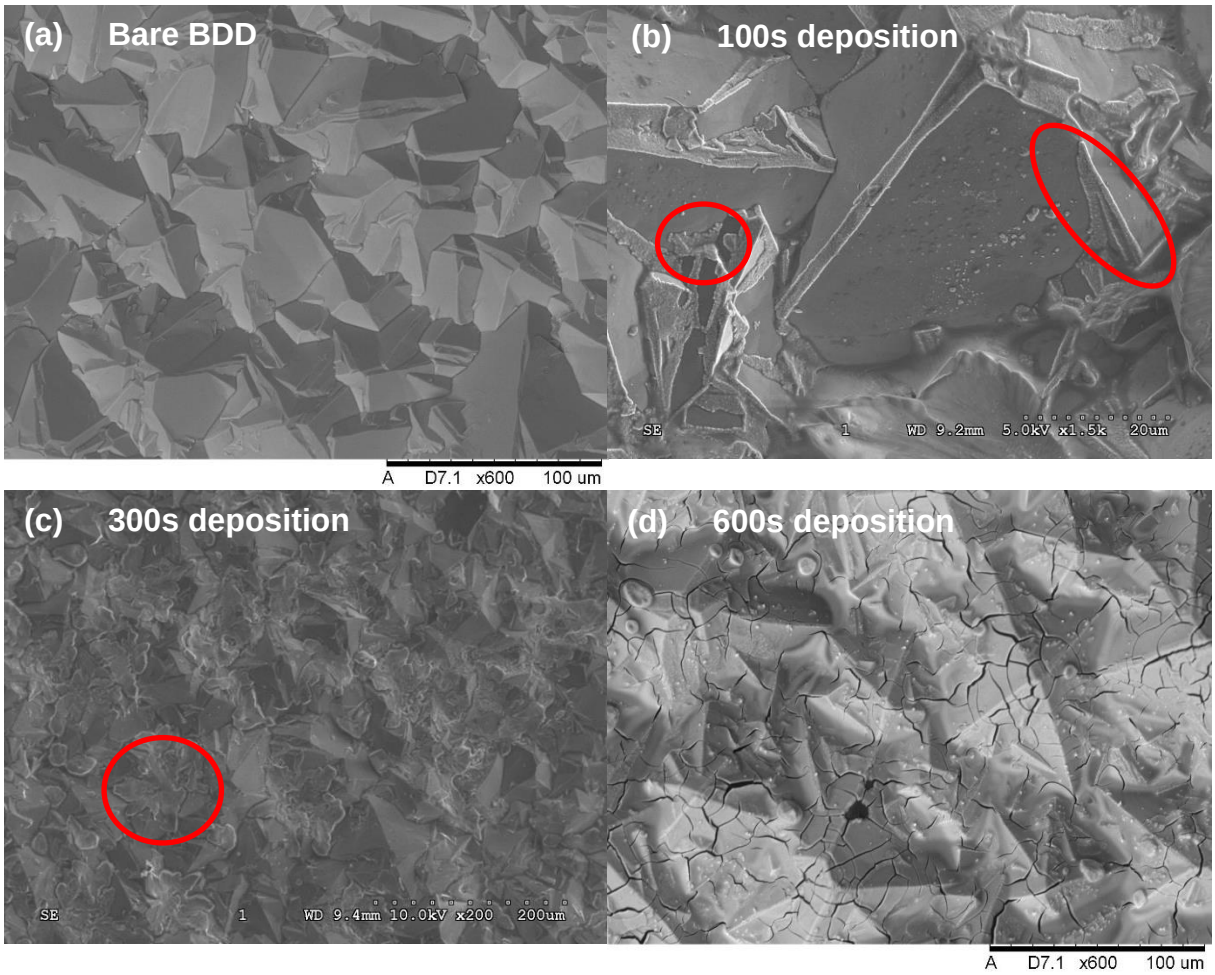

Figure 3.7 SEM images of a bare BDD (a) and MnO_2 deposited on BDD electrodes through chronoamperometry at +0.85V vs Ag/AgCl for 100 s (b), 300 s (c) and 600 s (d), respectively.

3.3.2.2 X-ray photoelectron spectroscopy

XPS spectra of the bare BDD and the MnO_2/BDD are presented in Figure 3.8. The survey scan indicates that the major components of the BDD surface are carbon (89.0%) and oxygen (10.4%). The dominant C 1s peak at 284.6 eV is attributed to the diamond carbon and the O 1s peak at 532.6 eV indicates the oxygen functionalities on the BDD surface. In addition to the C 1s and the O 1s peaks, Mn 2p and Mn 3s peaks are observed in the survey of the MnO_2/BDD electrode. Furthermore, the O 1s peak is larger while the C 1s peak is smaller after deposition, confirming the introduction of manganese oxides particles onto the BDD surface.

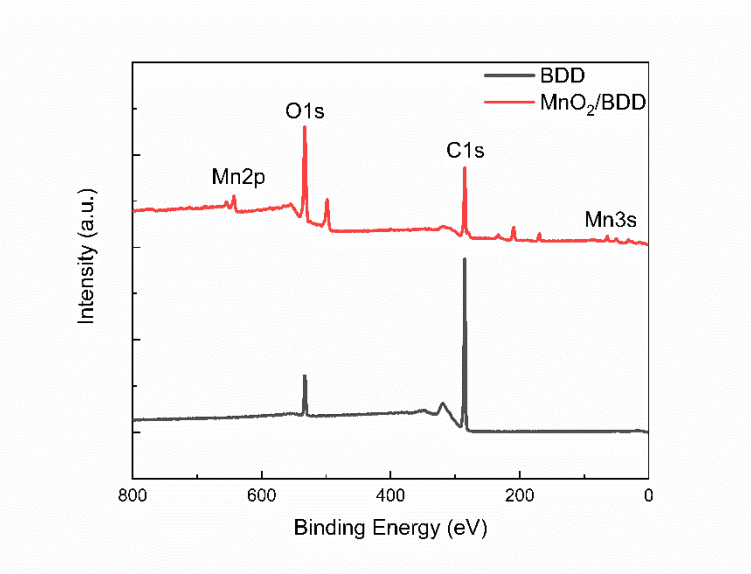

Figure 3.8 XPS spectra of survey scan of bare BDD and MnO_2/BDD (100 s, +0.85 V).

The high-resolution XPS spectra of Mn 2p and Mn 3s are shown in Figure 3.9. The Mn 2p spectrum shows significant split spin-orbit components (Mn $2p_{3/2}$ and Mn $2p_{1/2}$), and the Mn $2p_{3/2}$ component centred at ~642 eV is attributed to Mn(IV) as in MnO_2.[27] The Mn 3s peak with two multiplet split components is caused by coupling of non-ionised 3s electron with 3d valence-band electrons, as shown in Figure 3.10. The multiplet splitting of 4.8 eV in the Mn 3s region is obtained for Mn(IV), which further diagnoses the Mn oxidation state.[28]

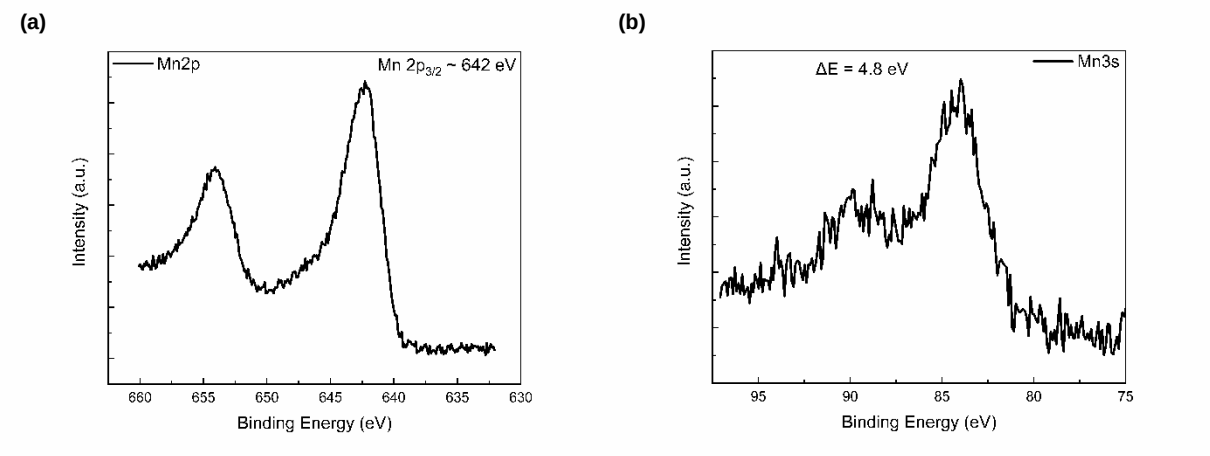

Figure 3.9 XPS spectra of (a) Mn 2p scan and (b) Mn 3s scan of MnO_2/ BDD (100 s, 0.85 V).

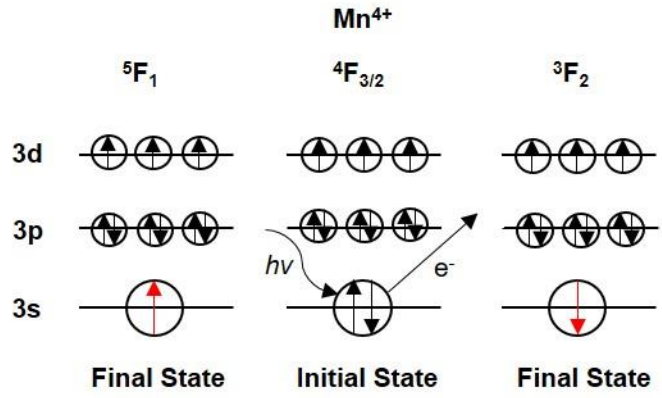

Figure 3.10 Schematic diagram of Mn 3s multiplet splitting of Mn^{4+}.

3.3.3 Electrochemical oxidation of Mn^{2+} on BDD electrodes

3.3.3.1 Cyclic voltammograms of Mn^{2+} at BDD electrodes

Figure 3.11 shows the CVs for oxidation of 0.1 M $MnCl_2$ in 0.1 M Na_2SO_4 on BDD electrodes. Na_2SO_4 acts as a supporting electrolyte for the Mn^{2+} precursors, and the solution is weakly acidic as Mn^{2+} can hydrolyse to form $Mn(OH)_x$ and H^+.[29] The anodic peak ($p_{a,1}$) can be assigned to the oxidation of Mn(II) to Mn(IV) on the electrode surface. On the reverse scan, the cathodic peak ($p_{c,1}$) is associated with the reduction of Mn(IV) to Mn(II). The mechanism of MnO_2 formation has been discussed in a number of papers.[30, 31, 32]

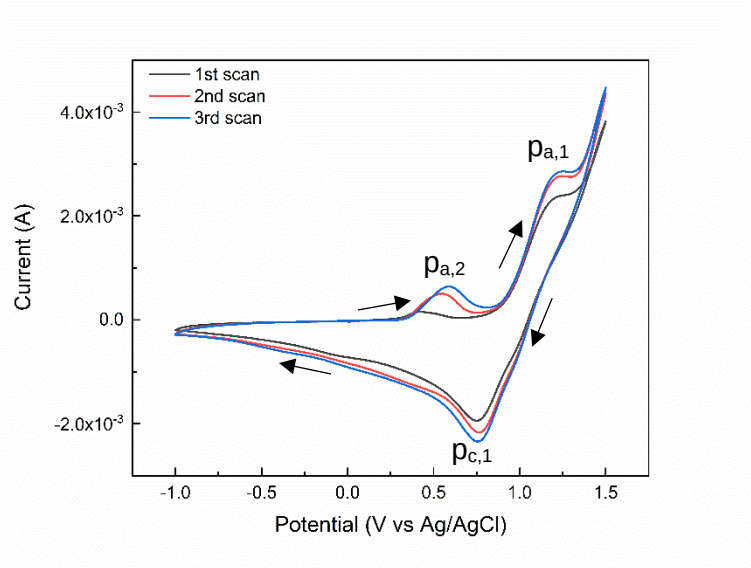

Figure 3.11 Cyclic voltammograms of Mn^{2+} on a bare BDD substrate (three scans). Electrolyte: 0.1 M $MnCl_2$ and 0.1 M Na_2SO_4; potential window: -1.0 to +1.5 V; scan rate: 100 mV s^{-1}.

The overall reaction for the anodic MnO_2 deposition is given by a two-electron transfer process:

$$Mn^{2+} + H_2O \rightarrow MnO_2 + 4H^+ + 2e^- \quad (3\text{-}4)$$

However, it is unlikely that the reaction can occur in one single step. Instead, a multiple-step mechanism has been proposed.[30, 31, 32] First, a single electron transfer step where Mn^{2+} ions are oxidised to soluble Mn^{3+} precursors has been suggested, shown in Reaction 3-5:

$$Mn^{2+} \rightarrow Mn^{3+} + e^- \quad (3\text{-}5)$$

The unstable Mn^{3+} formed in the previous step can disproportionate to Mn^{2+} and Mn^{4+}. Mn^{4+} ions are then hydrolysed to form MnO_2 on the substrate surface. Thus, the disproportionation pathway is given by Reaction 3-6 and 3-7:

$$2Mn^{3+} \rightarrow Mn^{2+} + Mn^{4+} \quad (3\text{-}6)$$

$$Mn^{4+} + 2H_2O \rightarrow MnO_2 + 4H^+ \quad (3\text{-}7)$$

On the other hand, the Mn^{3+} ions may hydrolyse to form an insulating intermediate, MnOOH. The intermediate is then oxidised to MnO_2 in the subsequent step. The mechanism of the hydrolysis pathway is shown as following:

$$Mn^{3+} + 2H_2O \rightarrow MnOOH + 3H^+ \quad (3\text{-}8)$$

$$MnOOH \rightarrow MnO_2 + H^+ + e^- \quad (3\text{-}9)$$

In addition to the formation of a Mn^{3+} intermediate, another possible electron transfer process of simultaneous H_2O oxidation can take place.[32] In this mechanism, H_2O is first oxidised at the electrode surface, which generates adsorbed hydroxyl radicals ($^{\bullet}OH_{ads}$). Mn^{2+} ions then undergo oxidation with $^{\bullet}OH_{ads}$ to form MnO_2. The mechanism of the H_2O oxidation pathway, also named advanced electrochemical oxidation process, is given by the following:

$$H_2O \rightarrow {}^{\bullet}OH_{ads} + H^+ + e^- \quad (3\text{-}10)$$

$$Mn^{2+} + 2{}^{\bullet}OH_{ads} \rightarrow MnO_2 + 2H^+ \quad (3\text{-}11)$$

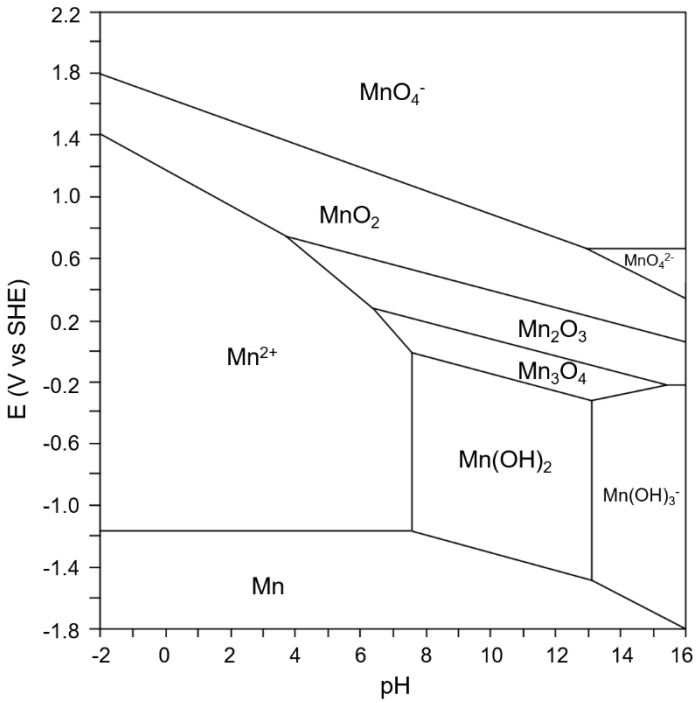

Figure 3.12 Pourbaix Diagram of Manganese (adapted from Pourbaix).[33]

As a transition metal, Mn has various valence states such as Mn(II), Mn(III), Mn(IV) and Mn(VII). Different manganese oxide phases (MnO_2, Mn_2O_3 and Mn_3O_4) can be synthesised electrochemically by adjusting the pH of solutions and the potential applied, according to the Pourbaix Diagram of Manganese in Figure 3.12.[33] In addition to the reactions of MnO_2 deposition discussed above, the following side reactions including formation of Mn_2O_3 and regeneration of Mn^{3+}/MnOOH occur inevitably at the electrode surface as a result of the complex chemistry of manganese[31]:

$$2Mn^{2+} + 3H_2O \rightarrow Mn_2O_3 + 6H^+ + 2e^- \quad (3\text{-}12)$$

$$MnO_2 + Mn^{2+} + 2H_2O \rightarrow 2MnOOH + 2H^+ \quad (3\text{-}13)$$

$$MnO_2 + Mn^{2+} + 4H^+ \rightarrow 2Mn^{3+} + 2H_2O \quad (3\text{-}14)$$

The oxidation peaks ($p_{a,2}$) appearing between +0.5 V and +0.6 V in Figure 3.11, which are more obvious in the second and the third cycles, can be attributed to the underlying reaction:

$$MnOOC \rightarrow MnO_2 + C^+ + e^- \quad (3\text{-}15)$$

where $C^+ = H^+$ or Na^+

Oxidation of the manganese (III) compounds formed during the first cycle give rise to the anodic peak ($p_{a,2}$) from the second cycle. In fact, Reaction 3-15 shows the charge storage mechanism for MnO_2 as a pseudocapacitive electrode material.[18, 34]

3.3.3.2 Effect of scan rate and cycle

Figure 3.13 shows the first CV scan of Mn^{2+} on BDD electrodes with varying scan rates from 2 to 75 mV s^{-1}. In all the CVs, the current saw a jump after +0.8 V until the oxidation peaks appeared between +1.3 and +1.45 V during the anodic scan. The anodic peak current increased, but the anodic peak potential shifted irregularly when the scan rate was raised. At low scan rates (e.g., 2 and 5 mV s^{-1}), the oxidation reactions had more time to take place on the electrode surface. For example, the scanning time at 2 mV s^{-1} is 37.5 times higher than that at 75 mV s^{-1}, while the larger current at 75 mV s^{-1} cannot compensate for the shorter scanning time, leading to the quantity of charge passed at 2 mV s^{-1} is larger than that at 75 mV s^{-1}. As a result, the insulating intermediate MnOOH and product MnO_2 with low electrical conductivity covered the active sites of the electrode at low scan rates. Thus, the oxidation peak moved to higher potentials at the partially deactivated electrode compared to one with clean surface. As an irreversible reaction, the overpotential for the oxidation of Mn^{2+} would increase at higher scan rates. Nonetheless, less intermediates and products were formed due to less time for the reaction at higher scan rates, so that the electrode surface had more active sites than the ones scanned at lower scan rates.[31, 35]

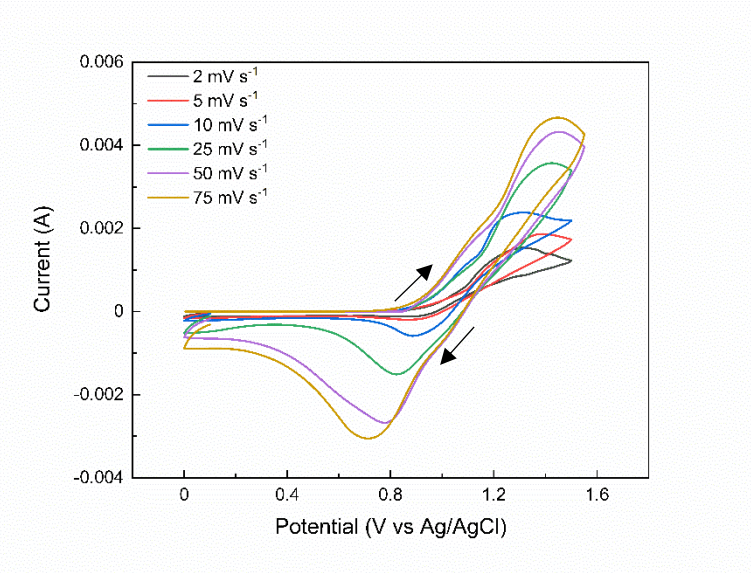

Figure 3.13 Cyclic voltammograms of Mn^{2+} on bare BDD substrate (first scan) at scan rates of 2, 5, 10, 25, 50 and 75 mV s^{-1}, respectively. Electrolyte: 0.1 M $MnCl_2$ and 0.1 M Na_2SO_4; potential window: 0 to +1.5 V.

The formation of the insulating layer can be further confirmed by the reduction of the anodic peak current in the second cycle, as shown in Figure 3.14. At the scan rate of 5 mV s^{-1}, a thick electro-deposited layer of MnO_2 should be formed during the anodic cycle at the electrode surface, but it was not completely reduced at the reverse scan. Therefore, the oxidation peak current after +1.2 V dropped rapidly at the second anodic cycle. When the scan rate went up to 75 mV s^{-1}, a smaller amount of MnOOH and MnO_2 were produced on account of less time for relevant reactions, leading to less changes in the shape of the CV during the second cycle.[31]

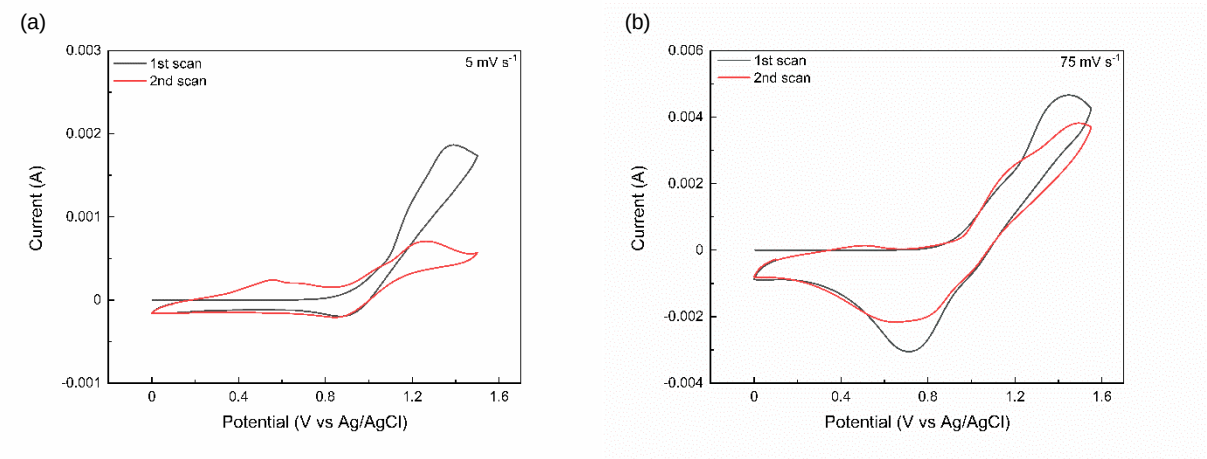

Figure 3.14 Cyclic voltammograms of Mn^{2+} on bare BDD substrate (1^{st} and 2^{nd} scans) at (a) 5 mV s^{-1} and (b) 75 mV s^{-1}, respectively. Electrolyte: 0.1 M $MnCl_2$ and 0.1 M Na_2SO_4; potential window: 0 to +1.5 V.

3.3.4 Potentiostatic deposition of MnO_2 on BDD electrodes

3.3.4.1 Effect of deposition potential

The anodic deposition of MnO_2 was first carried out by applying 8 operational potentials (i.e., +0.15 to +0.85 V vs Ag/AgCl) in the electrolyte of 0.1 M $MnCl_2$ and 0.1 M Na_2SO_4. The potential started from +0.15 V and ended at +0.85 V which lasted for 50 s at each potential, as shown in Figure 3.15. The current-time deposition curve saw an obvious increase in the current signal at +0.75 V, and the current jumped more rapidly at +0.85 V. To optimise the deposition parameter, three anodic potentials (+0.65 V, +0.75 V and +0.85 V vs Ag/AgCl) were selected for the following studies.

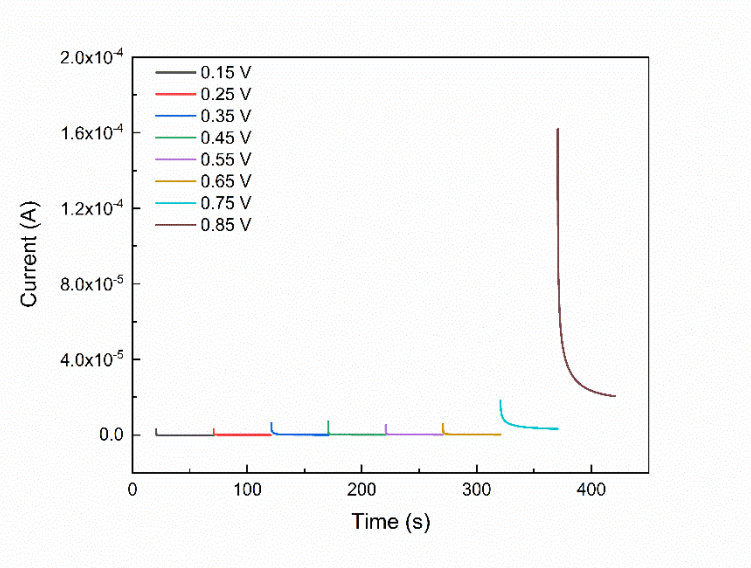

Figure 3.15 Chronoamperograms of MnO_2 deposition in 0.1 M $MnCl_2$ and 0.1 M Na_2SO_4 on bare BDD electrodes at constant potentials of +0.15, +0.25, +0.35, +0.45, +0.55, +0.65, +0.75 and +0.85 V vs Ag/AgCl for 50 s, respectively.

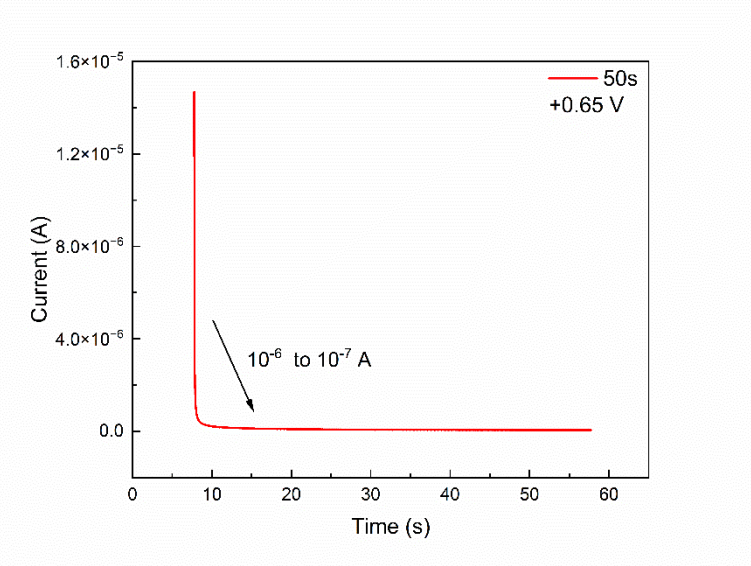

Figure 3.16 Chronoamperograms of MnO_2 deposition at +0.65 V vs Ag/AgCl for 50 s. Electrolyte: 0.1 M $MnCl_2$ and 0.1 M Na_2SO_4.

Figure 3.16 shows the *i-t* deposition curves at +0.65 V vs Ag/AgCl for 50 s with low current response (10^{-7} – 10^{-6} A). After each deposition (50 to 600 s), the electrolyte was replaced with

3 M KCl, and the cyclic voltammograms were then recorded at 100 mV s^{-1}, as shown in Figure 3.17. Although a larger current signal, namely capacitance, was observed after deposition in Figure 3.17 (a), the asymmetric CV curve did not exhibit the rectangular and symmetrical characteristics of pseudocapacitive MnO_2.[18] Furthermore, Figure 3.17 (b) shows that the voltammograms remained almost the same regardless of the deposition time as a result of low potential applied and current response. According to the Pourbaix Diagram in Figure 3.12 and other studies, Mn_2O_3 or Mn_3O_4 can be formed at low anodic potential, which explains the difference between the voltammograms in Figure 3.17 and what was expected for MnO_2.[36]

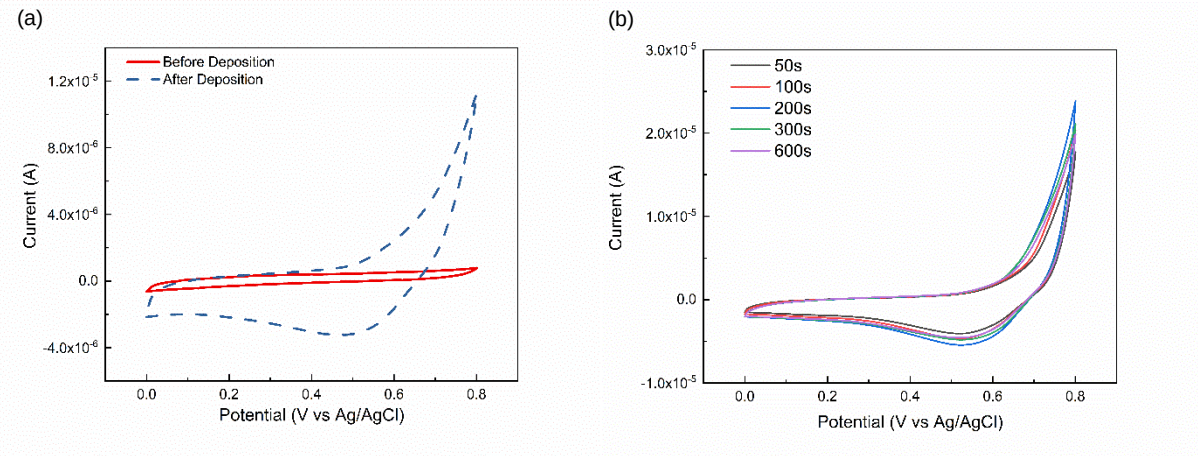

Figure 3.17 (a) Cyclic voltammograms of bare BDD and BDD electrode after deposition at 0.65 V for 600 s and (b) CVs of BDD after deposition at 0.65 V for 50, 100, 200, 300 and 600 s. Experimental parameters: scan rate: 100 mV s^{-1}; potential window: 0 to +0.8 V; electrolyte: 3M KCl.

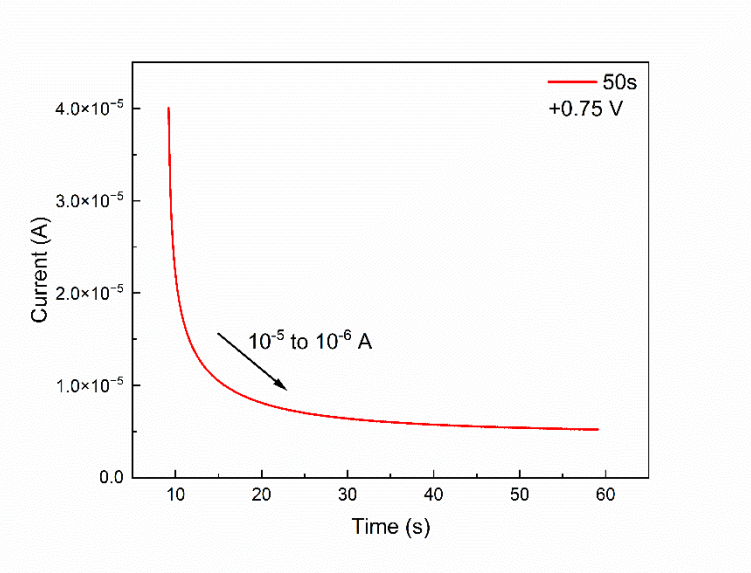

Figure 3.18 Chronoamperograms of MnO_2 deposition at +0.75 V vs Ag/AgCl for 50 s. Electrolyte: 0.1 M $MnCl_2$ and 0.1 M Na_2SO_4.

Figure 3.18 shows the *i-t* deposition curves at +0.75 V vs Ag/AgCl for 50 s with higher current response (10^{-6} – 10^{-5} A) than the *i-t* curves at +0.65 V (Figure 3.16). Presumably, the current drops off because an insulating layer is formed on BDD surface. Afterwards, CVs were conducted in 3 M KCl at 100 mV s^{-1}, as shown in Figure 3.19. Enhanced capacitive response was observed with quasi-rectangular and symmetrical characteristics, and the current increased with deposition time. The broad peak between +0.4 and +0.6 V results from the redox reaction of MnO_2 in electrolytes with cations (C^+ = K^+, Na^+, H^+, etc.), as mentioned above in Reaction 3-15:

$$MnOOC \rightarrow MnO_2 + C^+ + e^- \qquad (3\text{-}15)$$

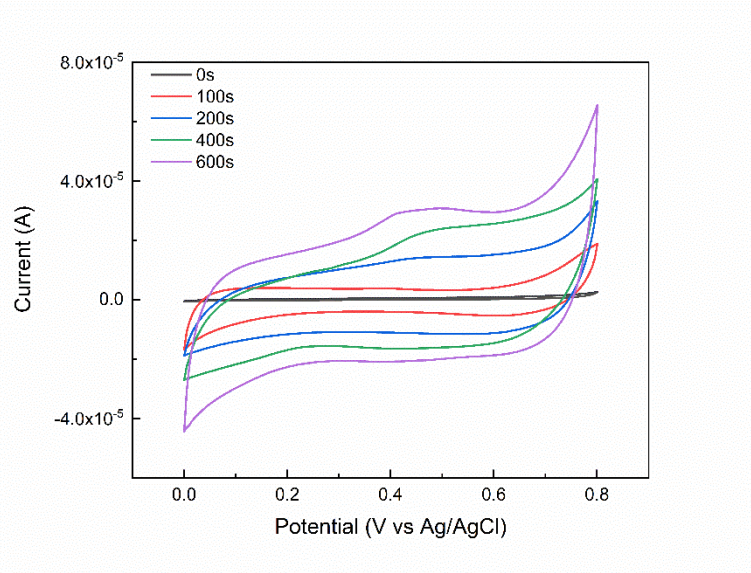

Figure 3.19 Cyclic voltammograms of bare BDD and BDD electrode after deposition at +0.75 V for 100, 200, 400 and 600 s. Experimental parameters: scan rate: 100 mV s^{-1}; potential window: 0 to +0.8 V; electrolyte: 3M KCl.

Assuming 100 % Faradaic efficiency via the electrodeposition of MnO_2 on the BDD electrode, the amount of MnO_2 can be calculated using the following equation:

$$m = \frac{QM_{MnO_2}}{2eN_A} \tag{3-16}$$

where Q is the charge passed (C) and integrated from the chronoamperograms in Figure 3.18, M is the molecular mass of MnO_2 (86.94 g mol^{-1}), 2 is the number of the electrons involved in the redox reaction, e is the electron charge (1.6×10^{-19} C), N_A is the Avogadro constant (6.02×10^{23} mol^{-1}). eN_A can also be denoted by F, the Faraday constant (96485.3 C mol^{-1}), which means the electric charge of one mole of electrons.

Figure 3.20 shows the mass of MnO_2 deposited is controllable by varying the potentiostatic deposition time at +0.75 V. Higher loading of MnO_2 can be readily achieved by extending the deposition time. For instance, a mass of 1.2 µg MnO_2 was obtained when the deposition time reached 600 s.

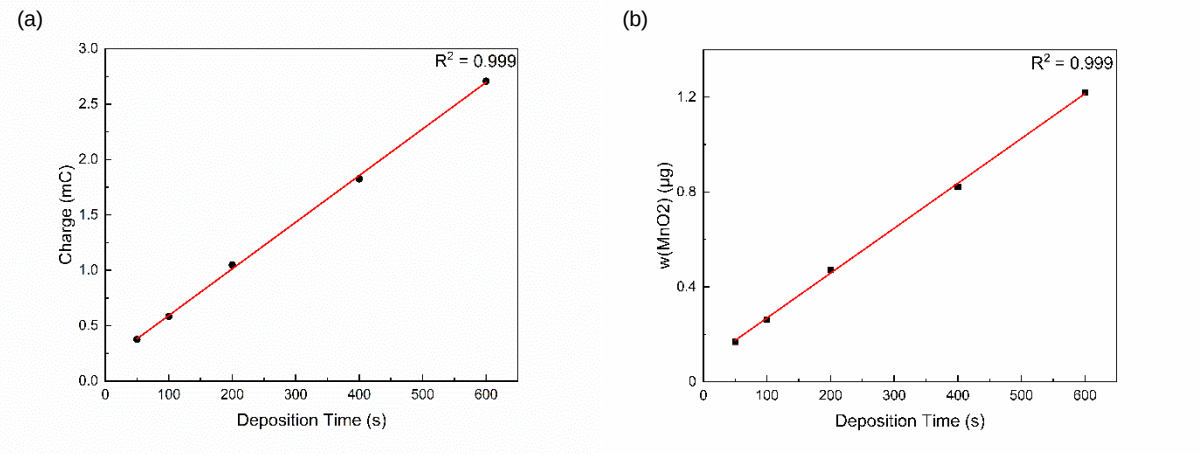

Figure 3.20 (a) Charge integrated from the chronoamperograms and (b) mass of MnO_2 calculated of BDD deposited at +0.75 V vs Ag/AgCl as a function of the deposition time, respectively.

The gravimetric specific capacitance (C_g) and the areal specific capacitance (C_a) are calculated from the CV measurements:

$$C_{gravimetric} = \frac{\int_{E1}^{E2} IdE}{2\Delta Evm} \quad (3\text{-}17)$$

$$C_{areal} = \frac{\int_{E1}^{E2} IdE}{2\Delta EvA} \quad (3\text{-}18)$$

where I is the current (A) with background current of bare BDD subtracted, E is the potential (V), ΔE is the potential window of 0.8 V, v is the scan rate of 0.1 V s^{-1}, m is the mass (g) of MnO_2, A is the geometrical area (0.38 cm^2) of the BDD electrode exposed to the electrolyte.

The specific capacitance and the mass of MnO_2 calculated are listed in Table 3.2. At the scan rate of 100 mV s^{-1}, the areal specific capacitance of MnO_2/BDD (0.12 – 0.56 mF cm^{-2}) is about 17 – 80 times higher than that (7.0 µF cm^{-2}) of a bare BDD electrode by introducing up to 1.2 µg of MnO_2. However, the gravimetric specific capacitance reached up to 217.9 F g^{-1} at the deposition time of 200 s, and retained lower than 200 F g^{-1} by increasing the deposition time. The reason is that only the MnO_2 surface is contributing to the capacitance due to the poor

electrical conductivity of MnO_2. The C_{areal} value increases when higher loading mass of MnO_2 is reached with more active surface area, but the $C_{gravimetric}$ value decreases as the active surface per amount of MnO_2 eventually reduces, as shown in Figure 3.21.

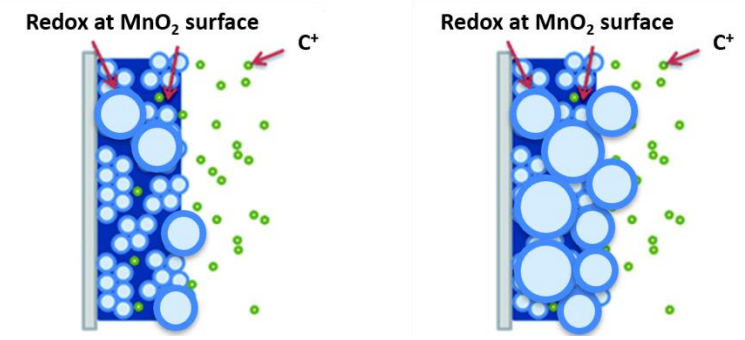

Figure 3.21 Schematic of MnO_2 growing (adapted from Augustyn, Simon et al. 2014).[37]

Table 3.2 Gravimetric and areal specific capacitance of MnO_2/BDD electrode calculated from CVs at 100 mV s^{-1} with different deposition time (0 to 600s) at +0.75 V.

Deposition time (s)	$C_{gravimetric}$ (F g^{-1})	C_{areal} (mF cm^{-2})	MnO_2 mass (µg)	MnO_2 loading (µg cm^{-2})	MnO_2 thickness (nm)
0	/	0.0070	/	/	/
100	167.7	0.12	0.26	0.68	0.52
200	217.9	0.27	0.47	1.2	0.93
400	177.4	0.38	0.82	2.1	1.6
600	174.5	0.56	1.2	3.1	2.4

In summary, the pseudocapacitive behaviour of MnO_2 is observed after the deposition at +0.75 V with a low mass loading (i.e., 3.1 µg cm^{-2} at the deposition time of 600 s). The deposition potential is further raised to +0.85 V to obtain higher mass loading of MnO_2 in the following experiments.

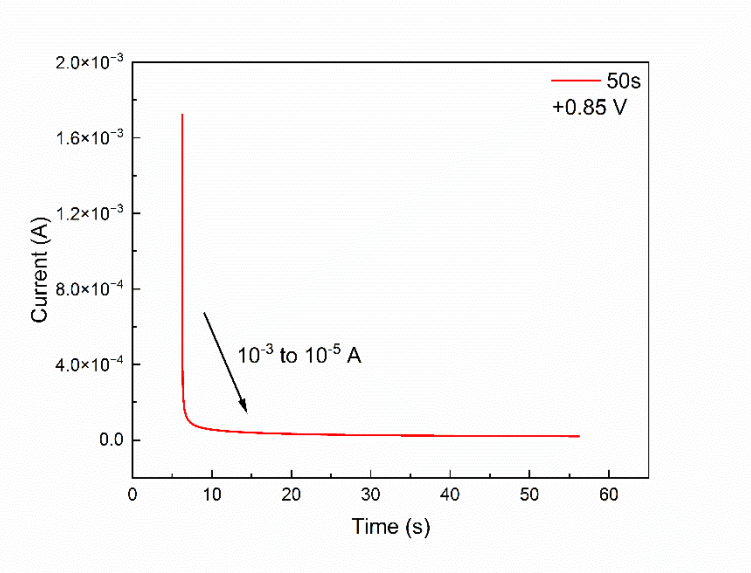

Figure 3.22 Chronoamperograms of MnO_2 deposition at +0.85 V vs Ag/AgCl for 50 s. Electrolyte: 0.1 M $MnCl_2$ and 0.1 M Na_2SO_4.

Figure 3.22 shows the chronoamperograms at +0.85 V vs Ag/AgCl for 50 s with much higher current response (10^{-5} – 10^{-3} A) than the *i-t* deposition curves (10^{-6} – 10^{-5} A) at +0.75 V (Figure 3.18). The capacitive current of the BDD substrate is negligible (< 0.05%) compared to the faradaic current, as shown in Figure 3.23, so the mass of MnO_2 can be directly calculated using the charge passed integrated from Figure 3.22.

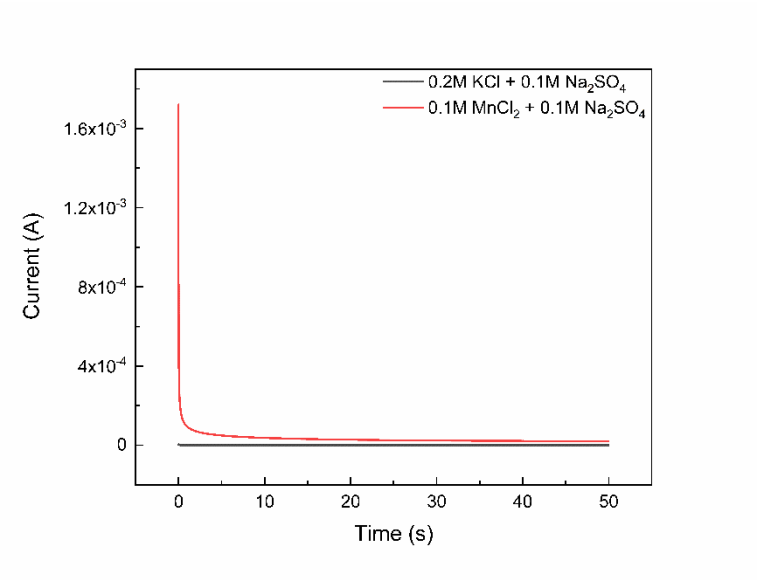

Figure 3.23 Chronoamperograms of bare BDD in a solution containing (red) 0.1 M $MnCl_2$ and (black) 0.2 M KCl, respectively in 0.1 M Na_2SO_4 at +0.85 V vs Ag/AgCl for 50 s.

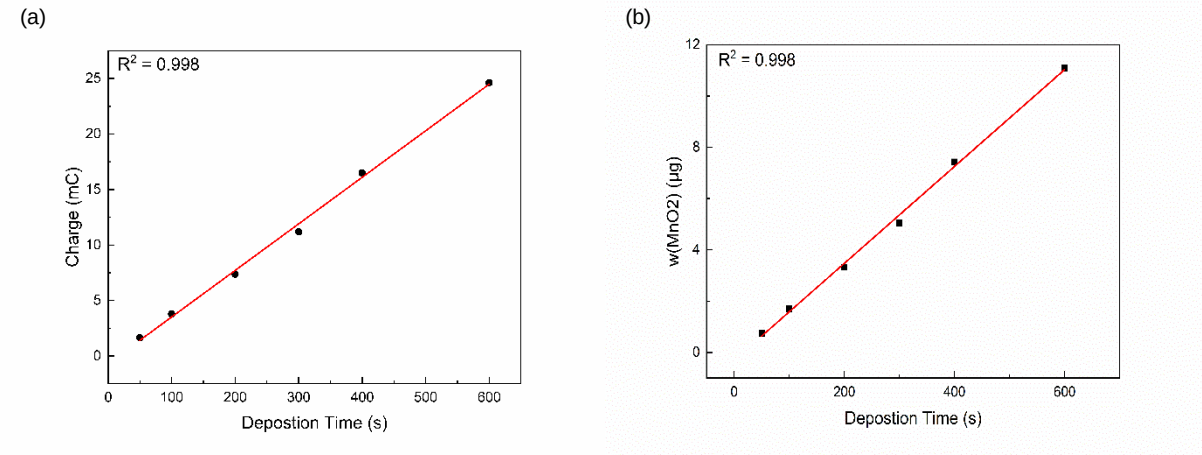

Figure 3.24 (a) Charge integrated from the chronoamperograms and (b) mass of MnO_2 calculated of BDD deposited at +0.85 V vs Ag/AgCl as a function of the deposition time, respectively.

Figure 3.24 shows that the mass of MnO_2 deposited rises linearly at +0.85 V. For example, a mass of 11 µg MnO_2 was easily obtained by extending the deposition time to 600 s at +0.85 V, which is 9.2 times higher than that of the same deposition time at +0.75 V.

Figure 3.25 (a) illustrates the cyclic voltammograms with the same deposition time of 200 s but different deposition potential (+0.75 and +0.85 V). While maintaining its rectangular shape, the electrode deposited at +0.85 V provided an enhanced CV signal on account of an increase in the amount and the surface of MnO_2. The rectangular consistency of the CV curves at the scan rate of 100 mV s^{-1} with different deposition time at +0.85 V is presented in Figure 3.25 (b), where excellent pseudocapacitive behaviour of MnO_2 is revealed with shorter deposition time. A rise of deposition time of 600 s leads to thicker MnO_2 film with less ideal voltammetric response, which reduces the electrical conductivity of the electrode.[11, 38]

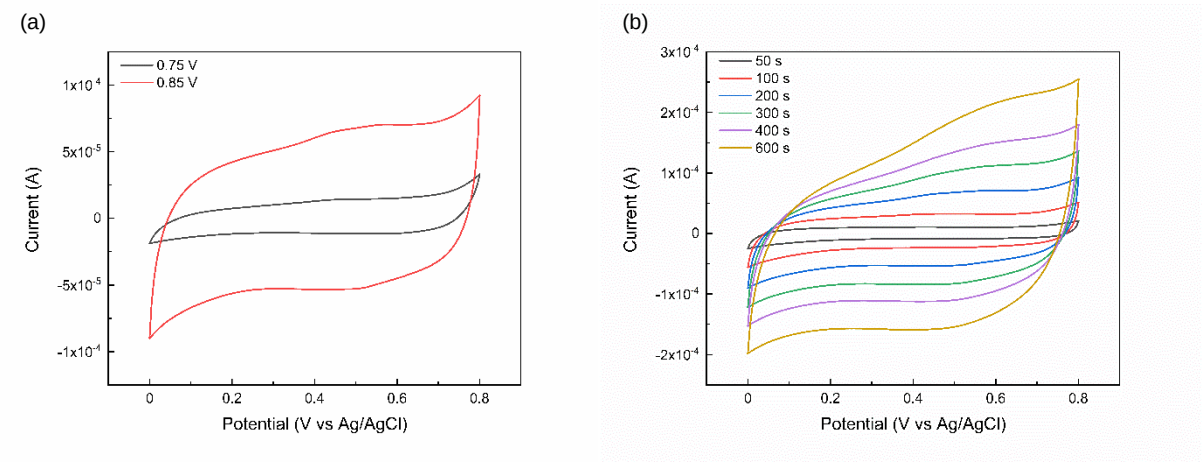

Figure 3.25 (a) Cyclic voltammograms of BDD after deposition at +0.75 and +0.85 V for 200 s, respectively, and (b) CVs of BDD after deposition at +0.85 V for 50 – 600 s. Experimental parameters: scan rate: 100 mV s^{-1}; potential window: 0 to +0.8 V; electrolyte: 3M KCl.

3.3.4.2 Effect of electrolyte

To evaluate whether oxygen affects performance of the electrode, CV was also conducted in an oxygen-free solution, as shown in Figure 3.26. The CV curve in the deoxygenated solution is similar to the one in an untreated solution, indicating dissolved oxygen has no influence on the CV response in the chosen potential range.

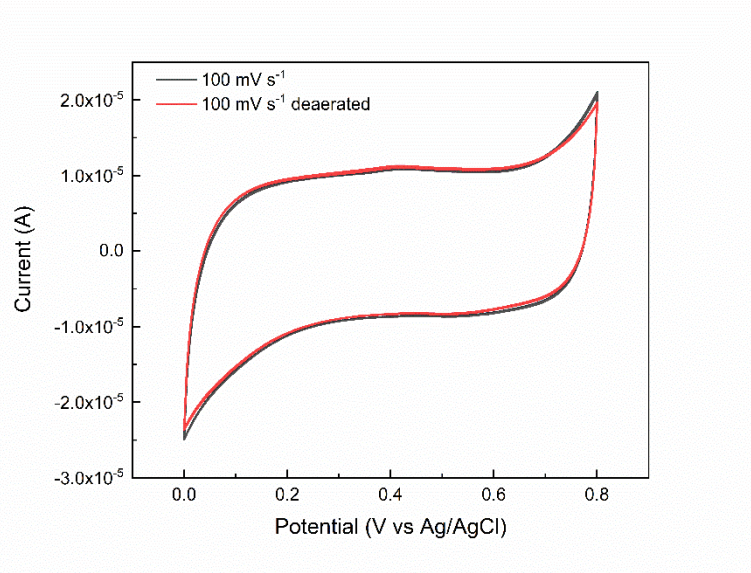

Figure 3.26 Cyclic voltammograms of MnO_2/BDD deposited at +0.85 V for 50 s in an untreated solution (black) and a de-aerated solution (red), respectively. Experimental parameters: scan rate: 100 mV s^{-1}; potential window: 0 to +0.8 V; electrolyte: 3M KCl.

Figure 3.27 shows CVs of the as-deposited electrode in KCl and NaCl solutions with different concentrations. Similar to the CVs of a bare BDD in neutral electrolytes, all CV curves in Figure 3.27 represent typical characteristics of MnO_2 without much difference. No simple correlation between ion mobility, solution viscosity and capacitance is found whilst other factors such as solvation effect, ion-ion interaction and pore size make it more difficult predict the most suitable concentration and electrolyte for a specific material.[39] The difference of the CVs in Figure 3.27 is most likely to be attributed to change of the electrode surface morphology during each CV scan.[40]

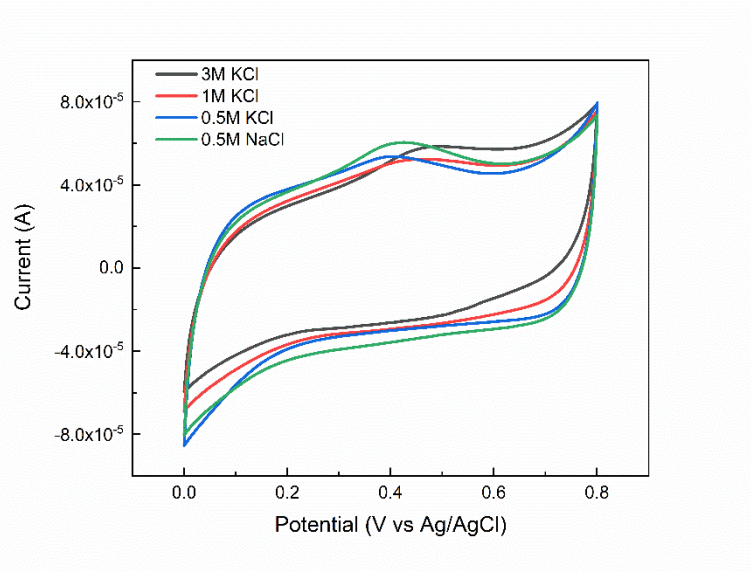

Figure 3.27 Cyclic voltammograms of MnO_2/BDD deposited at +0.85 V for 200 s in four electrolytes. Experimental parameters: scan rate: 100 mV s^{-1}; potential window: 0 to +0.8 V.

3.3.4.3 Effect of scan rate

The effect of scan rate on CV response of the MnO_2/BDD electrodes deposited for 300 s at +0.85 V was investigated over the range 5 – 200 mV s^{-1}, as shown in Figure 3.28. CVs of MnO_2/BDD electrodes deposited at different times (50 – 600 s) are shown in Figure A.1 (Appendix). In Figure 3.28, the current rises with scan rate for the MnO_2/BDD electrode. The electrode starts exhibiting deviation from ideal pseudocapacitive behaviour at higher scan rate in Fig 3.28 (b). Nevertheless, most cyclic voltammograms retain quasi-rectangular shapes and display remarkable rate performance. For example, The C_g value is 142.9 F g^{-1} at 5 mV s^{-1} and retains 141.2 F g^{-1} at 200 mV s^{-1} with 98.8 % retention of the capacitance in the 300 s deposition. The gravimetric specific capacitance is listed in Table 3.3. The C_g value reached up to 178.3 F g^{-1} at 5 mV s^{-1} with 50 s deposition, while it fell to 104.3 F g^{-1} at 200 mV s^{-1} with 600 s deposition. As mentioned above, the capacitance eventually deteriorated when the MnO_2 loading passed an optimal amount due to the poor electrical conductivity of MnO_2 (10^{-5} – 10^{-6} S cm^{-1}).[11, 38, 41] The insulating property of bulk MnO_2 is the main drawback for MnO_2 based

composite electrodes as it blocks ion transport within the electrode and increases the charge transfer resistance.[18]

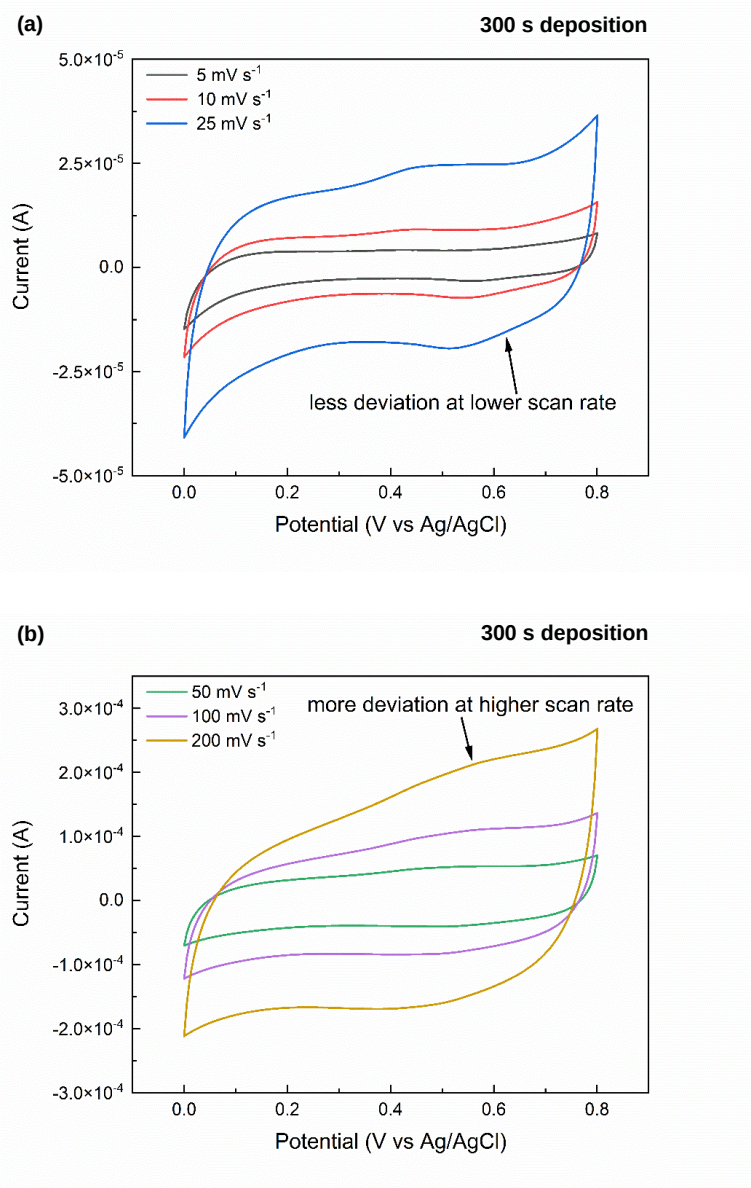

Figure 3.28 Cyclic voltammograms of MnO_2/BDD deposited for 300 s at +0.85 V at scan rate of (a) 5, 10, 25 and (b) 50, 100 and 200 mV s^{-1}, respectively. Experimental parameters: electrolyte: 3M KCl; potential window: 0 to +0.8 V. Less deviation and more rectangular shapes at lower scan rate in (a), while more deviation and less rectangular shapes at higher scan rate in (b).

Table 3.3 Gravimetric specific capacitance (F g^{-1}) of MnO_2/BDD electrodes with different deposition time from 50 to 600 s at +0.85 V calculated from CVs at 5 – 200 mV s^{-1}.

Scan rate	Deposition time (s)					
(mV s^{-1})	50	100	200	300	400	600
5	178.3	163.6	146.7	142.9	129.9	127.0
10	161.3	151.3	144.4	145.9	133.0	130.4
25	134.2	143.6	145.8	148.6	135.4	131.0
50	128.5	145.6	150.0	151.7	136.7	129.0
100	128.7	149.5	152.1	150.2	132.8	120.8
200	130.9	151.6	149.0	141.2	121.1	104.3

An empirical equation $i = av^b$, or $log_{10}\ i = log_{10}\ a + b\ log_{10}\ v$, can be used to decide the mechanism of the electrochemical system in CV measurements, where *a* and *b* are adjustable parameters, *i* is the peak current, and *v* is the scan rate. The *b*-value is determined from the slope of the $log_{10}\ i$ versus $log_{10}\ v$ plot, as shown in Figure 3.29. If $b = 0.5$, a diffusion-controlled mechanism (e.g., faradaic battery-type processes) is indicated. In contrast, a *b*-value of 1 represents a near-surface process (i.e., surface-controlled mechanism), such as non-faradaic capacitive behaviour in EDLCs and fast faradaic redox reactions in pseudocapacitors.[42] The *b*-value is used to distinguish pseudocapacitive materials (e.g., MnO_2) from battery-type electrodes (e.g., $LiCoO_2$ and $LiFePO_4$). Figure 3.29 shows that the slope of the plot of $log_{10}\ (i)$ against $log_{10}\ (v)$ is 1.033, which is close to 1 rather than 0.5. Therefore, the electrochemical behaviour of the MnO_2/BDD electrode has a surface-controlled mechanism due to the contribution from the pseudocapacitive material, MnO_2.

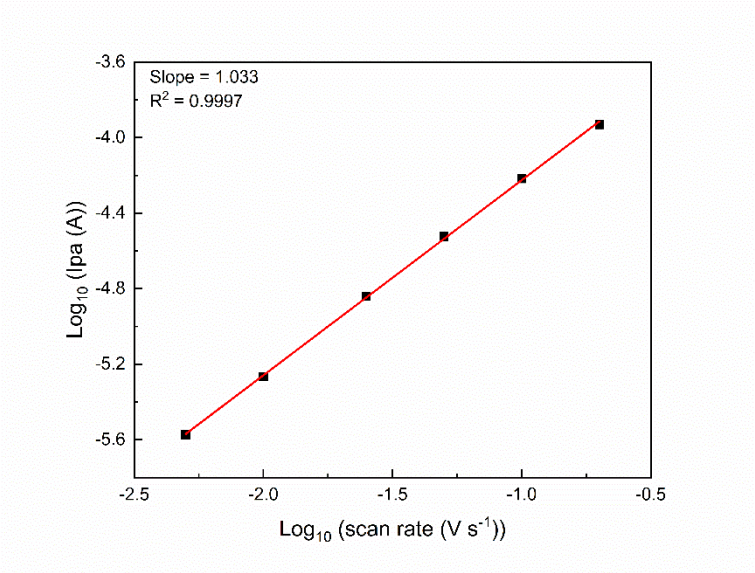

Figure 3.29 The common logarithm of anodic peak current of MnO_2/BDD electrode deposited at +0.85 V vs Ag/AgCl for 200 s as a function of $\log_{10}$ (scan rate).

3.3.4.4 Effect of cycling

Long-term cycling is another essential factor which determines the performance of a supercapacitor in practical applications.[38] The cycling stability of the MnO_2/BDD electrode was recorded in CV at a high scan rate of 100 mV s^{-1}. Figure 3.30 shows that the CV curve changed slightly during the first 200 cycles and then remained stable up to 2000 cycles. 84.5% of the initial capacitance was retained after 2000 cycles, as shown in Figure 3.31. Degradation of the capacitance is mainly due to weak binding between the BDD substrate and deposited MnO_2.[11]

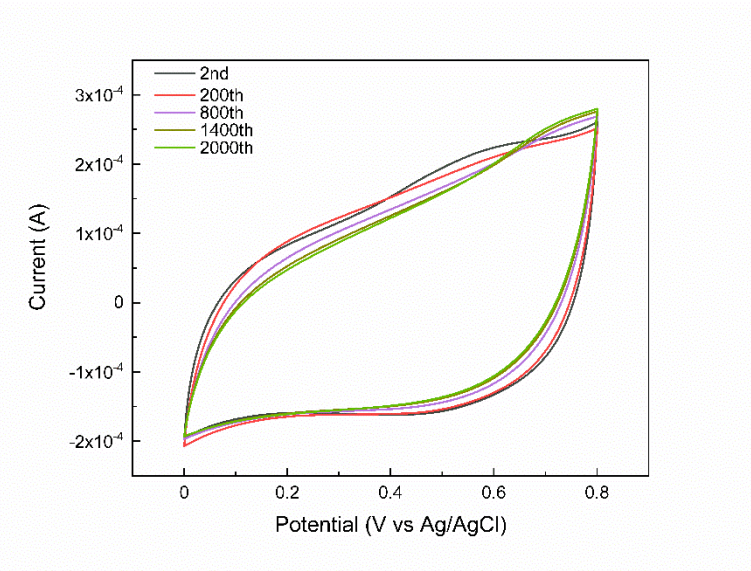

Figure 3.30 Cyclic voltammograms of MnO_2/BDD deposited at +0.85 V for 600 s. Experimental parameters: electrolyte: 3M KCl; potential window: 0 to +0.8 V; scan rate: 100 mV s^{-1} for 2000 cycles.

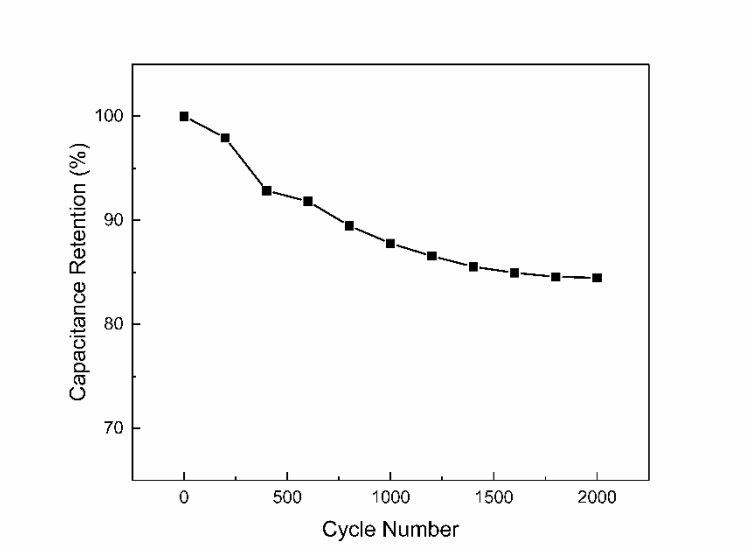

Figure 3.31 Capacitance retention of MnO_2/BDD deposited at +0.85 V for 600 s. Experimental parameters: electrolyte: 3M KCl; potential window: 0 to +0.8 V; scan rate: 100 mV s^{-1} for 2000 cycles.

3.4 Conclusion and comparison

The areal specific capacitance of MnO_2/BDD (0.12 – 3.8 mF cm^{-2}) in this work is larger than most of the conductive diamond based EDLCs reported (0.10 – 0.84 mF cm^{-2}), as the benefits of pseudocapacitive MnO_2 deposition.[15] Meanwhile, the gravimetric specific capacitance result (up to 218 F g^{-1}) is better than some other MnO_2 or carbon-based composite materials (e.g., Mn/Pb mixed oxides 185 F g^{-1}, MnO_2/nanographite 120 – 160 F g^{-1}, MnO_2/CNTs 80 – 200 F g^{-1}), but is poorer than some MnO_2/conducting polymer electrodes (e.g., MnO_2/polyaniline 715 F g^{-1}, MnO_2/polypyrrole 620 F g^{-1}).[43, 44] However, the MnO_2/BDD electrode keeps stable at a level of 84.5% capacitance retention after 2000 cycles, which is more competitive in practical supercapacitor applications than other BDD or MnO_2/conducting polymer-based materials with high capacitance value (~ 70% – 80% capacitance retention after 500 – 1000 cycles).[11, 44] Furthermore, it should be noted that the BDD electrode only acted as a conductive substrate with subtle background effects/contributions, and the specific capacitance would not be raised continuously by increasing MnO_2 mass loading due to its poor electrical conductivity.

In this chapter, the electrochemical behaviour of boron-doped diamond electrodes was investigated first. As a remarkable electrode for electrochemical sensing applications, the features of negligible capacitive current, high stability and wide potential window enable itself for studies of electrochemical energy applications. Electrochemical oxidation of Mn^{2+} ions on BDD electrodes was then carried out via cyclic voltammetry, leading to the formation of MnO_2 in multiple chemical and electrochemical steps. To improve the performance of energy storage devices, MnO_2/BDD pseudocapacitors were fabricated by depositing MnO_2 on diamond potentiostatically. The successful deposition of MnO_2 was confirmed by various characterisation techniques such as SEM and XPS. Effects of deposition potential, deposition time, electrolyte, scan rate and cycling were also studied. In the future, use of novel carbon

materials with porous and conductive nanostructure, and incorporation of other metal elements, including cobalt, iron, and nickel can be conducted to construct supercapacitors with enhanced performance.

References

(1) Yang, N.; Zhao, G.; Foord, J. S. *Nanocarbon Electrochemistry*; Wiley, 2020.

(2) Almeida, E. C.; Trava-Airoldi, V. J.; Ferreira, N. G.; Rosolen, J. M. Electrochemical insertion of lithium into a doped diamond film grown on carbon felt substrates. *Diamond and Related Materials* **2005**, *14* (10), 1673-1677. DOI: https://doi.org/10.1016/j.diamond.2005.06.004.

(3) Lyu, X.; Hu, J.; Foord, J. S.; Wang, Q. A novel electroless method to prepare a platinum electrocatalyst on diamond for fuel cell applications. *Journal of Power Sources* **2013**, *242*, 631-637. DOI: https://doi.org/10.1016/j.jpowsour.2013.05.057. Eguiluz, K. I. B.; Peralta-Hernández, J. M.; Hernández-Ramírez, A.; Guzmán-Mar, J. L.; Hinojosa-Reyes, L.; Martínez-Huitle, C. A.; Salazar-Banda, G. R. The Use of Diamond for Energy Conversion System Applications: A Review. *International Journal of Electrochemistry* **2012**, *2012*, 675124. DOI: 10.1155/2012/675124.

(4) González-González, I.; Tryk, D. A.; Cabrera, C. R. Polycrystalline boron-doped diamond films as supports for methanol oxidation electrocatalysts. *Diamond and Related Materials* **2006**, *15* (2), 275-278. DOI: https://doi.org/10.1016/j.diamond.2005.08.037. Mavrokefalos, C. K.; Hasan, M.; Rohan, J. F.; Foord, J. S. Enhanced Mass Activity and Stability of Bimetallic Pd-Ni Nanoparticles on Boron-Doped Diamond for Direct Ethanol Fuel Cell Applications. *ChemElectroChem* **2018**, *5* (3), 455-463. DOI: https://doi.org/10.1002/celc.201701105. Salazar-Banda, G. R.; Eguiluz, K. I. B.; Avaca, L. A. Boron-doped diamond powder as catalyst support for fuel cell applications. *Electrochemistry Communications* **2007**, *9* (1), 59-64. DOI: https://doi.org/10.1016/j.elecom.2006.08.038. Spătaru, T.; Marcu, M.; Spătaru, N. Electrocatalytic and photocatalytic activity of Pt–TiO2 films on boron-doped diamond substrate. *Applied Surface Science* **2013**, *269*, 171-174. DOI: https://doi.org/10.1016/j.apsusc.2012.09.121. Salazar-Banda, G. R.; Suffredini, H. B.;

Calegaro, M. L.; Tanimoto, S. T.; Avaca, L. A. Sol–gel-modified boron-doped diamond surfaces for methanol and ethanol electro-oxidation in acid medium. *Journal of Power Sources* **2006**, *162* (1), 9-20. DOI: https://doi.org/10.1016/j.jpowsour.2006.06.045.

(5) Samad, S.; Loh, K. S.; Wong, W. Y.; Lee, T. K.; Sunarso, J.; Chong, S. T.; Wan Daud, W. R. Carbon and non-carbon support materials for platinum-based catalysts in fuel cells. *International Journal of Hydrogen Energy* **2018**, *43* (16), 7823-7854. DOI: https://doi.org/10.1016/j.ijhydene.2018.02.154.

(6) Xu, J.; Natsui, K.; Naoi, S.; Nakata, K.; Einaga, Y. Effect of doping level on the electrochemical reduction of CO2 on boron-doped diamond electrodes. *Diamond and Related Materials* **2018**, *86*, 167-172. DOI: https://doi.org/10.1016/j.diamond.2018.04.028.

(7) Roy, N.; Hirano, Y.; Kuriyama, H.; Sudhagar, P.; Suzuki, N.; Katsumata, K.-i.; Nakata, K.; Kondo, T.; Yuasa, M.; Serizawa, I.; et al. Boron-doped diamond semiconductor electrodes: Efficient photoelectrochemical CO2 reduction through surface modification. *Scientific Reports* **2016**, *6* (1), 38010. DOI: 10.1038/srep38010.

(8) Roy, N.; Shibano, Y.; Terashima, C.; Katsumata, K.-i.; Nakata, K.; Kondo, T.; Yuasa, M.; Fujishima, A. Ionic-Liquid-Assisted Selective and Controlled Electrochemical CO2 Reduction at Cu-Modified Boron-Doped Diamond Electrode. *ChemElectroChem* **2016**, *3* (7), 1044-1047. DOI: https://doi.org/10.1002/celc.201600105.

(9) Panglipur, H. S.; Ivandini, T. A.; Wibowo, R.; Einaga, Y. Electroreduction of CO2 using copper-deposited on boron-doped diamond (BDD). *AIP Conference Proceedings* **2016**, *1729* (1). DOI: 10.1063/1.4946950 (acccessed 4/21/2023).

(10) Jiwanti, P. K.; Natsui, K.; Nakata, K.; Einaga, Y. The electrochemical production of C2/C3 species from carbon dioxide on copper-modified boron-doped diamond electrodes. *Electrochimica Acta* **2018**, *266*, 414-419. DOI: https://doi.org/10.1016/j.electacta.2018.02.041.

(11) Yu, S.; Yang, N.; Zhuang, H.; Meyer, J.; Mandal, S.; Williams, O. A.; Lilge, I.; Schönherr, H.; Jiang, X. Electrochemical Supercapacitors from Diamond. *The Journal of Physical Chemistry C* **2015**, *119* (33), 18918-18926. DOI: 10.1021/acs.jpcc.5b04719.

(12) Yu, S.; Yang, N.; Liu, S.; Jiang, X. Diamond supercapacitors: Progress and perspectives. *Current Opinion in Solid State and Materials Science* **2021**, *25* (3), 100922. DOI: https://doi.org/10.1016/j.cossms.2021.100922.

(13) Gu, W.; Yushin, G. Review of nanostructured carbon materials for electrochemical capacitor applications: advantages and limitations of activated carbon, carbide-derived carbon, zeolite-templated carbon, carbon aerogels, carbon nanotubes, onion-like carbon, and graphene. *WIREs Energy and Environment* **2014**, *3* (5), 424-473. DOI: https://doi.org/10.1002/wene.102.

(14) Honda, K.; Rao, T. N.; Tryk, D. A.; Fujishima, A.; Watanabe, M.; Yasui, K.; Masuda, H. Electrochemical Characterization of the Nanoporous Honeycomb Diamond Electrode as an Electrical Double-Layer Capacitor. *Journal of The Electrochemical Society* **2000**, *147* (2), 659. DOI: 10.1149/1.1393249. Gao, F.; Wolfer, M. T.; Nebel, C. E. Highly porous diamond foam as a thin-film micro-supercapacitor material. *Carbon* **2014**, *80*, 833-840. DOI: https://doi.org/10.1016/j.carbon.2014.09.007.

(15) Kondo, T.; Kodama, Y.; Ikezoe, S.; Yajima, K.; Aikawa, T.; Yuasa, M. Porous boron-doped diamond electrodes fabricated via two-step thermal treatment. *Carbon* **2014**, *77*, 783-789. DOI: https://doi.org/10.1016/j.carbon.2014.05.082. Gao, F.; Lewes-Malandrakis, G.; Wolfer, M. T.; Müller-Sebert, W.; Gentile, P.; Aradilla, D.; Schubert, T.; Nebel, C. E. Diamond-coated silicon wires for supercapacitor applications in ionic liquids. *Diamond and Related Materials* **2015**, *51*, 1-6. DOI: https://doi.org/10.1016/j.diamond.2014.10.009. Zhang, J.; Nakai, T.; Uno, M.; Nishiki, Y.; Sugimoto, W. Effect of the boron content on the steam

activation of boron-doped diamond electrodes. *Carbon* **2013**, *65*, 206-213. DOI: https://doi.org/10.1016/j.carbon.2013.08.015.

(16) Spătaru, N.; Zhang, X.; Spătaru, T. a.; Tryk, D. A.; Fujishima, A. Anodic Deposition of RuO[sub x]·nH[sub 2]O at Conductive Diamond Films and Conductive Diamond Powder for Electrochemical Capacitors. *Journal of The Electrochemical Society* **2008**, *155* (1), D73. DOI: 10.1149/1.2804379.

(17) Gao, F.; Nebel, C. E. Diamond nanowire forest decorated with nickel hydroxide as a pseudocapacitive material for fast charging–discharging. *physica status solidi (a)* **2015**, *212* (11), 2533-2538. DOI: https://doi.org/10.1002/pssa.201532131. Mieko da Silva, L.; Alves de Lima Almeida, D.; Oishi, S. S.; Couto, A. B.; Ferreira, N. G. Constituent material influence on the electrochemical performance and supercapacitance of PAni/diamond/CF composite. *Materials Science and Engineering B, Solid-State Materials for Advanced Technology* **2018**, 249-260. DOI: DOI:101016/jmseb201712004.

(18) Wei, W.; Cui, X.; Chen, W.; Ivey, D. G. Manganese oxide-based materials as electrochemical supercapacitor electrodes. *Chem Soc Rev* **2011**, *40* (3), 1697-1721. DOI: 10.1039/c0cs00127a From NLM.

(19) Shpilevaya, I.; Smirnov, W.; Hirsz, S.; Yang, N.; Nebel, C. E.; Foord, J. S. Nanostructured diamond decorated with Pt particles: preparation and electrochemistry. *RSC Advances* **2014**, *4* (2), 531-537, 10.1039/C3RA43763A. DOI: 10.1039/C3RA43763A.

(20) Liljeroth, P.; Johans, C.; Slevin, C. J.; Quinn, B. M.; Kontturi, K. Micro ring–disk electrode probes for scanning electrochemical microscopy. *Electrochemistry Communications* **2002**, *4* (1), 67-71. DOI: https://doi.org/10.1016/S1388-2481(01)00276-4.

(21) Limon-Petersen, J. G.; Han, J. T.; Rees, N. V.; Dickinson, E. J. F.; Streeter, I.; Compton, R. G. Quantitative Voltammetry in Weakly Supported Media. Chronoamperometric Studies on Diverse One Electron Redox Couples Containing Various Charged Species: Dissecting

Diffusional and Migrational Contributions and Assessing the Breakdown of Electroneutrality. *The Journal of Physical Chemistry C* **2010**, *114* (5), 2227-2236. DOI: 10.1021/jp9097149.

(22) Chen, P.; McCreery, R. L. Control of Electron Transfer Kinetics at Glassy Carbon Electrodes by Specific Surface Modification. *Analytical Chemistry* **1996**, *68* (22), 3958-3965. DOI: 10.1021/ac960492r.

(23) Weng, Y.-T.; Pan, H.-A.; Lee, R.-C.; Huang, T.-Y.; Chu, Y.; Lee, J.-F.; Sheu, H.-S.; Wu, N.-L. Spatially Confined MnO2 Nanostructure Enabling Consecutive Reversible Charge Transfer from Mn(IV) to Mn(II) in a Mixed Pseudocapacitor-Battery Electrode. *Advanced Energy Materials* **2015**, *5* (18), 1500772. DOI: https://doi.org/10.1002/aenm.201500772.

(24) Hong, M. S.; Lee, S. H.; Kim, S. W. Use of KCl Aqueous Electrolyte for 2 V Manganese Oxide/Activated Carbon Hybrid Capacitor. *Electrochemical and Solid-State Letters* **2002**, *5* (10), A227. DOI: 10.1149/1.1506463. Lee, H. Y.; Goodenough, J. B. Supercapacitor Behavior with KCl Electrolyte. *Journal of Solid State Chemistry* **1999**, *144* (1), 220-223. DOI: https://doi.org/10.1006/jssc.1998.8128.

(25) Shigemitsu, T.; Matsumoto, G.; Tsukahara, S. Electrical properties of glassy-carbon electrodes. *Medical and Biological Engineering and Computing* **1979**, *17* (4), 465-470. DOI: 10.1007/BF02447059.

(26) Mavrokefalos, C. K.; Nelson, G. W.; Poll, C. G.; Compton, R. G.; Foord, J. S. Electrochemical aspects of Pt–Cu and Cu modified boron-doped diamond. *physica status solidi (a)* **2015**, *212* (11), 2559-2567. DOI: https://doi.org/10.1002/pssa.201532163.

(27) Kumar, S. R. S.; Hedhili, M. N.; Alshareef, H. N.; Kasiviswanathan, S. Correlation of Mn charge state with the electrical resistivity of Mn doped indium tin oxide thin films. *Applied Physics Letters* **2010**, *97* (11), 111909. DOI: 10.1063/1.3481800.

(28) Cerrato, J. M.; Hochella, M. F.; Knocke, W. R.; Dietrich, A. M.; Cromer, T. F. Use of XPS to Identify the Oxidation State of Mn in Solid Surfaces of Filtration Media Oxide

Samples from Drinking Water Treatment Plants. *Environmental Science & Technology* **2010**, *44* (15), 5881-5886. DOI: 10.1021/es100547q.

(29) Broughton, J. N.; Brett, M. J. Variations in MnO2 electrodeposition for electrochemical capacitors. *Electrochimica Acta* **2005**, *50* (24), 4814-4819. DOI: https://doi.org/10.1016/j.electacta.2005.03.006. Perrin, D. D. 421. The hydrolysis of manganese(II) ion. *Journal of the Chemical Society (Resumed)* **1962**, (0), 2197-2200, 10.1039/JR9620002197. DOI: 10.1039/JR9620002197.

(30) Rodrigues, S.; Shukla, A. K.; Munichandraiah, N. A cyclic voltammetric study of the kinetics andmechanism of electrodeposition of manganese dioxide. *Journal of Applied Electrochemistry* **1998**, *28* (11), 1235-1241. DOI: 10.1023/A:1003472901760. Duarte, M. M. E.; Pilla, A. S.; Mayer, C. E. Electrooxidation of Mn(II) to MnO2 on graphite fibre electrodes. *Journal of Applied Electrochemistry* **2003**, *33* (5), 387-392. DOI: 10.1023/A:1024411515902. Yi, C.; Majid, S. The Electrochemical Performance of Deposited Manganese Oxide-Based Film as Electrode Material for Electrochemical Capacitor Application. 2018.

(31) Nijjer, S.; Thonstad, J.; Haarberg, G. M. Oxidation of manganese(II) and reduction of manganese dioxide in sulphuric acid. *Electrochimica Acta* **2000**, *46* (2), 395-399. DOI: https://doi.org/10.1016/S0013-4686(00)00597-1.

(32) McBeath, S. T.; Wilkinson, D. P.; Graham, N. J. D. Advanced electrochemical oxidation for the simultaneous removal of manganese and generation of permanganate oxidant. *Environmental Science: Water Research & Technology* **2020**, *6* (9), 2405-2415, 10.1039/D0EW00261E. DOI: 10.1039/D0EW00261E.

(33) Pourbaix, M. *Atlas of electrochemical equilibria in aqueous solutions*; Pergamon Press, 1966.

(34) Toupin, M.; Brousse, T.; Bélanger, D. Charge Storage Mechanism of MnO2 Electrode Used in Aqueous Electrochemical Capacitor. *Chemistry of Materials* **2004**, *16* (16), 3184-3190. DOI: 10.1021/cm049649j.

(35) Petitpierre, J. P.; Comninellis, C.; Plattner, E. Oxydation Du MnSO4 en dioxyde de manganese dans H2SO4 30%. *Electrochimica Acta* **1990**, *35* (1), 281-287. DOI: https://doi.org/10.1016/0013-4686(90)85071-T.

(36) Chang, J.-K.; Tsai, W.-T. Material Characterization and Electrochemical Performance of Hydrous Manganese Oxide Electrodes for Use in Electrochemical Pseudocapacitors. *Journal of The Electrochemical Society* **2003**, *150* (10), A1333. DOI: 10.1149/1.1605744. Chigane, M.; Ishikawa, M. Manganese Oxide Thin Film Preparation by Potentiostatic Electrolyses and Electrochromism. *Journal of The Electrochemical Society* **2000**, *147* (6), 2246. DOI: 10.1149/1.1393515. Hu, C.-C.; Tsou, T.-W. Ideal capacitive behavior of hydrous manganese oxide prepared by anodic deposition. *Electrochemistry Communications* **2002**, *4* (2), 105-109. DOI: https://doi.org/10.1016/S1388-2481(01)00285-5.

(37) Augustyn, V.; Simon, P.; Dunn, B. Pseudocapacitive oxide materials for high-rate electrochemical energy storage. *Energy & Environmental Science* **2014**, *7* (5), 1597-1614, 10.1039/C3EE44164D. DOI: 10.1039/C3EE44164D.

(38) Yu, Z.; Duong, B.; Abbitt, D.; Thomas, J. Energy Storage: Highly Ordered MnO2 Nanopillars for Enhanced Supercapacitor Performance (Adv. Mater. 24/2013). *Advanced Materials* **2013**, *25* (24), 3301-3301. DOI: https://doi.org/10.1002/adma.201370160.

(39) Fic, K.; Lota, G.; Meller, M.; Frackowiak, E. Novel insight into neutral medium as electrolyte for high-voltage supercapacitors. *Energy & Environmental Science* **2012**, *5* (2), 5842-5850, 10.1039/C1EE02262H. DOI: 10.1039/C1EE02262H. Forse, A. C.; Merlet, C.; Griffin, J. M.; Grey, C. P. New Perspectives on the Charging Mechanisms of

Supercapacitors. *Journal of the American Chemical Society* **2016**, *138* (18), 5731-5744. DOI: 10.1021/jacs.6b02115.

(40) Song, M.-K.; Cheng, S.; Chen, H.; Qin, W.; Nam, K.-W.; Xu, S.; Yang, X.-Q.; Bongiorno, A.; Lee, J.; Bai, J.; et al. Anomalous Pseudocapacitive Behavior of a Nanostructured, Mixed-Valent Manganese Oxide Film for Electrical Energy Storage. *Nano Letters* **2012**, *12* (7), 3483-3490. DOI: 10.1021/nl300984y.

(41) Lang, X.; Hirata, A.; Fujita, T.; Chen, M. Nanoporous metal/oxide hybrid electrodes for electrochemical supercapacitors. *Nature Nanotechnology* **2011**, *6* (4), 232-236. DOI: 10.1038/nnano.2011.13.

(42) Bard, A. J.; Faulkner, L. R. *Electrochemical Methods: Fundamentals and Applications, 2nd Edition*; John Wiley & Sons, Incorporated, 2000. Compton, R. G.; Banks, C. E. *Understanding Voltammetry (Third Edition)*; World Scientific Publishing Company, 2018. Jayachandran, M.; Rose, A.; Maiyalagan, T.; Poongodi, N.; Vijayakumar, T. Effect of various aqueous electrolytes on the electrochemical performance of α-MnO2 nanorods as electrode materials for supercapacitor application. *Electrochimica Acta* **2021**, *366*, 137412. DOI: https://doi.org/10.1016/j.electacta.2020.137412.

(43) Kim, H.; Popov, B. N. Synthesis and Characterization of MnO2-Based Mixed Oxides as Supercapacitors. *Journal of The Electrochemical Society* **2003**, *150* (3), D56. DOI: 10.1149/1.1541675. Wan, C.; Azumi, K.; Konno, H. Hydrated Mn(IV) oxide-exfoliated graphite composites for electrochemical capacitor. *Electrochimica Acta* **2007**, *52* (9), 3061-3066. DOI: https://doi.org/10.1016/j.electacta.2006.09.039. Yan, J.; Fan, Z.; Wei, T.; Qie, Z.; Wang, S.; Zhang, M. Preparation and electrochemical characteristics of manganese dioxide/graphite nanoplatelet composites. *Materials Science and Engineering: B* **2008**, *151* (2), 174-178. DOI: https://doi.org/10.1016/j.mseb.2008.05.018. Wu, Y.-T.; Hu, C.-C. Effects of Electrochemical Activation and Multiwall Carbon Nanotubes on the Capacitive

Characteristics of Thick MnO2 Deposits. *Journal of The Electrochemical Society* **2004**, *151* (12), A2060. DOI: 10.1149/1.1815151. Tan, D. Z. W.; Cheng, H.; Nguyen, S. T.; Duong, H. M. Controlled synthesis of MnO2/CNT nanocomposites for supercapacitor applications. *Materials Technology* **2014**, *29* (sup4), A107-A113. DOI: 10.1179/1753555714Y.0000000175.

(44) Sidhu, N. K.; Rastogi, A. C. Nanoscale Blended MnO2 Nanoparticles in Electro-polymerized Polypyrrole Conducting Polymer for Energy Storage in Supercapacitors. *MRS Online Proceedings Library (OPL)* **2013**, *1552*, 11-16. DOI: 10.1557/opl.2013.667 From Cambridge University Press Cambridge Core. Prasad, K. R.; Miura, N. Polyaniline- MnO2 Composite Electrode for High Energy Density Electrochemical Capacitor. *Electrochemical and Solid-State Letters* **2004**, *7* (11), A425. DOI: 10.1149/1.1805504.

Chapter 4 Carbonised Seaweed Paper for Supercapacitor Applications

A cellulose-derived biomass material, seaweed paper, is utilised as the carbon source in this project. The seaweed paper is first carbonised at various temperatures, which affects the morphology, surface area and pore size of the material. Afterwards, the electrochemical performance of the carbonised seaweed materials is measured by cyclic voltammetry (CV) in two potential ranges (0 to -0.8 V and 0 to +0.8 V vs Ag/AgCl). The highest specific capacitance of 226 F g^{-1} in the negative potential window is obtained whereas the value is 47.9 F g^{-1} in the positive potential window. To improve the performance at the positive potential side, pseudocapacitive MnO_2 is potentiostatically deposited on the carbonised seaweed paper, which raises the specific capacitance of the material to 156 F g^{-1} without obvious loss of stability. Characterisations and electrochemical measurements of the materials including SEM, EDS, XPS, CV, GCD and EIS are carried out. The results show an increase in the overall specific capacitance and hence the possibility of commerciality of the carbon-based materials.

4.1 Introduction

The supply and storage of energy is a key technological challenge for which electrochemical storage devices can play an important role. One important device is the supercapacitor, a device with capacitances typically in the range of 10^3 – 10^4 F offering rapid charge/discharge and repeated cycling.[1] To date, most supercapacitors have been fabricated based on carbon materials, with high surface area and porosity, typically activated carbon, although more recently manufactured nanocarbons such as carbon nanotubes (CNTs) and graphene have attracted considerable interest.[2, 3] The manufacturing processes for these new nanocarbon

materials however lacks scalability and eco-friendliness.[4] An alternative is to obtain carbon materials from natural resources, which are abundant, low cost, and environmentally friendly, and whose processing can be easily automated.[5] Cellulose fibre is an excellent candidate, for which seaweed is of interest since it grows in water and develops rapidly. Seaweed fibres can be converted into conductive carbon materials by a one-step thermal treatment to produce materials with high surface area.[6] Such materials could be ideal for supercapacitor applications where the electric double layer is the basis of the observed capacitance.[7] Nevertheless, nanocarbon materials have certain drawbacks - such as poor performance for the positive electrode, which can be typically addressed by adding pseudocapacitive materials (redox active chemical species) such as RuO_2.[8, 9] The high cost and the toxicity of RuO_2, however, make it less favourable.[10] Meanwhile, other low-cost materials such as MnO_2 have drawn researcher's interest.[9, 10] One purpose of the present project is therefore to investigate the preparation of supercapacitor materials based on thermally treated seaweed paper nanocarbons. The second is to modify the seaweed paper carbon materials with electrochemical deposition of pseudocapacitive MnO_2. The performance of the as-prepared materials as supercapacitors is then measured in electrochemical methods along with other characterisation techniques.

4.2 Experimental

4.2.1 Chemicals and materials

All solutions used as part of this project were prepared from Milli-Q water (resistivity ~ 18.2 MΩ cm at 25 °C). Manganese(II) chloride tetrahydrate [$MnCl_2 \cdot 4H_2O$, ACS reagent, ⩾98%], sodium sulphate [Na_2SO_4, ACS reagent, ⩾99.0%], and potassium chloride [KCl, ACS reagent, 99.0-100.5%] were purchased from Sigma-Aldrich. The precursor solution for deposition was prepared by dissolving 0.1 M $MnCl_2$ and 0.1 M Na_2SO_4 in distilled water. The electrolyte for electrochemical measurements was made of 3 M KCl.

4.2.2 Electrochemical measurements

All electrochemical experiments were performed with an Autolab PGSTAT128N potentiostat/galvanostat (Metrohm Autolab, Utrecht, Netherlands) equipped with Nova software. When a three-electrode configuration was used, it consisted of a Ag/AgCl reference electrode (3M KCl), a Platinum plate counter electrode (1×1 cm^2) and a Platinum current collector holding the sample (cut into 1×1 cm^2) as a working electrode. The carbonised seaweed paper was left to soak in distilled Milli-Q water for 3 days prior to use. CVs were measured at different scan rates of 2, 5, 10, 25, 50, 100 and 200 mV s^{-1} while GCD was carried out at current densities of 0.5, 1, 2.5, 5 and 10 A g^{-1} in 3M KCl.

The specific capacitance calculated from the CV is based on the following equation:

$$C = \frac{\int_{E1}^{E2} I(E)dE}{2(E1-E2)mv} \quad (4\text{-}1)$$

Where *I* is the current, *E* is the voltage, E_1-E_2 is the potential window (-0.8 to 0 V and 0 to +0.8 V), *v* is the scan rate and *m* is the mass of the material.

The specific capacitance calculated from the GCD is based on the following equation:

$$C = \mathrm{I}_m \Delta \mathrm{t}/\Delta \mathrm{V} \quad (4\text{-}2)$$

Where I_m is the discharge current density (A g^{-1}), Δt is the discharging time (s), and ΔV is the potential window of discharge (V).

4.2.3 Preparation of carbonised seaweed paper

The raw seaweed paper used in these experiments were obtained from Marine pulp Co. Korea. Raw seaweed paper was carbonised in a quartz tube reactor installed in a furnace. First, the samples were heated to 600 °C under an inert nitrogen atmosphere for 0.5 h in a pre-treatment step. Afterwards, the temperature was increased with a ramping rate of 5 °C min^{-1} for the

subsequent carbonisation at temperatures of 700 °C, 800 °C, 900 °C, 1000 °C, 1100 °C and 1300 °C. The latter carbonisation procedure lasted for 0.5 h.

4.2.4 Deposition of MnO_2 on carbonised seaweed paper

The carbonised seaweed paper was immersed in the Mn^{2+} precursor solution and a constant positive potential (+1.15 V vs Ag/AgCl) was applied for a fixed time (50 to 1200 s) to deposit MnO_2.

4.3 Results and discussion

4.3.1 Characterisation of carbonised seaweed paper

Morphological characterisation of carbonised seaweed paper was carried out using EDS and SEM while the specific surface area and the average pore size was analysed by BET. The chemical composition of carbonised seaweed paper was determined by both XPS and EDS.

4.3.1.1 Energy-dispersive X-ray spectroscopy

EDS was performed on seaweed paper after the carbonisation process, as shown in the spectrum in Figure 4.1. At a carbonisation temperature of 900 °C, the atomic percentages were 86.98% carbon, 10.74% oxygen, 0.52 % calcium and 1.76 % other elements altogether. Through carbonisation, the percentage of carbon increased whereas the percentage of oxygen decreased.

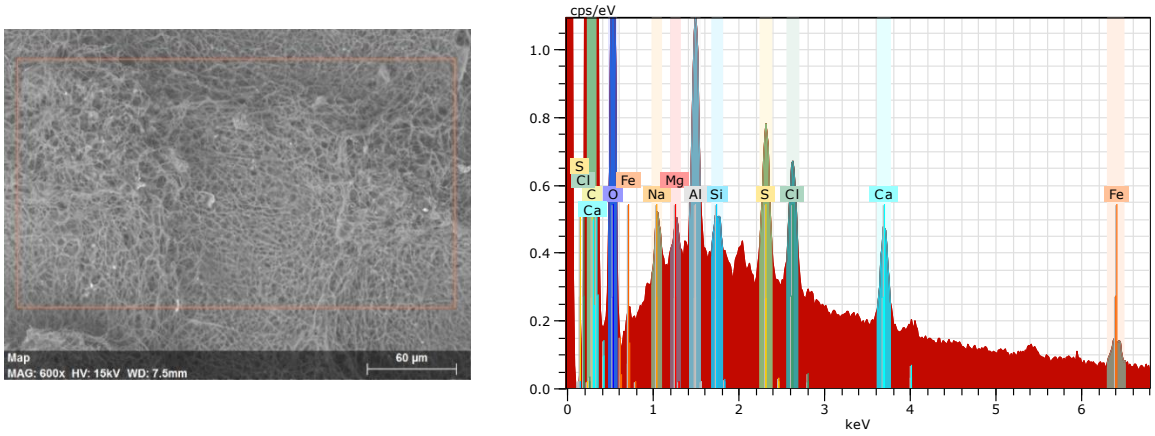

Figure 4.1 EDS images of seaweed paper carbonised at 900 °C.

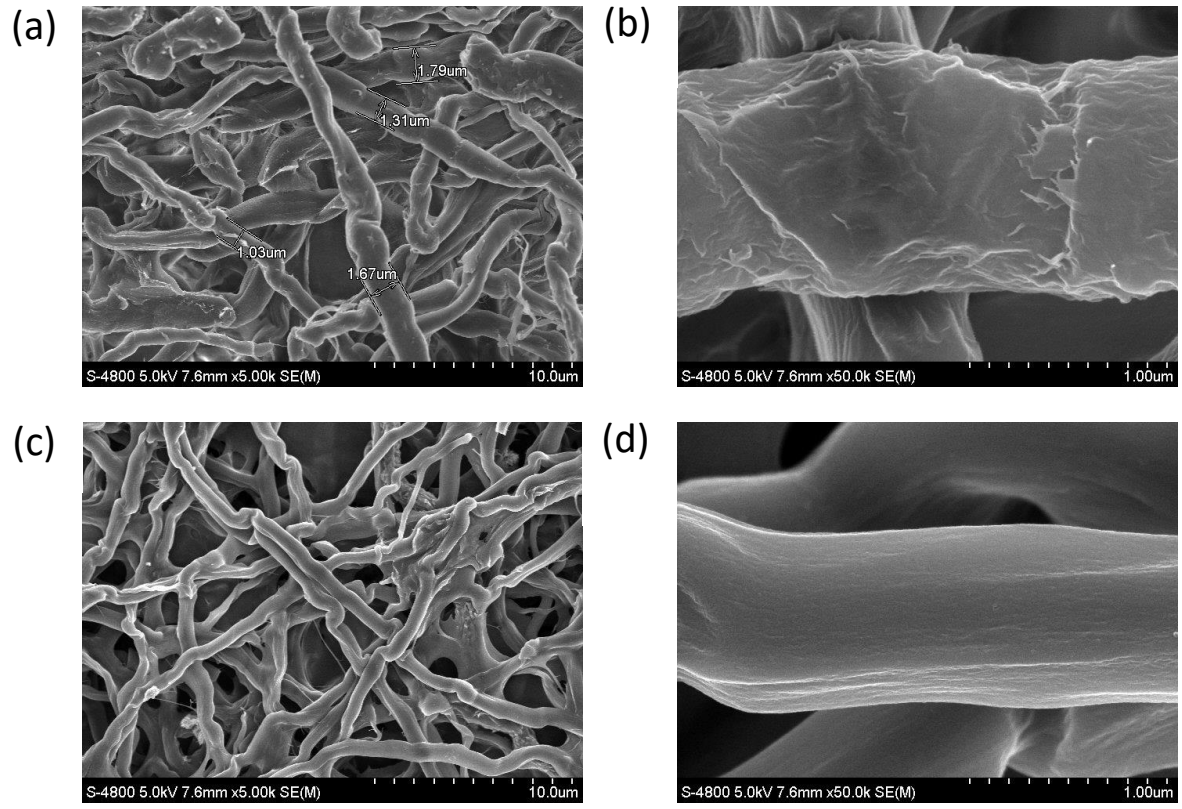

Figure 4.2 SEM images of (a) & (b) raw seaweed paper, and (c) & (d) seaweed paper carbonised at 1300 °C.

4.3.1.2 Scanning electron microscopy

SEM images showed the morphology change of the seaweed paper before and after carbonisation. Before carbonisation, the seaweed paper is made up of a network of rough and thick fibres, as shown in Figure 4.2. The images of seaweed paper after carbonisation showed that the fibres became smoother and thinner, yet the primary structure was not changed.

4.3.1.3 Brunauer-Emmett-Teller Surface Area Analysis

BET analysis of N_2 adsorption isotherms was carried out in order to estimate the surface area and pore size of the carbonised seaweed paper. The results are listed in Table 4.1 below.

Table 4.1 Surface area and pore size of seaweed paper carbonised at different temperatures obtained from BET analysis.

Carbonisation temperature (°C)	700	800	900	1000	1100	1300
Specific surface area (m^2 g^{-1})	277.39	304.34	340.98	89.40	5.30	6.40
Average pore size (nm)	2.1	2.2	2.1	2.8	15.8	15.3

As can be seen from Table 4.1, the surface area of carbonised seaweed paper increases to a maximum at 900 °C and then decreases rapidly. The average pore size starts increasing from 1000 °C and reaches a maximum size of 15.8 nm at 1100 °C, indicating that small pores in the seaweed paper were destructed during carbonisation.[11]

4.3.1.4 X-ray photoelectron spectroscopy

In addition to EDS, the chemical composition of carbonised seaweed paper at 900 °C was also studied using XPS. The survey and the fitted C 1s spectra are shown in Figure 4.3 and 4.4. The presence of carbon and oxygen is confirmed by C 1s and O 1s peaks at 285 eV and 532 eV, respectively. The seaweed paper carbonised at 900 °C is composed of 85.94% carbon, 11.70%

oxygen and 2.36% other impurities. It is confirmed that most of the materials are graphitised carbon with some oxygen containing functional groups after fitting the C 1s spectrum. This is particularly advantageous as other biomass derived materials (e.g., rice husks and coconut shell) contain large numbers of impurities which are difficult to remove.[12] The result is highly consistent with that of EDS, and the slight difference might be attributed to:

1. As seaweed is a natural material and prone to variations, all characterisations may vary for different pieces carbonised at the same temperature.
2. XPS, as a spectroscopic technique, only probes several nanometres into a sample surface whereas the surface area analysed by EDS is on a micrometre order.

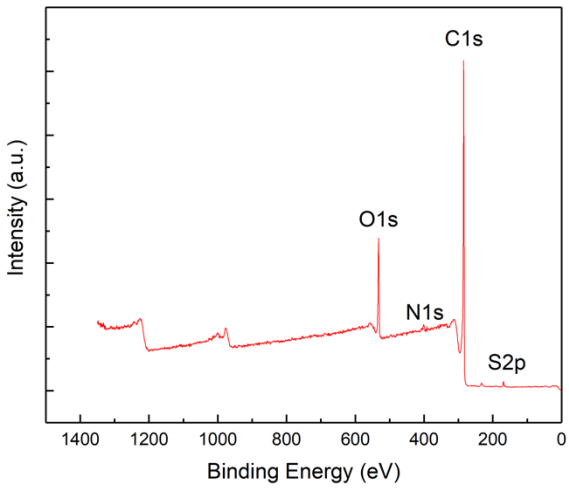

Figure 4.3 XPS survey spectrum of seaweed paper carbonised at 900 °C.

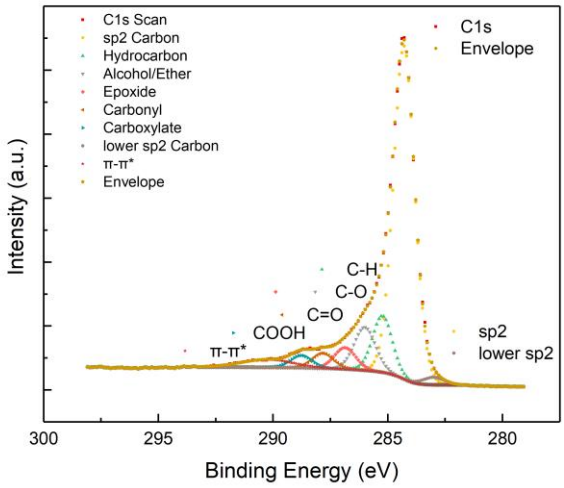

Figure 4.4 Fitting of XPS C 1s spectrum of seaweed paper carbonised at 900 °C.

4.3.2 Wetting effect on carbonised seaweed paper

In order to ensure that the electrolyte ions have maximum access to the pores, carbonised seaweed paper was soaked in distilled water for three days. This process aims to facilitate a higher capacitance, which allows the material to store larger amounts of energy. The seaweed paper carbonised at various temperatures was cut into 1x1 cm^2 and measured by CV. The pieces of seaweed paper were first soaked in water for different lengths of time. A piece of carbonised seaweed paper was then attached to a Pt current collector, and CVs were conducted at 200 mV s^{-1} to study the influence of soaking time on the performance of the material. It was found in Figure 4.5 that leaving the seaweed paper soaking for 72 h was necessary for an improved performance.

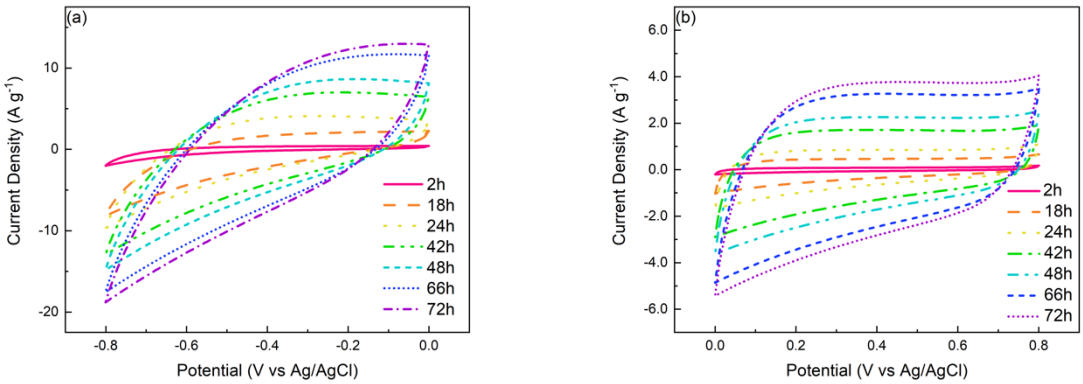

Figure 4.5 Cyclic voltammograms of seaweed paper carbonised at 900 °C at a scan rate of 200 mV s^{-1} with different soaking times in (a) negative and (b) positive potential windows.

4.3.3 Influence of metal current collector

In a commercial supercapacitor, current collectors made of conductive materials such as metal are employed.[13] A platinum-plate holder was used as a current collector here as it is inert, stable and conductive. To study whether the current collector would affect the capacitance performance, a system with the platinum plate only was compared to the one that held the seaweed paper carbonised at 900°C with the current collector, by taking CV scans of both at 200 mV s^{-1} from 0 to -0.8 V and 0 to +0.8 V. From the CV curves in Figure 4.6 it was confirmed that the current holder was making a negligible contribution to the overall capacitance.

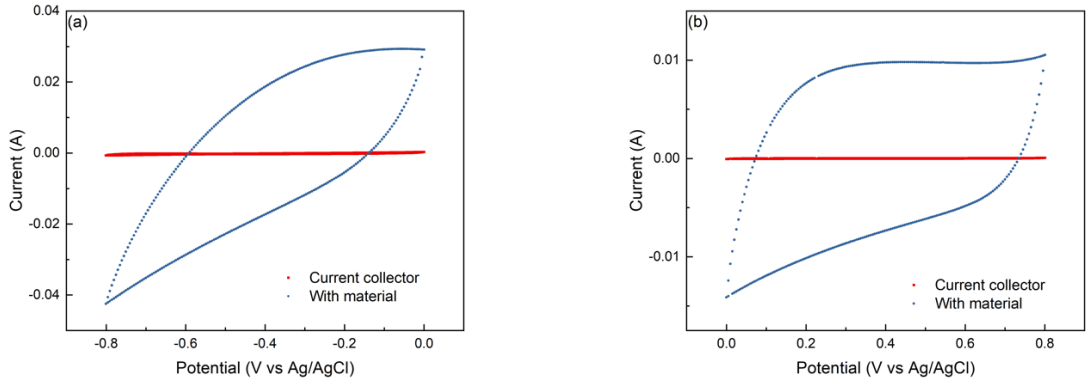

Figure 4.6 CV comparisons of seaweed paper carbonised at 900 °C and only current collector at (a) negative and (b) positive potential ranges at 200 mV s^{-1}.

4.3.4 Seaweed-based supercapacitors in aqueous electrolytes

4.3.4.1 Influence of carbonisation temperature

In supercapacitors, the structure of the carbon material which affects its surface area and porosity is a major factor that determines the specific capacitance.[14] As discussed in the characterisation analysis, the temperature of carbonisation has a significant influence on the structure of the carbonised seaweed paper.

In research on carbonised filter paper materials conducted by L. Jiang et al, filter paper carbonised at increasing temperatures from 600 °C to 1700 °C was studied for supercapacitor applications.[5] The result showed that a specific capacitance of 115.5 F g^{-1} was obtained for the sample carbonised 1500 °C. Nonetheless, a carbonisation temperature of 600 °C led to a specific capacitance of only 3.2 F g^{-1}. Similar to the filter paper, it was presumed that the temperature of carbonisation may well affect the capacitance of supercapacitors produced from carbonised seaweed paper here. Supercapacitors were made from seaweed paper carbonised at 600 °C, 700 °C, 800 °C, 900 °C, 1000 °C, 1100 °C and 1300 °C, and the electrochemical performance of the materials carbonised at various temperature was evaluated by cyclic

voltammetry from 0 to -0.8 V and 0 to +0.8 V, a negative and a positive potential window, as shown in Figure 4.7 (600 °C) and Figure 4.8 (900 °C). CVs of seaweed paper carbonised at other different temperatures (600 to 1300 °C) are shown in Figure A.2 (Appendix).

In general, the current response rises with increasing scan rates for samples carbonised at all temperatures. In Figure 4.7, the sample carbonised at 600 °C displayed a tiny current signal which was mainly attributed to the metal current collector. The material carbonised at 600 °C is neither porous nor conductive to achieve high capacitance. The more pores on the seaweed paper were generated when the carbonisation temperature increased, the more accessible they were by the electrolyte ions to form double-layer capacitance. In addition, the electrical conductivity of the material was improved upon carbonisation, leading to lower resistance and better capacitive performance of the material. However, when the highest temperature of carbonisation was reached, pores inside the material were destructed and it only worked as a smooth and conductive carbon electrode such as graphite and glassy carbon, resulting in low surface area and low capacitance.[11]

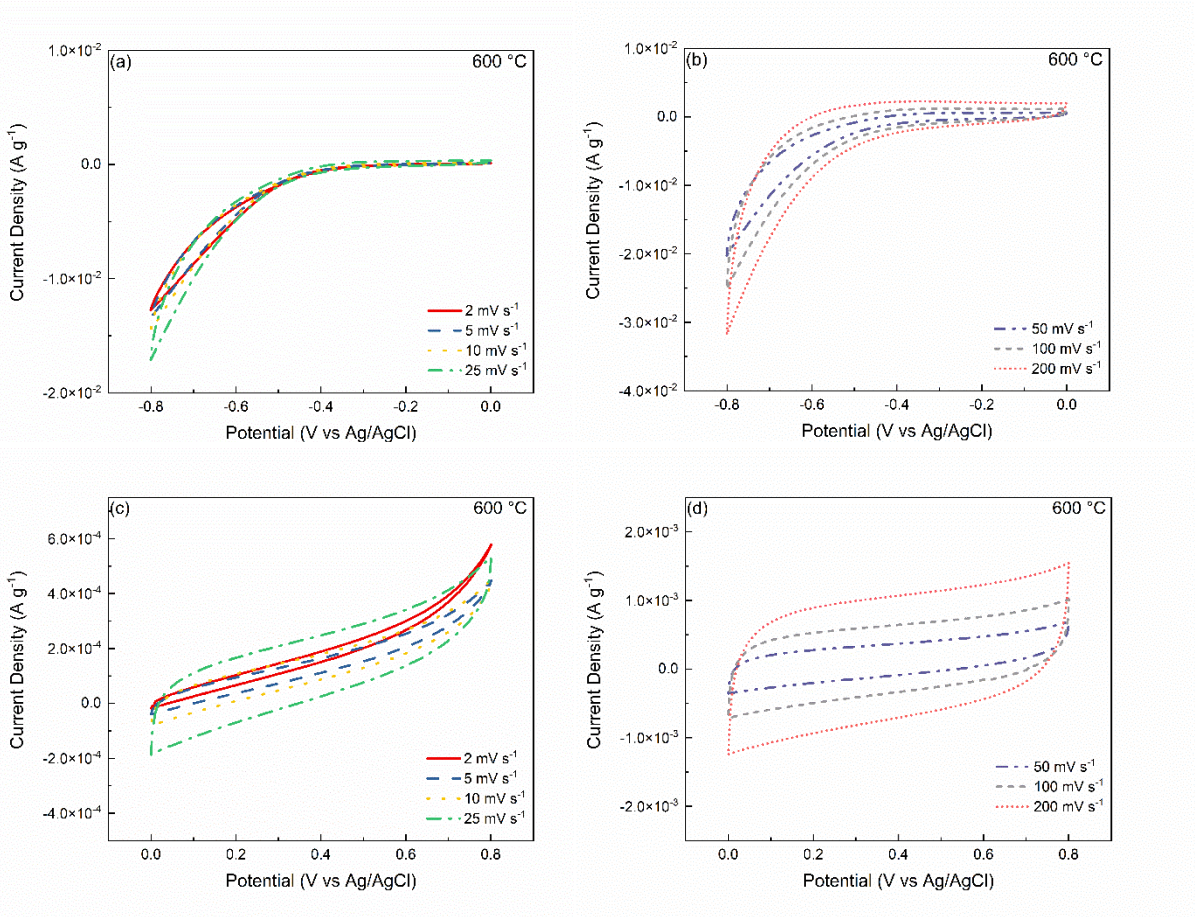

Figure 4.7 CV curves of seaweed paper carbonised at 600 °C with increasing scan rates and two potential windows. (a): 0 to -0.8 V, 2 to 25 mV s^{-1}, low current; (b) 0 to -0.8 V, 50 to 200 mV s^{-1}, increased current compared to (a); (c) 0 to +0.8 V, 2 to 25 mV s^{-1}, low current; (d) 0 to +0.8 V, 50 to 200 mV s^{-1}, increased current compared to (c). Overall, the current response is low in both potential windows and at all scan rates of the sample carbonised at 600 °C.

Figure 4.8 shows CV curves of the seaweed paper carbonised at 900 °C from 0 to -0.8 V and 0 to +0.8 V at different scan rates (2 to 200 mV s^{-1}). At low scan rates (2 to 25 mV s^{-1}), the CVs display ideal capacitive behaviour (quasi-rectangular shape). However, the ideal capacitive behaviour became more irregular with an obvious loss in the specific capacitance when the scan rate was raised (50 to 200 mV s^{-1}).

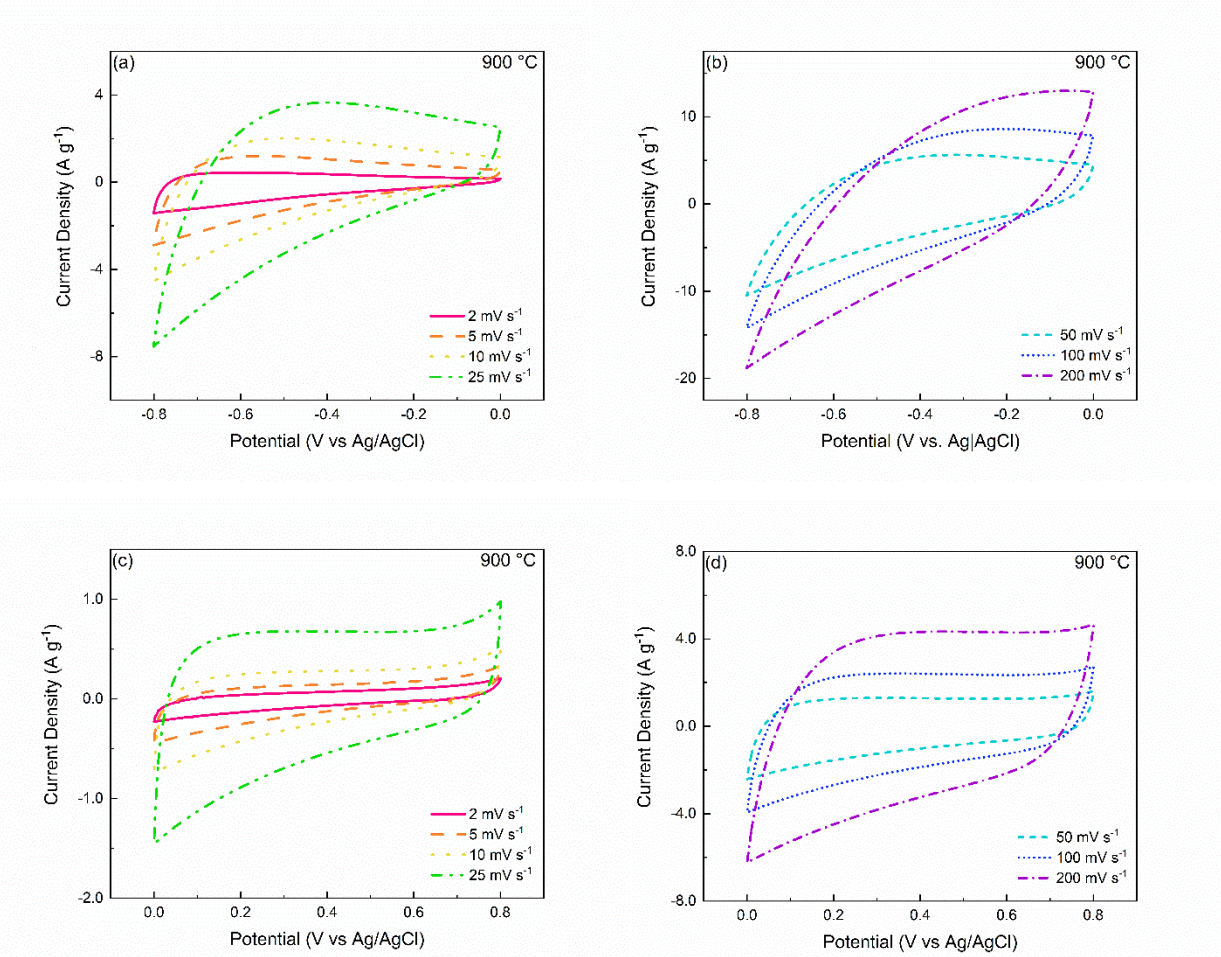

Figure 4.8 CV curves of seaweed paper carbonised at 900 °C with increasing scan rates and two potential windows. (a): 0 to -0.8 V, 2 to 25 mV s^{-1}, high current; (b) 0 to -0.8 V, 50 to 200 mV s^{-1}, increased current compared to (a); (c) 0 to +0.8 V, 2 to 25 mV s^{-1}, high current; (d) 0 to +0.8 V, 50 to 200 mV s^{-1}, increased current compared to (c). Overall, the current response is higher in both potential windows and at all scan rates compared to the sample carbonised at 600 °C. The difference of CVs between the two potential windows will be discussed in detail in 4.3.4.2.

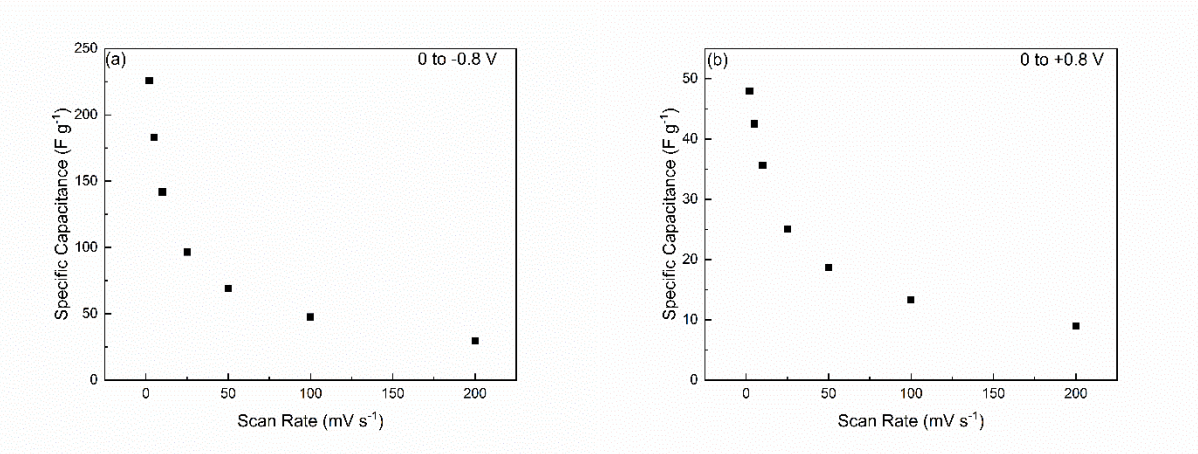

Figure 4.9 Dependency of specific capacitance of the 900 °C seaweed with increasing scan rates (2 to 200 mV s^{-1}) in two potential windows (a) 0 to -0.8 V and (b) 0 to +0.8 V.

The reason why the specific capacitance decreased with increasing scan rate in Figure 4.9 is that transfer of ions is limited to the carbon surface, giving rise to greater inaccessible pore portions of the electrode layer at higher scan rates. The phenomenon is characteristic of all types of EDLC supercapacitors, which reflects the limited mass transfer kinetics within the porous electrode layer.[15]

The structure, properties and electrochemical performance of the carbonised seaweed paper are affected by the temperature of carbonisation, as seen from the results above. Particularly, the specific capacitance of the material changed with carbonisation temperature. The best performance of carbonised seaweed paper was observed at 900 °C which achieved a specific capacitance of 226 F g^{-1} in the negative potential window and 47.9 F g^{-1} in the positive potential window at the scan rate of 2 mV s^{-1}. The values of specific capacitance calculated from the CVs of the materials taken at 2, 5, 10, 25, 50, 100 and 200 mV s^{-1} are listed in Table 4.2 and 4.3 below. The fact that the specific capacitance decreased with increasing scan rate is observed in all samples carbonised at different temperatures (600 to 1300 °C) and both potential windows (0 to -0.8 V and 0 to +0.8 V).

Table 4.2 The specific capacitance of seaweed paper at different carbonisation temperatures in the negative potential window (0 to -0.8V).

	Specific Capacitance/ F g^{-1} at temperature of carbonisation/ °C						
Scan rate/mV s^{-1}	600	700	800	900	1000	1100	1300
2	0.127	24.5	60.7	226	27.0	18.6	0.137
5	0.0488	12.8	54.4	183	24.7	17.1	0.0743
10	0.0323	7.27	46.9	142	23.9	16.2	0.0578
25	0.0246	3.22	34.1	96.5	15.8	15.1	0.0472
50	0.0221	1.63	22.5	69.3	13.9	9.53	0.0413
100	0.0205	0.794	12.6	47.6	12.3	5.32	0.0370
200	0.0167	0.340	6.24	29.7	10.0	2.86	0.0308

Table 4.3 The specific capacitance of seaweed paper at different carbonisation temperatures in the positive potential window (0 to +0.8V).

	Specific Capacitance/ F g^{-1} at temperature of carbonisation/ °C						
Scan rate/mV s^{-1}	600	700	800	900	1000	1100	1300
2	0.00914	5.49	19.5	47.9	4.38	3.31	1.80
5	0.00564	2.00	15.0	42.5	3.50	2.31	1.05
10	0.00496	0.896	10.8	35.6	3.26	1.79	0.626
25	0.0048	0.312	5.45	25.1	3.55	1.18	0.341
50	0.00495	0.163	3.10	18.7	3.93	0.953	0.236
100	0.00533	0.110	1.97	13.3	4.09	0.792	0.174
200	0.00472	0.0711	1.25	8.95	3.62	0.575	0.121

As discussed previously, the results of CVs and characterisation of the carbonised seaweed paper indicated that:

- As the temperature of carbonisation rises, electrical conductivity of the carbonised seaweed paper was boosted, which was advantageous to electron and ion transport. During carbonisation, a fraction of oxygen functional groups was removed, which caused a decrease in the electrical resistance.

- At certain temperatures of carbonisation (800 and 900 °C), large specific surface areas of the material were achieved, and the electrical conductivity was promoted at the same time. The capacitance of carbonised seaweed paper reached a maximum when the electrical conductivity and the specific surface area were appropriately balanced.

- The structure of the carbonised seaweed paper became smoother and most micropores in the carbon were destroyed upon carbonisation at higher temperatures, leading to a decrease in porosity and specific surface area. Although the ions could easily access the surface of the carbonised seaweed paper, a decrease in the specific capacitance was inevitable due to less pores available in spite of the continuous increase in electrical conductivity.

4.3.4.2 Difference between the positive and the negative potential windows

As seen in Figure 4.10, the positive range shows much lower capacitance yet more symmetric and quasi-rectangular CV shapes compared to the results of the negative potential one. The reason is that when a supercapacitor is being charged, cations are adsorbed into the negative electrode whereas anions are desorbed and/or exchanged with cations at the negative electrode.[16] The size of hydrated positively charged ions such as K^+ are smaller than that of hydrated negatively charged ions such as Cl^-, which enables cations to access the smaller micropores in the seaweed paper.[17] Furthermore, some oxygen-containing functional groups in the carbonised seaweed paper such as hydroxyls and carbonyls have greater affinity for cations

than anions, allowing easier diffusion into micropores of the material.[18] Meanwhile, these oxygen functional groups could provide pseudocapacitive contribution due to faradaic processes which could achieve higher capacitance and more asymmetric CV shape on the negative side.[19]

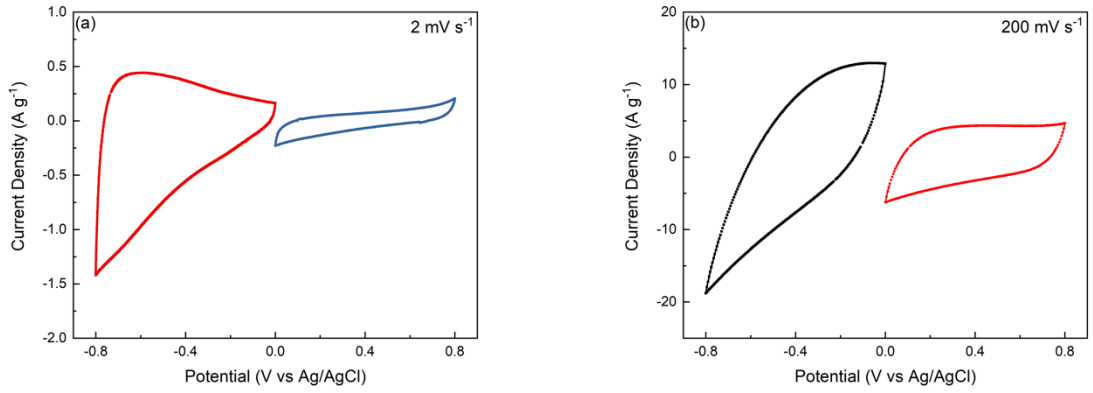

Figure 4.10 CV Comparisons of the 900 °C seaweed paper at (a) 2 mV s^{-1} and (b) 200 mV s^{-1} in different potential ranges.

4.3.5 Electrochemical deposition of manganese dioxide

As seen from the discussion above, the carbonised seaweed paper exhibits higher specific capacitance value in a negative potential window. In order to improve the performance at the positive side, pseudocapacitive material can be incorporated into the carbonised seaweed paper such as transition metal oxides and conductive polymers.[9, 20] Chronoamperometry, a potentiostatic deposition method, was introduced here by immersing the carbon material in a Mn^{2+} precursor solution and applying a constant positive potential for a fixed time to deposit MnO_2.

The method for the deposition has been employed and changed from A J. Saterlay.[21] Manganese chloride precursor was used instead of perchlorate as potassium perchlorate can

cause a solubility issue in long-standing electrochemical analysis when the inner electrolyte of a reference electrode is potassium chloride.[22]

When a positive potential is applied, the electrochemical oxidation of Mn^{2+} occurs on the seaweed paper surface, shown as follows:

$$Mn^{2+} + 2H_2O - 2e^- \rightarrow MnO_2 + 4H^+ \quad (4\text{-}3)$$

Due to the existence of non-faradaic current, current efficiency via this reaction would not reach 100%. The mass of MnO_2 deposited can be calculated by Faraday's law below:

$$m = \Delta Q * M/2F \quad (4\text{-}4)$$

Where ΔQ is the charge Q_1 passed during the deposition subtracts the background charge Q_2 given by non-faradaic current (capacitive current). The background solution consists of 0.2 M KCl + 0.1 M Na_2SO_4 without the 0.1 M $MnCl_2$ precursor, where the addition of 0.2 M KCl aims to keep the same ionic strength for the electrolyte system. M is the molecular weight of MnO_2, which is 86.94 g mol^{-1}, and F is the Faradaic constant, which is 96485 C mol^{-1}.

4.3.5.1 XPS characterisation of carbonised seaweed paper/MnO_2

The chemical composition of electrodeposited MnO_2 on carbonised seaweed paper was examined by XPS, as shown in Figure 4.11. The oxidation state is identified by the binding energy of Mn $2p_{3/2}$ peak at 642 eV and energy splitting of Mn 3s peak of 4.8 eV, which indicates that Mn (IV) was the main component from electrodeposition.[10]

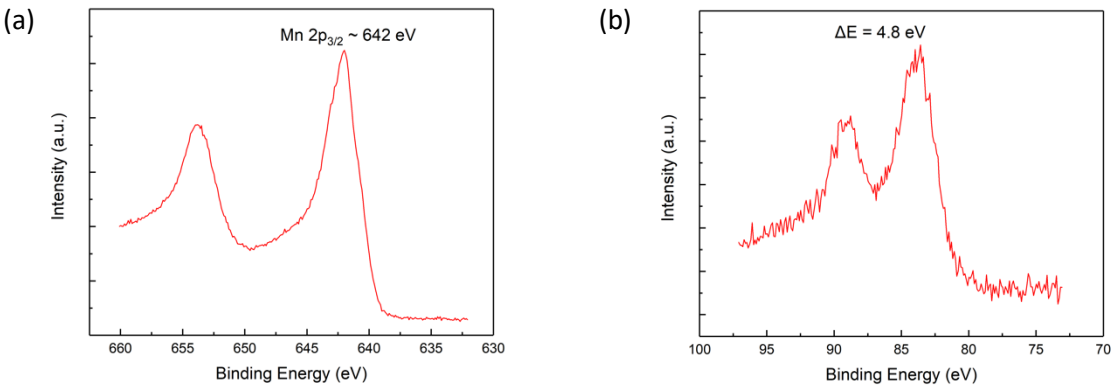

Figure 4.11 XPS (a) Mn 2p and (b) Mn 3s spectra of 900 °C carbonised seaweed paper/MnO_2.

4.3.5.2 FESEM characterisation of carbonised seaweed paper/MnO_2

FESEM images were recorded after deposition, as seen in Figure 4.12. Nanoflower-like MnO_2 were coated onto the skeleton of carbonised seaweed paper when the deposition time was 200 s. For a much longer deposition (1200 s), the material was fully covered by bulk MnO_2 and the carbon structure of the seaweed paper was difficult to observe.

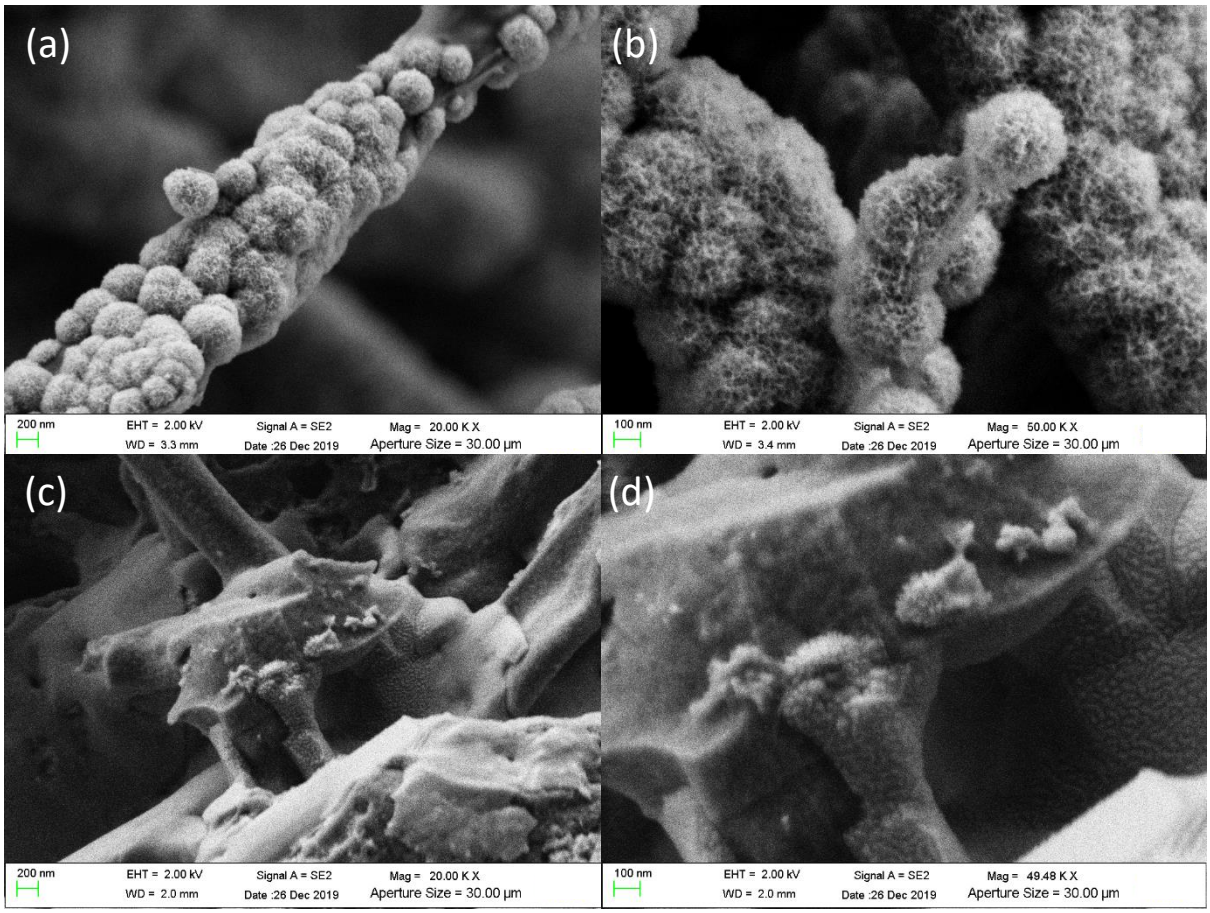

Figure 4.12 FESEM images of 900 °C carbonised seaweed paper/MnO_2 of (a&b) 200s and (c&d) 1200s deposition.

4.3.5.3 EDS characterisation of carbonised seaweed paper/MnO_2

It can also be confirmed from Figure 4.13 that MnO_2 was coated on the carbon structure. The overlap of Mn and O images show that it was metal oxide that was deposited. The percentage of carbon drops dramatically as most atoms were covered by MnO_2 and remained undetected.

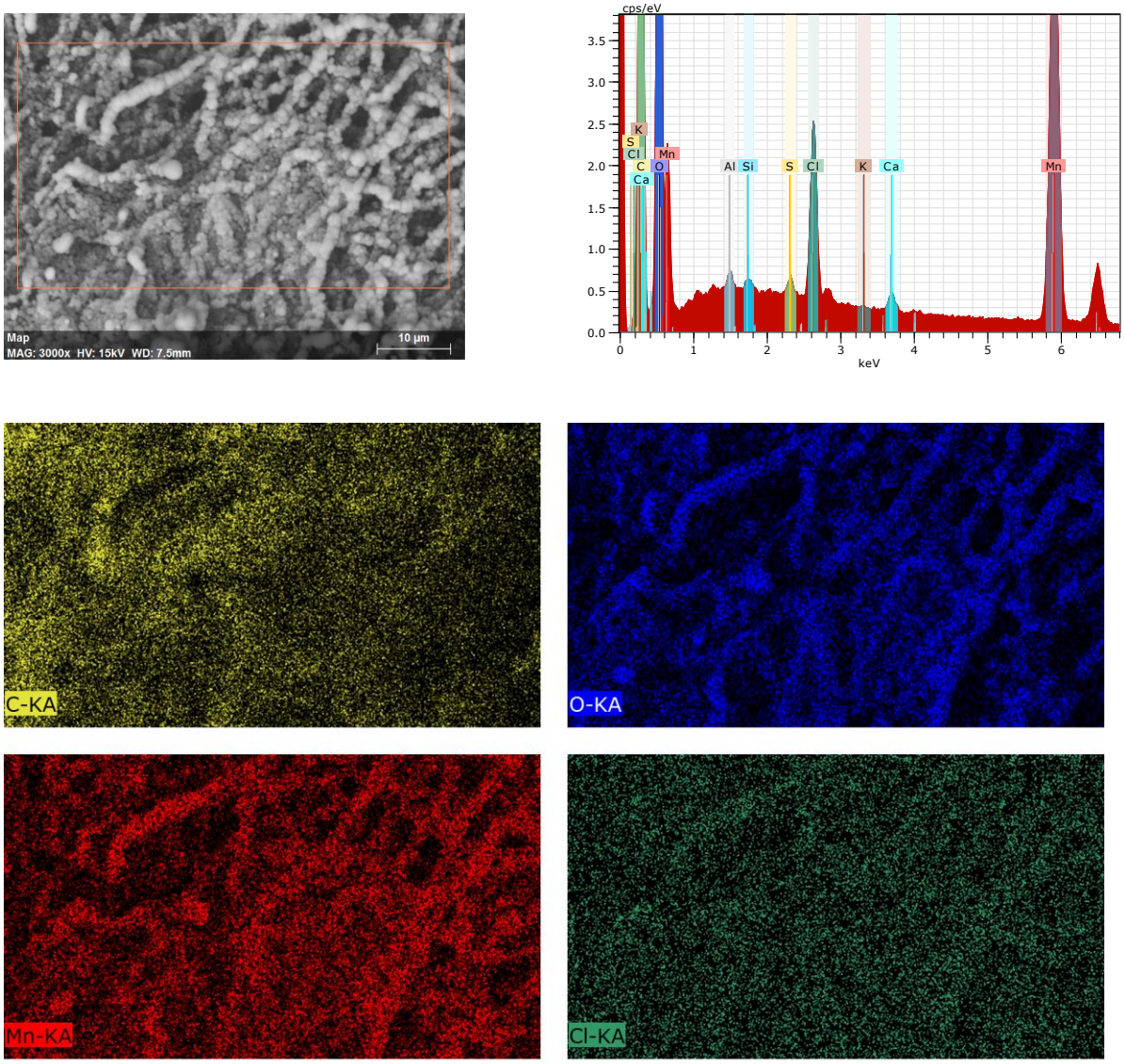

Figure 4.13 EDS images of 900 °C carbonised seaweed paper/MnO_2 with 200 s deposition.

4.3.5.4 Deposition potential

The deposition potential is an important parameter to obtain materials with enhanced electrochemical performance. For an anodic deposition, if the potential is too low, the electrode reaction cannot be driven or the reaction rate is too slow. However, if the potential is too high, the reaction rate would be too fast and other side reactions such as oxygen evolution reaction could make the deposition uncontrollable and irreproducible.[23] Seven positive potentials were studied here and it is found that deposition at +1.15 V vs. Ag/AgCl can provide a balance between reaction rate and stability, as shown in Figure 4.14.

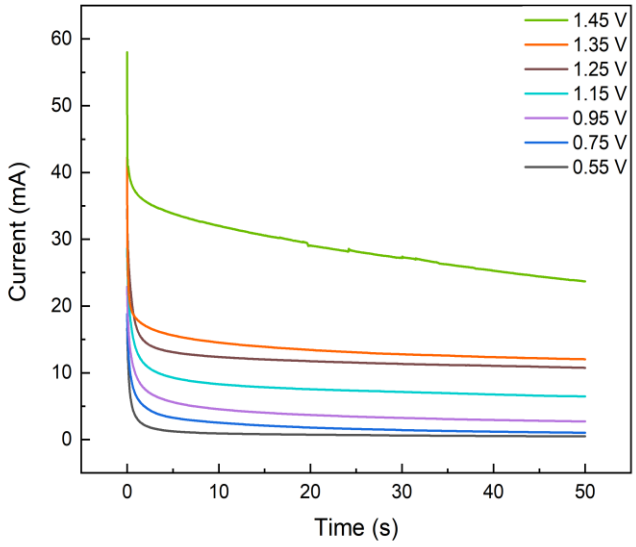

Figure 4.14 Chronoamperograms of MnO_2 deposition at different potentials.

4.3.5.5 Deposition time

After the deposition potential was chosen, direct deposition at +1.15 V vs. Ag/AgCl was carried out from 50 s to 1200 s, as shown in Figure 4.15 (50 s) and Figure A.3 (Appendix, 50 s to 1200 s). Mass of MnO_2 deposited was calculated by the method above using Faraday's law and the mass loading of MnO_2 is shown in Figure 4.16. Obviously, longer deposition time results in higher loading of MnO_2 on the carbonised seaweed paper. In addition, a linear relation can be observed from the deposition mass-time curve, which indicates the concentration of the deposition solution remains almost unchanged and no side reactions such as OER takes place.

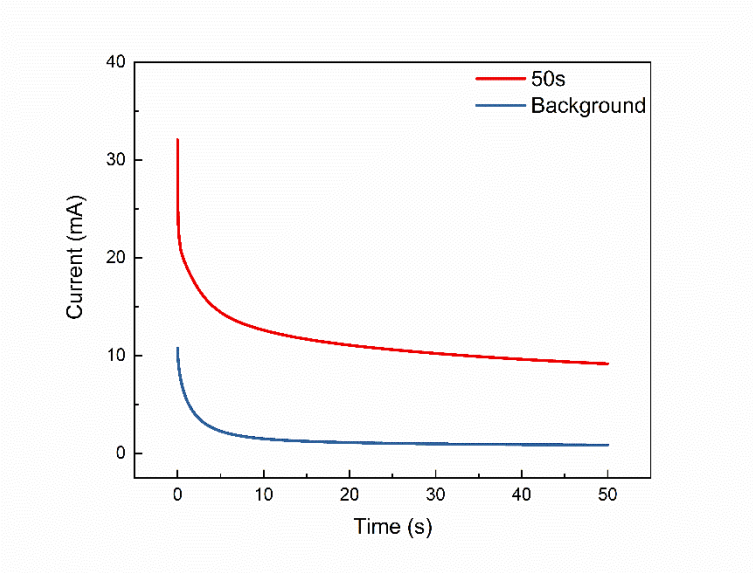

Figure 4.15 Chronoamperograms of MnO_2 deposition at 1.15V with 50 s deposition. The background current (blue) is much lower than the faradaic current (red) for deposition.

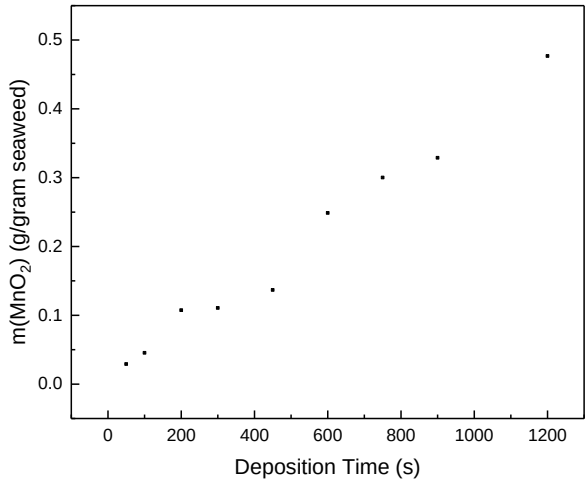

Figure 4.16 Mass loading of MnO_2 as a function of deposition time. The mass loading increases linearly with deposition time.

4.3.5.6 Electrochemical performance - cyclic voltammetry

To evaluate the improvement in performance of carbonised seaweed paper/metal oxide hybrid supercapacitors with different deposition times, cyclic voltammetry (CV) measurements were investigated first at scan rates from 2 to 200 mV s^{-1}. CVs and specific capacitance values of different samples and conditions are shown in Figure 4.17 (200 s deposition), Figure A.4 (Appendix, 50 to 1200 s deposition) and Table 4.4.

For function of these deposits as a pseudocapacitance source, two charge storage mechanisms of MnO_2 have been proposed:

$MnO_2 + C^+ + e^- \rightleftharpoons MnOOC$ (4-5) and $(MnO_2)_{surface} + C^+ + e^- \rightleftharpoons (MnO_2^-C^+)_{surface}$ (4-6)

where $C^+ = Na^+, K^+, Li^+, H_3O^+$. The first one is based on the intercalation and de-intercalation of protons or alkali metal cations. The second one implies the surface adsorption and desorption of cations on MnO_2.[13]

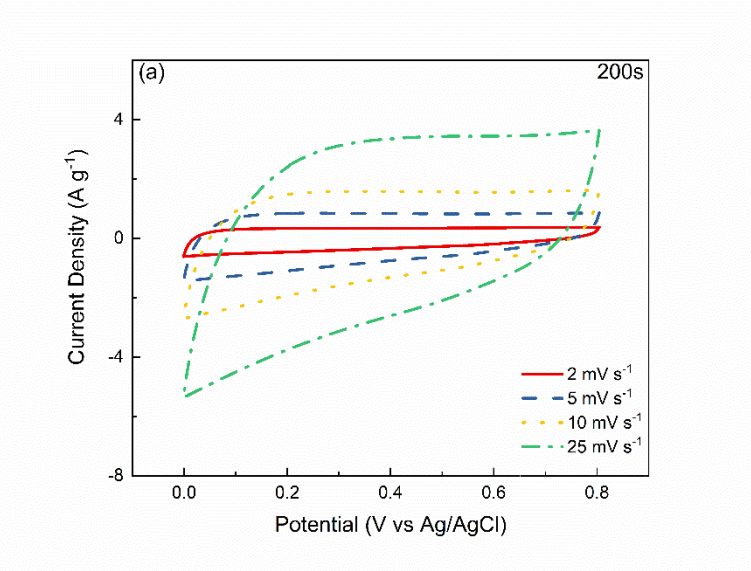

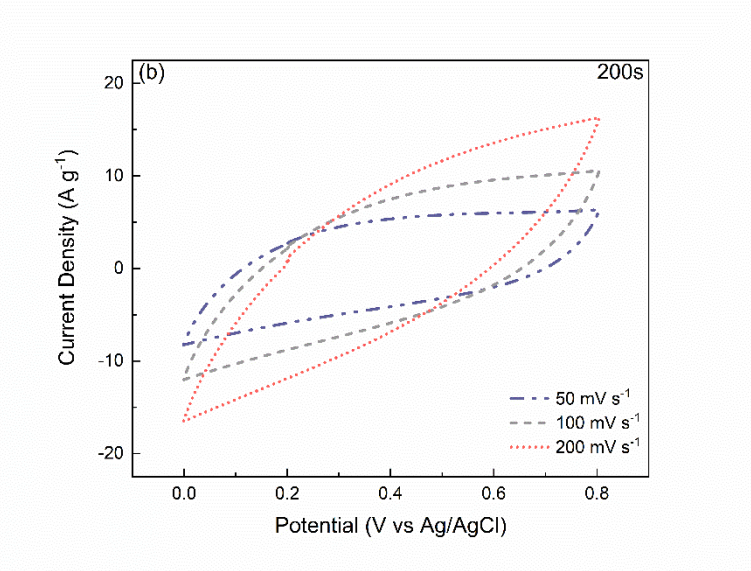

Figure 4.17 Cyclic voltammograms of carbonised seaweed paper/MnO_2 at deposition time of 200 s with increasing scan rates (a) 2 to 25 mV s^{-1} and (b) 50 to 200 mV s^{-1}. (a) At low scan rates, current response is lower but CV shapes are more rectangular; (b) At high scan rates, current response is higher but CVs face more deviation from rectangular shapes.

First, better current response was observed after depositing MnO_2 onto the seaweed paper due to contribution made by the pseudocapacitive MnO_2. Second, measurements under different scan rates were performed. The specific capacitance of seaweed paper/MnO_2 (200 s deposition) reached up to 156 F g^{-1} at 2 mV s^{-1} and 28.8 F g^{-1} at 200 mV s^{-1}. This excellent performance

can be attributed to the material structure which facilitates the transport of charges and provides abundant active surfaces for charge transfer reactions, ensuring a better utilisation of the material.[24]

At higher loading mass of MnO_2, the specific capacitance dropped more rapidly as the scan rate increased (e.g., 1200 s deposition), as shown in Table 4.4. Notably, the specific capacitance at higher scan rate (3.84 F g^{-1}, 200 mV s^{-1}, 1200 s) is even lower than that of a non-deposited sample (8.95 F g^{-1}, 200 mV s^{-1}) because the material is fully covered by MnO_2 and therefore increased electrical resistance limits the access of electrolytes into the material at faster scan rates.[25]

Table 4.4 The specific capacitance (F g^{-1}) of seaweed paper/MnO_2 at different deposition times from CVs.

	Deposition time (s)									
Scan rate (mV s^{-1})	0	50	100	200	300	450	600	750	900	1200
2	47.9	67.9	69.0	**156**	112	97.5	95.7	73.2	73.9	76.9
5	42.5	61.9	61.8	**147**	89.8	87.3	87.8	66.2	64.4	65.2
10	35.6	55.6	54.4	**130**	74.0	73.7	76.0	54.8	52.0	51.1
25	25.1	42.6	41.1	**98.7**	46.9	50.5	54.6	34.6	32.5	36.0
50	18.7	30.3	31.5	**73.7**	29.1	32.0	36.6	20.4	18.8	19.5
100	13.3	19.8	22.5	**49.6**	16.1	16.8	19.9	10.6	8.77	8.97
200	8.95	12.5	14.7	**28.8**	6.37	7.61	8.69	5.07	3.72	3.84

4.3.5.7 Electrochemical performance - galvanostatic charge-discharge

To learn more about the electrochemical performance of the material, GCD (also known as CP) measurements were carried out at five current densities (0.5 to 10 A g^{-1}), as shown in Figure 4.18 (200 s deposition) and Figure A.5 (Appendix, 50 to 1200 s deposition). Similar to the CV results, the specific capacitance of seaweed paper/MnO_2 and non-deposited seaweed paper at a current density of 0.5 A g^{-1} are 248 F g^{-1} and 55.2 F g^{-1}, respectively, as shown in Table 4.5. A remarkable enhancement in the specific capacitance also confirms the benefit of incorporating MnO_2.

As the current density increased from 0.5 to 10 A g^{-1}, the specific capacitance of seaweed paper/MnO_2 (200 s deposition) dropped from 248 F g^{-1} to 79.2 F g^{-1}. Meanwhile, for longer deposition time sample (1200 s deposition), the specific capacitance is as low as 1.20 F g^{-1} at 10 A g^{-1}.

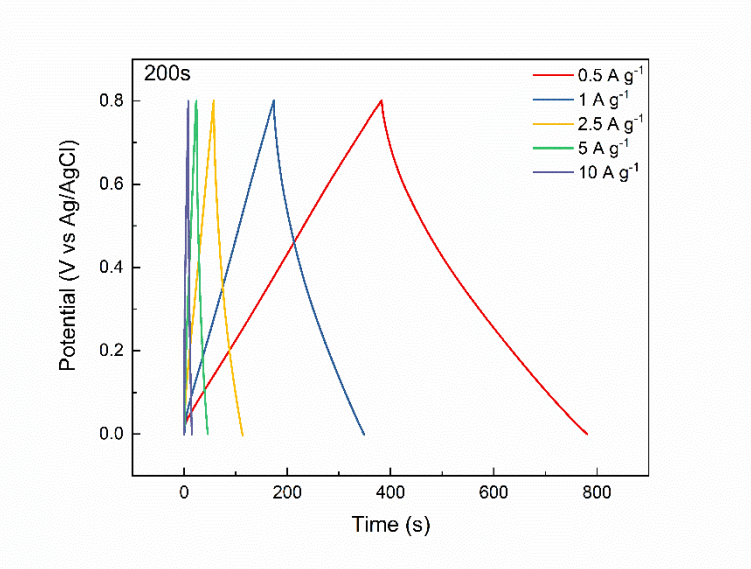

Figure 4.18 Chronopotentiograms of seaweed paper/MnO_2 at the deposition time of 200 s with increasing current densities (0.5 to 10 A g^{-1}). The GCD curves are linear at all current densities, and the charge-discharge time is longer at lower current density.

Table 4.5 The specific capacitance (F g^{-1}) of seaweed paper/MnO_2 at different deposition times from GCD.

Current Density ($A\ g^{-1}$)	Deposition time (s)									
	0	50	100	200	300	450	600	750	900	1200
0.5	55.2	87.1	114	**248**	189	120	114	79.9	81.6	95.5
1	46.4	70.8	73.1	**218**	139	113	91.3	70.0	68.8	83.1
2.5	29.5	43.8	47.7	**173**	84.4	88.8	60.0	48.1	44.9	57.0
5	19.6	27.1	31.3	**135**	41.7	62.7	33.8	24.8	21.8	28.8
10	10.7	11.3	25.0	**79.2**	11.3	25.5	3.75	4.17	1.67	1.20

4.3.5.8 Electrochemical performance - stability test

Stability is another important factor which determines the performance of supercapacitors in practical applications.[26] The cycling performance at 1 A g^{-1} of the sample carbonised at 900 °C without deposition is shown in Figure 4.19. The capacitance retention of the carbonised seaweed paper retains above 90.0% of its initial value after 10000 cycles, indicating this biomass-derived carbon material has an excellent stability.

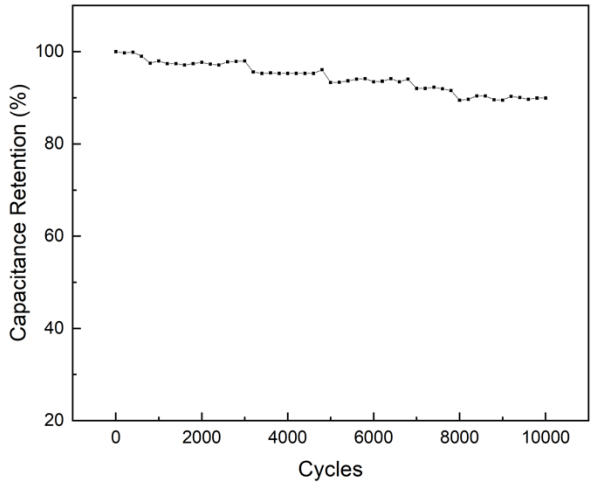

Figure 4.19 The capacitance retention of the 900 °C carbonised seaweed paper at the current density of 1 A g^{-1} for 10000 cycles.

High MnO_2 mass loading samples gave rise to degraded long-term electrochemical cyclability. For example, the material (900 s deposition) only retained approximately 60% of its original capacitance value after 2000 cycles (Figure 4.20 (b)). Noticeably, nearly 20% of the initial capacitance was lost just after 50 cycles, as shown in Figure 4.20 (a). The result can be explained by the electrochemical dissolution of MnO_2 during the test and its low structural stability and flexibility.[9, 27]

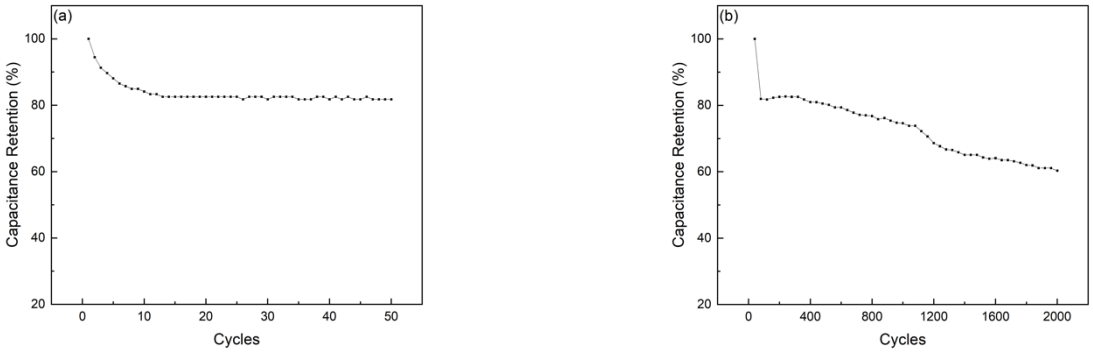

Figure 4.20 The capacitance retention of seaweed paper/MnO_2 (900 s deposition) at the current density of 1 A g^{-1} after (a) 50 cycles and (b) 2000 cycles.

However, for samples with relatively lower MnO_2 mass loading, the capacitance retention is better with a percentage of 88.3%, as shown in Figure 4.21 (200 s deposition) and Figure A.6 (Appendix, 50 to 600 s deposition). Furthermore, higher specific capacitance values than the initial were observed during cycling due to activation of more porous structure in the carbonised seaweed paper which was beneficial for diffusion of ions.[4, 5, 28]

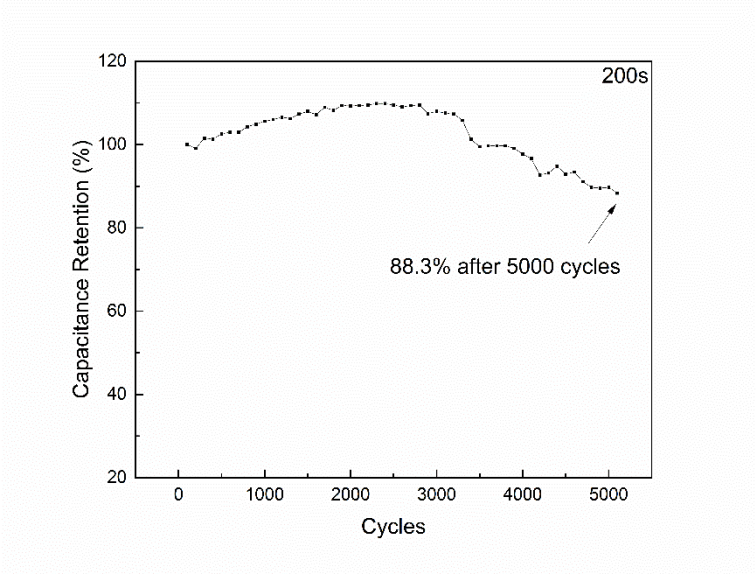

Figure 4.21 The capacitance retention of seaweed paper/MnO_2 with the deposition time of 200 s at the current density of 1 A g^{-1}.

4.3.5.9 Electrochemical performance - electrochemical impedance spectroscopy

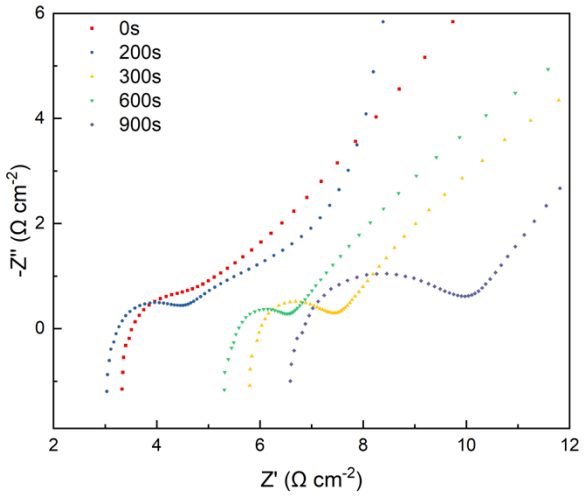

Figure 4.22 Nyquist Plots of seaweed paper and seaweed paper/MnO_2 with different deposition times.

EIS is an important tool for the study of the characteristics of conductivity and charge transport in the material/electrolyte interface.[29] Figure 4.22 shows the Nyquist plot of carbonised seaweed paper and seaweed paper/MnO_2 of different deposition times (200 s, 300 s, 600 s and 900 s) in 3 M KCl solution. The intersection of the curves at the real part represents the equivalent series resistance (ESR) of the electrochemical system (including the bulk resistance of the electrolyte solution, inherent resistance of electroactive material, and contact resistance at the active material/current collector interface), whereas the semicircles display the charge transfer resistance (R_{ct}) at the working electrode/electrolyte interface.[30] The Nyquist plot in Figure 4.22 shows that the low MnO_2 mass loading samples have only slight effect on the electrical conductivity loss of the overall system compared with the high MnO_2 mass loading samples. For the sample with the deposition time of 900 s, a larger semicircle at the high-frequency region and a higher ESR value indicate a bigger R_{ct} and a poorer electrical

conductivity. Additionally, the steep shape of the low-frequency region represents an ideal capacitive behaviour, indicating the fast mass transport for the 200 s deposition sample.[31]

4.4 Conclusion and comparison

The carbonised seaweed paper was first employed as negative electrode materials (0 to -0.8 V vs Ag/AgCl) in neutral aqueous electrolytes for supercapacitor applications, providing high specific capacitance of 226 F g^{-1} and capacitance retention (~90% after 10000 cycles). The obtained capacitance is mainly based on electric double layer capacitance (EDLC), and is higher than a number of biomass-derived carbon (e.g., bamboo, wood, rice husk) or novel carbon-based (e.g., CNTs and graphene) negative electrode materials whose specific capacitance is normally less than 200 F g^{-1} with shorter cycle life.[3, 14, 24, 32] In order to improve the electrochemical performance of carbonised seaweed paper as positive electrode materials (0 to +0.8 V vs Ag/AgCl), MnO_2 was deposited onto the carbonised seaweed paper via a simple potentiostatic method. The specific capacitance and capacitance retention of as-prepared MnO_2/carbonised seaweed paper is compared to other MnO_2/carbon-based electrodes reported, as listed in Table 4.6. The MnO_2/carbonised seaweed paper reveals high specific capacitance and cycle life in contrast to other MnO_2/carbon composites. In addition, a free-standing MnO_2/carbon composite is fabricated conveniently, and is made from renewable and fast grown seaweed-based biomass with low cost, scalability and eco-friendliness, which bears favourable comparison with production of other carbon-based materials. In the future, seaweed paper-derived carbon composite materials with specific micro/mesopore structures and chemical modification can be studied to further improve their electrochemical performance.

Table 4.6 Electrochemical performance of MnO_2/carbon-based electrodes for supercapacitors.

Sample	Specific Capacitance ($F\ g^{-1}$)	Scan Rate ($mV\ s^{-1}$)	Current Density ($A\ g^{-1}$)	Capacitance Retention (cycles)
MnO_2/seaweed paper (this work)	248	/	0.5	~88%, 5000
MnO_2/CNTs[33]	115	/	0.5	~95%, 1000
MnO_2/Graphene[25]	310	2	/	~95%, 15000
MnO_2/Graphene/CNTs[34]	331	200	/	~90%, 1000
MnO_2/wood carbon[35]	55	/	1	~93%, 10000
MnO_2/banana peel carbon[36]	140	/	0.3	~92%, 1000
MnO_2/carbon aerogel[37]	124	5	/	~60%, 1000
MnO_2/hemp carbon[38]	340	/	1	~98%, 3000

In this chapter, a novel carbon material derived from biomass, carbonised seaweed paper, was used to produce hybrid supercapacitors. Carbonisation of seaweed paper imparted the material with good supercapacitor characteristics. This was confirmed by a range of characterisation techniques, including SEM, XPS and EDS. After carbonisation, the seaweed fibre structure was found to be smoother and smaller. When the carbonisation temperature increased to a certain degree, the electrical conductivity increased as well as the porosity and the surface area. For electrochemical measurements of the carbonised seaweed paper, cyclic voltammetry was used and showed that the material has an excellent specific capacitance (226 $F\ g^{-1}$) in a negative potential range. Electrodeposition of manganese dioxide by chronoamperometry was employed,

which enhanced the specific capacitance from 47.9 F g^{-1} to 156 F g^{-1} in a positive potential range without obvious loss of the stability (i.e., >88% after 5000 cycles).

In later chapters, we will focus on improving the performance of other biomass-derived materials such as filter paper as hybrid supercapacitors. This could be achieved by incorporating other electroactive materials (e.g., transition metal hydroxides, metal oxides and metal organic frameworks) into the carbon structure. This chapter has presented a method to synthesise a hybrid supercapacitor from a novel and environmentally friendly material. The demonstrated good capacitance retention and competitive capacitance value qualifies modified carbonised seaweed paper for usage in supercapacitor applications.

References

(1) Liu, C.; Yu, Z.; Neff, D.; Zhamu, A.; Jang, B. Z. J. N. l. Graphene-based supercapacitor with an ultrahigh energy density. **2010**, *10* (12), 4863-4868.

(2) Gamby, J.; Taberna, P.; Simon, P.; Fauvarque, J.; Chesneau, M. J. J. o. p. s. Studies and characterisations of various activated carbons used for carbon/carbon supercapacitors. **2001**, *101* (1), 109-116. Fan, Z.; Yan, J.; Wei, T.; Zhi, L.; Ning, G.; Li, T.; Wei, F. J. A. F. M. Asymmetric supercapacitors based on graphene/MnO2 and activated carbon nanofiber electrodes with high power and energy density. **2011**, *21* (12), 2366-2375.

(3) Zhang, L. L.; Zhao, X. J. C. S. R. Carbon-based materials as supercapacitor electrodes. **2009**, *38* (9), 2520-2531.

(4) Jiang, L.; Nelson, G. W.; Han, S. O.; Kim, H.; Sim, I. N.; Foord, J. S. J. E. A. Natural cellulose materials for supercapacitors. **2016**, *192*, 251-258.

(5) Jiang, L.; Nelson, G. W.; Kim, H.; Sim, I.; Han, S. O.; Foord, J. S. J. C. Cellulose‐derived supercapacitors from the carbonisation of filter paper. **2015**, *4* (5), 586-589.

(6) Raymundo‐Piñero, E.; Leroux, F.; Béguin, F. J. A. m. A high‐performance carbon for supercapacitors obtained by carbonization of a seaweed biopolymer. **2006**, *18* (14), 1877-1882.

(7) Senthilkumar, S. T.; Selvan, R. K.; Lee, Y. S.; Melo, J. S. Electric double layer capacitor and its improved specific capacitance using redox additive electrolyte. *Journal of Materials Chemistry A* **2013**, *1* (4), 1086-1095, 10.1039/C2TA00210H. DOI: 10.1039/C2TA00210H.

(8) Hu, C.-C.; Chang, K.-H.; Lin, M.-C.; Wu, Y.-T. J. N. l. Design and tailoring of the nanotubular arrayed architecture of hydrous RuO2 for next generation supercapacitors. **2006**, *6* (12), 2690-2695.

(9) Wei, W.; Cui, X.; Chen, W.; Ivey, D. G. J. C. s. r. Manganese oxide-based materials as electrochemical supercapacitor electrodes. **2011**, *40* (3), 1697-1721.

(10) Lokhande, C. D.; Dubal, D. P.; Joo, O.-S. Metal oxide thin film based supercapacitors. *Current Applied Physics* **2011**, *11* (3), 255-270. DOI: https://doi.org/10.1016/j.cap.2010.12.001.

(11) Jiang, L.; Han, S. O.; Pirie, M.; Kim, H. H.; Seong, Y.-H.; Kim, H.; Foord, J. S. Seaweed biomass waste-derived carbon as an electrode material for supercapacitor. *Energy & Environment* **2021**, *32* (6), 1117-1129. DOI: 10.1177/0958305x19882398.

(12) Mi, J.; Wang, X.-R.; Fan, R.-J.; Qu, W.-H.; Li, W.-C. Coconut-Shell-Based Porous Carbons with a Tunable Micro/Mesopore Ratio for High-Performance Supercapacitors. *Energy & Fuels* **2012**, *26* (8), 5321-5329. DOI: 10.1021/ef3009234. Kim, H.; Sohail, M.; Wang, C.; Rosillo-Lopez, M.; Baek, K.; Koo, J.; Seo, M. W.; Kim, S.; Foord, J. S.; Han, S. O. Facile One-Pot Synthesis of Bimetallic Co/Mn-MOFs@Rice Husks, and its Carbonization for Supercapacitor Electrodes. *Scientific Reports* **2019**, *9* (1), 8984. DOI: 10.1038/s41598-019-45169-0.

(13) Liu, L.; Zhao, H.; Lei, Y. Review on Nanoarchitectured Current Collectors for Pseudocapacitors. *Small Methods* **2019**, *3* (8), 1800341. DOI: https://doi.org/10.1002/smtd.201800341.

(14) Yu, Z.; Tetard, L.; Zhai, L.; Thomas, J. Supercapacitor electrode materials: nanostructures from 0 to 3 dimensions. *Energy & Environmental Science* **2015**, *8* (3), 702-730, 10.1039/C4EE03229B. DOI: 10.1039/C4EE03229B.

(15) Yu, A.; Chabot, V.; Zhang, J. *Electrochemical supercapacitors for energy storage and delivery: fundamentals and applications*; CRC press, 2013.

(16) Forse, A. C.; Merlet, C. l.; Griffin, J. M.; Grey, C. P. J. J. o. t. A. C. S. New perspectives on the charging mechanisms of supercapacitors. **2016**, *138* (18), 5731-5744.

(17) Lee, H. Y.; Manivannan, V.; Goodenough, J. B. J. C. r. d. l. A. d. s.-S. I.-C. Electrochemical capacitors with KCl electrolyte. **1999**, *2* (11-13), 565-577. Reddy, R. N.; Reddy, R. G. J. J. o. P. S. Sol–gel MnO2 as an electrode material for electrochemical capacitors. **2003**, *124* (1), 330-337.

(18) Hulicova‐Jurcakova, D.; Kodama, M.; Shiraishi, S.; Hatori, H.; Zhu, Z. H.; Lu, G. Q. J. A. F. M. Nitrogen‐enriched nonporous carbon electrodes with extraordinary supercapacitance. **2009**, *19* (11), 1800-1809.

(19) Oh, Y. J.; Yoo, J. J.; Kim, Y. I.; Yoon, J. K.; Yoon, H. N.; Kim, J.-H.; Park, S. B. J. E. A. Oxygen functional groups and electrochemical capacitive behavior of incompletely reduced graphene oxides as a thin-film electrode of supercapacitor. **2014**, *116*, 118-128.

(20) Yang, N.; Zhao, G.; Foord, J. S. *Nanocarbon Electrochemistry*; Wiley, 2020.

(21) Saterlay, A. J.; Foord, J. S.; Compton, R. G. J. A. Sono-cathodic stripping voltammetry of manganese at a polished boron-doped diamond electrode: application to the determination of manganese in instant tea. **1999**, *124* (12), 1791-1796.

(22) Bott, A. Practical problems in voltammetry 3: reference electrodes for voltammetry. *Current Separations* **1995**, *14*, 64-69.

(23) Jiang, L.; Shanmuganathan, S.; Nelson, G.; Han, S.; Sim, I. N.; Foord, J. Hybrid system of nickel–cobalt hydroxide on carbonised natural cellulose materials for supercapacitors. *Journal of Solid State Electrochemistry* **2018**, *22*. DOI: 10.1007/s10008-017-3723-z.

(24) Bi, Z.; Kong, Q.; Cao, Y.; Sun, G.; Su, F.; Wei, X.; Li, X.; Ahmad, A.; Xie, L.; Chen, C.-M. Biomass-derived porous carbon materials with different dimensions for supercapacitor electrodes: a review. *Journal of Materials Chemistry A* **2019**, *7* (27), 16028-16045, 10.1039/C9TA04436A. DOI: 10.1039/C9TA04436A.

(25) Yan, J.; Fan, Z.; Wei, T.; Qian, W.; Zhang, M.; Wei, F. Fast and reversible surface redox reaction of graphene–MnO2 composites as supercapacitor electrodes. *Carbon* **2010**, *48* (13), 3825-3833. DOI: https://doi.org/10.1016/j.carbon.2010.06.047.

(26) Zhang, Q.-Z.; Zhang, D.; Miao, Z.-C.; Zhang, X.-L.; Chou, S.-L. Research Progress in MnO2–Carbon Based Supercapacitor Electrode Materials. *Small* **2018**, *14* (24), 1702883. DOI: https://doi.org/10.1002/smll.201702883.

(27) Zhu, J.; He, J. Facile Synthesis of Graphene-Wrapped Honeycomb MnO2 Nanospheres and Their Application in Supercapacitors. *ACS Applied Materials & Interfaces* **2012**, *4* (3), 1770-1776. DOI: 10.1021/am3000165.

(28) Jiang, L.; Seong, Y.-H.; Han, S. O.; Kim, H.; Kim, H. H.; Foord, J. S. Nickel treatment of biomass-derived nanocarbon for energy devices. *Carbon* **2018**, *130*, 724-729. DOI: https://doi.org/10.1016/j.carbon.2018.01.063. Jiang, L.; Shanmuganathan, S.; Nelson, G. W.; Han, S. O.; Kim, H.; Na Sim, I.; Foord, J. S. Hybrid system of nickel–cobalt hydroxide on carbonised natural cellulose materials for supercapacitors. *Journal of Solid State Electrochemistry* **2018**, *22* (2), 387-393. DOI: 10.1007/s10008-017-3723-z.

(29) Fan, H.; Wang, H.; Zhao, N.; Zhang, X.; Xu, J. Hierarchical nanocomposite of polyaniline nanorods grown on the surface of carbon nanotubes for high-performance supercapacitor electrode. *Journal of Materials Chemistry* **2012**, *22* (6), 2774-2780, 10.1039/C1JM14311E. DOI: 10.1039/C1JM14311E.

(30) Shao, Y.; El-Kady, M. F.; Sun, J.; Li, Y.; Zhang, Q.; Zhu, M.; Wang, H.; Dunn, B.; Kaner, R. B. Design and Mechanisms of Asymmetric Supercapacitors. *Chemical Reviews* **2018**, *118* (18), 9233-9280. DOI: 10.1021/acs.chemrev.8b00252.

(31) Wang, J.-G.; Yang, Y.; Huang, Z.-H.; Kang, F. Effect of temperature on the pseudo-capacitive behavior of freestanding MnO2@carbon nanofibers composites electrodes in mild

electrolyte. *Journal of Power Sources* **2013**, *224*, 86-92. DOI: https://doi.org/10.1016/j.jpowsour.2012.09.075.

(32) Azwar, E.; Wan Mahari, W. A.; Chuah, J. H.; Vo, D.-V. N.; Ma, N. L.; Lam, W. H.; Lam, S. S. Transformation of biomass into carbon nanofiber for supercapacitor application – A review. *International Journal of Hydrogen Energy* **2018**, *43* (45), 20811-20821. DOI: https://doi.org/10.1016/j.ijhydene.2018.09.111.

(33) Tan, D. Z. W.; Cheng, H.; Nguyen, S. T.; Duong, H. M. Controlled synthesis of MnO2/CNT nanocomposites for supercapacitor applications. *Materials Technology* **2014**, *29* (sup4), A107-A113. DOI: 10.1179/1753555714Y.0000000175.

(34) Xiong, C.; Li, T.; Dang, A.; Zhao, T.; Li, H.; Lv, H. Two-step approach of fabrication of three-dimensional MnO2-graphene-carbon nanotube hybrid as a binder-free supercapacitor electrode. *Journal of Power Sources* **2016**, *306*, 602-610. DOI: https://doi.org/10.1016/j.jpowsour.2015.12.056.

(35) Chen, C.; Zhang, Y.; Li, Y.; Dai, J.; Song, J.; Yao, Y.; Gong, Y.; Kierzewski, I.; Xie, J.; Hu, L. All-wood, low tortuosity, aqueous, biodegradable supercapacitors with ultra-high capacitance. *Energy & Environmental Science* **2017**, *10* (2), 538-545, 10.1039/C6EE03716J. DOI: 10.1039/C6EE03716J.

(36) Yang, G.; Park, S.-J. MnO2 and biomass-derived 3D porous carbon composites electrodes for high performance supercapacitor applications. *Journal of Alloys and Compounds* **2018**, *741*, 360-367. DOI: https://doi.org/10.1016/j.jallcom.2018.01.108.

(37) Ren, Y.; Xu, Q.; Zhang, J.; Yang, H.; Wang, B.; Yang, D.; Hu, J.; Liu, Z. Functionalization of Biomass Carbonaceous Aerogels: Selective Preparation of MnO2@CA Composites for Supercapacitors. *ACS Applied Materials & Interfaces* **2014**, *6* (12), 9689-9697. DOI: 10.1021/am502035g.

(38) Yang, M.; Kim, D. S.; Hong, S. B.; Sim, J.-W.; Kim, J.; Kim, S.-S.; Choi, B. G. MnO2 Nanowire/Biomass-Derived Carbon from Hemp Stem for High-Performance Supercapacitors. *Langmuir* **2017**, *33* (21), 5140-5147. DOI: 10.1021/acs.langmuir.7b00589.

Chapter 5 Carbonised Filter Paper with Nickel Treatment for Supercapacitor Applications

In this project, another type of carbon material derived from biomass, carbonised filter paper is produced at relatively low temperatures with a simple *in situ* nickel treatment. The as-prepared nickel treated carbonised filter paper (Ni-FP) is then easily constructed as a positive electrode by electrochemical cycling in aqueous alkaline media for supercapacitor application. The Ni-FP carbonised at 800 °C exhibits a high specific capacitance of 258 F g^{-1} while the material carbonised at 1100 °C retains 99.3% of its original specific capacitance at a high discharge current density of 5 A g^{-1} after 2000 cycles. The electrochemical performance renders Ni-FP as a promising substitute for other novel carbon-based materials as supercapacitors in an environmentally friendly and economical way.

5.1 Introduction

In last chapter, carbonisation of seaweed paper was followed with electrochemical deposition of MnO_2. Alternatively, functionalisation prior to carbonisation can be achieved as well. A low-cost carbon source filter paper and a popular metal element Ni are selected here. The carbonisation process with nickel treatment helps to obtain graphitised carbon materials from filter paper with lower thermal energy input and less chemical contamination, as opposed to other complicated physical or chemical treatments to produce carbon.[1] On the other hand, nickel nanoparticle-based NiO and $Ni(OH)_2$ are considered to be promising battery-type electrode materials for supercapacitors due to their excellent theoretical specific capacitance values (i.e., NiO 2573 F g^{-1}, and $Ni(OH)_2$ 2081 F g^{-1}), low cost and environmentally friendly impact.[2] However, the poor cyclability and electrical conductivity has limited their

applications, leading to unsatisfactory specific capacitance and cycle life.[3] Recently, incorporation of nickel oxide/hydroxide into conductive carbon-based materials to form composites has been proposed to enhance the electrical conductivity and overall performance.[4]

Previous studies showed that the carbonised filter paper modified with nickel acts as an efficient catalyst for hydrogen evolution reaction (HER) after electrochemical activation and a promising capacitive negative electrode material in neutral electrolytes for aqueous-based supercapacitors after chemical etching of the nickel nanoparticles.[5] However, its application in supercapacitors on the positive potential side remains unexplored. Therefore, one aim of this project is to convert Ni-FP into energy storage materials by electrochemical activation in alkaline solutions on the positive potential side. In the meantime, Ni etched filter paper is studied as a counterpart on the negative potential side. To evaluate the properties and performance of the materials, characterisation and electrochemical methods such as FE-SEM, XRD, CV, GCD and EIS are conducted in this work.

5.2 Experimental

5.2.1 Chemicals and materials

Nickel(II) nitrate hexahydrate [$Ni(NO_3)_2 \cdot 6H_2O$, puriss. p.a., ⩾ 98.5% (KT)], potassium chloride [KCl, ACS reagent, 99.0-100.5%], potassium hydroxide [KOH, ACS reagent, ≥85%], sodium sulphate [Na_2SO_4, ACS reagent, ⩾99.0%] were purchased from Sigma-Aldrich. All solutions used as part of this project were prepared from Milli-Q water (resistivity ~ 18.2 MΩ cm at 25 °C).

5.2.2 Preparation of carbonised filter paper with nickel treatment (Ni-FP)

For nickel treatment, the Whatman® Cellulose Filter Paper was immersed in a methanol solution containing 30 wt.% ($Ni(NO_3)_2 \cdot 6H_2O$) under microwave for one hour, after which it

was soaked for 11 h at 50 °C and dried at 80 °C in the oven. The samples were then heated at 600 °C for 0.5 h in a N_2 atmosphere with a temperature ramp of 25 °C h^{-1}. Afterwards, they were carbonised at 700, 800, 900, 1000, 1100 and 1300 °C for 0.5 h under vacuum (10^{-7} mbar) with a temperature ramp of 5 °C min^{-1}, respectively.[5] The as-prepared Ni-FP samples were used to evaluate the electrochemical performance.

5.2.3 Electrochemical measurements

All electrochemical experiments were performed with an Autolab PGSTAT128N potentiostat/galvanostat (Metrohm Autolab, Utrecht, Netherlands) equipped with Nova software. A three-electrode system, consisting of the sample held by a platinum current collector as the working electrode, a platinum plate (1×1 cm^2) as the counter electrode, and mercury-mercuric oxide electrode (Hg/HgO electrode with 1 M KOH as the internal electrolyte, +0.110 V vs NHE) as the reference electrode, was used through CV, GCD, and EIS analysis. The equilibrium reactions of the Hg/HgO electrode are shown as below:

$$Hg \rightleftharpoons Hg^{2+} + 2e^- \quad (5\text{-}1)$$

$$Hg^{2+} + 2OH^- \rightleftharpoons Hg(OH)_2 \rightleftharpoons HgO + H_2O \quad (5\text{-}2)$$

In alkaline solutions, a Ag/AgCl reference electrode has a limited life time as silver oxide can be formed on the silver wire, but a Hg/HgO electrode remains stable under this condition. Therefore, the electrochemical performance was studied in an alkaline electrolyte (1 M KOH vs Hg/HgO) and in three neutral electrolytes (1 M KCl, 1 M Na_2SO_4 and 3 M KCl aqueous solutions vs Ag/AgCl with 3 M KCl, +0.210 V vs NHE) for comparison.

5.3 Results and discussion

5.3.1 Surface characterisation of Ni-FP

5.3.1.1 Scanning electron microscopy

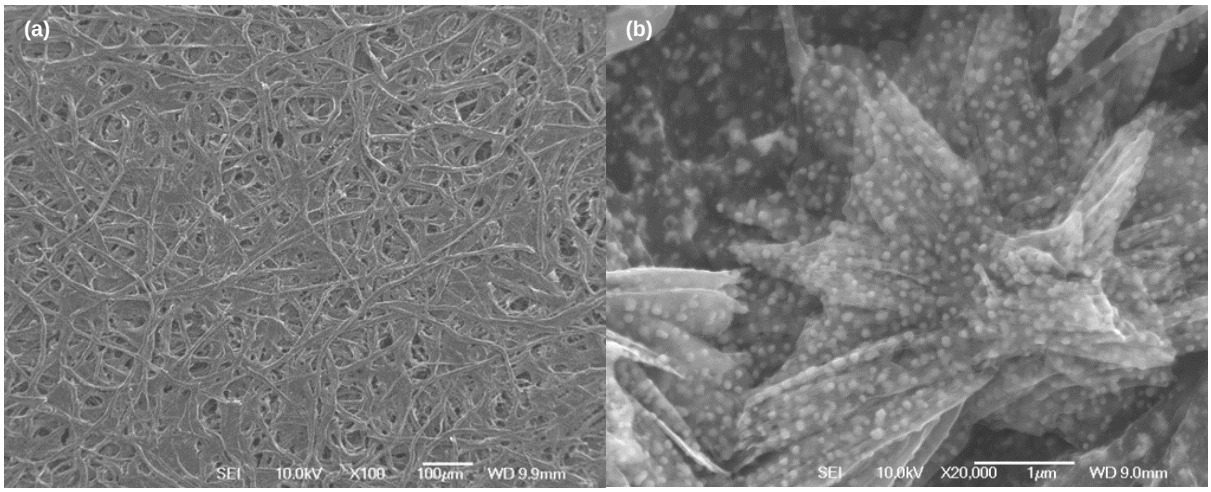

Figure 5.1 FE-SEM images of (a) raw filter paper and (b) Ni-FP carbonised at 800 °C.

Figure 5.1 shows the FE-SEM images of raw filter paper and Ni-FP carbonised at 800 °C. Layered and long fibres are observed in the raw filter paper, whereas spherical nanoparticles are distributed densely and homogeneously on the surface and in the bulk of the Ni-FP carbonised at 800 °C. The layered and long fibres were also broken into leaves with embodied particles upon carbonisation, as shown in Figure 5.1 (b).

5.3.1.2 X-ray diffraction

The XRD patterns of Ni-FP carbonised at 800 °C are shown in Figure 5.2. The nickel diffraction peaks (JCPDS 04-0850) are observable in the pattern, demonstrating that the nanoparticles seen in the FE-SEM image are Ni metal. Calcium carbonate impurities (JCPDS 47-1743) are also observed in XRD, which is common in biomass-derived carbon materials.[6] In addition, the peak at 2θ value of 26° can be attributed to the (002) plane of the graphitic layer, which indicates Ni treatment also lowered the temperature for obtaining conductive carbon compared to non-Ni treated filter paper.[5, 7, 8]

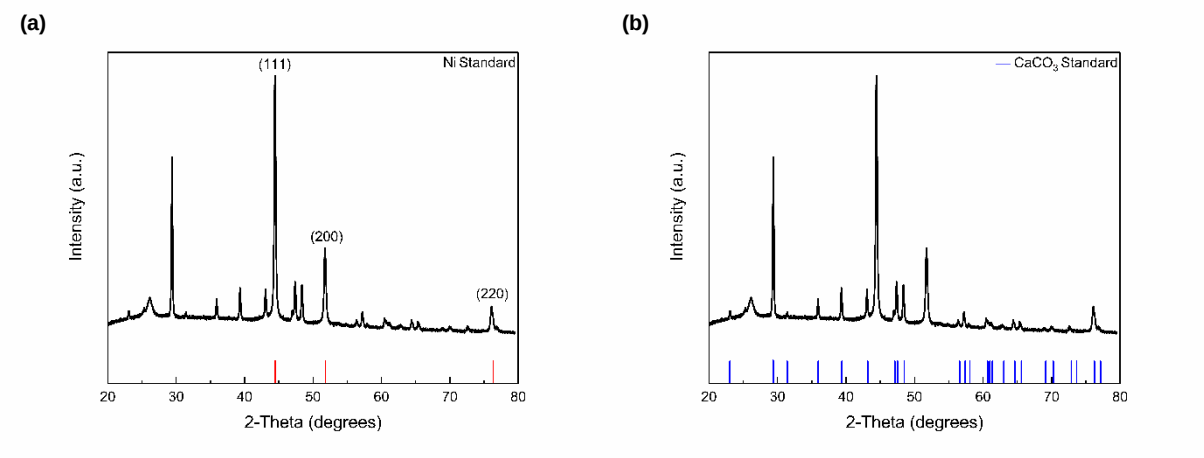

Figure 5.2 XRD patterns of Ni-FP carbonised at 800 °C with (a) Ni and (b) $CaCO_3$ characteristic peaks.

5.3.2 Alkaline and neutral electrolytes

An alkaline electrolyte (1 M KOH vs Hg/HgO) and three neutral electrolytes (1 M KCl, 1 M Na_2SO_4 and 3 M KCl vs Ag/AgCl) were used to study the electrochemical performance of the Ni-FP carbonised at 800 °C by CV in a three-electrode system at room temperature (298 K). CV curves were taken at a scan rate of 2 mV s^{-1} with the potential range from 0.1 to +0.8 V for KOH and 0.1 to +0.9 V for the others. To compare the voltammograms more easily, all potentials were converted to a standard hydrogen electrode (SHE) as the reference electrode.

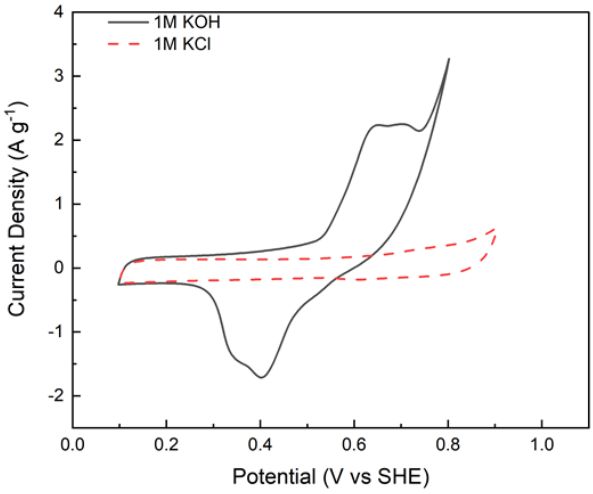

Figure 5.3 Cyclic voltammograms of Ni-FP carbonised at 800 ℃ in 1 M KOH and 1 M KCl at the scan rate of 2 mV s^{-1}.

The CV curves of the material in 1 M KOH and 1 M KCl are shown in Figure 5.3. Apparently, redox peaks are observed from the CV in 1 M KOH, which corresponds to the electron transfer process of Ni(II) ↔ Ni(III).[9] The reason is that spontaneous dissolution of Ni occurs followed by the formation of $Ni(OH)_2$ film after being immersed in alkaline electrolytes.[10, 11] Additionally, the gradual growth of $Ni(OH)_2$ structures is accelerated by electrochemical oxidation during CV scans in KOH solution.[10] In contrast to the CV in KOH, only a quasi-rectangular shape was detected for the CV in 1 M KCl, which is normally attributed to electric double layer capacitance only. Similarly, CV curves displaying quasi-rectangular shapes without redox peaks in 1 M Na_2SO_4 and 3 M KCl are observed in Figure 5.4. Hence, it is found that OH^- ions took part in the electrochemical reaction and are related to the redox peaks from the difference of the CV curves. The strong redox peaks in 1 M KOH are ascribed to the following electrochemical process occurring at the electrode/electrolyte interface:

$$Ni(OH)_2 + OH^- \rightleftharpoons NiOOH + H_2O + e^- \quad (5\text{-}3)$$

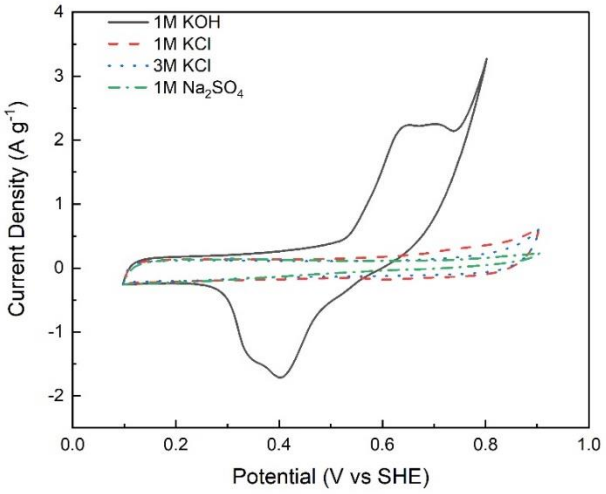

Figure 5.4 Cyclic voltammograms of Ni-FP carbonised at 800 ℃ in 1 M KOH, 1 M KCl, 1 M Na_2SO_4 and 3 M KCl at the scan rate of 2 mV s^{-1}.

5.3.3 Potential range

For comparison, CV curves were also taken at 2 mV s^{-1} from 0.2 to -0.6 V (vs SHE) in the same electrolytes as mentioned above. It is clearly seen from Figure 5.5 that the area enclosed by the CV in 1 M KOH is basically the same as that in 1 M KCl apart from redox peaks around 0 V in KOH. The peaks are attributed to redox reactions of oxygen functional groups and adsorbed or dissolved oxygen on the surface of the materials.[12] The possible reactions in alkaline electrolytes are as follows:

$$>C=O + H_2O + e^- \rightarrow >C\text{-}OH + OH^- \quad (5\text{-}4)$$

$$*O_2 + 2H_2O + 4e^- \rightarrow 4*OH^- \quad (5\text{-}5)$$

$$*O_2 + H_2O + 2e^- \rightarrow *HO_2^- \; ; \; *HO_2^- + H_2O + 2e^- \rightarrow 3*OH^- \quad (5\text{-}6)$$

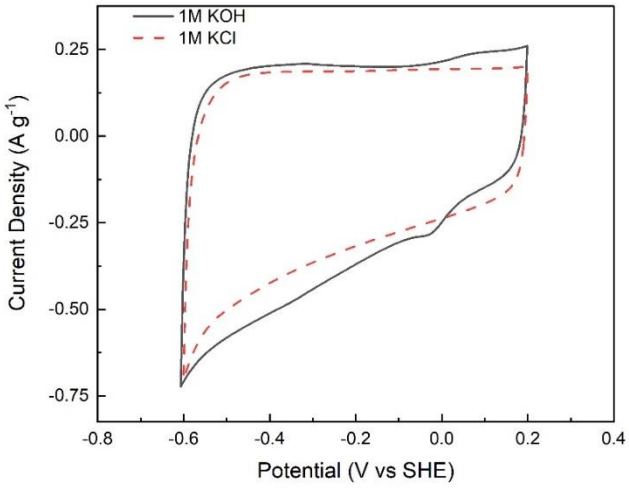

Figure 5.5 Cyclic voltammograms of Ni-FP carbonised at 800 ℃ in 1 M KOH and 1 M KCl at the scan rate of 2 mV s^{-1} from 0.2 to -0.6 V vs SHE.

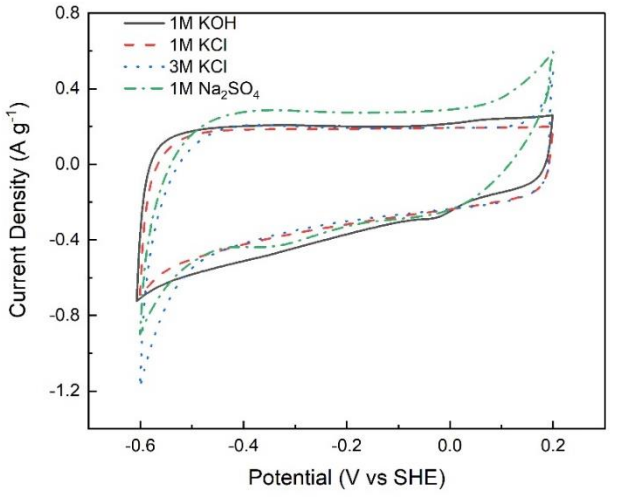

Figure 5.6 Cyclic voltammograms of Ni-FP carbonised at 800 ℃ in 1 M KOH, 1 M KCl, 1 M Na_2SO_4 and 3 M KCl at the scan rate of 2 mV s^{-1} from 0.2 to -0.6 V vs SHE.

The CV curves in the same potential range in 1 M Na_2SO_4 and 3 M KCl are similar to those discussed above, as shown in Figure 5.6. Therefore, the Ni-FP works better as a positive electrode material in alkaline than in neutral electrolytes due to faradaic contributions.

5.3.4 Removal of nickel particles

In a previous study, nickel particles were removed by immersing the Ni-FP in 30% HNO_3 and the consequent Ni-removed FP was used for supercapacitor application in a negative potential range (0 to -0.8 V vs Ag/AgCl).[2] It was also suggested in the work that nickel could lead to a faster graphitisation at 800 °C, which was normally 1500 °C without nickel treatment.[5, 8, 13]

To better understand the role of nickel in the material, the electrochemical performance of Ni-removed FP and FP without nickel treatment was also evaluated by CV. Both samples were carbonised at 800 °C, tested in 1M KOH as the electrolyte in two potential ranges (0.1 to -0.7 V and 0 to +0.7 V vs Hg/HgO), after which the results are compared to the CV of Ni-FP carbonised at 800 °C.

Figure 5.7 shows that the largest specific capacitance obtained from the enclosed curve area within the CV was observed in the Ni-removed sample in the potential range of 0.1 to -0.7 V. The value is more than three times as large as that of the Ni-FP sample, whereas non-nickel treated sample has the lowest capacitance. The reason is that more micropores were exposed to the electrolytes after the removal of nickel particles, which increased the accessibility of the material and thus the current response as well.[5]

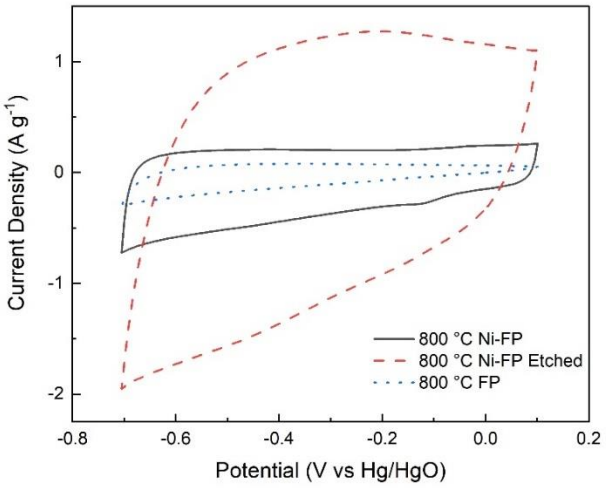

Figure 5.7 Cyclic voltammograms of 800 °C Ni-FP, Ni-FP Etched and FP in 1 M KOH at the scan rate of 2 mV s^{-1} in a potential range of 0.1 to -0.7 V.

However, the Ni-FP sample shows a higher enclosed area than the other two when CV was conducted in the potential window of 0 to 0.7 V, as shown in Figure 5.8. This enhanced electrochemical behaviour is owing to the faradaic process where electrons transfer between the electrode and the electrolyte, changing the oxidation state of $Ni(OH)_2$ as discussed previously. As for the FP sample without nickel treatment, its porosity and conductivity properties are poorer, therefore leading to the least competitive electrochemical performance in both potential windows among all three samples.

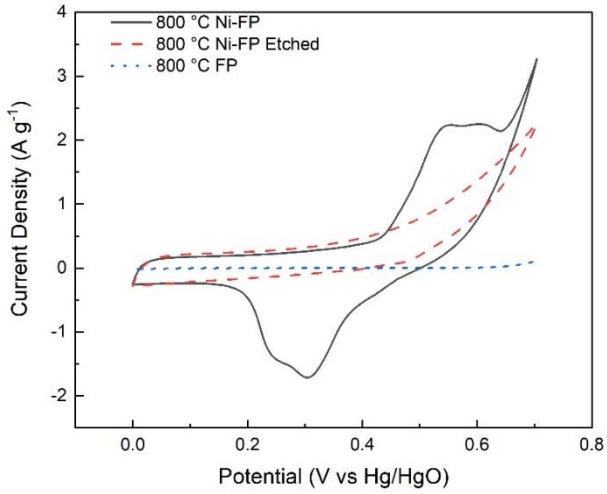

Figure 5.8 Cyclic voltammograms of 800 °C Ni-FP, Ni-FP Etched and FP in 1 M KOH at the scan rate of 2 mV s^{-1} in a positive potential window of 0 to +0.7 V.

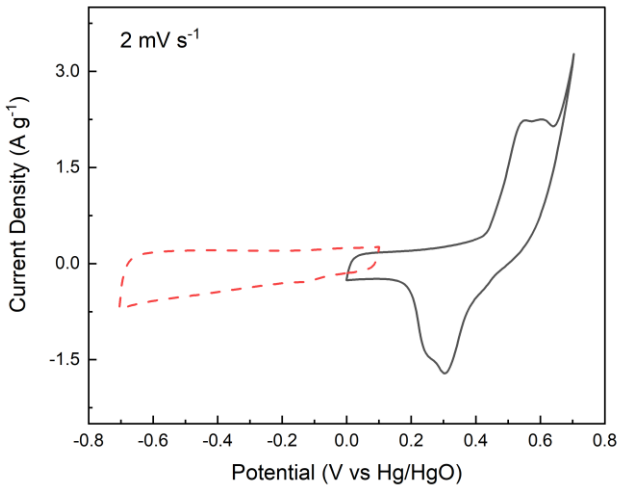

Figure 5.9 Comparison of CV curves of Ni-FP carbonised at 800 °C in 1 M KOH at the scan rate of 2 mV s^{-1} in two potential windows.

Figure 5.9 compares the CV curve of Ni-FP carbonised at 800 °C in the negative potential range to that in the positive range. In addition to the capacitive charge storage within both given potential windows, the faradaic behaviour of the Ni-FP in the positive potential window enables itself to be a promising positive faradaic electrode for energy storage devices.[9, 10, 14]

5.3.5 Influence of scan rate and temperature of carbonisation

The important roles of alkaline electrolytes and nickel for the application were discussed above. On the other hand, the structure of carbon also affects its performance as a supercapacitor. Hence, a prior question comes that what parameters can be changed when we convert cellulose-based biomass into conductive carbon via thermal treatment.[15] In this section, the influence of carbonisation temperature on the electrochemical properties of carbonised Ni-FP was examined. The nickel treatment was the same but samples were carbonised under different temperatures in vacuum at 700, 800, 900, 1000, 1100 and 1300 °C, respectively.

The electrochemical performance of the Ni-FP was first determined by CV in 1 M KOH from 0 to +0.7 V vs Hg/HgO. Figure 5.10 to 5.17 compare the CV curves of samples carbonised at different temperatures, with increasing scan rates at 2, 5, 10, 25, 50, 100 and 200 mV s^{-1}.

Figure 5.10 shows that samples carbonised at 800 °C and 900 °C exhibited larger current response than the other samples at the scan rate of 2 mV s^{-1}. Furthermore, the CV curve of the 800 °C sample consists of two couples of faradaic redox peaks, as labelled in Figure 5.10. The observed faradaic peaks are corresponded to the redox reactions of α and β-$Ni(OH)_2$.[16]

Figure 5.11 shows the enlarged CVs of the 600, 700, 1000, 1100 and 1300 °C samples between +0.3 and +0.6 V, indicating that although the current recorded was much lower than the 800 °C and 900 °C ones, redox peaks can still be observed.

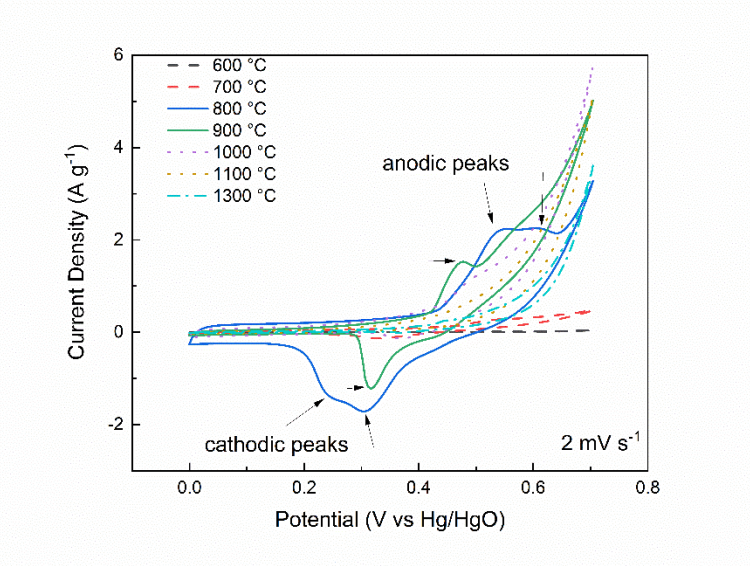

Figure 5.10 Cyclic voltammograms of 600 to 1300 ℃ Ni-FP in 1M KOH at the scan rate of 2 mV s^{-1} from 0 to +0.7 V. Peaks observed for 800 and 900 ℃ Ni-FP.

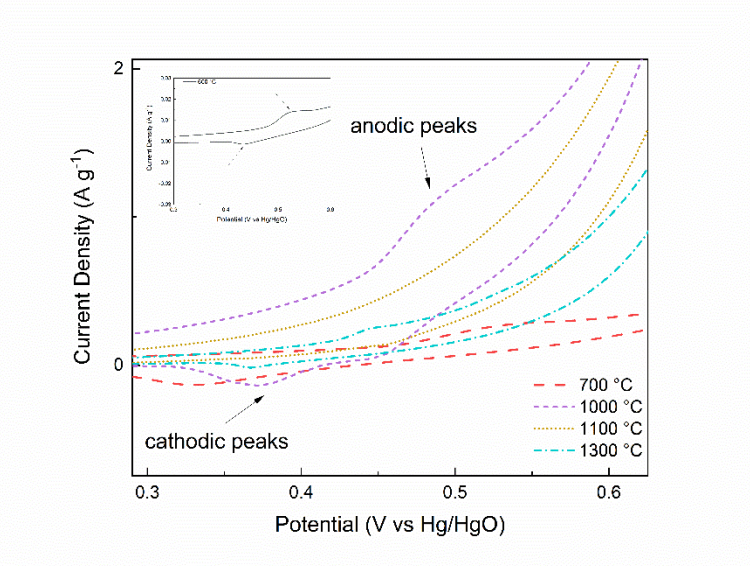

Figure 5.11 Close-up cyclic voltammograms of 600 (enlarged), 700, 1000, 1100 and 1300 °C Ni-FP at the scan rate of 2 mV s^{-1} between +0.3 and +0.6 V. Peaks also observed for these samples apart from 800 and 900 ℃ Ni-FP.

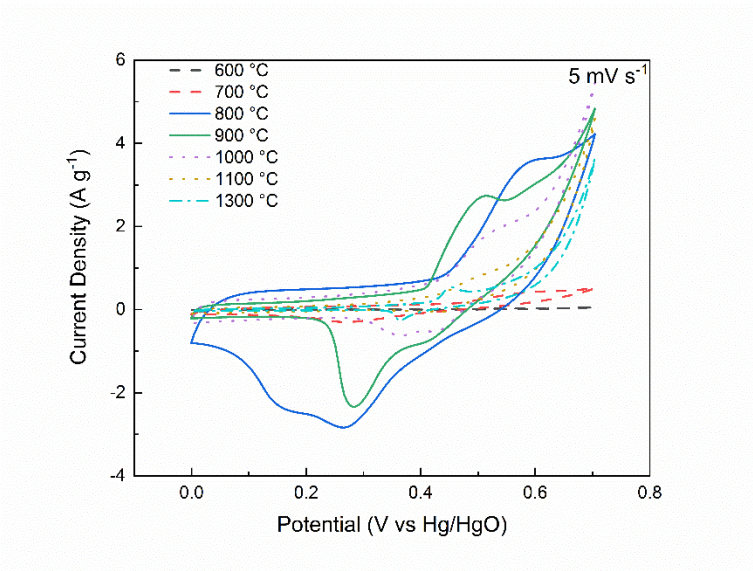

Figure 5.12 Cyclic voltammograms of 600 to 1300 ℃ Ni-FP in 1M KOH at the scan rate of 5 mV s^{-1} from 0 to +0.7 V. At 5 mV s^{-1}, CVs of 800 and 900 ℃ Ni-FP are observed with more distortion. Current response of other samples is still low.

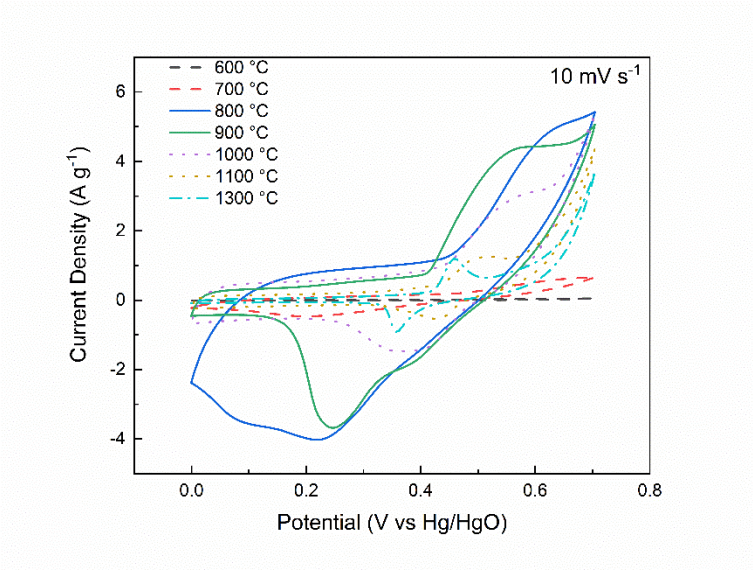

Figure 5.13 Cyclic voltammograms of 600 to 1300 ℃ Ni-FP in 1M KOH at the scan rate of 10 mV s^{-1} from 0 to +0.7 V. At 10 mV s^{-1}, CVs of 800 and 900 ℃ Ni-FP face further distortion compared to 5 mV s^{-1}. Current response of 1000 to 1300 ℃ Ni-FP starts increasing.

The CV curves are similar at low scan rates (5 and 10 mV s^{-1}) except the reduction peaks shifted to more negative values with the increase of the scan rate, whereas the anodic peaks shifted to more positive values and overlapped with the current from water oxidation process (i.e., oxygen evolution reaction) for the 800 °C and 900 °C samples, as shown in Figure 5.12 and 5.13.

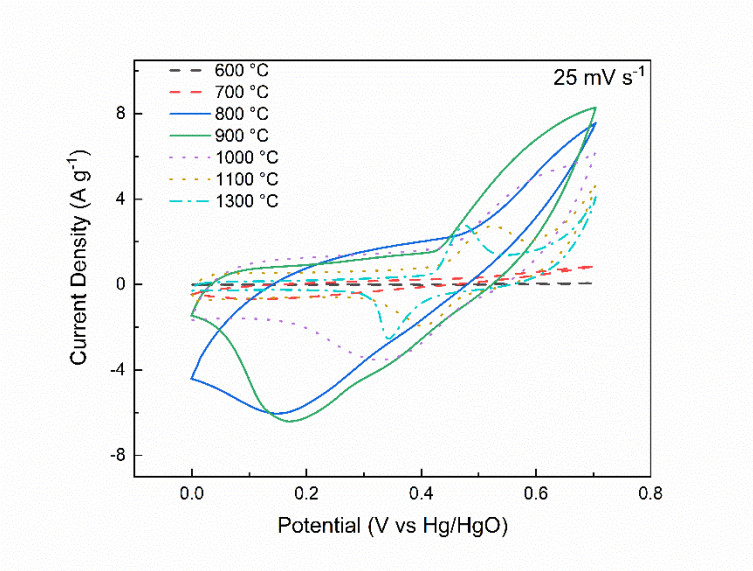

Figure 5.14 Cyclic voltammograms of 600 to 1300 ℃ Ni-FP in 1M KOH at the scan rate of 25 mV s^{-1} from 0 to +0.7 V. At 25 mV s^{-1}, CVs of 800 and 900 ℃ Ni-FP are further distorted, where anodic peaks disappear but cathodic peaks still exist. CVs of 1100 and 1300 ℃ Ni-FP are observed with peak separation.

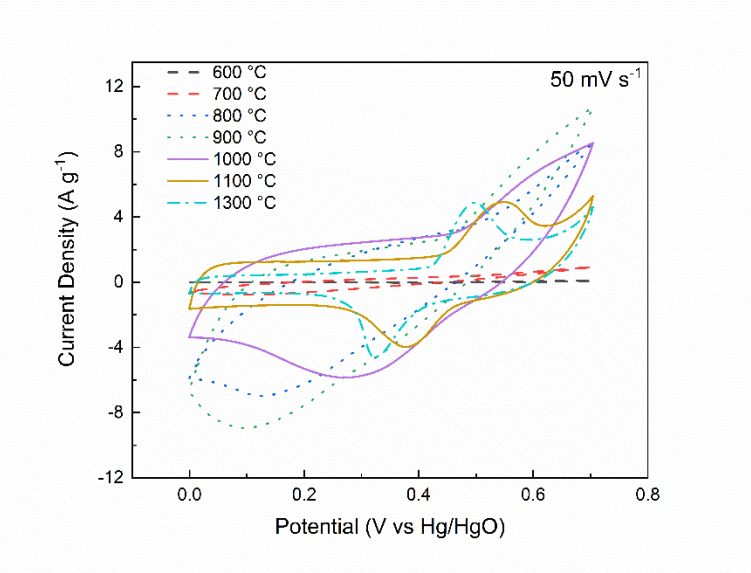

Figure 5.15 Cyclic voltammograms of 600 to 1300 ℃ Ni-FP in 1M KOH at the scan rate of 50 mV s^{-1} from 0 to +0.7 V. At 50 mV s^{-1}, CVs of 800 and 900 ℃ Ni-FP are further distorted as well as CV of 1000 ℃ Ni-FP. CVs of 1100 and 1300 ℃ Ni-FP are still observed with clear peak separation and higher current response.

As shown in Figure 5.14 and 5.15, when the scan rate increased to 25 and 50 mV s^{-1}, the CV shapes of the 800, 900 and 1000 °C samples faced more distortion and the oxidation peaks disappeared. Meanwhile, the reduction peaks also became less obvious when the scan rate further reached 100 and 200 mV s^{-1} for these samples. However, we observed well-defined redox peaks from the CV curves of the 1100 and 1300 °C samples at all medium and high scan rates (25 to 200 mV s^{-1}), as shown in Figure 5.14 to 5.17. In particular, Figure 5.17 shows that the CV of the 1300 ℃ sample still exhibited a symmetrical peak shape at the highest scan rate of 200 mV s^{-1}.

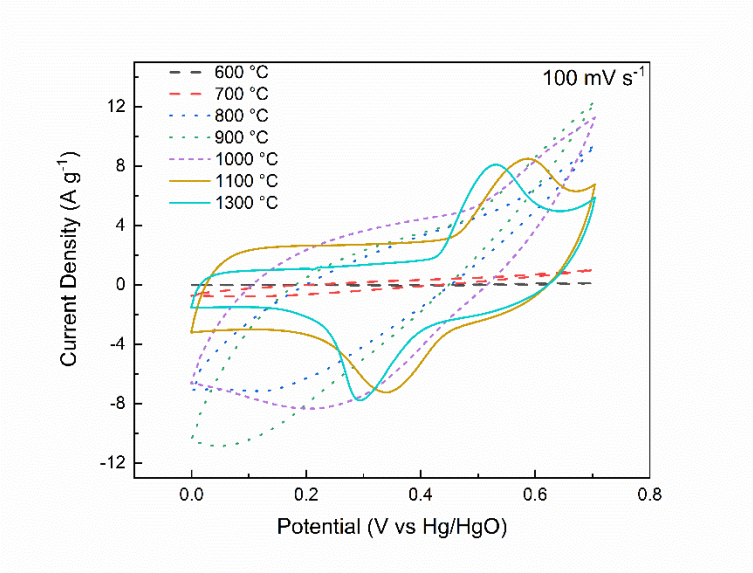

Figure 5.16 Cyclic voltammograms of 600 to 1300 ℃ Ni-FP in 1M KOH at the scan rate of 100 mV s^{-1} from 0 to +0.7 V. At 100 mV s^{-1}, CVs of 800 and 900 ℃ Ni-FP are further distorted with cathodic peaks also disappeared. CV of 1000 ℃ Ni-FP still has cathodic peak. Well-defined peaks and CVs with high current are observed for 1100 and 1300 ℃ Ni-FP.

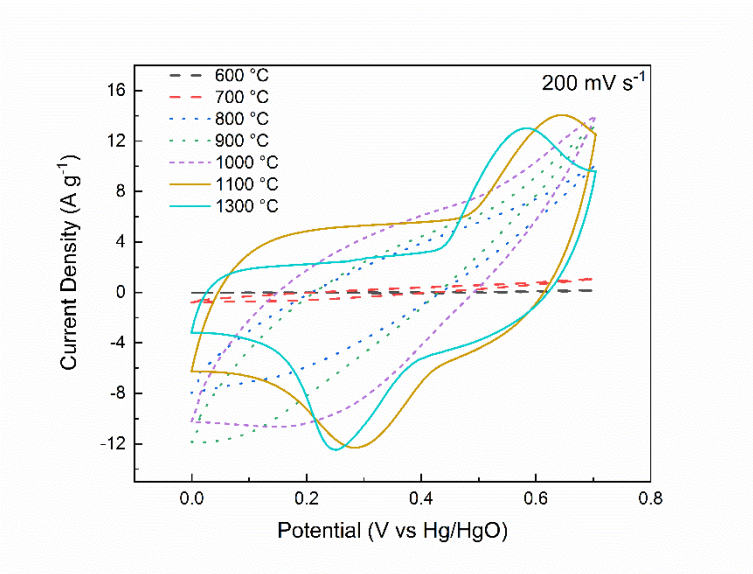

Figure 5.17 Cyclic voltammograms of 600 to 1300 ℃ Ni-FP in 1M KOH at the scan rate of 200 mV s^{-1} from 0 to +0.7 V. At 200 mV s^{-1}, CV of 1300 ℃ Ni-FP is still well-defined, but CV of 1100 ℃ Ni-FP faces distortion at high potential. CVs of 800, 900 & 1000 Ni-FP are more distorted. In addition, CV signals of 600 & 700 ℃ Ni-FP are low at all scan rates.

It is known that peak separation in CV is commonly used to evaluate the reversibility of the redox reaction. In general, all samples have better reversibility at low scan rates. However, the observation above indicates that the samples have slow electrode kinetics of charge transfer and limited ion transport to accessible pore surfaces with increasing scan rates, resulting in a reduced reversibility of the process, whereas the 1100 and 1300 °C samples show lower peak separation dependency on the scan rate and more excellent reversibility due to higher electrical conductivity and lower resistance.[10]

The specific capacitance was calculated from the integrated area of the CV curves, according to the following equation:

$$C = \frac{\int I dE}{2mv\Delta E} \tag{5-7}$$

Where C is the specific capacitance (F g^{-1}), I is the current (A), E is the potential (V), m is the mass of the material (g), v is the scan rate (V s^{-1}) and ΔE is the potential window (V).

The cyclic voltammograms are shown in Figure 5.18 (a) & (b) for 800 °C Ni-FP, (c) & (d) for 1100 °C Ni-FP, and the calculated specific capacitance is listed in Table 5.1. CVs of Ni-FP carbonised at others temperatures (600 to 1300 °C) are shown in Figure A.7 (Appendix).

Table 5.1 The specific capacitance (F g^{-1}) of Ni-FP carbonised at different temperatures.

	Temperature of carbonisation (°C)						
Scan rate (mV s^{-1})	600	700	800	900	1000	1100	1300
2	0.974	27.0	258	131	96.9	70.6	34.9
5	0.783	21.1	219	120	77.8	30.8	19.8
10	0.555	15.5	147	116	74.0	28.3	18.8
25	0.383	7.39	72.8	92.1	66.9	32.2	21.9
50	0.284	3.77	38.3	54.9	54.1	34.3	24.8
100	0.198	1.89	19.4	25.0	35.8	33.9	25.7
200	0.130	0.906	9.42	11.8	20.4	30.0	24.2

The CV curve shows tiny current flow and specific capacitance (< 1 F g^{-1}) for the Ni-FP carbonised at 600 °C in spite of observed redox peaks. The current response and the specific capacitance (0.9 – 27 F g^{-1}) saw a rise at 700 °C, as shown in Table 5.1. At the low scan rates (2, 5 & 10 mV s^{-1}), the specific capacitance reached a maximum for the Ni-FP carbonised at 800 °C (e.g., 258 F g^{-1} at 2 mV s^{-1}, 219 F g^{-1} at 5 mV s^{-1} and 147 F g^{-1} at 10 mV s^{-1}) in Figure 5.18 (a) & Table 5.1, and dropped gradually for the samples carbonised at higher temperatures of 900 to 1300 °C (~ 96.9 to 18.8 F g^{-1}). As discussed above, the CV curves faced more distortion at higher scan rates for all samples but those carbonised at higher temperatures were less affected (e.g., Figure 5.18 (c) & (d) for 1100 °C Ni-FP). As a consequence, the specific capacitance of the Ni-FP carbonised at 900 °C was the highest among all samples at the medium scan rates of 25 mV s^{-1} (92.1 F g^{-1}) and 50 mV s^{-1} (54.9 F g^{-1}). When the scan rate

increased to 100 and 200 mV s^{-1}, the best results were recorded for the Ni-FP samples carbonised at 1000 °C (35.8 F g^{-1}) and 1100 °C (30.0 F g^{-1}), respectively.

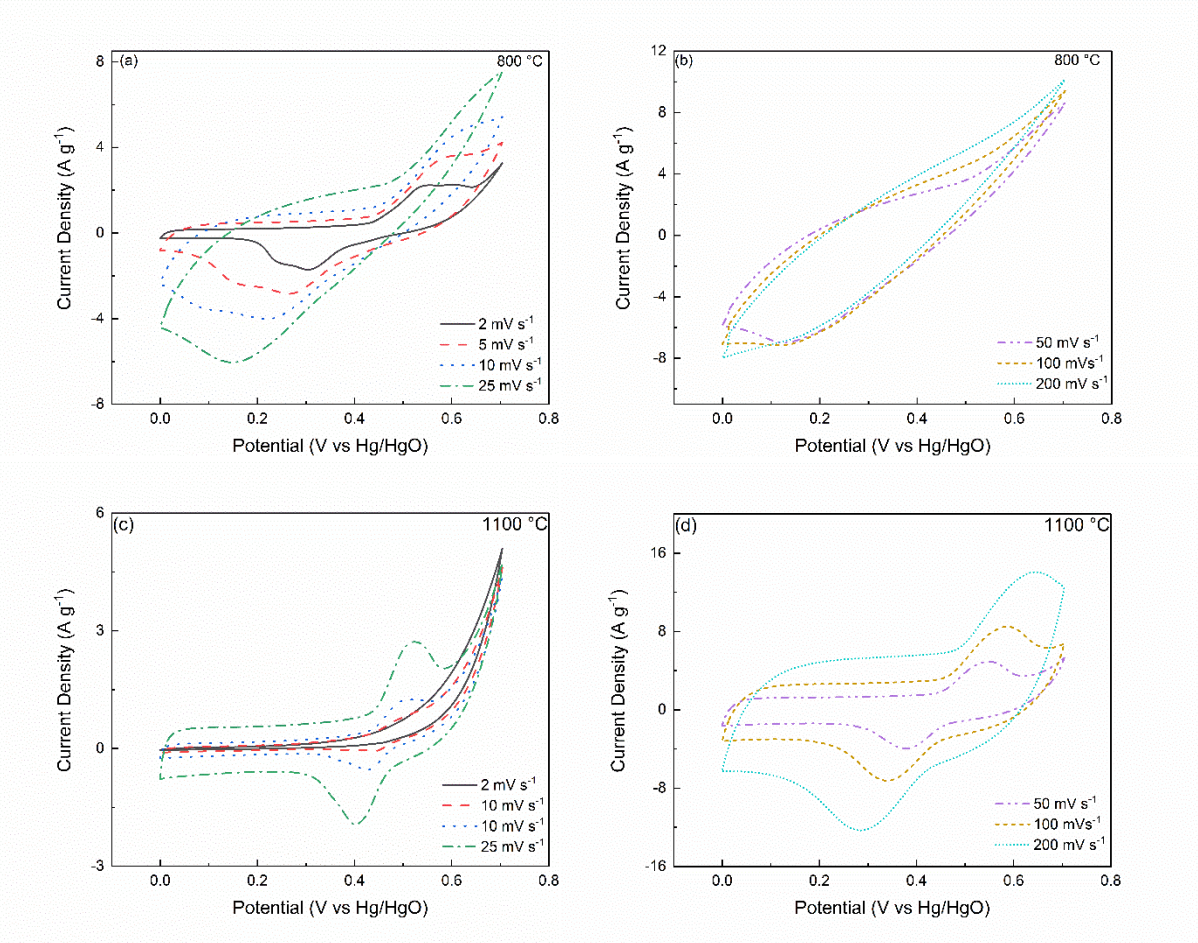

Figure 5.18 Cyclic voltammograms of 800 °C Ni-FP at (a) 2 to 25 mV s^{-1}, (b) 50 to 200 mV s^{-1}, and 1100 °C Ni-FP at (c) 2 to 25 mV s^{-1}, (d) 50 to 200 mV s^{-1}, in 1M KOH in a positive potential range of 0 to +0.7 V. 800 °C Ni-FP only shows CVs with well-defined peaks at low scan rates in (a) but faces distortion at high scan rates in (b); 1100 °C Ni-FP still shows CVs with well-defined peaks at all scan rates in (c) & (d).

The reasons are considered as follow:

- During carbonisation, most cellulose content was removed and pores were generated. The porosity reached its highest value at 800 °C and then went down as pore structure was destroyed at higher temperatures. The samples carbonised at higher temperatures

have larger pore size, but lower pore volume and smaller specific surface area. It is known that more micropores and suitable pore size are related to better double-layer capacitive performance and easier diffusion of ions into pores.[5]

- Meanwhile, as the temperature of carbonisation increased, the electrical conductivity of the materials increased, which led to a decrease in the resistance of the system as higher temperature could contribute to removal of oxygen-containing functional groups and thus improve the degree of graphitisation. The increase in conductivity gives rise to faster faradaic processes without which the current response could be hindered.[17]
- Therefore, a high capacitive response was observed for the 800 °C Ni-FP at low scan rates. Although lower conductivity is correlated with a decrease in the specific capacitance, the high surface area and enough time for the faradaic reaction and diffusion of ions into pores could easily compensate for the loss.
- Also, better results were obtained for the samples carbonised at higher temperatures (900, 1000 and 1100 °C) at faster scan rates, where quick mass transport and charge transfer could still be achieved because of larger pore size and better conductivity. However, when the temperature of carbonisation reached 1300 °C, the specific capacitance dropped again at all scan rates because the increase in conductivity and the pore size could not counteract the closure of micropores and interparticle voids, and the lower surface area.[18]

The correlation between the scan rate and the specific capacitance of the Ni-FP is shown in Figure 5.19. Overall, the specific capacitance values decreased with increasing scan rates, as the electrolyte ions lacked sufficient time to approach the inner pore surfaces of the Ni-FP samples and the electrode kinetics was slow at higher scan rates. At low scan rates, the ions intercalated well with the outer and inner pore surfaces of the material and the electrode reaction can keep pace with the electron flow rate.[19] Such a capacitance decrease can be less obvious with the increase of the carbonisation temperature. For example, the Ni-FP carbonised at 1100 °C still had its 70% capacitance retention at high scan rates, as shown in Figure 5.20. In addition, the 1100 °C and 1300 °C samples face increase of specific capacitance at the scan rates from 10 to 100 mV s^{-1} due to further activation of the materials.

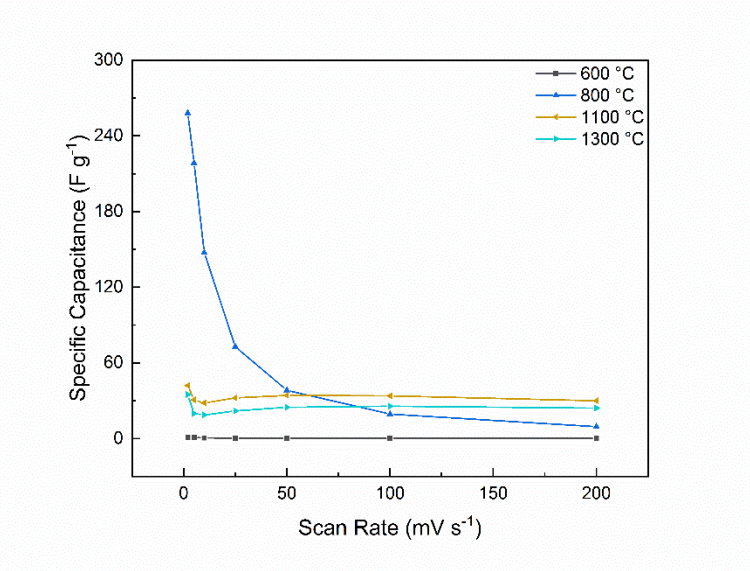

Figure 5.19 The specific capacitance of 600, 800, 1100 and 1300 °C Ni-FP as a function of the scan rate.

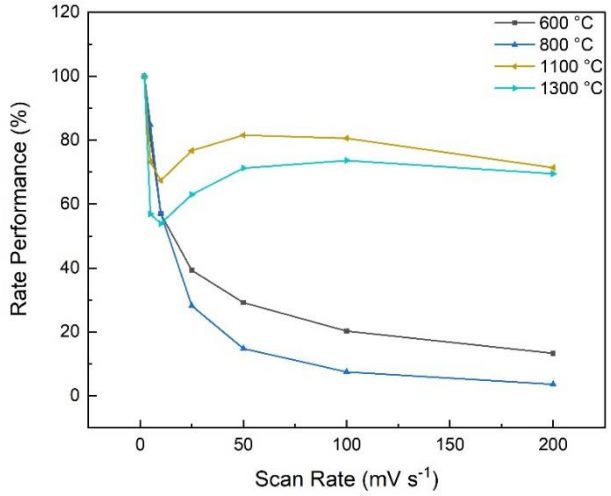

Figure 5.20 The specific capacitance retention of 600, 800, 1100 and 1300 °C Ni-FP as a function of the scan rate.

It is also noticed from Figure 5.21 that the CV curve has an excellent linear relationship between the cathodic peak current and the square root of the scan rate for 1100 °C Ni-FP, indicating that the faradaic electrode reaction is a diffusion-controlled process.[20]

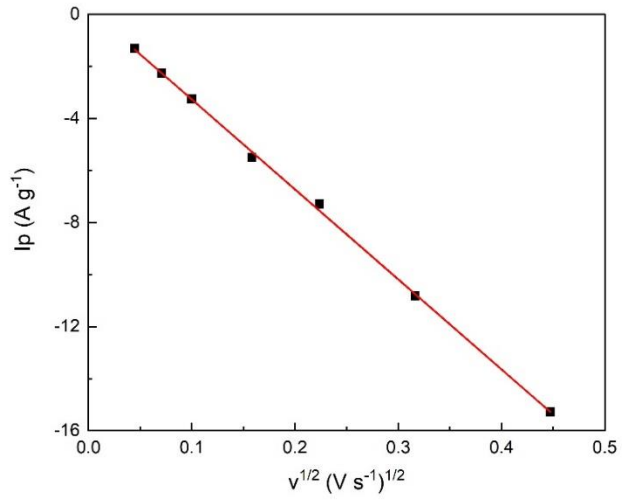

Figure 5.21 Plots of I_p (cathodic peak) as a function of $v^{1/2}$ for Ni-FP carbonised at 1100 °C.

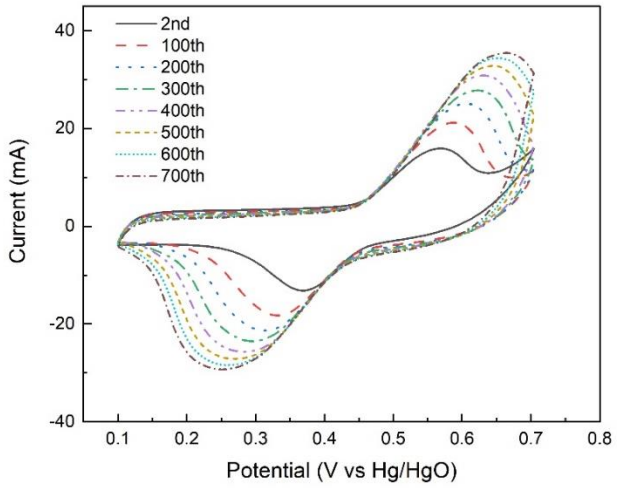

Figure 5.22 Cyclic voltammograms of 1100 °C Ni-FP at the scan rate of 50 mV s^{-1} for 700 cycles.

A significant increase in currents and peak separation was noted with increasing cycle number at a constant scan rate of 50 mV s^{-1} for 1100 °C Ni-FP, which showed an enhanced electrochemical performance and a slightly degraded reversibility in Figure 5.22. The specific capacitance would increase in the first ~700 cycles and then became stable, as shown in Figure 5.23, presumably owing to the gradual conversion of conductive Ni to faradaic $Ni(OH)_2$ by electrochemical oxidation and activation of pores in the carbon-based material during the cycling.[10]

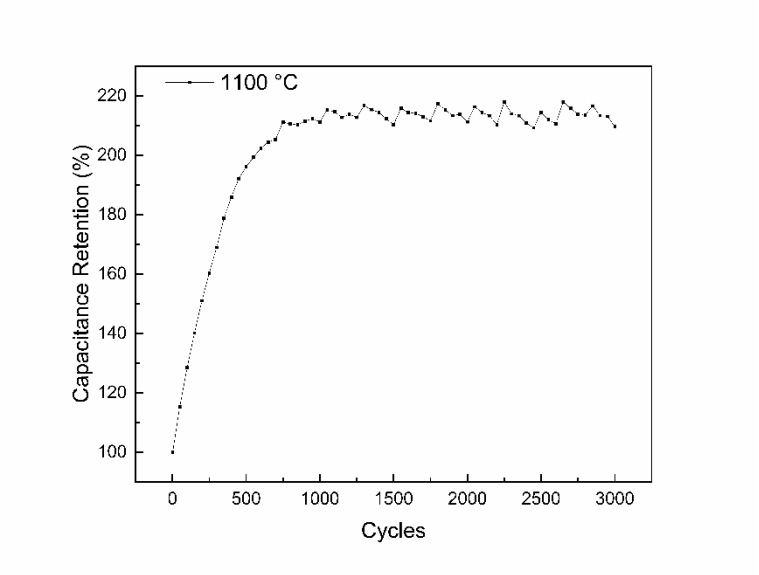

Figure 5.23 Cycling performance of 1100 ℃ Ni-FP at the scan rate of 50 mV s^{-1} for 3000 cycles.

5.3.6 Galvanostatic charge-discharge

The specific capacitance of the 800 ℃ and the 1100 ℃ Ni-FP was also calculated from the GCD measurements at different current densities of 0.5, 1, 2.5, 5 and 10 A g^{-1}, according to the following:

$$C_{galvanostatic\ discharge} = \int Idt/\Delta E \quad (5\text{-}8)$$

Where I is the discharge current density ($A \cdot g^{-1}$), t is the discharge time (s) and ΔE is the potential window (V).

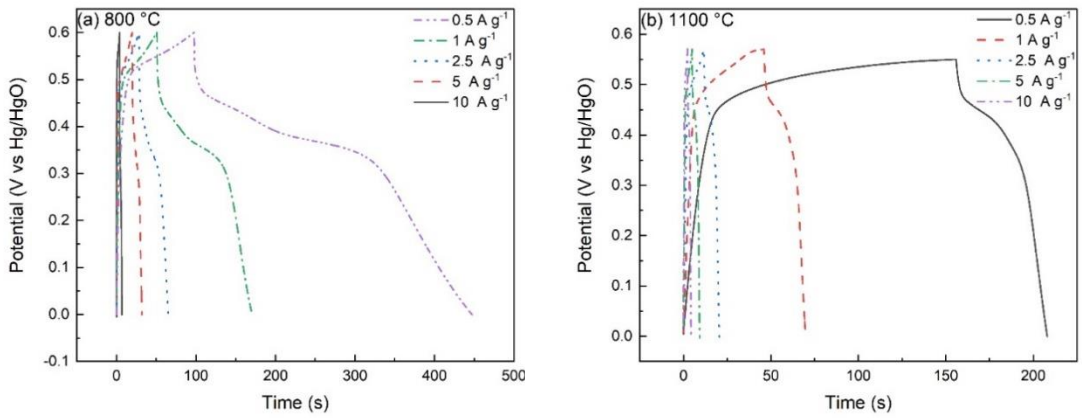

Figure 5.24 GCD curves of (a) 800 °C & (b) 1100 °C Ni-FP at various current densities. Non-linear discharge curves are observed due to contributions from faradaic battery-type materials. Results from the figure are calculated and listed in Table 5.2.

Table 5.2 The specific capacitance (F g^{-1}) of 800 & 1100 °C Ni-FP at different current densities.

	Current Density (A g^{-1})				
Temperature of Carbonisation (°C)	0.5	1	2.5	5	10
800	291	199	153	101	49.2
1100	45.7	41.8	38.7	38	36.3

The nonlinear curves display charge/discharge plateaus originating from the conversion of $Ni(OH)_2$ to NiOOH, indicating a typical faradaic battery-type electrode behaviour.[21] Table 5.2 and Figure 5.24 show the gravimetric specific capacitance at different current densities according to the equation above. Although the specific capacitance of the 800 °C Ni-FP is much higher than that of the 1100 °C Ni-FP at 0.5 A g^{-1}, this value of the 800 °C Ni-FP decreased more rapidly than that of the 1100 °C Ni-FP when the current density increased, as shown in Figure 5.25 and 5.26. The reason is that a higher conductivity and a larger pore size

of the electrode lead to better rate performance by maintaining fast electron transfer and ion transport.[5, 22] The specific capacitance and rate performance of the samples are consistent with the results of the cyclic voltammograms analysed previously.

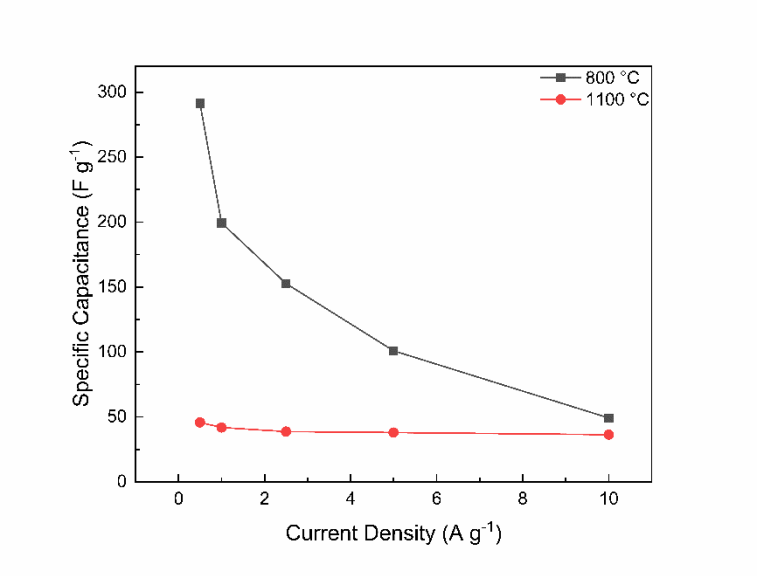

Figure 5.25 The specific capacitance of 800 & 1100 °C Ni-FP at different current densities.

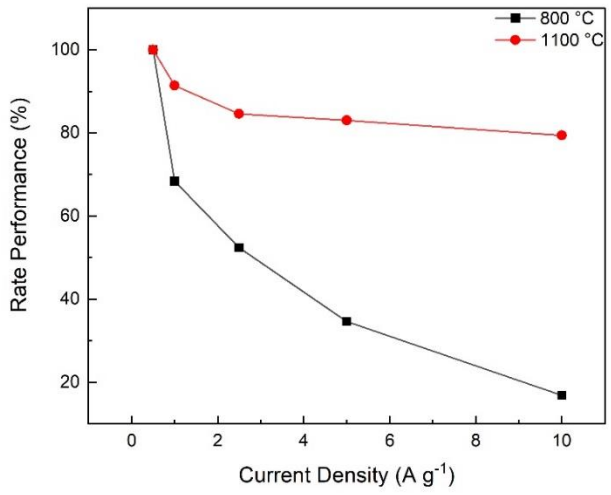

Figure 5.26 The capacitance retention of 800 & 1100 °C Ni-FP at different current densities.

5.3.7 Stability test

The cycling stability is also crucial for the practical application of the electrode. Therefore, the cycling performances of the 800 °C and the 1100 °C Ni-FP were carried out up to 2000 cycles at a high current density of 5 A g^{-1}. As shown in Figure 5.27, the capacitance retention of the 800 °C Ni-FP is 74.3% after 1000 cycles and 54.4% after 2000 cycles. However, the 1100 °C Ni-FP sample still retained about 99.3% of its capacitance after 2000 cycles. The excellent capacitance retention and rate performance of 1100 °C Ni-FP confirm potential application of nickel hydroxide modified biomass-derived carbon supercapacitors in the future.

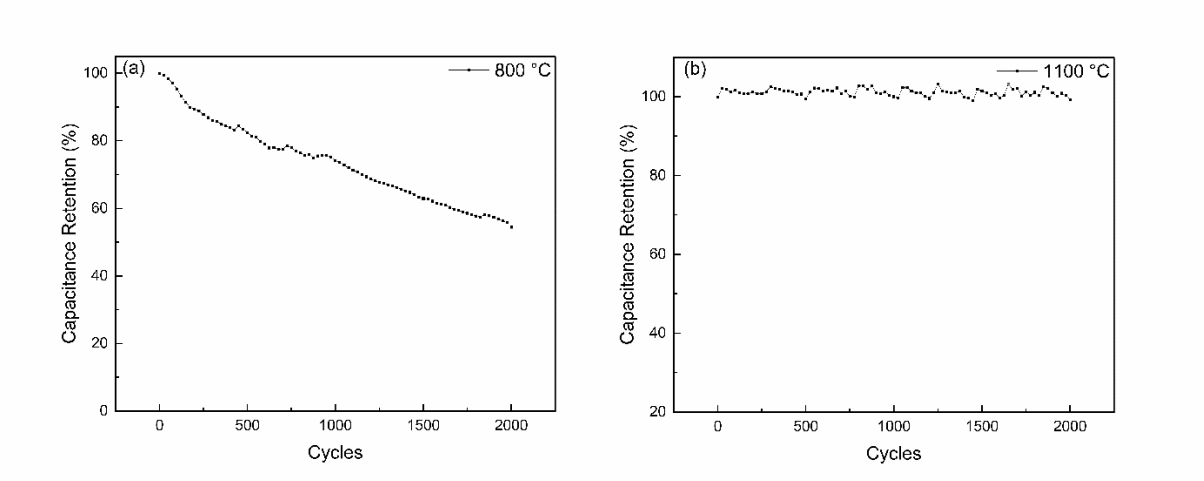

Figure 5.27 Plots of specific capacitance retention of (a) 800 °C & (b) 1100 °C Ni-FP against cycling number.

5.3.8 Electrochemical impedance spectroscopy

EIS is a useful tool for the study of the characteristics of conductivity and charge transport in the material/electrolyte interface.[23] Both equivalent series resistance (ESR, the intersection of the curves at the real part) and charge transfer resistance (R_{ct}, the semicircles in Nyquist plots) increased after cycling. The Nyquist plot of the 1100 °C Ni-FP indicates a lower R_{ct} and a higher electrical conductivity compared to those of the 800 °C Ni-FP, which explains better

electrochemical performance at higher scan rates, larger current densities and more cycling numbers, as shown in Figure 5.28 and 5.29.

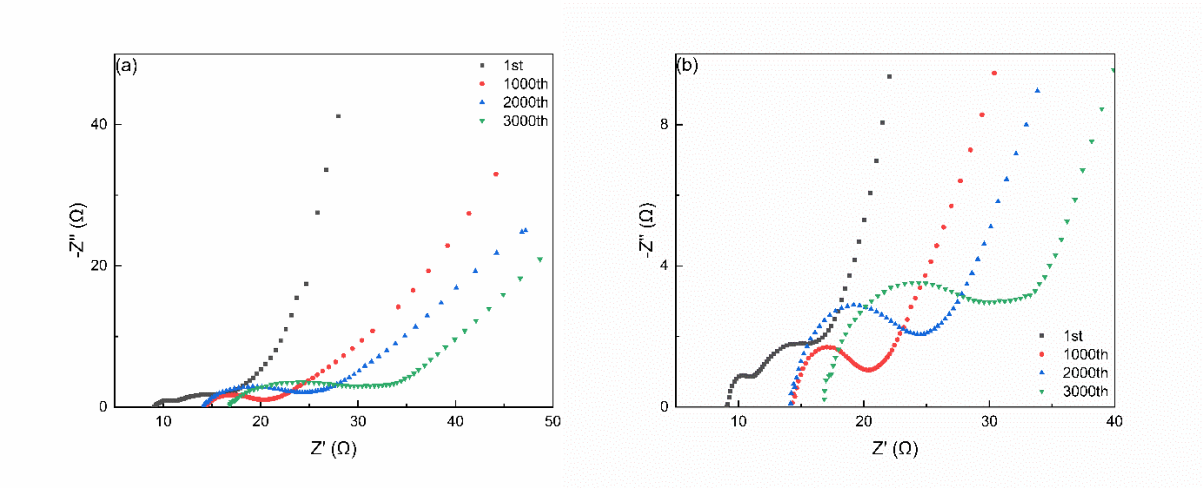

Figure 5.28 (a) Nyquist plots and high-frequency region (b) of 800 °C Ni-FP after 1st, 1000th, 2000th & 3000th cycles. Both ESR and R_{ct} increased with cycles.

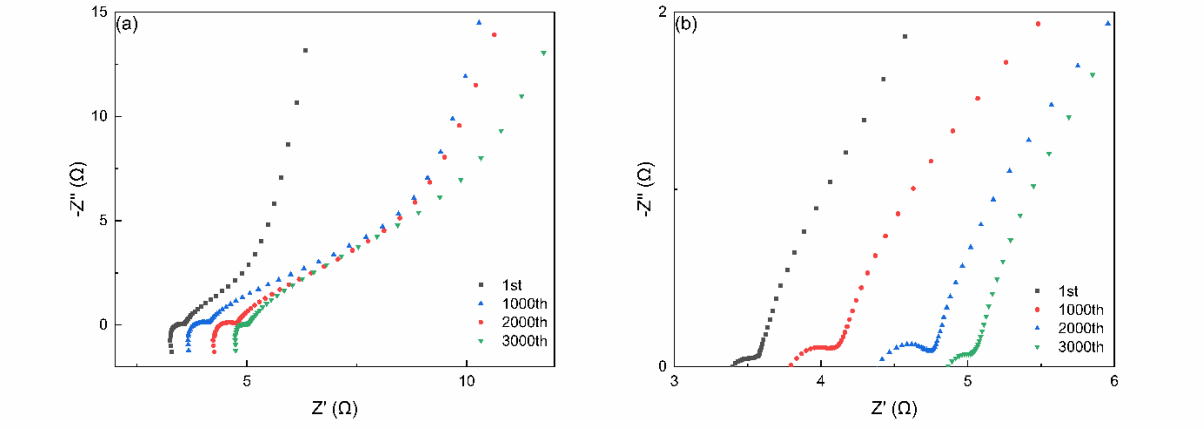

Figure 5.29 (a) Nyquist plots and high-frequency region (b) of 1100 °C Ni-FP after 1st, 1000th, 2000th & 3000th cycles. The ESR and R_{ct} values of 1100 °C Ni-FP are lower compared to 800 °C Ni-FP in Figure 5.28.

5.4 Conclusion and comparison

To clarify the electrochemical performance of Ni-FP in this work for supercapacitor applications, the results are listed and compared to other carbon-based composite materials modified with nickel hydroxide species or transition metal oxides in Table 5.3. The specific capacitance of Ni-FP carbonised at 800 °C is comparable to some reported carbon-based composite electrode materials, but its capacitance retention is worse as a result of the typical drawback of battery-type materials. However, Ni-FP carbonised at 1100 °C shows longer cycle life with subtle capacitance loss, indicating both high specific capacitance and capacitance retention might be achieved simultaneously in Ni-FP materials with more precise modifications in the future.

Table 5.3 Electrochemical performance of carbon-based composite electrodes modified with $Ni(OH)_2$ or transition metal oxides for supercapacitors.

Sample	Specific Capacitance ($F\ g^{-1}$)	Scan Rate ($mV\ s^{-1}$)	Current Density ($A\ g^{-1}$)	Capacitance Retention
Ni-FP 800 °C (this work)	258	2	/	~74.3%, 1000 cycles
Ni-FP 1100 °C (this work)	71	2	/	~99.3%, 2000 cycles
$Ni(OH)_2$/Graphene[9]	218	1	/	~94.3%, 3000 cycles
NiO/CNTs[24]	245	2	/	/
MnO_2/CNTs[25]	115	/	0.5	~95%, 1000 cycles
NiO/Activated carbon[26]	90	10	/	/

In addition, it is worth mentioning that the specific capacitance of NiO/carbon or $Ni(OH)_2$/carbon composites reported in some studies reaches more than 3000 F g^{-1}, which is even higher than the theoretical specific capacitance of $Ni(OH)_2$ (i.e., 2081 F g^{-1}).[3, 4, 27] The possible reason is that only the weight of electroactive materials is considered in the capacitance calculation, but the weight of carbon substrates, binders and conductive additives (i.e., 'dead weight') is excluded, which does not compromise Ni-FP prepared in this work as a competitive candidate for supercapacitor applications.

In this work, we have successfully developed an approach to fabricating Ni-FP and converted the as-prepared Ni-FP to energy storage materials by electrochemical activation and cycling in alkaline solutions on the positive potential side where the material exhibits an obvious faradaic response, superior specific capacitance and excellent cycling stability. The Ni-FP carbonised at 800 °C showed a high specific capacitance of 258 F g^{-1} while the material carbonised at 1100 °C retained 99.3% of its original specific capacitance at a high discharge current density of 5 A g^{-1} after 2000 cycles due to their faradic battery-type behaviour. Additionally, Ni etched FP provided ideal electric double-layer capacitance on the negative potential side. This study illustrates that the composite possesses potential as an active material in high-performance energy-storage applications. Furthermore, the carbon substrate derived from biomass material in this study, which is more environmentally friendly and economical, could be a promising substitute for other novel carbon materials such as graphene and carbon nanotubes.

References

(1) Zhai, Y.; Dou, Y.; Zhao, D.; Fulvio, P. F.; Mayes, R. T.; Dai, S. Carbon Materials for Chemical Capacitive Energy Storage. *Advanced Materials* **2011**, *23* (42), 4828-4850. DOI: https://doi.org/10.1002/adma.201100984.

(2) Feng, L.; Zhu, Y.; Ding, H.; Ni, C. Recent progress in nickel based materials for high performance pseudocapacitor electrodes. *Journal of Power Sources* **2014**, *267*, 430-444. DOI: https://doi.org/10.1016/j.jpowsour.2014.05.092.

(3) Faraji, S.; Ani, F. N. Microwave-assisted synthesis of metal oxide/hydroxide composite electrodes for high power supercapacitors – A review. *Journal of Power Sources* **2014**, *263*, 338-360. DOI: https://doi.org/10.1016/j.jpowsour.2014.03.144.

(4) Zhang, L.; Shi, D.; Liu, T.; Jaroniec, M.; Yu, J. Nickel-based materials for supercapacitors. *Materials Today* **2019**, *25*, 35-65. DOI: https://doi.org/10.1016/j.mattod.2018.11.002.

(5) Jiang, L.; Seong, Y.-H.; Han, S. O.; Kim, H.; Kim, H. H.; Foord, J. S. Nickel treatment of biomass-derived nanocarbon for energy devices. *Carbon* **2018**, *130*, 724-729. DOI: https://doi.org/10.1016/j.carbon.2018.01.063.

(6) Beda, A.; Le Meins, J.-M.; Taberna, P.-L.; Simon, P.; Matei Ghimbeu, C. Impact of biomass inorganic impurities on hard carbon properties and performance in Na-ion batteries. *Sustainable Materials and Technologies* **2020**, *26*, e00227. DOI: https://doi.org/10.1016/j.susmat.2020.e00227.

(7) Jiao, X.; Qiu, Y.; Zhang, L.; Zhang, X. Comparison of the characteristic properties of reduced graphene oxides synthesized from natural graphites with different graphitization degrees. *RSC Advances* **2017**, *7* (82), 52337-52344, 10.1039/C7RA10809E. DOI: 10.1039/C7RA10809E.

(8) Jiang, L.; Nelson, G. W.; Kim, H.; Sim, I.; Han, S. O.; Foord, J. S. J. C. Cellulose‐derived supercapacitors from the carbonisation of filter paper. **2015**, *4* (5), 586-589.

(9) Yan, J.; Fan, Z.; Sun, W.; Ning, G.; Wei, T.; Zhang, Q.; Zhang, R.; Zhi, L.; Wei, F. Advanced Asymmetric Supercapacitors Based on Ni(OH)2/Graphene and Porous Graphene Electrodes with High Energy Density. *Advanced Functional Materials* **2012**, *22* (12), 2632-2641, https://doi.org/10.1002/adfm.201102839. DOI: https://doi.org/10.1002/adfm.201102839 (acccessed 2021/04/27).

(10) Urhan, B. K.; Demir, Ü. Electrochemical fabrication of Ni or Ni(OH)2@Ni nanoparticle-decorated reduced graphene oxide for supercapacitor applications. *Electrochimica Acta* **2019**, *302*, 109-118. DOI: https://doi.org/10.1016/j.electacta.2019.02.020.

(11) Giovanelli, D.; Lawrence, N. S.; Jiang, L.; Jones, T. G. J.; Compton, R. G. Electrochemical determination of sulphide at nickel electrodes in alkaline media: a new electrochemical sensor. *Sensors and Actuators B: Chemical* **2003**, *88* (3), 320-328.

(12) Ma, R.; Lin, G.; Zhou, Y.; Liu, Q.; Zhang, T.; Shan, G.; Yang, M.; Wang, J. A review of oxygen reduction mechanisms for metal-free carbon-based electrocatalysts. *npj Computational Materials* **2019**, *5* (1), 78. DOI: 10.1038/s41524-019-0210-3. He, Y.; Zhang, Y.; Li, X.; Lv, Z.; Wang, X.; Liu, Z.; Huang, X. Capacitive mechanism of oxygen functional groups on carbon surface in supercapacitors. *Electrochimica Acta* **2018**, *282*, 618-625. DOI: https://doi.org/10.1016/j.electacta.2018.06.103.

(13) Jiang, L.; Nelson, G. W.; Kim, H.; Sim, I. N.; Han, S. O.; Foord, J. S. Cellulose-Derived Supercapacitors from the Carbonisation of Filter Paper. *ChemistryOpen* **2015**, *4* (5), 586-589. DOI: https://doi.org/10.1002/open.201500150.

(14) Zhang, J. T.; Liu, S.; Pan, G. L.; Li, G. R.; Gao, X. P. A 3D hierarchical porous α-Ni(OH)2/graphite nanosheet composite as an electrode material for supercapacitors. *Journal*

of Materials Chemistry A **2014**, *2* (5), 1524-1529, 10.1039/C3TA13578K. DOI: 10.1039/C3TA13578K.

(15) Jiang, L.; Nelson, G. W.; Han, S. O.; Kim, H.; Sim, I. N.; Foord, J. S. J. E. A. Natural cellulose materials for supercapacitors. **2016**, *192*, 251-258.

(16) Wang, H.; Casalongue, H. S.; Liang, Y.; Dai, H. Ni(OH)2 Nanoplates Grown on Graphene as Advanced Electrochemical Pseudocapacitor Materials. *Journal of the American Chemical Society* **2010**, *132* (21), 7472-7477. DOI: 10.1021/ja102267j. Mao, Y.; Zhou, B.; Peng, S. Simple deposition of mixed α, β-nickel hydroxide thin film onto nickel foam as high-performance supercapacitor electrode material. *Journal of Materials Science: Materials in Electronics* **2020**, *31* (12), 9457-9467. DOI: 10.1007/s10854-020-03485-6.

(17) Gutić, S. J.; Kozlica, D. K.; Korać, F.; Bajuk-Bogdanović, D.; Mitrić, M.; Mirsky, V. M.; Mentus, S. V.; Pašti, I. A. Electrochemical tuning of capacitive response of graphene oxide. *Physical Chemistry Chemical Physics* **2018**, *20* (35), 22698-22709.

(18) Jiang, L.; Han, S. O.; Pirie, M.; Kim, H. H.; Seong, Y.-H.; Kim, H.; Foord, J. S. Seaweed biomass waste-derived carbon as an electrode material for supercapacitor. *Energy & Environment* **2021**, *32* (6), 1117-1129. DOI: 10.1177/0958305x19882398.

(19) Zheng, D.; Li, M.; Li, Y.; Qin, C.; Wang, Y.; Wang, Z. A Ni (OH) 2 nanopetals network for high-performance supercapacitors synthesized by immersing Ni nanofoam in water. *Beilstein journal of nanotechnology* **2019**, *10* (1), 281-293.

(20) Faulkner, L. R.; Bard, A. J. *Electrochemical methods: fundamentals and applications*; John Wiley and Sons, 2002.

(21) Brisse, A.-L.; Stevens, P.; Toussaint, G.; Crosnier, O.; Brousse, T. $Ni(OH)_2$ and NiO Based Composites: Battery Type Electrode Materials for Hybrid Supercapacitor Devices. *Materials (Basel)* **2018**, *11* (7), 1178. DOI: 10.3390/ma11071178 PubMed.

(22) Jiang, L.; Shanmuganathan, S.; Nelson, G. W.; Han, S. O.; Kim, H.; Na Sim, I.; Foord, J. S. Hybrid system of nickel–cobalt hydroxide on carbonised natural cellulose materials for supercapacitors. *Journal of Solid State Electrochemistry* **2018**, *22* (2), 387-393. DOI: 10.1007/s10008-017-3723-z. Sun, X.; Wang, G.; Hwang, J.-Y.; Lian, J. Porous nickel oxide nano-sheets for high performance pseudocapacitance materials. *Journal of Materials Chemistry* **2011**, *21* (41), 16581-16588.

(23) Li, R.; Hu, Z.; Shao, X.; Cheng, P.; Li, S.; Yu, W.; Lin, W.; Yuan, D. Large Scale Synthesis of NiCo Layered Double Hydroxides for Superior Asymmetric Electrochemical Capacitor. *Scientific Reports* **2016**, *6* (1), 18737. DOI: 10.1038/srep18737.

(24) Abdalla, A. M.; Sahu, R. P.; Wallar, C. J.; Chen, R.; Zhitomirsky, I.; Puri, I. K. Nickel oxide nanotube synthesis using multiwalled carbon nanotubes as sacrificial templates for supercapacitor application. *Nanotechnology* **2017**, *28* (7), 075603. DOI: 10.1088/1361-6528/aa53f3 From NLM.

(25) Tan, D. Z. W.; Cheng, H.; Nguyen, S. T.; Duong, H. M. Controlled synthesis of MnO2/CNT nanocomposites for supercapacitor applications. *Materials Technology* **2014**, *29* (sup4), A107-A113. DOI: 10.1179/1753555714Y.0000000175.

(26) Lota, K.; Sierczynska, A.; Lota, G. Supercapacitors Based on Nickel Oxide/Carbon Materials Composites. *International Journal of Electrochemistry* **2011**, *2011*, 321473. DOI: 10.4061/2011/321473.

(27) Kumar, S.; Saeed, G.; Zhu, L.; Hui, K. N.; Kim, N. H.; Lee, J. H. 0D to 3D carbon-based networks combined with pseudocapacitive electrode material for high energy density supercapacitor: A review. *Chemical Engineering Journal* **2021**, *403*, 126352. DOI: https://doi.org/10.1016/j.cej.2020.126352.

Chapter 6 Metal–Organic Frameworks Modified Biomass for Supercapacitor Applications

In this chapter, bimetallic Mn/Co metal-organic frameworks (MOFs) are grown on novel carbon materials derived from abundant or waste biomass such as Hinoki wood (Japanese cypress), rice husks, seaweed paper and phenolic resin modified Hinoki wood (floor board waste). Mixed metal oxides/nanocarbon hybrids obtained after carbonisation are characterised by SEM, XPS and electrochemical methods including cyclic voltammetry (CV). Apart from the electric double-layer capacitance provided by the carbon source, the materials show improved electrochemical performance due to faradaic redox reactions from the pyrolysed MOFs when CV is conducted in alkaline electrolytes. In particular, the carbonised MOFs/phenolic resin modified Hinoki material synthesised via an *in-situ* growth of MOFs exhibits a good specific capacitance (128 F g^{-1}), rate capability and stability (90.0% retention after 10000 cycles) in KOH solution, which acts as an innovative bulk electrode material in supercapacitor applications.

6.1 Introduction

In recent studies, a number of carbon materials were used as electric double-layer capacitor electrodes due to their intrinsic physical and chemical properties, long stability, processability and compatibility, etc.[1] Among all widely investigated sources, biomass derived materials which are rich in carbon have shown excellent electrochemical performance for supercapacitor electrodes.[2-5] However, some of them are industrial products or agricultural produce such as potato starch and soybean, which are less economical as compared to biomass waste materials.[6]

Herein, cheap biomass such as Hinoki wood and seaweed paper together with bio-waste such as rice husks and floor board waste made of phenolic resin modified Hinoki wood are utilised as potential electric double-layer electrode materials.

On the other hand, metal–organic frameworks (MOFs), novel materials with metal ions and organic ligands (Figure 6.1), have been broadly studied in various fields including gas storage and separation (e.g., H_2, CO_2, CH_4 and NH_3), drug delivery, sensing and catalysis.[7] Recently, research on MOFs as a faradaic source of energy has been carried out in electrochemical devices for energy storage.[8, 9] In some studies, MOFs are directly employed as electrode materials due to their regular porous structures. However, most MOFs have poor electrical conductivity and their stability performance is only limited to several hundred cycles.[9]

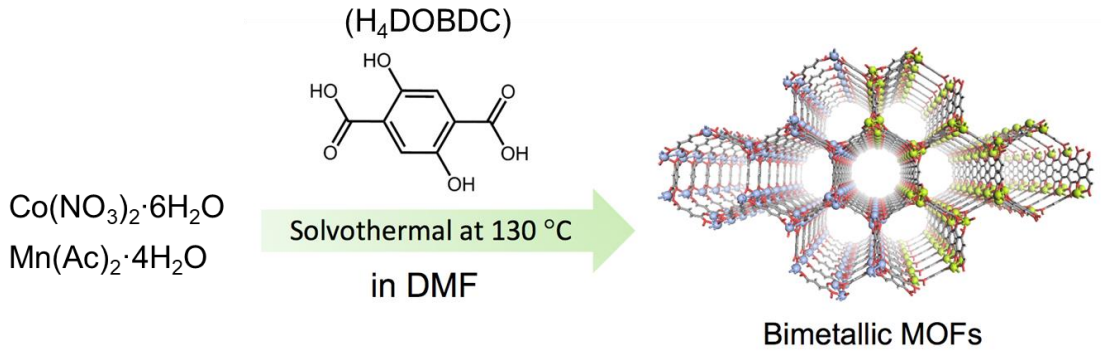

Figure 6.1 Schematic diagram of bimetallic MOFs synthesis.[2]

Combination of MOFs with conductive materials to form composites is first proposed to solve the electrical conductivity issue.[10] For example, MOFs/polyaniline composites are prepared as free-standing electrodes as the conducting polymer allows fast electron transport.[11] More work is based on compositing MOFs with carbon to obtain electrode materials such as Co-MOF/carbon cloth, Zn-MOF/reduced graphene oxide and Ni-MOF/carbon nanotube.[12] The as-obtained materials can be further converted into metal oxide/carbon composites through pyrolysis which eliminates the organic ligands in MOFs.[10]

Herein, mixed metal oxides in conductive carbon structures are obtained after pyrolysis of bimetallic Mn/Co MOFs-based biomass-derived carbon hybrids. Pyrolysed MOFs here are electroactive (faradaic battery-type) electrode materials while carbonised biomass serves as an EDLC (non-faradaic and capacitive) electrode and a conductive substrate. In this way, the hybrid supercapacitors are assembled for high performance electrochemical energy storage devices.

6.2 Experimental

6.2.1 Chemicals and materials

Potassium chloride [KCl, ACS reagent, 99.0-100.5%], potassium hydroxide [KOH, ACS reagent, ≥85%], DMF [$HCON(CH_3)_2$, ACS reagent, ≥99.8%], Nafion™ 117 containing solution, manganese(II) acetate tetrahydrate [$Mn(Ac)_2{\cdot}4H_2O$, ≥99%], and cobalt(II) nitrate hexahydrate [$Co(NO_3)_2{\cdot}6H_2O$, ACS reagent, ≥98%] were purchased from Sigma-Aldrich. 2,5-Dihydroxyterephthalic acid (H_4DOBDC) was obtained from TCI. Hinoki wood (Japanese cypress trees) and phenolic resin modified Hinoki wood (floor board waste) were obtained from Daeshin Lumber. Rice husks were obtained from Daewon GSI, and was ground in mortars with pestles. Seaweed paper was obtained from Marine pulp Co.

6.2.2 Preparation of carbonised MOFs/biomass

6.2.2.1 Synthesis of carbonised MOFs/Hinoki wood

$Mn(Ac)_2{\cdot}4H_2O$ (0.340 mmol), $Co(NO_3)_2{\cdot}6H_2O$ (0.227 mmol) and H_4DOBDC (0.150 mmol) were dissolved in a mixture solution of 10 mL DMF, 0.6 mL ethanol and 0.6 mL water. The solution was then heated at 130 °C in an oil bath. The reaction was carried out for 16 hours. Afterwards, the solution was cooled to room temperature, and the product was collected on a

filter paper. Finally, the product was rinsed with DMF and methanol, and then dried under vacuum.

Hinoki was carbonised with two temperature steps in a quartz tube furnace under N_2 atmosphere. First, a piece of Hinoki wood was heated up to 600 °C with a ramping rate of 0.5 °C min^{-1}, and then further carbonised until 1000 °C with a ramping rate of 5 °C min^{-1}. After carbonisation, the bulk carbon sample was milled to a thin disk with a thickness of 0.3 mm.

3.0 g of MOF-74 (Mn/Co) was dispersed in 15 mL methanol with a mild sonication for 1 min. The MOF solution was then poured on a piece of pre-treated Hinoki carbon under a vacuum condition. The MOFs/Hinoki carbon was dried at room temperature, and then carbonised in a quartz tube furnace at 700 °C for 2 h with a ramping rate of 2 ˚C min^{-1} under N_2 atmosphere.

6.2.2.2 Synthesis of carbonised MOFs/rice husks

$Mn(Ac)_2 \cdot 4H_2O$ (0.340 mmol), $Co(NO_3)_2 \cdot 6H_2O$ (0.227 mmol) and H_4DOBDC (0.150 mmol) were dissolved in a mixture solution of 10 mL DMF, 0.6 mL ethanol and 0.6 mL water. Ground rice husks (30 mg) pre-activated at 400 °C were added to the solution, and then heated at 130 °C in an oil bath. The reaction was carried out for 16 h after which the solution was cooled to room temperature, and the product was collected on a filter paper. Finally, the product was rinsed with DMF and methanol, and then dried under vacuum. The as-prepared MOFs/rice husks were carbonised in a quartz tube furnace at 700 °C for 6 h with a ramping rate of 2 ˚C min^{-1} under N_2 atmosphere.

6.2.2.3 Synthesis of carbonised MOFs/seaweed paper

$Mn(Ac)_2 \cdot 4H_2O$ (0.340 mmol), $Co(NO_3)_2 \cdot 6H_2O$ (0.227 mmol) and H_4DOBDC (0.150 mmol) were dissolved in a mixture solution of 10 mL DMF, 0.6 mL ethanol and 0.6 mL water. A piece of seaweed paper was added to the solution, and then heated at 130 °C in an oil bath. The reaction was carried out for 16 h after which the solution was cooled to room temperature, and

the product was collected on a filter paper. Finally, the product was rinsed with DMF and methanol, and then dried under vacuum. The as-prepared MOFs/rice husks were carbonised in a quartz tube furnace at 700 °C for 4 h with a ramping rate of 2 ˚C min^{-1} under N_2 atmosphere.

6.2.2.4 Synthesis of carbonised MOFs/phenolic resin modified Hinoki wood

For Sample 1 prepared by a two-step approach, the process was the same as the synthesis of carbonised MOFs/Hinoki carbon in 6.2.2.1 where a piece of phenolic resin modified Hinoki wood was substituted for normal Hinoki here. In this method, MOFs were synthesised first and mixed with pre-treated biomass before final carbonisation.

For Sample 2 prepared in an *in-situ* way, the process was similar to the synthesis of carbonised MOFs/rice husks in 6.2.2.2 where a pre-treated piece of phenolic resin modified Hinoki wood was substituted for rice husks. Herein, MOFs were synthesised on pre-treated biomass before final carbonisation.

6.2.3 Equipment and experimental set-up

All electrochemical experiments were performed with an Autolab PGSTAT128N potentiostat/galvanostat (Metrohm Autolab, Utrecht, Netherlands) equipped with Nova software. The measurements were conducted at room temperature using a standard three-electrode configuration, as described in Chapter 2. All potentials mentioned in this chapter were measured against the Ag/AgCl electrode (3M KCl, +0.210 V vs NHE), unless specified. Other experimental parameters such as scan rate, potential window, current density, electrolyte type and cycle number are specifically mentioned in Chapter 6.3 below.

For MOFs modified rice husks and seaweed paper samples, the set-up consists of a platinum coil counter electrode and a silver/silver chloride reference electrode (immersed in 3 M KCl), along with a glassy carbon working electrode assembled in a home-built PTFE holder with a circular area of 0.38 cm^2 (a diameter of 0.70 cm) exposed to the solution. A 2 mg mL^{-1}

suspension was prepared by mixing the milled samples in water. After homogenisation by sonication, 10 μL of the suspension was drop coated on the glassy carbon electrode and coated with 10 μL of Nafion™ 117 solution.

For the other bulk samples (modified Hinoki wood and waste), the materials were directly used as working electrodes (held by a Platinum current collector). The experimental set-up is the same as that in Chapter 4 and 5.

6.3 Results and discussion

6.3.1 Surface characterisation of carbonised MOFs/biomass materials

6.3.1.1 Scanning electron microscopy

SEM images in Figure 6.2 clearly show that the pyrolysed MOFs particles are well dispersed among the biomass carbon surfaces. The homogeneous nanoparticles indicate the formation of mixed bimetallic metal oxides on carbon structures. Hence, the SEM results suggest that hybrid materials are synthesised successfully and are eligible for further studies.

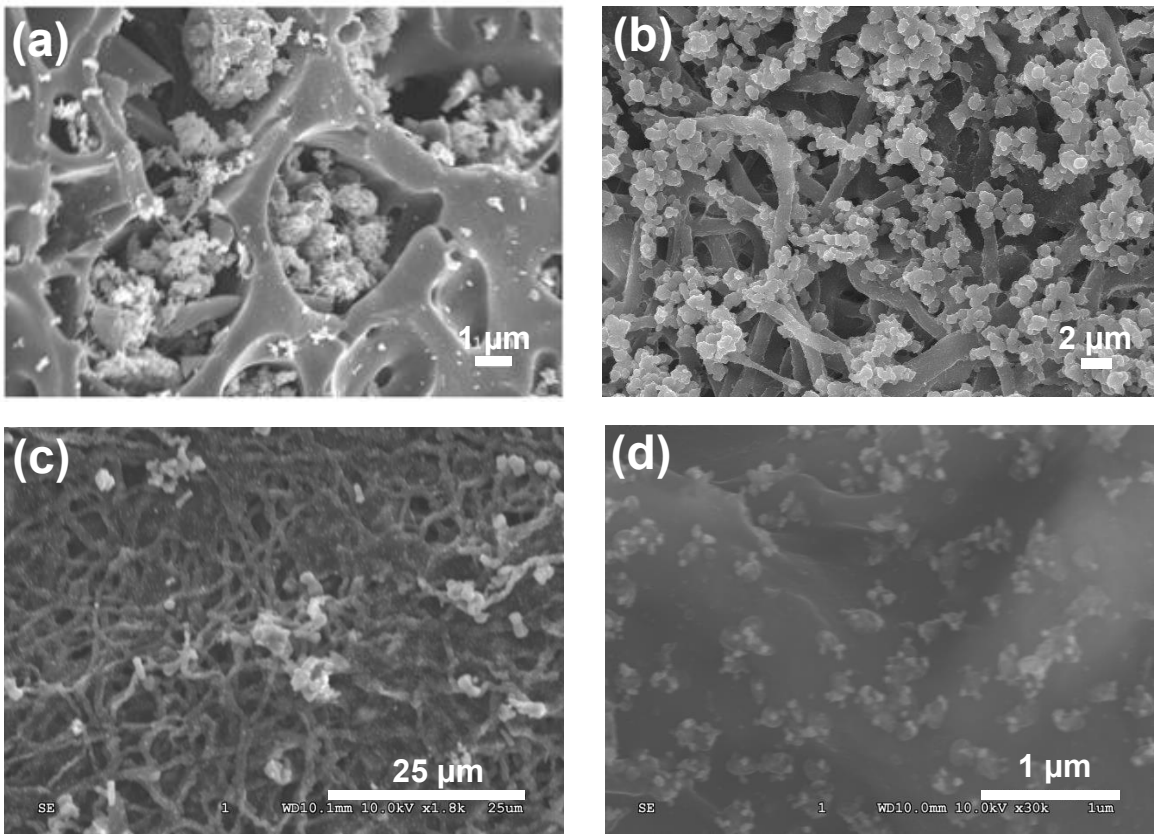

Figure 6.2 SEM images of carbonised MOFs modified (a) rice husks, (b) seaweed paper, (c) & (d) Hinoki wood waste (via *in-situ* method).

6.3.1.2 X-ray photoelectron spectroscopy

XPS survey spectra were undertaken to analyse the surface chemical composition of the carbonised MOFs modified materials, as shown in Figure 6.3 and Table 6.1. Carbon and oxygen are dominant while manganese and cobalt are detected as well in all samples. The reason why a high amount of manganese and cobalt in the carbonised MOFs/rice husks was observed is that it is easier for powdery rice husks to adsorb MOFs during the synthesis, whereas lower amounts of bimetallic species were found in other biomass samples. From the high-resolution spectrum of Mn 3s, a peak splitting of 6.0 eV pointed to an oxidation state of Mn(II). The satellite feature of Co 2p indicated mixed valency, with mixed oxidation states of Co(II) and Co(III), as shown in Figure 6.4.

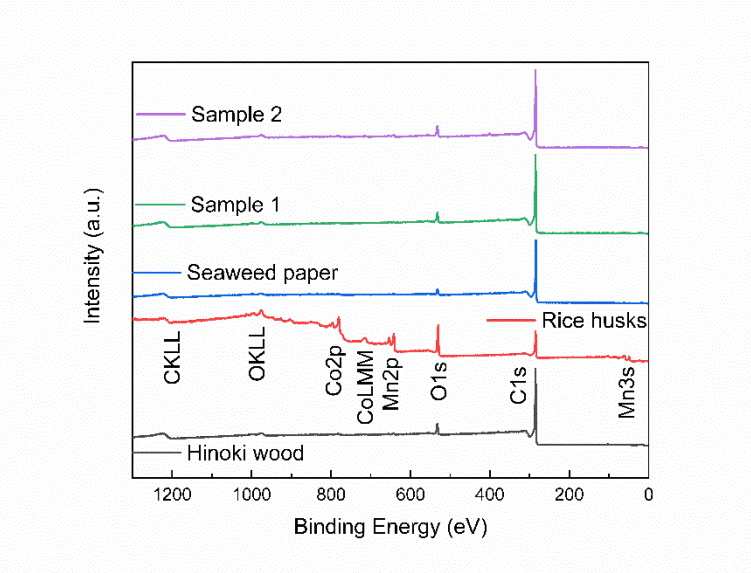

Figure 6.3 XPS spectra of carbonised MOFs modified biomass materials.

Table 6.1 Atomic ratios of samples according to XPS survey spectra.

Carbonised MOFs/biomass	C	O	Mn	Co
Rice husk	57.28	28.25	7.21	6.45
Hinoki wood	91.57	7.13	0.17	0.12
Seaweed paper	91.82	6.46	0.52	0.33
Sample 1	93.57	6.23	0.09	0.11
Sample 2	92.65	6.90	0.27	0.18

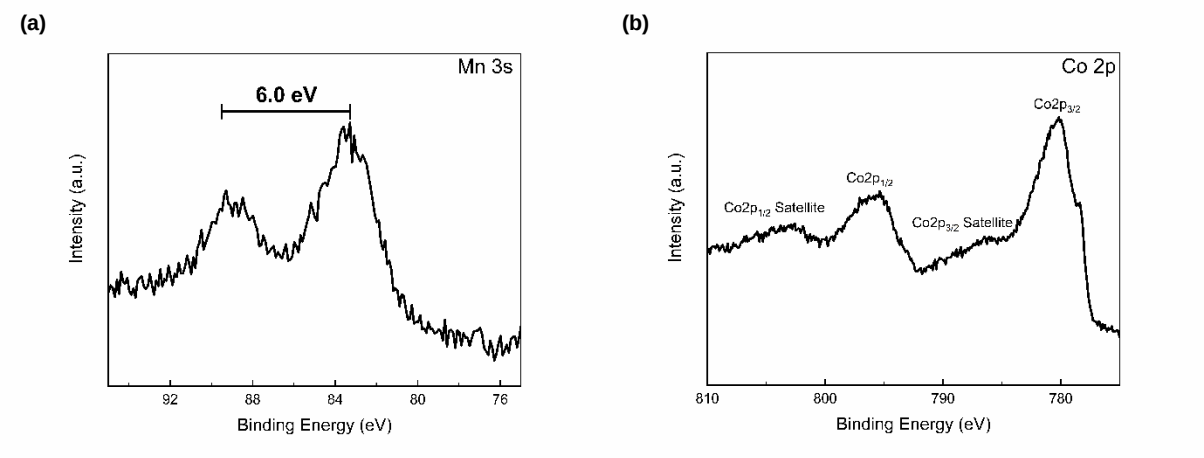

Figure 6.4 XPS spectra of (a) Mn 3s and (b) Co 2p regions of carbonised MOFs/rice husks. (a): Mn(II) indicated from peak splitting of 6.0 eV; (b): Co(II) and Co(III) confirmed from satellite features.

6.3.2 Electrochemical performance of carbonised MOFs/Hinoki wood

The CV curves of the carbonised MOFs/Hinoki wood sample in aqueous 1M KOH electrolyte at increasing scan rates from 2 to 200 mV s^{-1} are presented in Figure 6.5. The observed redox peaks can be attributed to the mixed metal oxides from the pyrolysed bi-metallic MOFs, while other current mainly results from the capacitive behaviour of carbonised biomass. Notably, the CV curve retains the shape of a combination of faradaic current and capacitive current at a high scan rate of 200 mV s^{-1}, indicating good rate performance of the composite electrode.

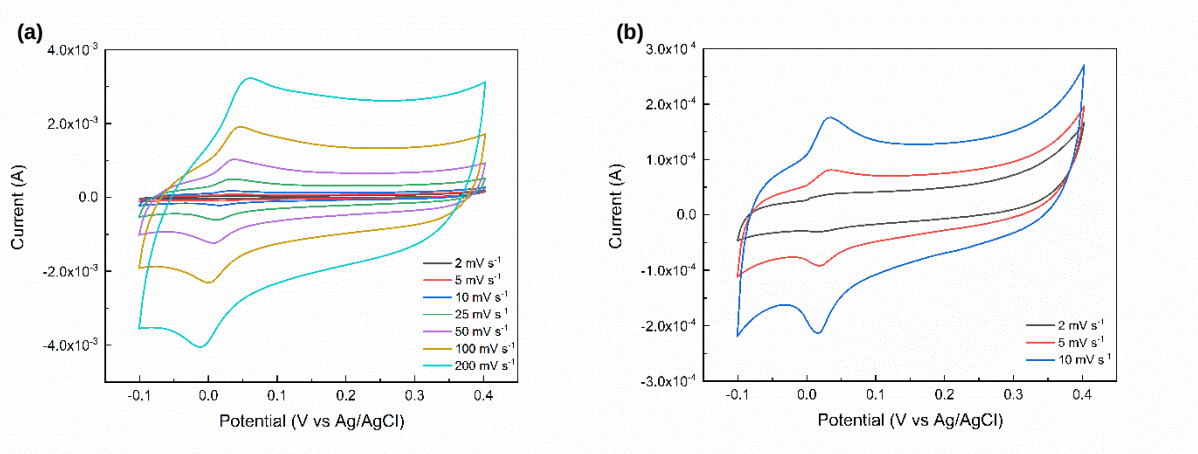

Figure 6.5 Cyclic voltammograms of carbonised MOFs/Hinoki wood in 1 M KOH at scan rates of 2, 5, 10, 25, 50, 100 and 200 mV s^{-1} (a) and (b) 2, 5, 10 mV s^{-1}. Potential range: -0.1 to +0.4 V.

Figure 6.6 shows the comparison of the CV curves recorded at 100 mV s^{-1} in 1 M KOH and 3 M KCl solutions, respectively. The CV curve in 3 M KCl has a quasi-rectangular shape without apparent redox peaks, which is similar to a pure capacitive response. The reason is that the redox reaction here involves the participation of hydroxide, OH^-, and the concentration of OH^- in the neutral KCl solution (10^{-7} mol L^{-1}) is much lower than that in 1 M KOH (1 mol L^{-1}), as introduced in Chapter 1.3. Therefore, the redox peaks are almost unobservable in KCl and the system does not benefit much from the faradaic process. In addition, the fact that the relevant electrode process is pH dependant leads to the shift of the peak potential.

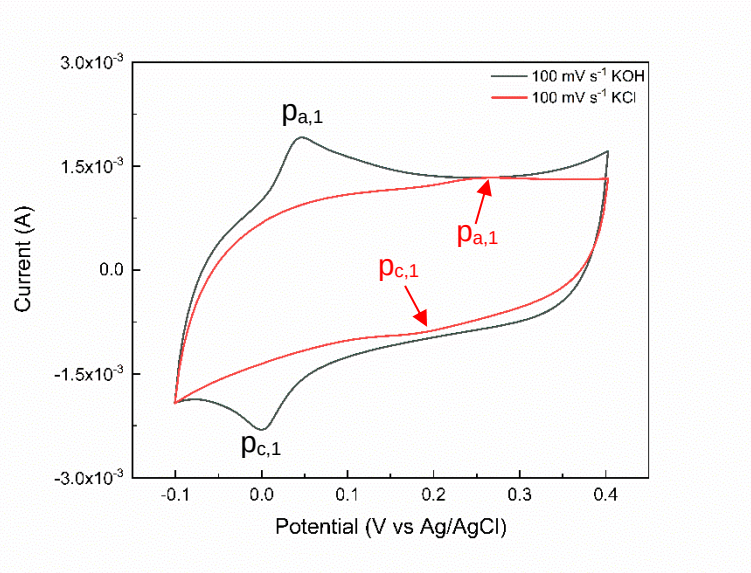

Figure 6.6 Cyclic voltammograms of carbonised MOFs/Hinoki wood at 100 mV s^{-1} in 1 M KOH (black) and 3 M KCl (red).

To investigate whether the operating potential window (-0.1 to +0.4 V) can be widened, CVs of the material were conducted at 50 mV s^{-1} under different potential ranges, as shown in Figure 6.7. The upper potential limit can be extended to +0.5 V with a stable current, whereas higher upper limits gave rise to a sharp increase in the current due to oxygen evolution reaction (OER). On the other hand, the lower potential limit is related to the dissolution of the mixed oxides to lower valences. The irreversible transformation can lead to capacitance fading in a stability test.[13]

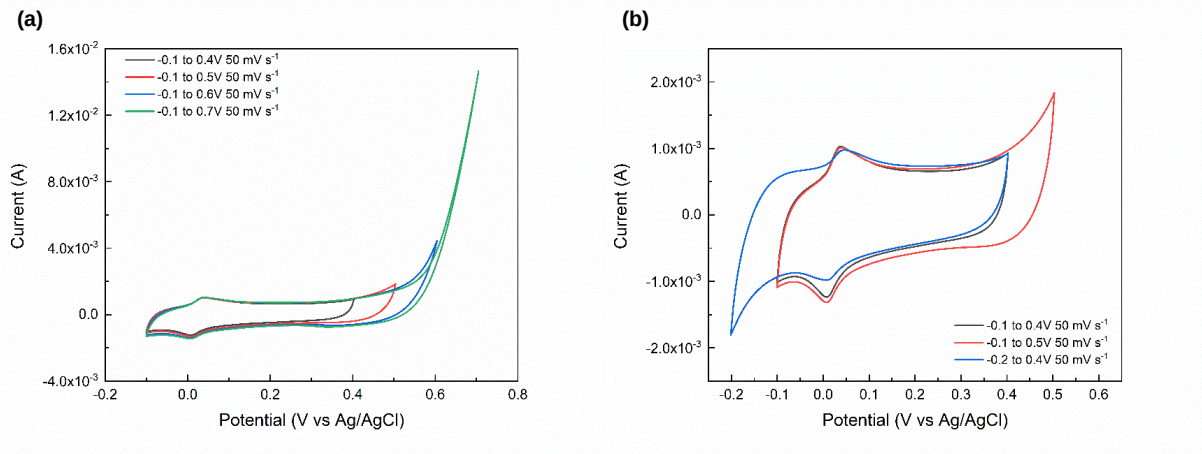

Figure **6.7** Cyclic voltammograms of carbonised MOFs/Hinoki wood at 50 mV s^{-1} in 1 M KOH with different potential windows. (a): upper potential limited by OER; (b): lower potential limited by dissolution of metal oxides.

Figure 6.8 shows the CV curves from -0.1 to +0.5 V in KOH (a) and KCl (b), respectively. The specific capacitance derived from the voltammograms as a function of the scan rate are summarised in Figure 6.9. In general, the specific capacitance in KOH is higher than that in KCl, mainly due to the contribution from the mixed metal oxides. Furthermore, the higher rate capability in KOH indicates the structure of the carbonised MOFs/Hinoki sample provides pathways for OH^- diffusion and faster electron transfer at all scan rates.[4, 14]

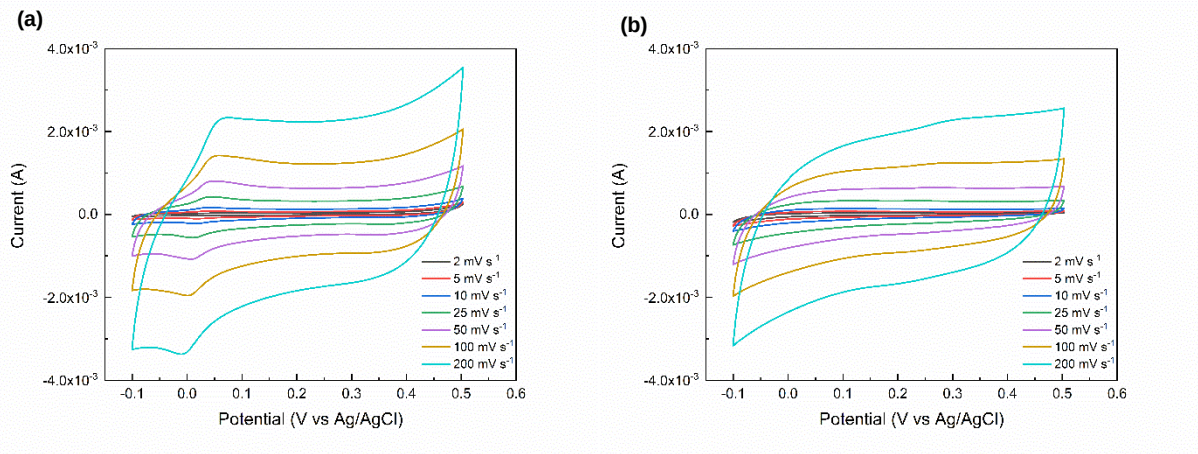

Figure 6.8 Cyclic voltammograms of carbonised MOFs/Hinoki wood in (a) 1 M KOH and (b) 1 M KCl at different scan rates. Potential range: -0.1 to +0.5 V. (a): faradaic peaks and capacitive response are both observed in KOH; (b): only capacitive response observed in KCl.

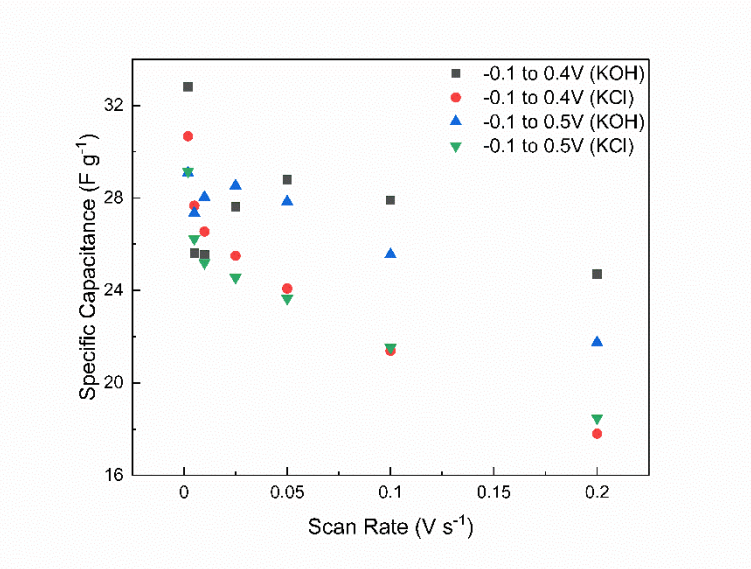

Figure 6.9 Specific capacitances of carbonised MOFs/Hinoki wood as a function of scan rate in KOH and KCl with two potential windows. Sample tested in KOH has better capacitance than tested in KCl due to faradaic contributions.

6.3.3 Electrochemical performance of carbonised MOFs/rice husks

CV curves of the carbonised MOFs/rice husks sample in KOH at scan rates from 2 to 200 mV s^{-1} are shown in Figure 6.10. Similar to the CVs of the previous sample, both anodic and cathodic peaks are observed at all scan rates. Meanwhile, the peak separation is less than 80 mV at a high scan rate of 200 mV s^{-1}, indicating fast and reversible faradaic process at the electrode surface.

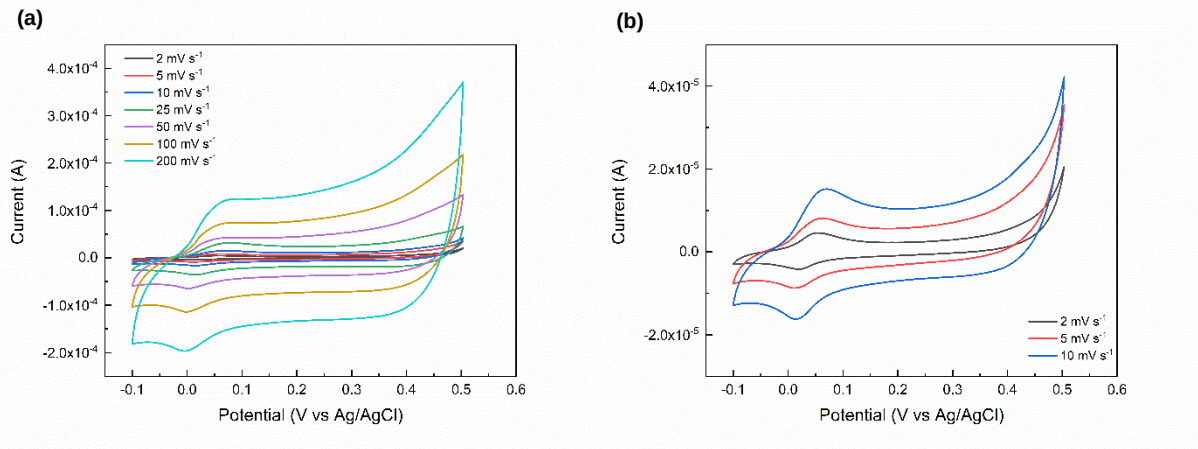

Figure 6.10 Cyclic voltammograms of carbonised MOFs/rice husks in 1 M KOH at different scan rates (a) 2 to 200 mV s^{-1} and (b) 2, 5, 10 mV s^{-1}. Potential range: -0.1 to +0.5 V.

The mixed metal oxides also acted as a catalyst for OER, which limited the upper potential window, as shown in Figure 6.11 (a). Different from the CV curve in KOH, Figure 6.11 (b) shows that the CV in KCl has no obvious redox peaks as the faradaic contributions from the mixed metal oxides are negligible in a neutral electrolyte. The specific capacitance is proportional to the integral area of the CV curve at the same scan rate. Therefore, a much larger CV shape in KOH corresponds to a higher specific capacitance value compared to the CV conducted in KCl.

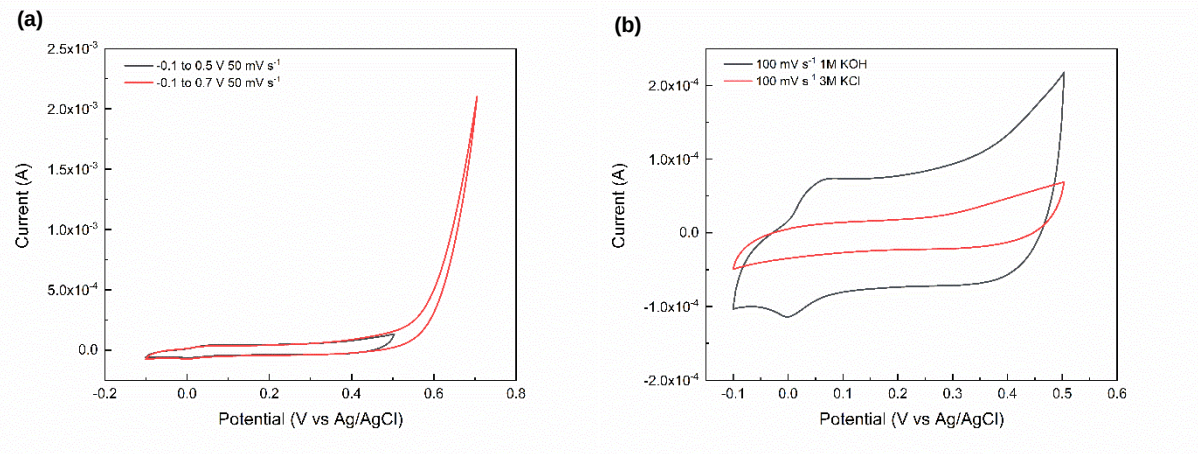

Figure 6.11 Cyclic voltammograms of carbonised MOFs/rice husks in (a) 1 M KOH at 50 mV s^{-1} with two potential windows and (b) CV comparison in KOH and KCl electrolytes at 100 mV s^{-1}.

6.3.4 Electrochemical performance of carbonised MOFs/seaweed paper

Figure 6.12 (a) & (b) show the CV curves of the carbonised MOFs/seaweed paper sample at different scan rates with potential windows ranging from -0.1 to +0.4 V and -0.1 to +0.5 V, respectively. As shown in Figure 6.12 (a), a pair of redox peaks appeared between 0 and +0.1 V, demonstrating the integration of the faradaic behaviour of metal oxides and the capacitive behaviour of carbonised seaweed paper. In contrast, another cathodic peak at around +0.35 to +0.4 V was observed in Figure 6.12 (b) when the upper potential limit was extended to +0.5 V. The reason is that the oxygen evolution reaction was stronger in the latter case, and therefore the peak is related to higher activity in oxygen reduction reaction on the reverse scan.[15]

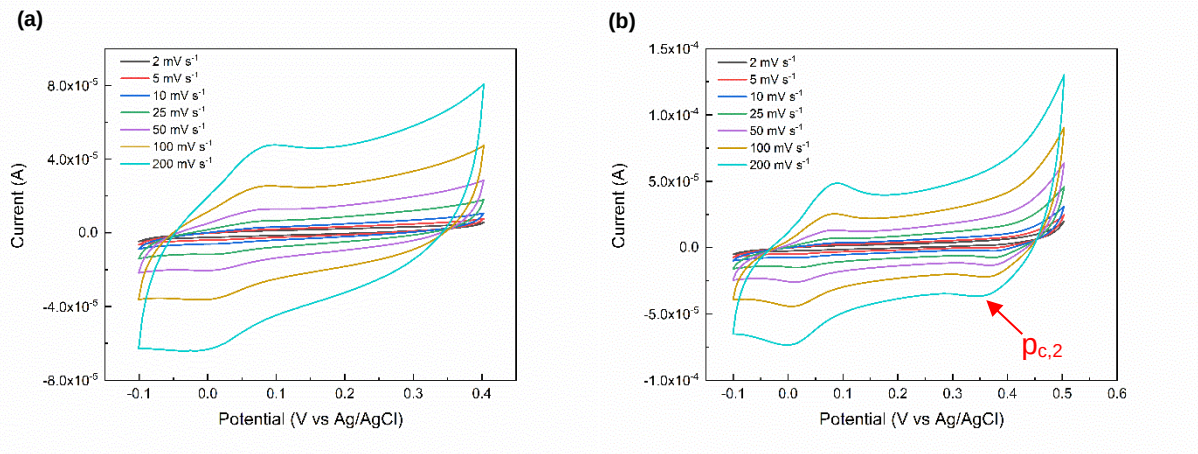

Figure 6.12 Cyclic voltammograms of carbonised MOFs/seaweed paper in 1 M KOH at different scan rates (2 – 200 mV s^{-1}). Potential range: (a) -0.1 to +0.4 V & (b) -0.1 to +0.5 V.

Figure 6.13 (a) shows that the carbonised MOFs/seaweed paper also face the problem of a limited potential window, which is akin to the carbonised Hinoki wood and rice husk samples. However, better electrochemical performance was obtained in KOH originating from the faradaic process, as shown in Figure 6.12 (b).[9]

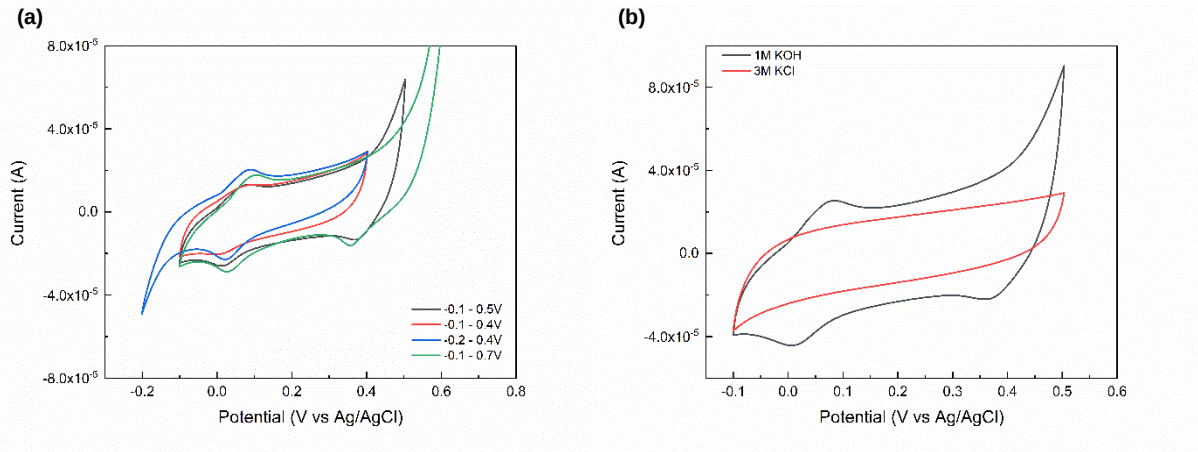

Figure 6.13 (a) Cyclic voltammograms of carbonised MOFs/seaweed paper in 1 M KOH at 50 mV s^{-1} with different potential windows and (b) CV comparison in KOH and KCl electrolytes at 100 mV s^{-1}.

The specific capacitances of MOFs modified carbonised Hinoki wood, rice husks and seaweed paper are listed in Table 6.2. The rate performance for carbonised MOFs/Hinoki wood maintains well across all scan rates. For example, the capacitance at 200 mV s^{-1} retains 74.9% of that at 2 mV s^{-1}. However, specific capacitances of MOFs modified rice husks and seaweed paper decrease faster with increasing scan rates. The decreasing trend is a result of the limited diffusion of the electrolyte within the pores.[3] The higher capacitive performance of MOFs modified rice husks and seaweed paper at low scan rates is attributed to higher loading amount of mixed metal oxides via the *in-situ* synthesis of the materials, which increases the faradaic behaviour of the materials.

Table 6.2 Specific capacitance of the carbonised MOFs/biomass sample. Experimental parameters: electrolyte: 1 M KOH; potential window: -0.1 to +0.5 V.

Sample (MOFs/)	Hinoki wood	Rice husks	Seaweed paper
Scan rate (mV s^{-1})	Specific capacitance (F g^{-1})		
2	29.1	49.1	71.1
5	27.3	48.8	53.6
10	28.0	46.1	43.6
25	28.5	44.0	33.6
50	27.8	41.3	28.3
100	25.6	37.2	24.0
200	21.8	32.4	20.3

Before preparation for electrochemical measurements, rice husks and seaweed paper samples were ball milled and drop coated onto a glassy carbon electrode, which means only micrograms of the material was tested. Furthermore, drop-coated samples may well detach from the electrode even with a protective binding agent, leading to decreased capacitive performance during further tests. On the contrary, the Hinoki sample (~mg) could be directly used as a working electrode. Although carbonised MOFs/Hinoki exhibited lower capacitance compared to the other two samples, bulk carbon (Hinoki) is more attractive than powder carbon (milled rice husks and seaweed paper) in supercapacitor applications.

6.3.5 Electrochemical performance of carbonised MOFs/Phenolic resin modified Hinoki

In order to obtain bulk materials with improved electrochemical performance, phenolic resin modified Hinoki, an industrial waste, was modified with MOFs in two ways. For **Sample 1**, MOFs were synthesised first, and then mixed with pre-treated biowaste before final carbonisation, while MOFs were *in-situ* synthesised in the presence of pre-treated biowaste before final carbonisation for **Sample 2**. Thus, more bimetallic particles could enter the channels of biomass-derived carbon due to *in situ* growth of MOFs in Sample 2.

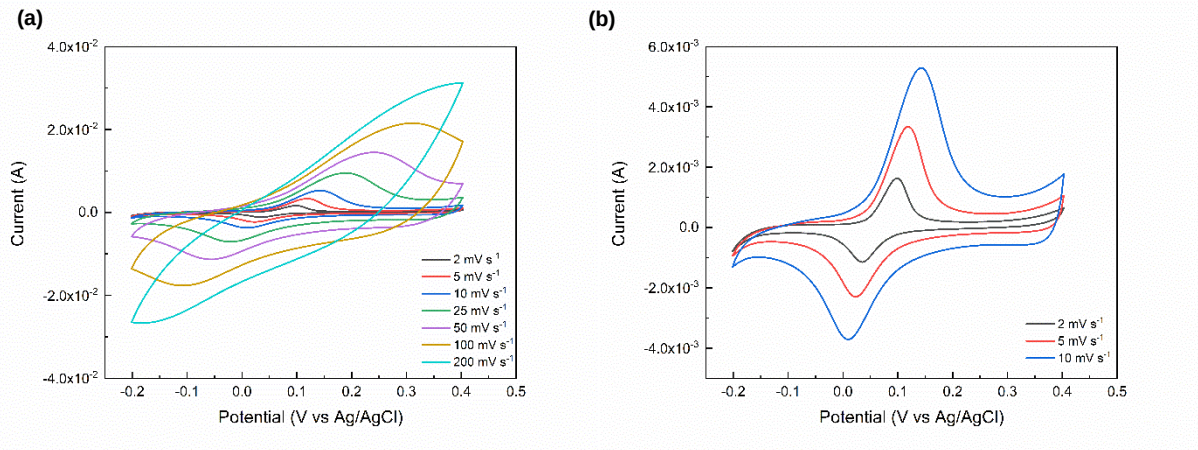

Figure 6.14 Cyclic voltammograms of Sample 1 at different scan rates (a) 2 to 200 mV s^{-1} and (b) 2, 5, 10 mV s^{-1} in 1 M KOH. Potential range: -0.2 to +0.4 V.

The CV curves of Sample 1 at various scan rates in KOH are shown in Figure 6.14. A pair of redox peaks are well defined at certain scan rates (2 to 100 mV s^{-1}), whereas the peaks are unobservable at 200 mV s^{-1}. The reason is that higher scan rates gave rise to larger peak separation as the faradaic process became more irreversible.[16]

Figure 6.15 (a) shows the CV curves in KCl with changing scan rates. Compared to the CV in KOH, the quasi-rectangular CV shapes in KCl solution without obvious redox peaks are indicative of an electric double-layer capacitance mechanism. Furthermore, the current response in KCl is smaller due to lack of faradaic contributions, as shown in Figure 6.15 (b).

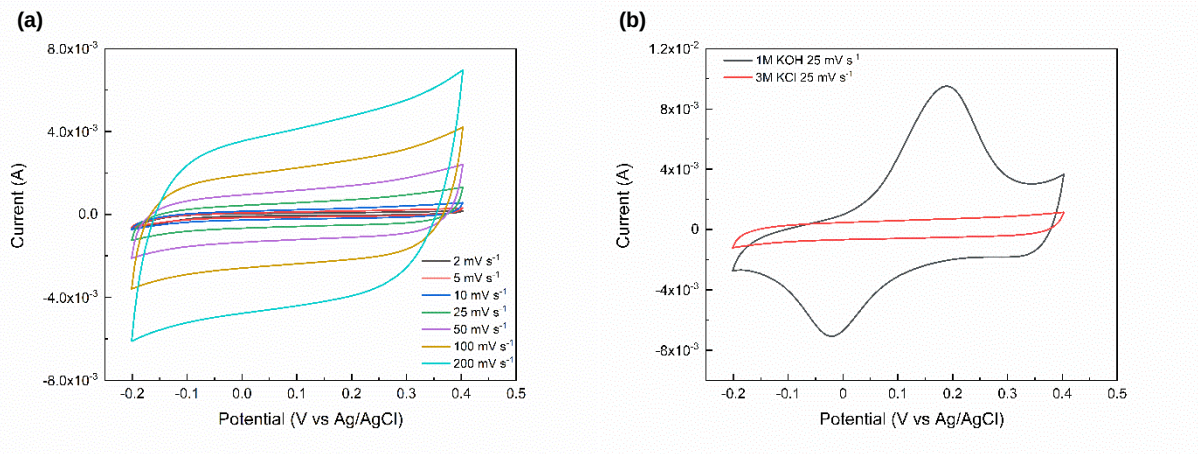

Figure 6.15 (a) Cyclic voltammograms of Sample 1 in 3 M KCl at different scan rates and (b) CV comparison in KOH and KCl electrolytes at 25 mV s^{-1}. Potential range: -0.2 to +0.4 V.

The peak separation and the specific capacitance of Sample 1 at different scan rates in KOH and KCl solutions are listed in Table 6.3. The results in KOH show that the sample has an excellent rate capability until a scan rate of 50 mV s^{-1}. At high scan rates such as 100 and 200 mV s^{-1}, slow electrode kinetics and inaccessible surface area caused by limited ion transport time led to decreased specific capacitance.[17] However, the specific capacitance in KOH is still higher than that in KCl at all scan rates as a result of contributions from faradaic redox reactions.

Table 6.3 Summary of peak separation and specific capacitance of Sample 1 in KOH and KCl.

Scan rate ($mV\ s^{-1}$)	ΔE_p (mV)	Specific Capacitance in KOH ($F\ g^{-1}$)	Specific Capacitance in KCl ($F\ g^{-1}$)
2	65.5	51.0	14.1
5	95.6	54.1	9.66
10	131.0	54.9	9.00
25	211.4	52.4	9.25
50	297.1	46.3	9.38
100	417.9	33.7	8.79
200	/	17.3	7.67

As shown in Figure 6.16 (a), the linear relationship between the anodic/cathodic peak current and the square root of the scan rate indicates diffusion-controlled electrode processes in KOH solution.[16, 18] In contrast to a diffusion-controlled mechanism where a square root dependence is seen, Figure 6.16 (b) shows that the current is directly proportional to the scan rate in KCl solution, demonstrating a typical capacitive behaviour.[16, 19]

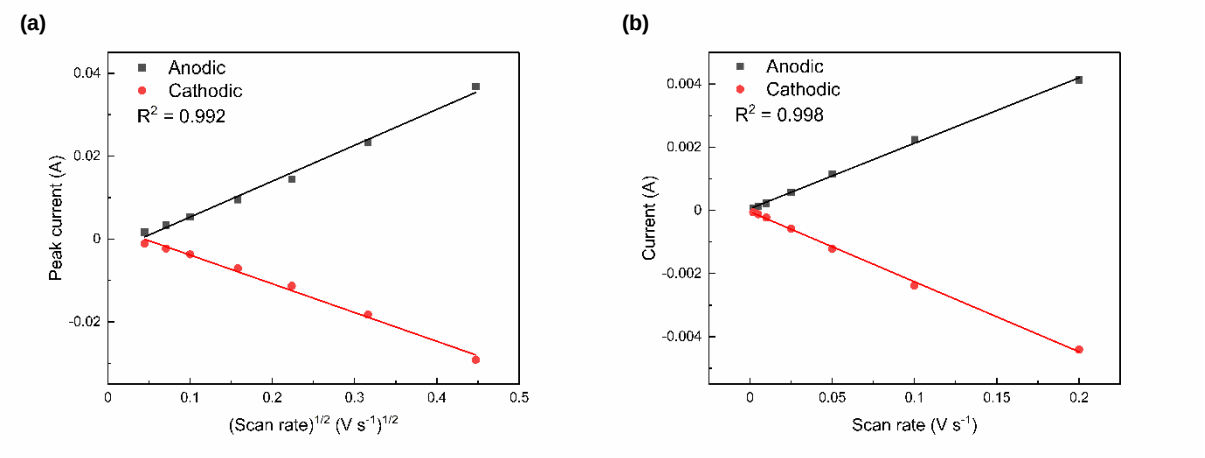

Figure 6.16 (a) Anodic and cathodic peak current of Sample 1 in 1 M KOH as a function of square root of scan rate and (b) current of Sample 1 in 3 M KCl as a function of scan rate.

Figure 6.17 shows CV curves at different scan rates for Sample 2 in 1 M KOH solution. Two redox peaks are notably observed at low scan rates and disappeared at 200 mV s^{-1}, which resembles the voltammograms of Sample 1. However, large current response is present in Sample 2, indicating that it has more excellent electrochemical performance than Sample 1. In addition, the peak separation in Sample 2 shifts more with increasing scan rates compared to Sample 1 because more MOFs entered the channels of biomass owing to the *in-situ* growth of MOFs in Sample 2, resulting in greater electrochemical irreversibility with faster scan rates.

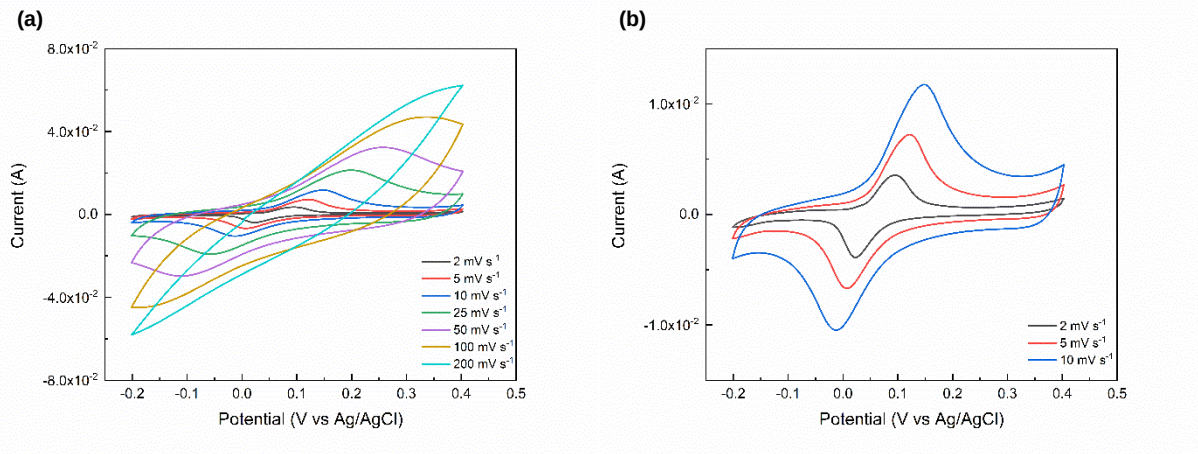

Figure 6.17 Cyclic voltammograms of Sample 2 at different scan rates (a) 2 to 200 mV s^{-1} and (b) 2, 5, 10 mV s^{-1} in 1 M KOH. Potential range: -0.2 to +0.4 V.

Figure 6.18 (a) shows the CV curves of Sample 2 in 3 M KCl at various scan rates ranging from 2 to 200 mV s^{-1}. The quasi-rectangular shape without obvious redox peaks is observed, which is typical for electric double-layer capacitance and different from the CV curve in KOH due to faradaic contributions, as shown in Figure 6.18 (b).

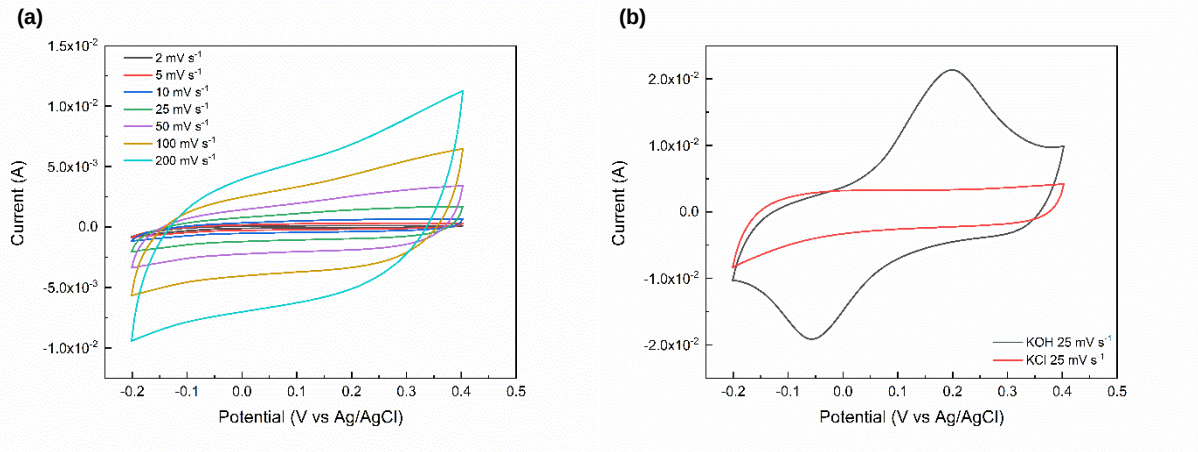

Figure 6.18 (a) Cyclic voltammograms of Sample 2 in 3 M KCl at different scan rates (2 to 200 mV s^{-1}) and (b) CV comparison in KOH and KCl electrolytes at 25 mV s^{-1}. Potential range: -0.2 to +0.4 V.

The peak separation and the specific capacitance of Sample 2 in KOH at different scan rates are summarised in Table 6.4, along with the specific capacitance in KCl. A highest specific capacitance of 128 F g^{-1} is obtained at low scan rates of 5 and 10 mV s^{-1} in KOH while the rate capability remains excellent from 2 to 50 mV s^{-1}. Furthermore, the specific capacitance of Sample 2 in KCl is also higher than that of Sample 1, indicating that the *in-situ* growth of MOFs in Sample 2 not only improves the faradaic behaviour but also provides the sample with better electric double-layer performance.

Table 6.4 Summary of peak separation and specific capacitance of Sample 2 in KOH and KCl.

Scan rate (mV s^{-1})	ΔE_p (mV)	Specific Capacitance in KOH (F g^{-1})	Specific Capacitance in KCl (F g^{-1})
2	75.6	127	32.4
5	115.8	128	33.0
10	156.0	128	32.8
25	251.8	115	31.1
50	367.6	87.9	28.6
100	528.7	50.1	24.6
200	/	19.7	19.4

The anodic and cathodic peak currents of Sample 2 in KOH solution were plotted against the square root of the scan rate. The linear relationship in Figure 6.19 (a) exhibits a diffusion-controlled process for Sample 2 in KOH, which is same as Sample 1 as discussed above. In Figure 6.19 (b), the peak current in KCl solution was plotted on a natural logarithm scale for

Sample 2. The slope values are 0.94 and 0.86 for the anodic and cathodic peaks with linearity, clearly demonstrating that the non-faradaic mechanism has a dominant position in the electrode behaviour of Sample 2 in KCl.

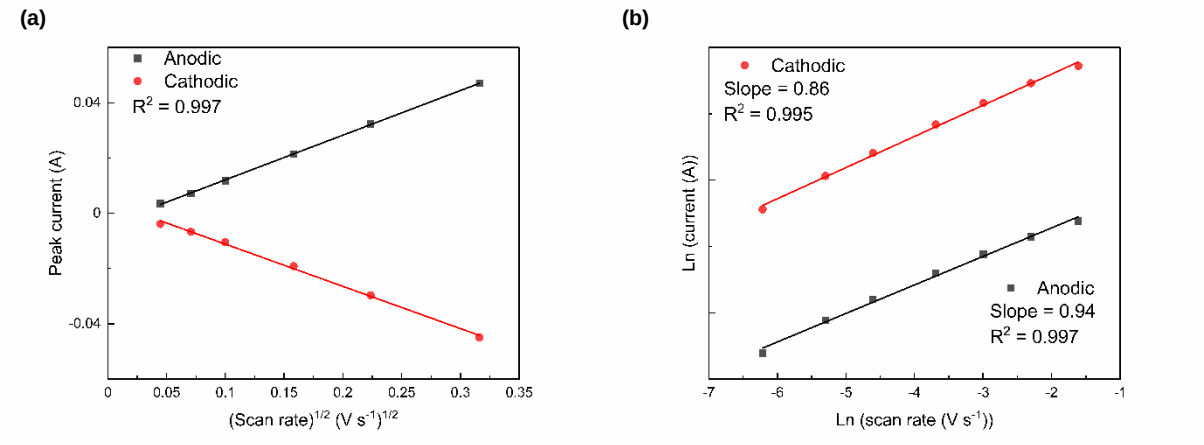

Figure 6.19 (a) Anodic and cathodic peak current of Sample 2 in 1 M KOH as a function of square root of scan rate and (b) natural logarithm (current) of Sample 2 in 3 M KCl as a function of natural logarithm (scan rate).

To further evaluate the electrochemical properties of Sample 2, chronopotentiometry (CP), also known as galvanostatic charge-discharge (GCD) measurement, was performed in 1 M KOH solution at various current densities from 0.5 to 20 A g^{-1}, as shown in Figure 6.20. The non-linear charge discharge curves at all current densities are representative of faradaic behaviour of the sample in KOH, which is consistent with the CV results.

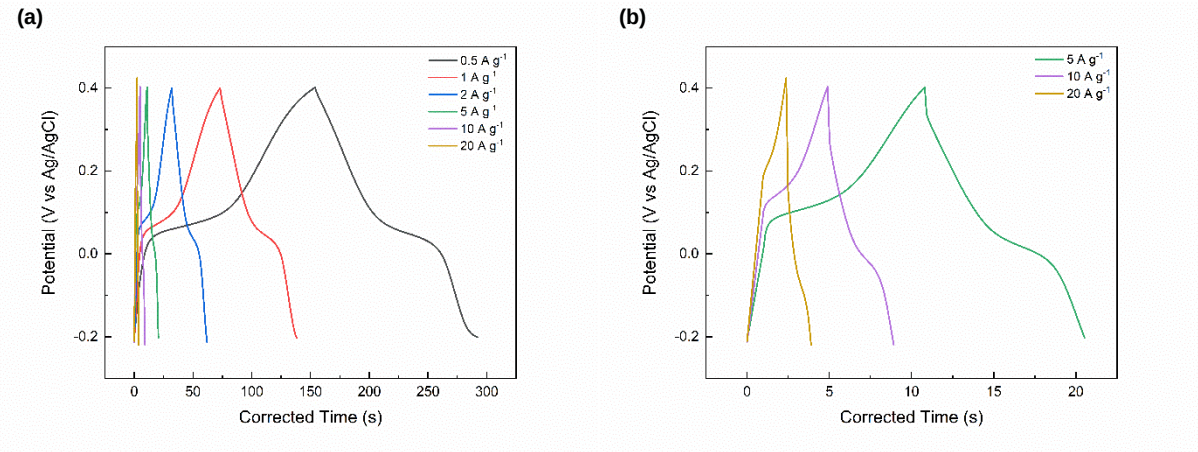

Figure 6.20 Galvanostatic charge-discharge curves of Sample 2 in KOH at different current densities (a) 0.5 to 20 A g^{-1} and (b) 5, 10, 20 A g^{-1}.

Table 6.5 Summary of specific capacitance of Sample 2 in 1 M KOH via CV and GCD.

Scan rate (mV s^{-1})	Specific Capacitance (F g^{-1})	Current Density (A g^{-1})	Specific Capacitance (F g^{-1})
2	127	0.5	115
5	128	1	108
10	128	2	96.7
25	115	5	80.0
50	87.9	10	65.0
100	50.1	20	46.7
200	19.7	/	/

The specific capacitance of the sample can be calculated based on the equation: $C_s = I\Delta t/m\Delta V$, where I/m is the current density (A g^{-1}), Δt is the discharge time (s), and ΔV is the voltage window (V). As shown in Table 6.5, a highest specific capacitance of 115 F g^{-1} was observed

at 0.5 A g^{-1}, and increasing current density led to decreased specific capacitance, which is in accordance with the specific capacitance obtained from CV.

The stability test was also examined by CP at a current density of 1 A g^{-1} for 10000 cycles, as shown in Figure 6.21. The specific capacitance was 90.0% of the initial value afterwards, suggesting remarkable long-term stability of the material. Therefore, Sample 2 is the most competitive candidate for high-performance electrochemical supercapacitor applications among all MOFs modified materials studied in this chapter.

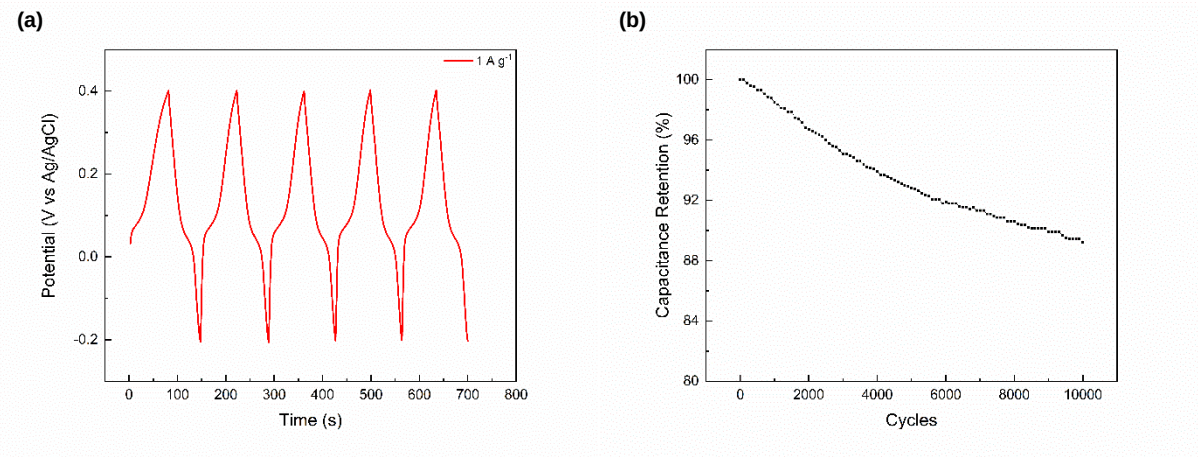

Figure 6.21 (a) Galvanostatic charge-discharge stability test of Sample 2 and (b) capacitance retention against cycle number at a current density of 1 A g^{-1} in KOH.

6.4 Conclusion and comparison

The electrochemical performance of Sample 2 (i.e., pyrolysed MOFs/biowaste-derived carbon) is compared to some reports on MOF and carbon-based supercapacitor applications, as listed in Table 6.6. Although the specific capacitance is moderate (128 F g^{-1}) among selected MOF-based electrodes (57.5 – 207 F g^{-1}), the biowaste-derived carbon sample in this work survived in the stability test with only 10% capacitance loss after 10000 cycles, which is more competitive than most MOF based materials with cycle life up to several thousand cycles. More importantly, MOF based materials are mixed with conductive agent (e.g., acetylene black) and binder (e.g., polyvinylidene fluoride) and then coated on a current collector (e.g., nickel foam) for electrochemical measurements in many studies, but free-standing and additive/binder-free composite materials are produced here.

Table 6.6 Electrochemical performance of MOF and carbon-based electrodes for supercapacitors.

Sample	Specific Capacitance (F g^{-1})	Scan Rate (mV s^{-1})	Current Density (A g^{-1})	Capacitance Retention
Sample 2 (this work)	128	10	/	~90.0%, 10000 cycles
Calcined Co-MOF[20]	150	/	1	~100%, 3400 cycles
Fe-MOF/CNTs[21]	57.5	5	/	up to 200 cycles
Co-BPDC MOF[22]	179	10	/	~77.4%, 1000 cycles
Co-MOF film[23]	207	/	0.6	~98.5%, 1000 cycles
Calcined Fe-MOF/carbon[24]	139	/	0.5	~83.3%, 4000 cycles

Herein, a group of biomass-derived novel carbon materials were modified with bimetallic Co/Mn metal–organic frameworks (MOFs). The carbonised composite materials were then used for supercapacitor applications. In contrast to the electrochemical behaviour in neutral solutions, the electrochemical performance of the material in alkaline solutions not only benefited from the carbonised biomass (electric double-layer capacitance) but also from the pyrolysed MOFs (faradaic redox reactions). The sample synthesised via the *in-situ* growth of MOFs in phenolic resin modified Hinoki wood showed a specific capacitance of 128 F g^{-1} in KOH electrolyte, indicating better electrochemical performance than in KCl electrolyte as well as other samples measured in KOH. Different from powdery samples such as milled rice husks or seaweed paper, the bulk material can be directly employed as a working electrode without binding agents (Nafion) or conductive substrates (glassy carbon electrodes). Furthermore, the material has excellent rate capability to some extent and long stability (90.0% of its initial specific capacitance retained after 10000 cycles at 1 A g^{-1}) in a galvanostatic charge-discharge test. Therefore, the studies demonstrate that MOFs modified carbon derived from cheap and waste biomass materials provides the energy storage and supercapacitor applications with a positive effect.

References

(1) Bichat, M. P.; Raymundo-Piñero, E.; Béguin, F. High voltage supercapacitor built with seaweed carbons in neutral aqueous electrolyte. *Carbon* **2010**, *48* (15), 4351-4361. DOI: https://doi.org/10.1016/j.carbon.2010.07.049. Simon, P.; Gogotsi, Y. Materials for electrochemical capacitors. *Nature Materials* **2008**, *7* (11), 845-854. DOI: 10.1038/nmat2297. Zhai, Y.; Dou, Y.; Zhao, D.; Fulvio, P. F.; Mayes, R. T.; Dai, S. Carbon Materials for Chemical Capacitive Energy Storage. *Advanced Materials* **2011**, *23* (42), 4828-4850. DOI: https://doi.org/10.1002/adma.201100984.

(2) Kim, H.; Sohail, M.; Wang, C.; Rosillo-Lopez, M.; Baek, K.; Koo, J.; Seo, M. W.; Kim, S.; Foord, J. S.; Han, S. O. Facile One-Pot Synthesis of Bimetallic Co/Mn-MOFs@Rice Husks, and its Carbonization for Supercapacitor Electrodes. *Scientific Reports* **2019**, *9* (1), 8984. DOI: 10.1038/s41598-019-45169-0.

(3) Zequine, C.; Ranaweera, C. K.; Wang, Z.; Singh, S.; Tripathi, P.; Srivastava, O. N.; Gupta, B. K.; Ramasamy, K.; Kahol, P. K.; Dvornic, P. R.; et al. High Per formance and Flexible Supercapacitors based on Carbonized Bamboo Fibers for Wide Temperature Applications. *Scientific Reports* **2016**, *6* (1), 31704. DOI: 10.1038/srep31704.

(4) Jiang, L.; Shanmuganathan, S.; Nelson, G. W.; Han, S. O.; Kim, H.; Na Sim, I.; Foord, J. S. Hybrid system of nickel–cobalt hydroxide on carbonised natural cellulose materials for supercapacitors. *Journal of Solid State Electrochemistry* **2018**, *22* (2), 387-393. DOI: 10.1007/s10008-017-3723-z.

(5) Jiang, L.; Nelson, G. W.; Han, S. O.; Kim, H.; Sim, I. N.; Foord, J. S. Natural Cellulose Materials for Supercapacitors. *Electrochimica Acta* **2016**, *192*, 251-258. DOI: https://doi.org/10.1016/j.electacta.2015.12.138. Jiang, L.; Nelson, G. W.; Kim, H.; Sim, I. N.; Han, S. O.; Foord, J. S. Cellulose-Derived Supercapacitors from the Carbonisation of Filter Paper. *ChemistryOpen* **2015**, *4* (5), 586-589. DOI: https://doi.org/10.1002/open.201500150.

Jiang, L.; Seong, Y.-H.; Han, S. O.; Kim, H.; Kim, H. H.; Foord, J. S. Nickel treatment of biomass-derived nanocarbon for energy devices. *Carbon* **2018**, *130*, 724-729. DOI: https://doi.org/10.1016/j.carbon.2018.01.063. Jiang, L.; Han, S. O.; Pirie, M.; Kim, H. H.; Seong, Y.-H.; Kim, H.; Foord, J. S. Seaweed biomass waste-derived carbon as an electrode material for supercapacitor. *Energy & Environment* **2021**, *32* (6), 1117-1129. DOI: 10.1177/0958305x19882398.

(6) Zhao, S.; Wang, C.-Y.; Chen, M.-M.; Wang, J.; Shi, Z.-Q. Potato starch-based activated carbon spheres as electrode material for electrochemical capacitor. *Journal of Physics and Chemistry of Solids* **2009**, *70* (9), 1256-1260. DOI: https://doi.org/10.1016/j.jpcs.2009.07.004. Ferrero, G. A.; Fuertes, A. B.; Sevilla, M. From Soybean residue to advanced supercapacitors. *Scientific Reports* **2015**, *5* (1), 16618. DOI: 10.1038/srep16618.

(7) Li, H.; Wang, K.; Sun, Y.; Lollar, C. T.; Li, J.; Zhou, H.-C. Recent advances in gas storage and separation using metal–organic frameworks. *Materials Today* **2018**, *21* (2), 108-121. DOI: https://doi.org/10.1016/j.mattod.2017.07.006. Abánades Lázaro, I.; Forgan, R. S. Application of zirconium MOFs in drug delivery and biomedicine. *Coordination Chemistry Reviews* **2019**, *380*, 230-259. DOI: https://doi.org/10.1016/j.ccr.2018.09.009. Dolgopolova, E. A.; Rice, A. M.; Martin, C. R.; Shustova, N. B. Photochemistry and photophysics of MOFs: steps towards MOF-based sensing enhancements. *Chemical Society Reviews* **2018**, *47* (13), 4710-4728, 10.1039/C7CS00861A. DOI: 10.1039/C7CS00861A. Zhu, L.; Liu, X.-Q.; Jiang, H.-L.; Sun, L.-B. Metal–Organic Frameworks for Heterogeneous Basic Catalysis. *Chemical Reviews* **2017**, *117* (12), 8129-8176. DOI: 10.1021/acs.chemrev.7b00091.

(8) Zhang, X.; Chen, A.; Zhong, M.; Zhang, Z.; Zhang, X.; Zhou, Z.; Bu, X.-H. Metal–Organic Frameworks (MOFs) and MOF-Derived Materials for Energy Storage and Conversion. *Electrochemical Energy Reviews* **2019**, *2* (1), 29-104. DOI: 10.1007/s41918-

018-0024-x. Shrivastav, V.; Sundriyal, S.; Goel, P.; Kaur, H.; Tuteja, S. K.; Vikrant, K.; Kim, K.-H.; Tiwari, U. K.; Deep, A. Metal-organic frameworks (MOFs) and their composites as electrodes for lithium battery applications: Novel means for alternative energy storage. *Coordination Chemistry Reviews* **2019**, *393*, 48-78. DOI: https://doi.org/10.1016/j.ccr.2019.05.006. Zhao, Y.; Song, Z.; Li, X.; Sun, Q.; Cheng, N.; Lawes, S.; Sun, X. Metal organic frameworks for energy storage and conversion. *Energy Storage Materials* **2016**, *2*, 35-62. DOI: https://doi.org/10.1016/j.ensm.2015.11.005.

(9) Jiao, Y.; Pei, J.; Chen, D.; Yan, C.; Hu, Y.; Zhang, Q.; Chen, G. Mixed-metallic MOF based electrode materials for high performance hybrid supercapacitors. *Journal of Materials Chemistry A* **2017**, *5* (3), 1094-1102, 10.1039/C6TA09805C. DOI: 10.1039/C6TA09805C.

(10) Xu, B.; Zhang, H.; Mei, H.; Sun, D. Recent progress in metal-organic framework-based supercapacitor electrode materials. *Coordination Chemistry Reviews* **2020**, *420*, 213438. DOI: https://doi.org/10.1016/j.ccr.2020.213438.

(11) Wang, L.; Feng, X.; Ren, L.; Piao, Q.; Zhong, J.; Wang, Y.; Li, H.; Chen, Y.; Wang, B. Flexible Solid-State Supercapacitor Based on a Metal–Organic Framework Interwoven by Electrochemically-Deposited PANI. *Journal of the American Chemical Society* **2015**, *137* (15), 4920-4923. DOI: 10.1021/jacs.5b01613.

(12) Yu, D.; Qian, Q.; Wei, L.; Jiang, W.; Goh, K.; Wei, J.; Zhang, J.; Chen, Y. Emergence of fiber supercapacitors. *Chemical Society Reviews* **2015**, *44* (3), 647-662, Review. DOI: 10.1039/c4cs00286e Scopus. Wang, L.; Wei, T.; Sheng, L.; Jiang, L.; Wu, X.; Zhou, Q.; Yuan, B.; Yue, J.; Liu, Z.; Fan, Z. “Brick-and-mortar” sandwiched porous carbon building constructed by metal-organic framework and graphene: Ultrafast charge/discharge rate up to 2Vs−1 for supercapacitors. *Nano Energy* **2016**, *30*, 84-92. DOI: https://doi.org/10.1016/j.nanoen.2016.09.042. Wen, P.; Gong, P.; Sun, J.; Wang, J.; Yang, S. Design and synthesis of Ni-MOF/CNT composites and rGO/carbon nitride composites for an

asymmetric supercapacitor with high energy and power density. *Journal of Materials Chemistry A* **2015**, *3* (26), 13874-13883, 10.1039/C5TA02461G. DOI: 10.1039/C5TA02461G.

(13) Weng, Y.-T.; Pan, H.-A.; Lee, R.-C.; Huang, T.-Y.; Chu, Y.; Lee, J.-F.; Sheu, H.-S.; Wu, N.-L. Spatially Confined MnO2 Nanostructure Enabling Consecutive Reversible Charge Transfer from Mn(IV) to Mn(II) in a Mixed Pseudocapacitor-Battery Electrode. *Advanced Energy Materials* **2015**, *5* (18), 1500772. DOI: https://doi.org/10.1002/aenm.201500772.

(14) Shabangoli, Y.; Rahmanifar, M. S.; El-Kady, M. F.; Noori, A.; Mousavi, M. F.; Kaner, R. B. An integrated electrochemical device based on earth-abundant metals for both energy storage and conversion. *Energy Storage Materials* **2018**, *11*, 282-293. DOI: https://doi.org/10.1016/j.ensm.2017.09.010.

(15) Goswami, C.; Hazarika, K. K.; Bharali, P. Transition metal oxide nanocatalysts for oxygen reduction reaction. *Materials Science for Energy Technologies* **2018**, *1* (2), 117-128. DOI: https://doi.org/10.1016/j.mset.2018.06.005.

(16) Compton, R. G.; Banks, C. E. *Understanding Voltammetry (Third Edition)*; World Scientific Publishing Company, 2018.

(17) Li, H. B.; Yu, M. H.; Wang, F. X.; Liu, P.; Liang, Y.; Xiao, J.; Wang, C. X.; Tong, Y. X.; Yang, G. W. Amorphous nickel hydroxide nanospheres with ultrahigh capacitance and energy density as electrochemical pseudocapacitor materials. *Nature Communications* **2013**, *4* (1), 1894. DOI: 10.1038/ncomms2932.

(18) Zhang, J. T.; Liu, S.; Pan, G. L.; Li, G. R.; Gao, X. P. A 3D hierarchical porous α-Ni(OH)2/graphite nanosheet composite as an electrode material for supercapacitors. *Journal of Materials Chemistry A* **2014**, *2* (5), 1524-1529, 10.1039/C3TA13578K. DOI: 10.1039/C3TA13578K.

(19) Wang, Y.; Hong, Z.; Wei, M.; Xia, Y. Layered H2Ti6O13-Nanowires: A New Promising Pseudocapacitive Material in Non-Aqueous Electrolyte. *Advanced Functional Materials* **2012**, *22* (24), 5185-5193. DOI: https://doi.org/10.1002/adfm.201200766.

(20) Meng, F.; Fang, Z.; Li, Z.; Xu, W.; Wang, M.; Liu, Y.; Zhang, J.; Wang, W.; Zhao, D.; Guo, X. Porous Co3O4 materials prepared by solid-state thermolysis of a novel Co-MOF crystal and their superior energy storage performances for supercapacitors. *Journal of Materials Chemistry A* **2013**, *1* (24), 7235-7241, 10.1039/C3TA11054K. DOI: 10.1039/C3TA11054K.

(21) Campagnol, N.; Romero-Vara, R.; Deleu, W.; Stappers, L.; Binnemans, K.; De Vos, D. E.; Fransaer, J. A Hybrid Supercapacitor based on Porous Carbon and the Metal-Organic Framework MIL-100(Fe). *ChemElectroChem* **2014**, *1* (7), 1182-1188. DOI: https://doi.org/10.1002/celc.201402022.

(22) Lee, D. Y.; Shinde, D. V.; Kim, E.-K.; Lee, W.; Oh, I.-W.; Shrestha, N. K.; Lee, J. K.; Han, S.-H. Supercapacitive property of metal–organic-frameworks with different pore dimensions and morphology. *Microporous and Mesoporous Materials* **2013**, *171*, 53-57. DOI: https://doi.org/10.1016/j.micromeso.2012.12.039.

(23) Lee, D. Y.; Yoon, S. J.; Shrestha, N. K.; Lee, S.-H.; Ahn, H.; Han, S.-H. Unusual energy storage and charge retention in Co-based metal–organic-frameworks. *Microporous and Mesoporous Materials* **2012**, *153*, 163-165. DOI: https://doi.org/10.1016/j.micromeso.2011.12.040.

(24) Meng, W.; Chen, W.; Zhao, L.; Huang, Y.; Zhu, M.; Huang, Y.; Fu, Y.; Geng, F.; Yu, J.; Chen, X.; et al. Porous Fe3O4/carbon composite electrode material prepared from metal-organic framework template and effect of temperature on its capacitance. *Nano Energy* **2014**, *8*, 133-140. DOI: https://doi.org/10.1016/j.nanoen.2014.06.007.

Chapter 7 Conclusions

In this thesis, novel carbon-based materials were investigated with regard to renewable energy and energy storage devices. In detail, the carbon sources (e.g., boron-doped diamond, carbonised seaweed paper, filter paper, biowaste, etc.) were modified with various electroactive materials (e.g., manganese dioxide, nickel hydroxide, and pyrolysed bimetallic metal-organic frameworks) for electrochemical studies in supercapacitor applications.

In Chapter 3, the electrochemical behaviour of boron-doped diamond electrodes was studied for electrochemical energy applications. Electrochemical oxidation of Mn^{2+} on the electrodes was conducted via cyclic voltammetry, resulting in the formation of MnO_2 in multiple steps. To improve their performance for energy storage, MnO_2/BDD hybrid pseudocapacitors were fabricated by incorporating MnO_2 into BDD via potentiostatic deposition. As a result, the current response and obtained specific capacitance of the hybrid was much larger than that of a bare BDD electrode on account of pseudocapacitive MnO_2 deposition. Experimental parameters such as deposition potential, deposition time, electrolyte, scan rate and cycling were also studied. Other carbon structure with better performance should be considered in the future for supercapacitor applications.

In Chapter 4, a carbon source derived from seaweed paper was substituted for BDD to construct supercapacitors. The seaweed paper was carbonised at different temperatures, and some samples showed good specific capacitance in a negative potential range in CV. Potentiostatic deposition of manganese dioxide was employed to prepare hybrid supercapacitors, which enhanced the specific capacitance in a positive potential range without obvious loss of the stability. In addition, this improved performance was achieved by a relatively low mass loading of MnO_2 deposited, indicating that an economical and convenient modification method was

employed here. Other biomass-derived carbon is to be focused on as well as electroactive materials later.

In Chapter 5, another biomass-derived carbon material, carbonised filter paper, was produced at relatively low temperatures with a simple *in situ* nickel treatment. The as-prepared nickel treated carbonised filter paper (Ni-FP) was easily constructed as a negative electrode material by etching the Ni particles. Meanwhile, a positive electrode is obtained by electrochemical activating Ni-FP in aqueous alkaline media for supercapacitor applications. The Ni-FP exhibited a superior specific capacitance and excellent cycling stability on the positive potential side due to faradaic battery-type contributions from converted nickel hydroxide in KOH. Cheaper biomass sources and novel faradaic species are to be studied.

In Chapter 6, a number of biomass-derived novel carbon materials (i.e., seaweed paper, rice husks, Hinoki wood, and floor board waste) were modified with bimetallic Co/Mn metal–organic frameworks (MOFs). The electrochemical performance of the material in alkaline solutions not only benefited from the carbonised biomass (i.e., capacitive source) but also from the pyrolysed MOFs (i.e., faradaic source). Notably, better electrochemical performance in KOH than in KCl electrolyte was observed owing to the faradaic mechanism of metal oxides. In addition, different from powdery samples, bulk materials can be directly employed as an electrode without binding agents or substrates for electrochemical experiments. MOFs modified carbon derived from cheap and biowaste materials has a positive effect in supercapacitor applications.

To compare the results in each chapter, BDD electrodes in Chapter 3 mainly acted as conductive substrates in supercapacitors with subtle capacitive contributions. The electrochemical performance was largely improved by introducing pseudocapacitive MnO_2 via potentiostatic deposition as hybrid supercapacitor electrode materials. However, the specific

capacitance cannot be increased continuously with higher MnO_2 mass loading. In Chapter 4, seaweed paper derived carbon with porous and conductive nanostructure was thus produced. Different from BDD, carbonised seaweed paper not only served as a conductive substrate, but also provided considerable electric double layer capacitance in a negative potential window. The incorporation of MnO_2 into carbonised seaweed paper via a potentiostatic deposition method similar to Chapter 3 further improved the specific capacitance at a positive potential side with excellent stability. Apart from the use of pseudocapacitive MnO_2 in Chapter 3 and 4, faradaic battery-type material was employed in Chapter 5. Nickel treated filter paper carbonised at 800 °C showed superior specific capacitance but inferior stability compared to the MnO_2/carbonised seaweed paper composites in Chapter 4 due to the battery-type electroactive contribution and behaviour of $Ni(OH)_2$. In addition, the Ni treatment of filter paper was produced under lower carbonisation temperatures, and ideal electric double-layer capacitance was observed on nickel treated filter paper after Ni particles being removed. In Chapter 6, a battery of cheaper biomass/biowaste derived carbons were prepared with pyrolysed bimetallic Co/Mn MOFs modification. Although the specific capacitances were not as high as those of MnO_2/carbonised seaweed paper in Chapter 4 and Ni-FP in Chapter 5, these bulk biowaste derived carbon composite materials showed potential of scalability and stability in commercial applications. To summarise, the whole work displayed competitive results among a number of studies in supercapacitors, as discussed in the conclusion section of each chapter. In particular, carbon materials were prepared with low cost and simple steps, modified with electroactive materials at convenience, and employed as composite electrodes for measurements directly in this work. Hence, the potential of novel carbon-based materials for supercapacitor applications provides us with a competitive candidate in energy storage from a new perspective.

In the future, different types of raw materials such as other fast grown seaweed/algae species and biomass wastes can be studied as novel sources of high-quality carbon, which requires fundamental understanding of conversion mechanisms of activation/carbonisation processes. More importantly, most biomass materials have their unique natural structures through biological evolution, and such diverse structural templates should be utilised well for biomass carbon fabrication. Therefore, preparation of controllable and hierarchical porous nanocarbon structures is highly promising and desirable, as parameters including porosity and pore size distribution have a significant impact on the electrochemical performance such as specific capacitance and rate capability. Furthermore, incorporation of other electroactive components into carbon can be optimised and developed, and the as-prepared carbon-based composite materials can not only provide additional electrochemical performance in supercapacitors but also see plenty of scope for a wider range of applications. Last, preparation of flexible, free-standing and large-scale devices for practical and commercial applications remains challenging, but carbon-based materials fabricated as fibres or foams may meet such requirements.

Appendix

Figure A.1 Cyclic voltammograms of MnO_2/BDD deposited at +0.85 V for (a) 50 s, (b) 100 s, (c) 200 s, (d) 300 s, (e) 400 s and (f) 600 s at scan rate of 5, 10, 25, 50, 100 and 200 mV s^{-1}, respectively. Experimental parameters: electrolyte: 3M KCl; potential window: 0 to +0.8 V. Calculation of specific capacitance in Table 3.3 is based on CVs in this figure.

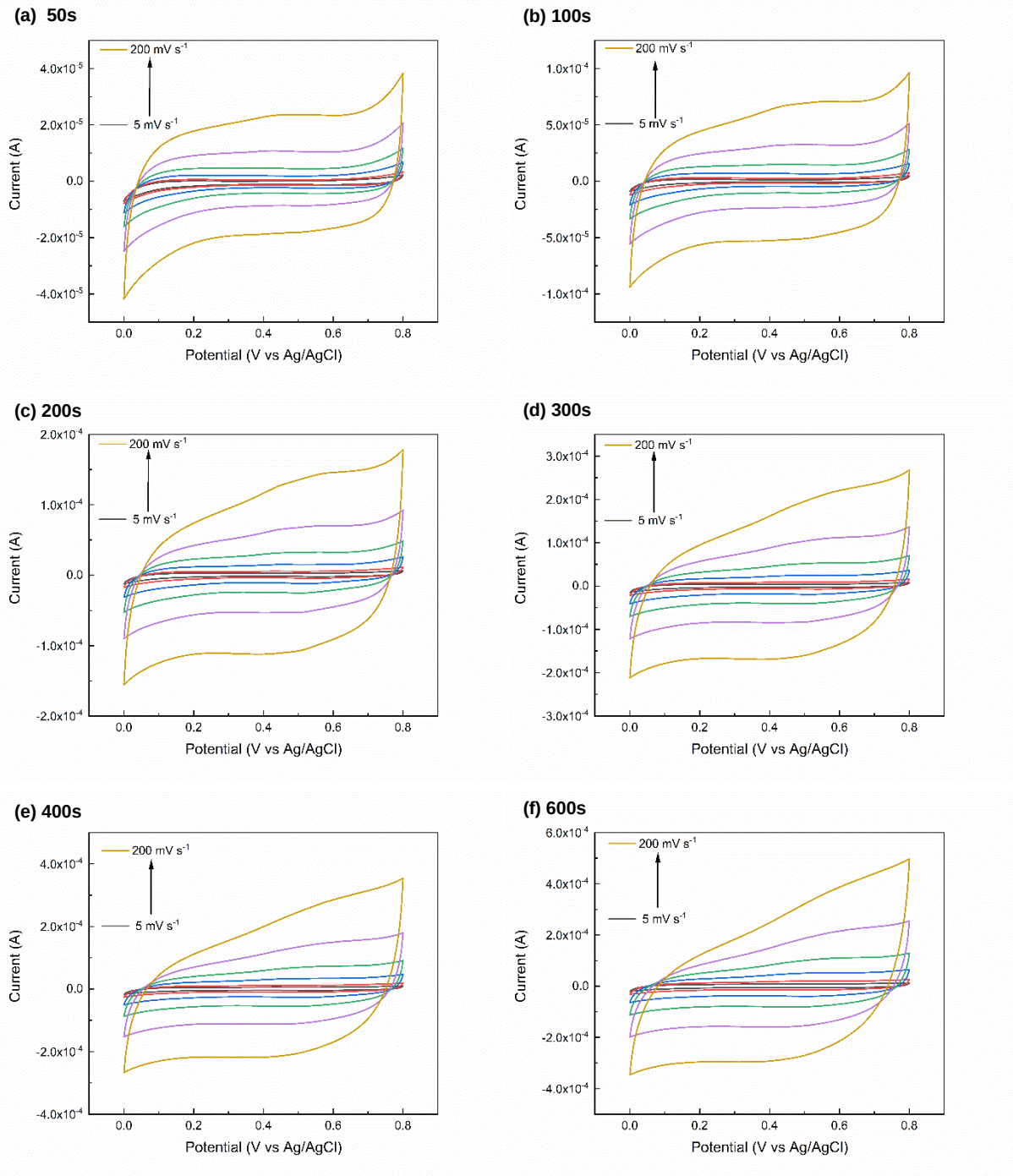

Figure A.2 CV curves of seaweed paper carbonised at different temperatures (600 to 1300 °C) with increasing scan rates (2 to 200 mV s^{-1}) in two potential windows (0 to -0.8 V & 0 to +0.8 V). Calculation of specific capacitance in Table 4.2 & 4.3 is based on CVs in this figure.

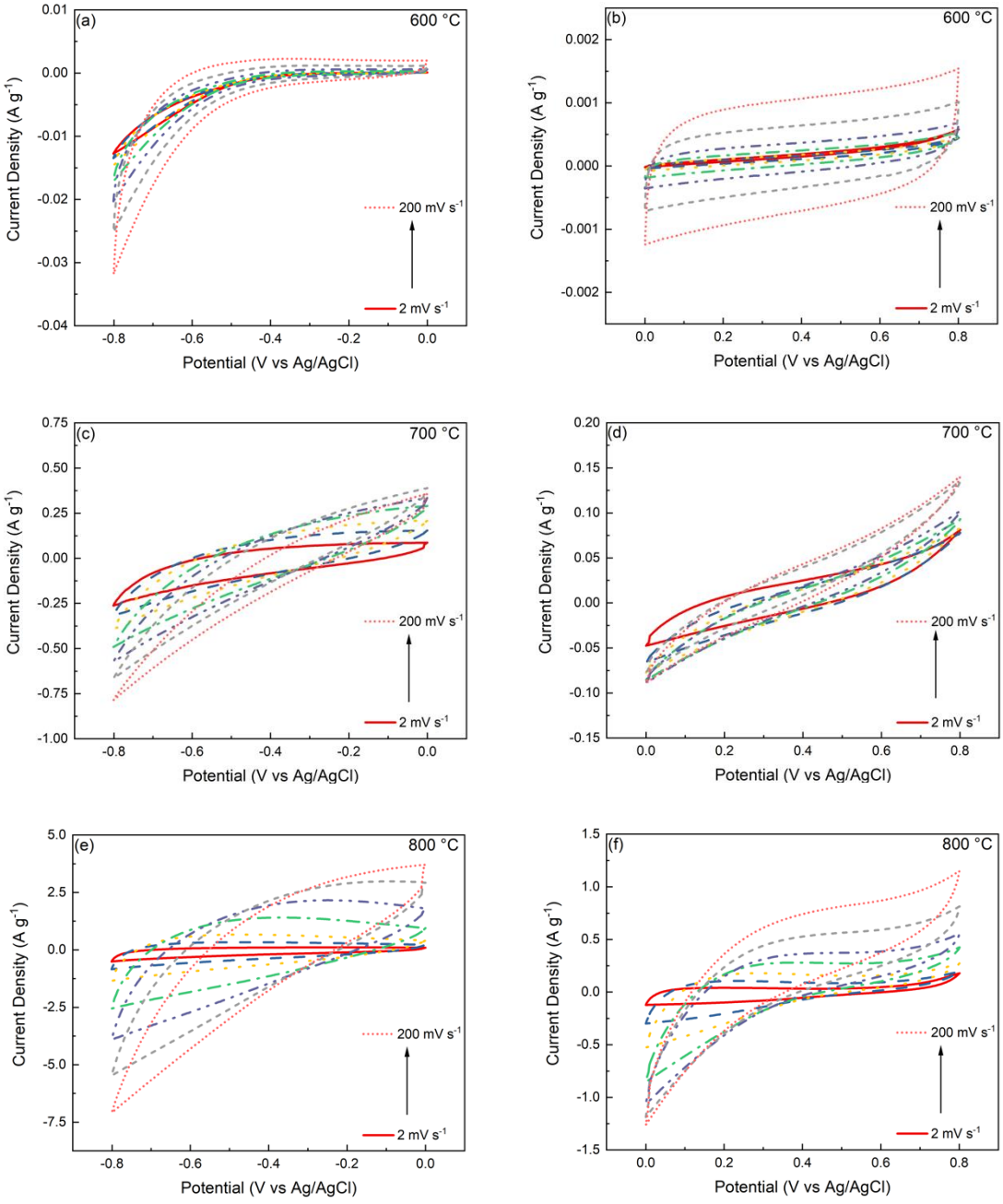

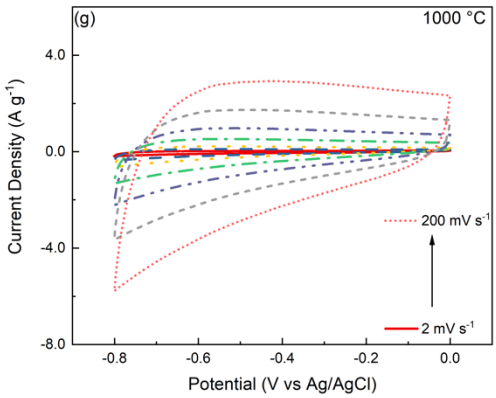
(g)
1000 °C
Current Density (A g-1)
Potential (V vs Ag/AgCl)
200 mV s-1
2 mV s-1

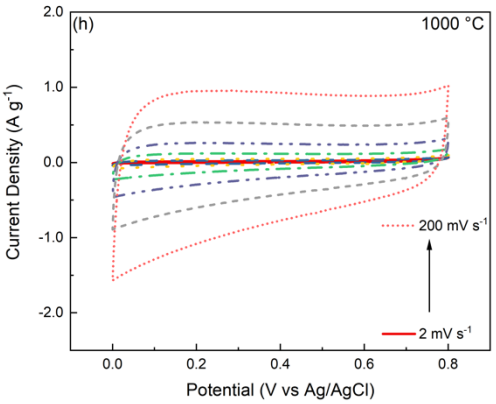
(h)
1000 °C
Current Density (A g-1)
Potential (V vs Ag/AgCl)
200 mV s-1
2 mV s-1

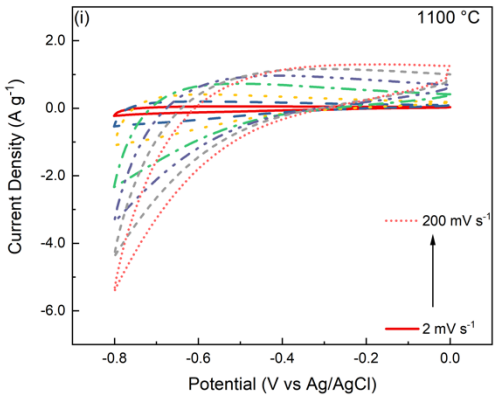
(i)
1100 °C
Current Density (A g-1)
Potential (V vs Ag/AgCl)
200 mV s-1
2 mV s-1

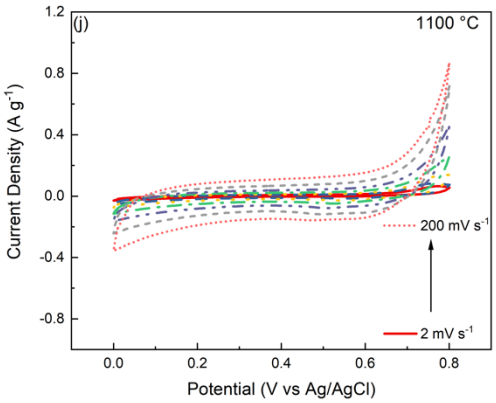
(j)
1100 °C
Current Density (A g-1)
Potential (V vs Ag/AgCl)
200 mV s-1
2 mV s-1

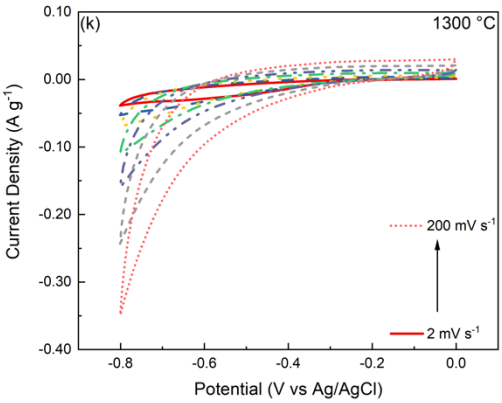
(k)
1300 °C
Current Density (A g-1)
Potential (V vs Ag/AgCl)
200 mV s-1
2 mV s-1

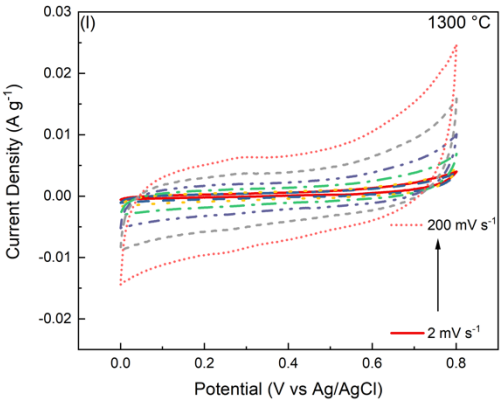
(l)
1300 °C
Current Density (A g-1)
Potential (V vs Ag/AgCl)
200 mV s-1
2 mV s-1

Figure A.3 Chronoamperograms of MnO_2 deposition at +1.15V with different deposition times (50 to 1200 s) compared to background current. Calculation of mass of MnO_2 deposited is based on the *i-t* curves in this figure.

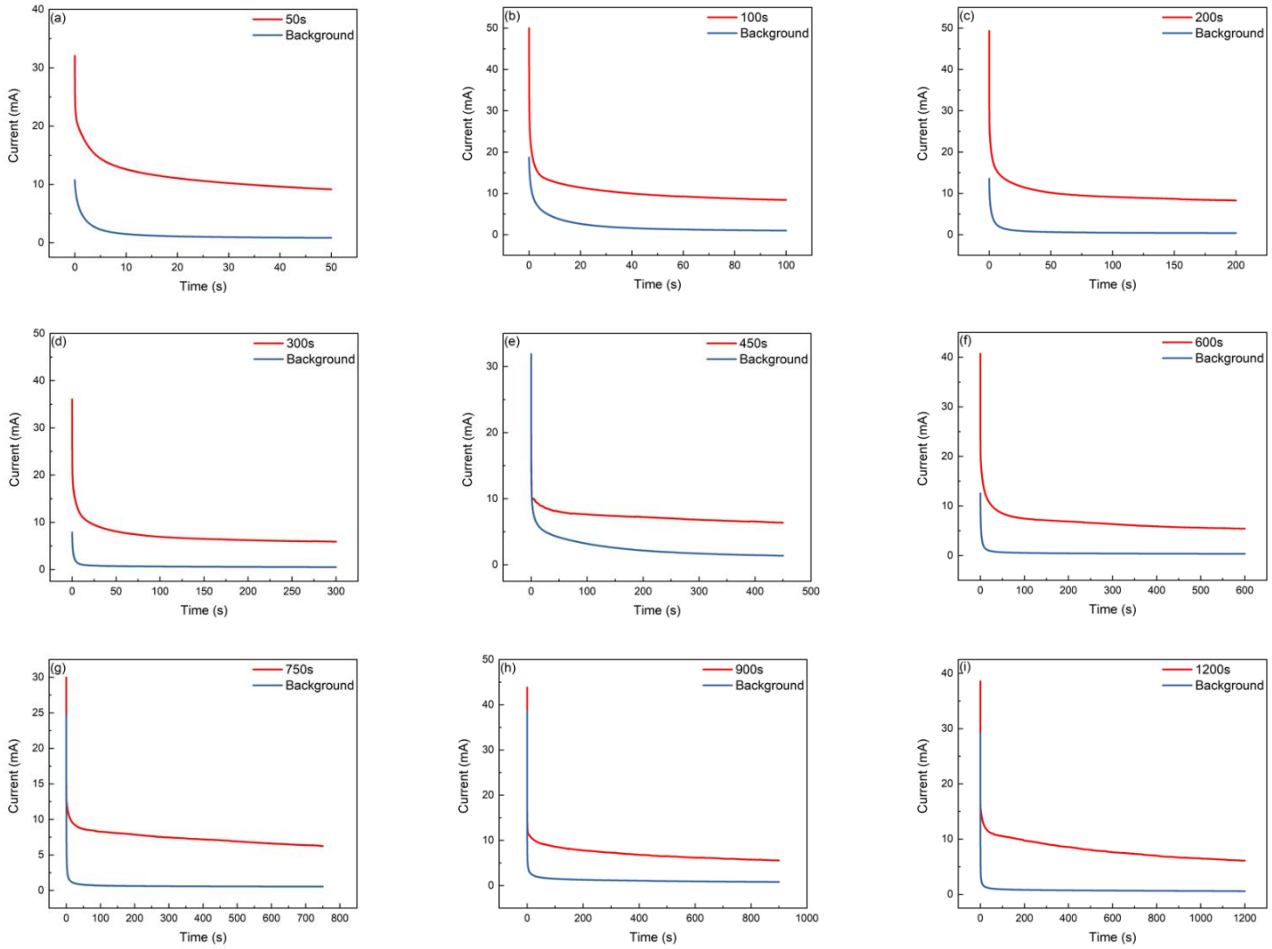

Figure A.4 Cyclic voltammograms of carbonised seaweed paper/MnO_2 at different deposition times (50 to 1200 s) with increasing scan rates (2 to 200 mV s^{-1}). Calculation of specific capacitance in Table 4.4 is based on CVs in this figure.

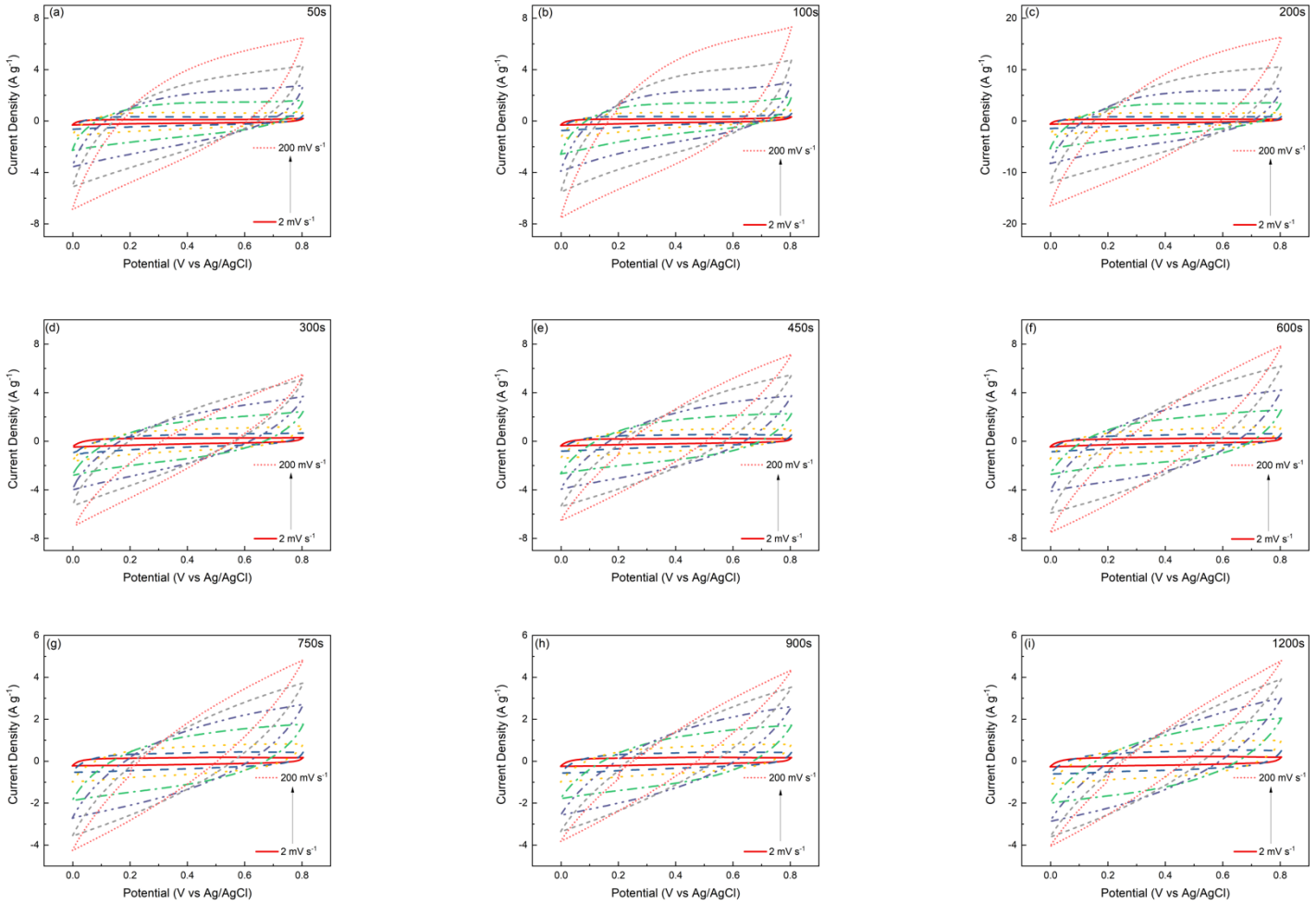

Figure A.5 Chronopotentiograms (GCD) of seaweed paper/MnO_2 at different deposition times (50 to 1200 s) with increasing current densities (0.5 to 10 A g^{-1}). Calculation of specific capacitance in Table 4.5 is based on GCD curves in this figure.

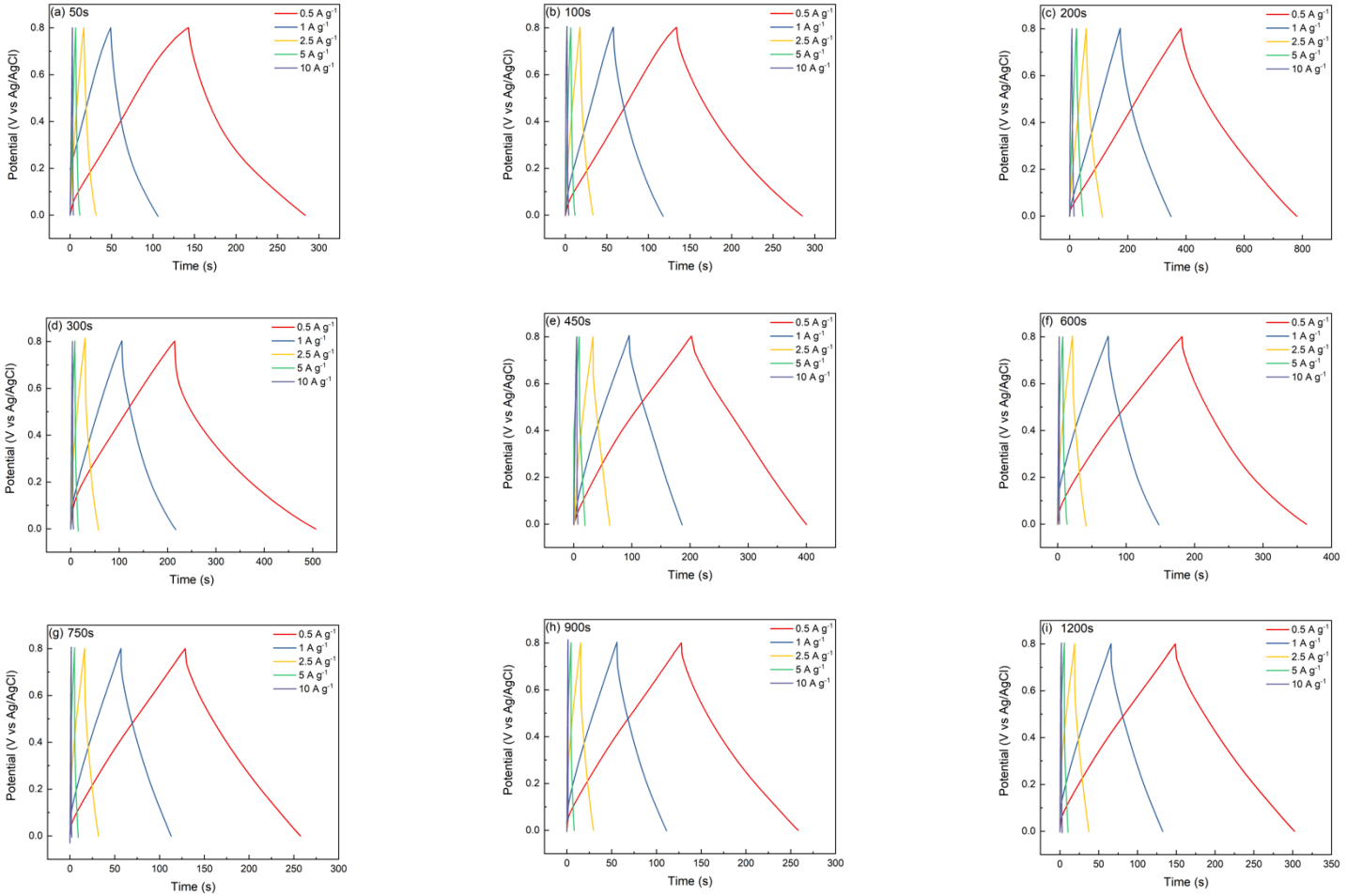

Figure A.6 The capacitance retention of seaweed paper/MnO_2 with different deposition times (50 to 600 s) at the current density of 1 A g^{-1}.

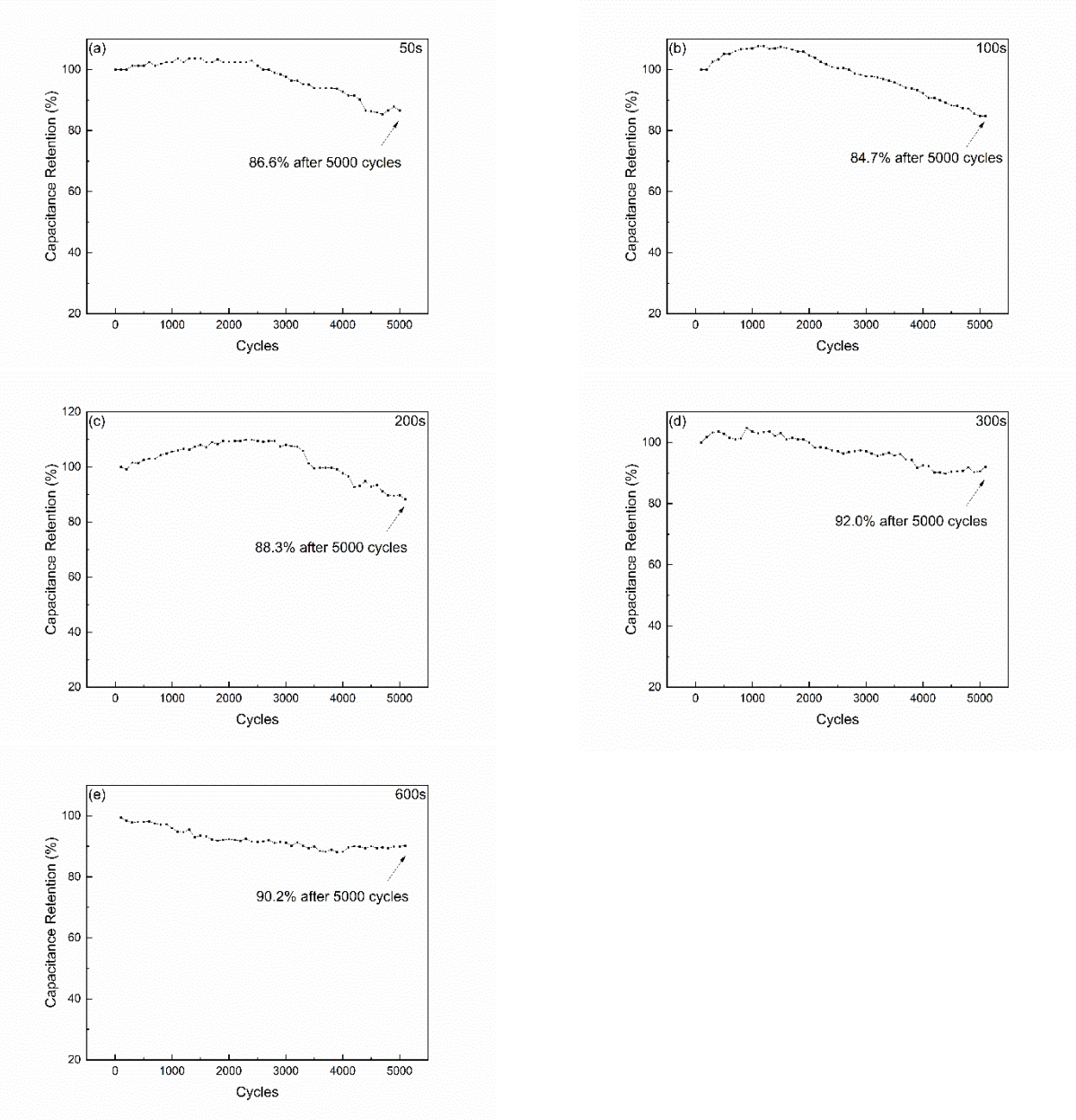

Figure A.7 Cyclic voltammograms of 600 to 1300 °C carbonised Ni-FP in 1M KOH from 2 to 200 mV s^{-1} in a positive potential range of 0 to +0.7 V. Calculation of specific capacitance in Table 5.1 is based on CVs in this figure.

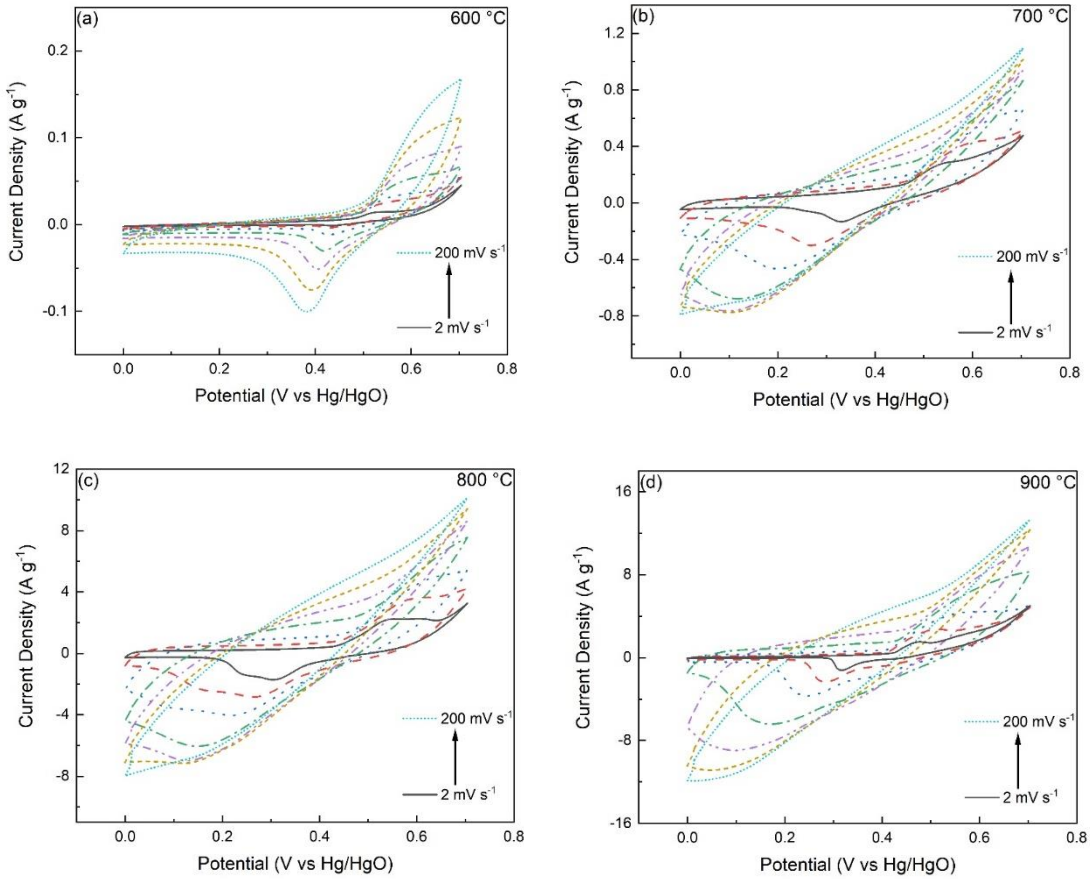

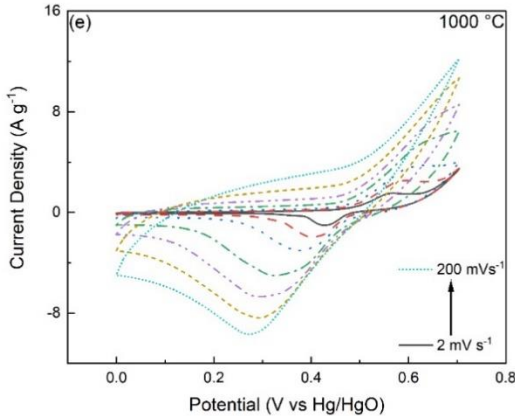
(e)
1000 °C
Current Density (A g-1)
Potential (V vs Hg/HgO)
200 mVs-1
2 mV s-1

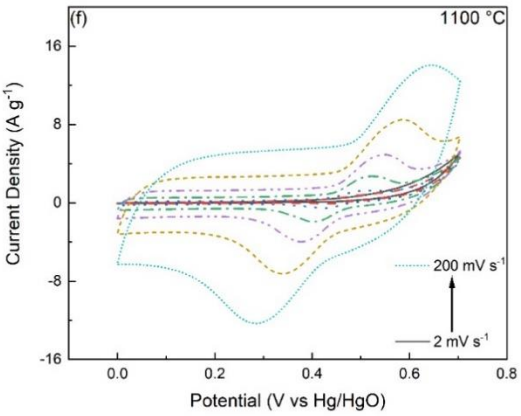
(f)
1100 °C
Current Density (A g-1)
Potential (V vs Hg/HgO)
200 mV s-1
2 mV s-1

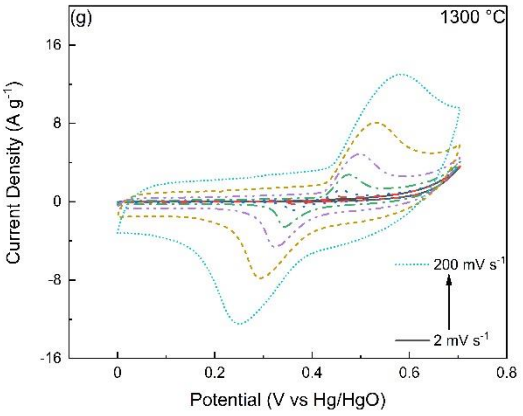
(g)
1300 °C
Current Density (A g-1)
Potential (V vs Hg/HgO)
200 mV s-1
2 mV s-1